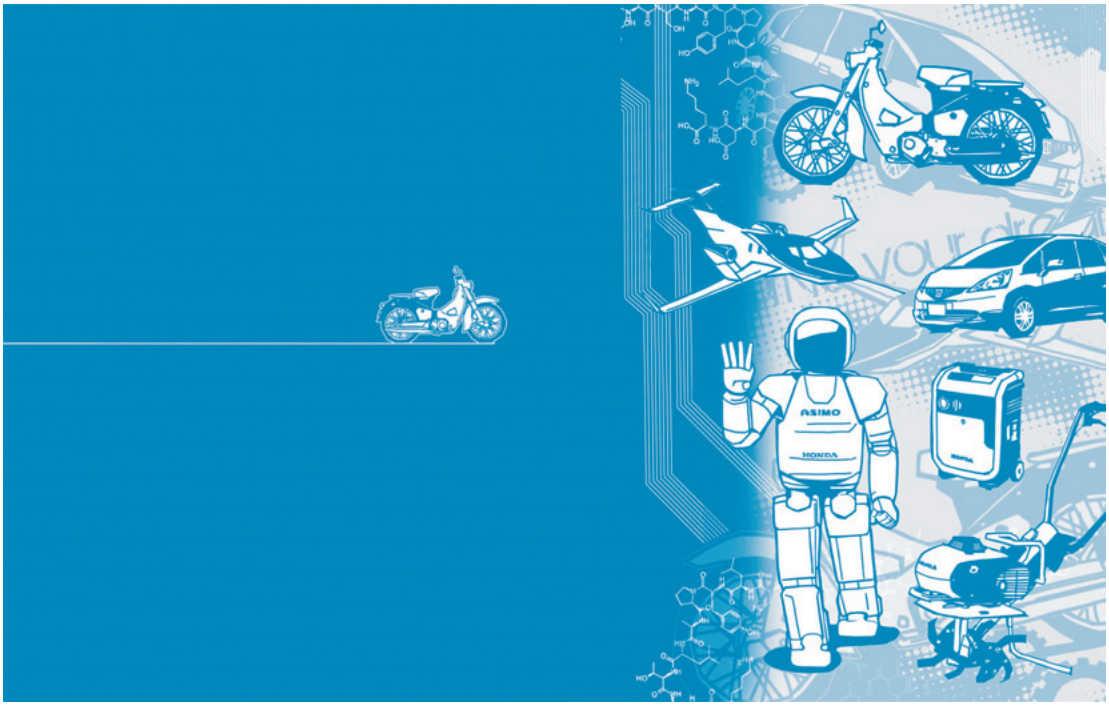

Honda R&D
Technical Review
ASIMO
HONDA
October 2012
Vol.24 No.2



Comment on the Cover

Honda's role as a company is to enrich daily life with technologies and ideas – this spirit remains as strong today as it was in the past.

We will go forward into the future as an enterprise offering products of such excellence that they become intimate companions to our customers and a benefit to the planet.

It is these qualities which we have sought to manifest through design.



Automobile R&D Center
Ayako Kato

Technical Review

October
2012

Honda R&D

CONTENTS

Introduction of new technologies

Styling Design of New Accord . . . . . Toshiyuki OKUMOTO・Hiroki SHIGEHARA
. . . . . Satoshi UCHIDA・Mie KOBAYASHI 1

Styling Design of New CR-V . . . . . Manabu KONAKA・Takehiro ISHIBASHI
. . . . . Daisuke MORISHITA・Hiroaki RYU 8

Styling Design of NC700 Series . . . . . Kazuhiro KUDO 15

Development of NC700 Series . . . . . Koki KOBAYASHI・Masaaki NEGORO・Takanori OSUKA
. . . . . Toshimasa MITSUBORI・Tadashi OSHIMA 23

Development of NSF250R Commercial Road Racer with 4-stroke Engine
. . . . . Tomio ONOSATO・Yoshiyuki KURAYOSHI 32

Development of BF250 Flagship Outboard Motor
. . . . . Yoshihiro HARADA・Kazuhiro ISHIZAKA・Go TANAKA
Kunihiko ISHIZUKA・Fumiya ISONO 40

Development of New CVT for Midsize Vehicle
. . . . . Koichiro INUKAI・Akihiro SHIBAHARA・Yasunori MURAKAMI
Takeshi UCHINO・Michio KOJIMA・Keiichi NISHIYAMA 47

Development of New Manual Transmission for Middle-Torque Engine
. . . . . Takashi YOKOYAMA・Keiji KUZUHARA・Masahiro HAGINIWA
Takumi TAKAHASHI・Akira NAKAMURA 54

Development of Rare Earth-saving Magnet Using Localized Diffusion Method
. . . . . Takehiro MIYOSHI・Takayuki HIGASHI
Masashi INOUE・Kojiro OHSAKI 62

Development of Anti-allergenic Compound for Durability of Automotive Seat Fabric . . . . . Rie HAYASHI 69

Verification Test of High Differential Pressure Water Electrolysis-type Solar Hydrogen Station (SHS2)
. . . . . Hisashi NAGAOKA・Nobuyoshi YOSHIDA・David CUN
Ikuya YAMASHITA・Masanori OKABE 74

Technical papers

Control Method to Reduce Degradation in Fuel Cell System at Start-up
. . . . . Koichiro FURUSAWA・Kentaro NAGOSHI・Satoshi TANIMOTO 82

Hydrogen Adsorption MOF Design and Adsorption Characteristics . . . . . .Terumi FURUTA・Mitsuya HOSOE
Izuru KANOYA・Hiroshi SAKAI 89

Analysis on Mechanism of Early Clogging in Suction Filter with Use of Ethanol Blended Fuel
and Development of Long-life Filter . . . . . Shingo ARAI・Atsushi ITO・Tsubasa ISHII
Hideaki ANDO・Keita KINOSHITA・Fujio UMEBAYASHI 98

Development of Real-time Aerodynamic Design System
. . . . . .Takahiro FUKUSHIGE・Tokitomo ARIYOSHI・Yusuke UDA
. . . . . Yuki OKUMA・Tatsuya OKABE・Koichi YAMAMOTO
Lars GRAENING・Stefan MENZEL・Markus OLHOFER 107

Development of High-strength and High-wear Resistance Nitrocarburizing Steel by Precipitation
Strengthening of Mo-V Carbonitride . . . . . .Hiroki MASUDA・Hideki MATSUDA・Ayumi YAMAZAKI 117

Development of High-performance Engine Plant Model and Sequential System Identification Environment
for Realization of Model-based Development
. . . . . .Shigeki FUJIMOTO・Yoshiyuki OHTAKA・Satoshi KODO 126

Estimation of CO_2 Reduction Potential by Traffic-flow Smoothing and Eco-driving Promotion
. . . . . Hidetoshi IMAIZUMI・Koji SENGOKU 134

Styling Design of New Accord

Toshiyuki OKUMOTO* Hiroki SHIGEHARA*
Satoshi UCHIDA** Mie KOBAYASHI**

ABSTRACT

With “Excels in All Areas” as the grand concept, the new Accord was developed as a family sedan that could be used comfortably, and with pleasure and pride, every day.

Organized around the themes “Exhilaration,” “Advancement,” and “Superior Craftsmanship,” the design realizes a comfortable space and a strong presence as a family sedan. The exterior design was based on the concepts “Exhilaration” and “Condensation,” while “Luxurious Modern Interior” served as the concept for the interior design. Interior and exterior colors and interior fabrics were developed to further highlight these characteristics.

1. Introduction

Successive Accord models have continued to find favor with large numbers of users due to many characteristics including reliability and safety, and customer satisfaction with their Accords is uniformly high. In the U.S. market in particular, the popularity of the Accord has grown to the extent that the vehicle can be seen as synonymous with the category “midsize family sedan.” For the development of the 9th-generation Accord, a survey of U.S. family sedan users was conducted to study the patterns of vehicle use. By contrast with the results of previous surveys showing that sedans were mainly used for commuting to and from work, this study indicated an increase in the frequency of sedan use for family outings on the weekends rather than the use of minivans.

This background picture indicated that the rising price of gasoline and increasing environmental awareness had resulted in a greater number of customers making judicious use of sedans based on their good fuel efficiency. As they used their sedans with greater frequency, users were saying that they wanted a more comfortable interior space and increased ease of use, and suggesting that the vehicles were slightly too large. These were also valuable hints for the development process.

The design team set the realization of “Excels in All Areas,” which would offer the maximum pleasure to users as its grand concept. Seeking to delight customers with a level of luxury in excess of expectations based on the price of the vehicle, the team set itself the target of expressing true value and realizing a family sedan that would be globally popular and actively desired by customers through the creation of the optimal package and a design that maintained a careful focus on even the smallest details (Fig. 1).

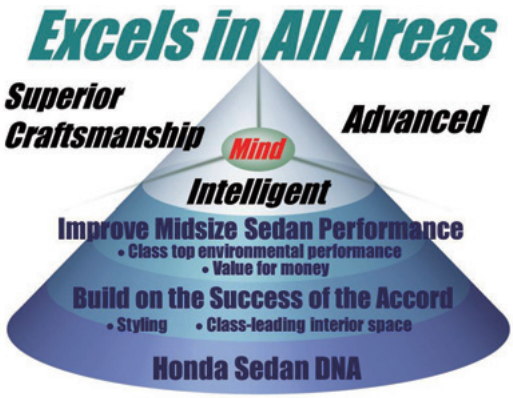


Fig. 1 Grand concept

2. Design Goals

The design of the new Accord was developed on the basis of three themes: “Exhilaration,” “Advancement,” and “Superior Craftsmanship.”

Under the theme “Exhilaration,” designers aimed at a further evolution of the large cabin space that is one of the strengths of the Accord. The design of the space sought not merely to create a sense of roominess, but also to realize a bright space with a wide field of vision, one that users would find comfortable and pleasurable every day.

* Automobile R&D Center
** HONDA R&D AMERICAS, INC.

Under the theme "Advancement," the aim was to make the vehicle a pleasure to use by providing user support via more advanced technology, and creating a vehicle that users would find intuitively easy to understand and easy to use. The design aimed for a new expression of value by incorporating ease of movement and operation as an aspect of design at the same time as expressing new technology via new design.

Under the theme "Superior Craftsmanship," designers aimed to focus on even the smallest details of the design in order to create a sense of real, crafted quality, producing a car that the owner could be proud of and that engendered a feeling of satisfaction and fulfillment.

3. Package Layout

The concept for the package layout was to create an exhilarating and efficient package incorporating an optimized body framework to respond to fuel efficiency demands and other environmental considerations, and carrying over the Accord's comfortable cabin space while realizing new value for the sedan class.

Seeking to realize a feeling of "Exhilaration," the design team aimed to achieve a wider forward field of vision offering a sense of freedom and increased cabin comfort by rounding the front windshield and moving the front pillars forward, in addition to reducing the pillar diameters and modifying their cross-sectional shape. The wheelbase was shortened by 25 mm against previous Accords while modification of the passenger seating position and the form of the seats increased knee space by 0.5 mm, resulting in a comfortable cabin space with a superb level of space.

With the aim of realizing a sense of exhilaration and new level of sedan value, the rear passenger seats were moved inward by 15 mm each side to produce a V-shaped layout, and the center pillars were moved outwards, creating a layout offering the sense of a broad field of vision from the rear seats as well (Fig. 2).

To realize a sense of "Advancement," vehicle aerodynamic performance was refined through a reexamination from the framework up in order to increase fuel efficiency. The air flow around the sides of the vehicle body was optimized by narrowing the overall body, extending the surrounds of the center pillars outwards, and moving the front pillars and the rear pillars inwards to produce a barrel-shaped form. The total height of the vehicle was lowered by 10 mm without sacrificing cabin space, reducing the front projected area and increasing aerodynamic performance.

With regard to the size of the body, the design sought to increase fuel efficiency by reducing weight and realizing the optimum easy-to-handle mid-size package for a family car by shortening the wheelbase and reducing the front-rear overhang to shorten the total length by 90 mm (Fig. 3).

Under the theme "Superior Craftsmanship," designers worked to give users the sense of a high level of product quality by realizing an interior space with sufficient room for four adults to relax in comfort, and applying detailed attention even to the trunk floor in order to produce a flat surface with minimal irregularities.

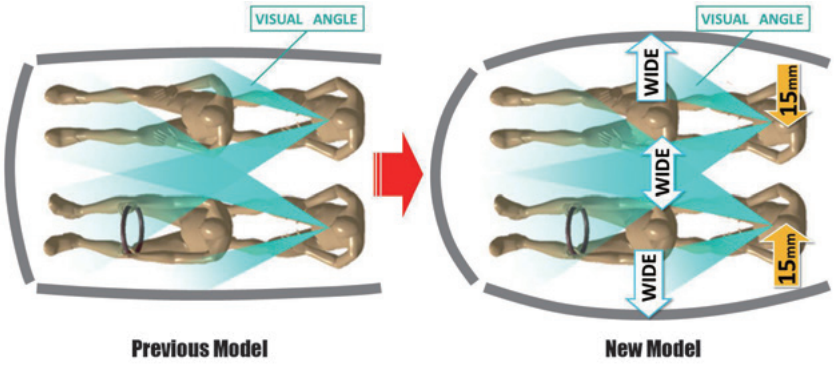


Fig. 2 Passenger layout

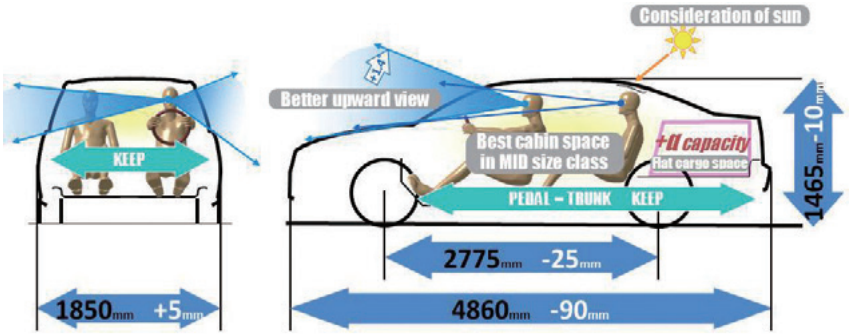


Fig. 3 Package layout

4. Exterior Design

The exterior design of the new Accord is styled to project a dynamic and intelligent presence, based around a concept of "Exhilaration and Condensation" (Fig. 4). "Condensation" in this context refers to the vehicle's dynamic and deeply sculpted form, powerfully tensed and with a strong continuity between all the body surfaces.

To realize a feeling of "Exhilaration," the designers worked to create a sense of the width and comfort of the cabin space even from outside the vehicle. They achieved this by making the front windscreen area look wider through the use of narrow front pillars and low belt lines in addition to using three-dimensionally curved glass in order to emphasize the image of overall rounding.

To achieve a feeling of "Advancement," the vehicle incorporates a new wide and strong-looking front face that extends horizontally, employing a configuration with continuity between the front grille and the headlights (Fig. 5). The vehicle uses projector-type headlights as standard, while the luxury Touring model employs LED low beams for the first time, in a design that offers a sense of strength and advancement (Fig. 6). The bottom edges of the front and rear bumpers are designed to produce the impression that metal-plated bars are floating, aiming for a new light and sporty expression (Fig. 7).

To realize a sense of "Superior Craftsmanship," the body framework was created on a horizontal base line extending from the nose to the trunk in order to present a powerful dynamism and a traditional sedan-like body feel. The areas surrounding the vehicle's cabin appear large, and this might have given an impression of instability due to the apparently high center of gravity and might have emphasized the smallness of the body, but the continuity of the form extending from the nose to the cabin and from the cabin to the trunk has given the vehicle a solid form with a sense of integration. Additionally, the thick and powerful hood and trunk forms present a luxury vehicle feel.

The sides of the body present two sharp character lines formed from deeply sculpted negative planes, and the extended forms of the powerful front and rear fenders create a dynamic, high-quality and three-dimensional surface that transforms from negative to positive planes (Fig. 8).



Fig. 4 Exterior design concept


Fig. 6 LED headlight



Fig. 5 Front design



Fig. 7 Bumper design


Fig. 8 Final rendering

From the rear, the narrowed plane extending from the cabin to the trunk and the overhanging form of the rear fender emphasize a vehicle posture in which the tires appear to strongly grip the ground, and present a luxury vehicle feel. In addition, the large trunk lid lights and the metal-plated garnish strip connecting the rear combination lights emphasize the vehicle's basic side styling, expressing a sense of presence based on width and stability (Fig. 9).



Fig. 9 Rear design

5. Interior Design

Organized around the concept "Luxurious Modern Interior," the interior design of the new Accord sought to provide a pleasant and exhilarating space, an easy-to-see and easy-to-use interface, and a clear sense of high quality (Fig. 10).

To realize "Exhilaration," the design theme was to maximally emphasize the horizontal width of the cabin via the symmetry and extension to the sides of the instrument panel. A sense of exhilaration was expressed with consideration of a balance of structural volumes that would help prevent vehicle occupants from feeling exposed while the vehicle is in motion. Another design theme was the imparting of a sense of freedom around the level of occupants' shoulders by means of interior styling in which the surface skin of the door linings extends to the upper surfaces (Fig. 11).



Fig. 10 Interior design concept

"Advancement" was realized by arraying the displays in the upper area of the instrument panel, minimizing the angle in the driver's line of sight at which the driver looks down and shifts resulting in easier-to-read displays. The vehicle's operational controls are positioned so as to make them more accessible to vehicle occupants, and the air conditioning, audio, and other controls are separated by function, making the operational interface easier to understand and easier to use (Fig. 12).

A large, eight-inch center display is positioned in the middle of the instrument panel to display a variety of information, including fuel consumption and audio information, and information to provide support for vehicle operation. In addition, the display screens employ simple graphic design to create a functional and advanced interface that enables information to be taken in instantly while driving.

New "On-demand Audio" has been used for the audio switches. This consists of a touch panel monitor designed for easier operability that employs an interface design tailored for intuitive operation and displays only the necessary switches at the necessary time and at the optimum size. This design sought both to realize a sense of "Advancement" and to increase ease of use (Fig. 13).



Fig. 11 Interior design



Fig. 12 Interface concept



Fig. 13 On-demand audio

The area around the console has also been designed to increase ease of use by newly positioning a USB jack in an easily accessible front tray to make it possible for vehicle users to easily use portable devices.

To realize "Superior Craftsmanship," the sense of quality of the interior as a whole was increased through the application of soft padding to the upper sections of the instrument panel and the door panels, and the effective use of ornamentation in areas that would tend to attract the attention of vehicle occupants. Designers sought to increase ease of recognition and achieve a sense of high quality by ornamenting functional components with chrome plating that would reflect light both during the day and at night (Fig. 14).

Design features including the use of large and bold ornamentation at the sides of the console present the feel of a midsize sedan. The position of the rear outlet has been moved upwards to increase the comfort of rear seat passengers (Fig. 15).

For the design of the seats, stitching and other features have been employed more effectively than in previous Accords in order to increase the sense of quality. The center of the seat backs is designed as a concave negative form, offering occupants a better sense of fit (Fig. 16).



Fig. 14 Chrome plating



Fig. 15 Console design

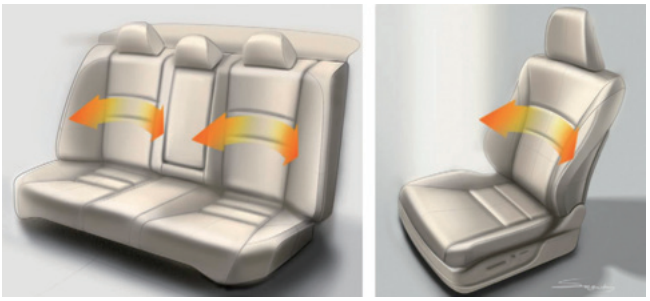


Fig. 16 Seat design

6. Color and Fabric Design

6.1. Exterior Color

Based on the concept "LIQUID TENSION COLOR," designers aimed for textures with a sense of tension and firmness like the surface of a liquid (Fig. 17). The lineup features a total of eight colors including four new: two "character colors" created from combinations of relaxing chromatic colors suggestive of the image of family sedans, and two standard colors that have been evolved to suit the times.

The "character colors," HEMATITE M. and CHAMPAGNE FROST P., combine minute amounts of dichromatic pearl pigments with fine-grained brightening agents to increase the complexity of the shades. CHAMPAGNE FROST P. suggests a soft blue tone amidst bright ivory, while HEMATITE M. was created with gray as the base color underlying a surface green tone.

The evolved standard colors MODERN STEEL M. and OBSIDIAN BLUE P. were designed based on extensive consideration of trends in colors used in previous models and examination of tones. To realize a sense of high quality in MODERN STEEL M., finer aluminum flakes than conventionally used were added, and the direction of previous trends was followed by adding a red tone and reducing the level of brightness, thus producing a stylish ambience and a sense of powerful three-dimensionality. The design of OBSIDIAN BLUE P. considered how to realize a blue tinge and a sense of depth, and employed an interference pearl of



Fig. 17 Exterior color concept

greater intensity than usual to realize a beautiful chromatic transition from a dark base color with a feeling of depth to a blue tone with vibrant highlights (Fig. 18).

The refinement and evolved textures offered by both the new character colors and the new standard colors serve to further highlight the feeling of presence produced by the styling.

6.2. Interior Color

Around the concept of "Premium Harmony," the interior color design coordinated internal fittings for three different possible color choices - a bright, elegant ivory, gray, and black - in order to create a sense of integration (Fig. 19).

Muting the intensity of the color of the ivory and gray internal fittings to a greater degree than has conventionally been the case has heightened the clean and elegant impression of the interiors. In both cases the standard colors have been revived.

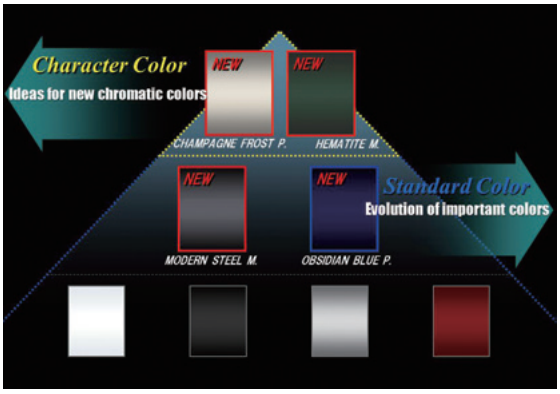


Fig. 18 Exterior color line-up



Fig. 19 Interior color concept

The three color choices for the internal fittings are offered in the basic grades (LX, EX, and EXL), while the newly added SPORTS grade offers two colors, with interior fittings restricted to black or ivory (Fig. 20).

To give vehicle occupants a sense of security and high quality, soft pads have been employed on doors and other parts with which occupants will come into physical contact, in order to enhance a soft feel and texture. Stitching has been increased to further heighten the sense of quality, and small areas of lustrous silver ornamentation and metal platings are used throughout the interior in an elegant and luxurious coordination of materials.

Designers sought to use a leather-grain pattern throughout the interior to realize a sense of high quality and soft textures, and materials that would offer the natural texture and three-dimensionality of real leather were developed for this purpose. To increase the integration of the interior textures, simple grain configurations were used that took differences in the methods of manufacture of parts into consideration (skins are wound onto the instrument panel and upper sections of the door linings, while etching is used for other parts). A total of three types of interior ornamentation have been employed, composed of coatings used to increase the sense of quality, and films of two patterns. Variations on the latter are able to be produced using the same molds.

METAL MESH, used in the LX-grade vehicles, applies a metallic coating to a fine-meshed, light-diffusing grain pattern to realize high-brightness metallic ornamentation that does not rely exclusively on the quality of the coating material.

SELENITE BROWN, used in the EX- and EXL-grade vehicles, is a film ornamentation that combines a pattern suggestive of mineral crystals and a dark brown metallic color to realize a texture, neither wood grain or metallic, which offers new value. FULL GLOSS DOT BLACK, used in the Sports-grade model, is a film ornamentation featuring small silver dots on a base of full-cloth fabrics that give an impression of sharpness to realize a sense of detail and elaboration.

For the seat trim fabrics, the LX-grade uses double russel, while the EX-grade uses velour tricot. The fabrics have a thick feel and offer a sense of security. A soft-weave

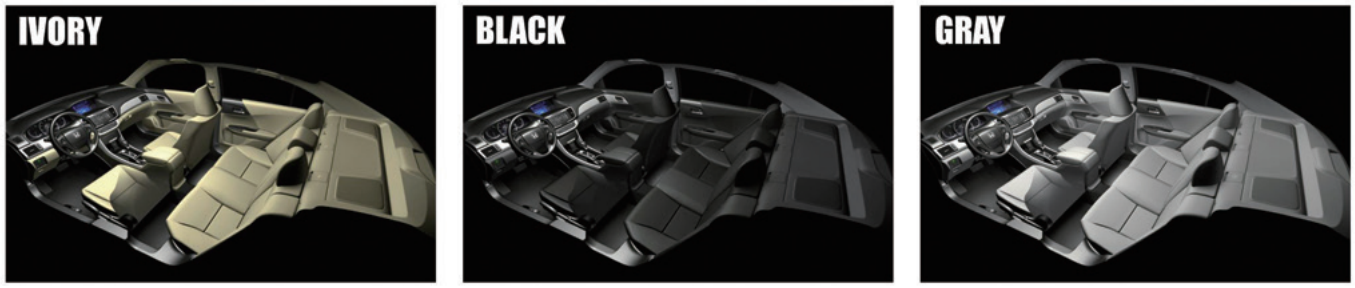


Fig. 20 Interior color variations

fabric that offers a heightened impression of sharpness is used in the Sports-grade model. Perforation rather than the previous gathering is used for the leather in the EXL-grade vehicle to give a sense of lightness. In addition, the use of gradated perforations that trace the design of the broad seat pattern imparts a sense of tempo to the interior as a whole (Fig. 21).

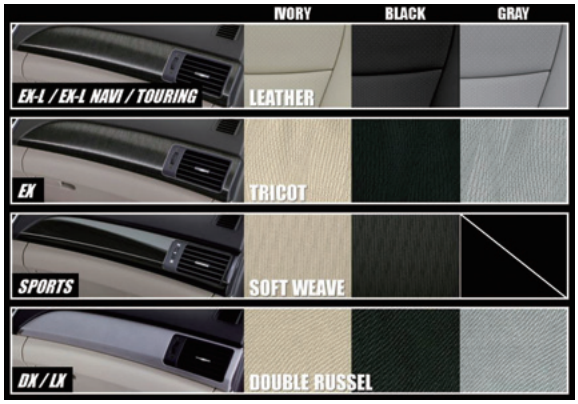


Fig. 21 Fabric design

7. Conclusion

The successive Accord vehicles have been developed to reflect the changes in the social environment and customer values with the times, and Accords have been chosen and loved by a large number of customers over the years.

"Excels in All Areas" was established as the grand concept for the new Accords, representing the vehicle's ninth generation, in order to respond to changes in customer values and expectations originating in significant changes in the social atmosphere. Designers set out to create a family sedan that could be chosen willingly, and that was competitive around the world.

We believe that the design of the new Accords is able to optimally satisfy an even greater number of users due to its embodiment of three themes: "Exhilaration," making it possible to use the vehicles comfortably and enjoyably every day; "Advancement," making the vehicles easy to understand and enjoy intuitively through more advanced technologies; and "Superior Craftsmanship," aiming for the realization of a sense of real, crafted quality through a focus on even the smallest details of the design.

It is our hope that in the future, no matter how the social environment may change, the Accord will continue to evolve in the quest to bring society, people and vehicles into harmony, and that the vehicle will go on being loved by its users.

■ Author ■


Toshiyuki OKUMOTO


Hiroki SHIGEHARA


Satoshi UCHIDA


Mie KOBAYASHI

Styling Design of New CR-V

Manabu KONAKA* Takehiro ISHIBASHI*
Daisuke MORISHITA* Hiroaki RYU*

ABSTRACT

The new CR-V was developed as a passenger vehicle to help customers lead daily lives that are active, stress-free and smart.

The new CR-V has been developed and fashioned into a vehicle capable of a self-expression of convenience and rich lifestyles transcending the boundaries of customers' life stages. It represents a synergistic crossover of the efficiency and premium character of a sedan or similar passenger car (EFFICIENT), the function of a minivan (FUNCTIONAL) and the confidence of an SUV (CONFIDENT).

The exterior design was based on the theme of BOLD AND ADVANCE to embody an expression of a bold, strong construction and expression of advanced functionality, while the interior design was based on the theme of CROSS CONSTRUCTION to simultaneously achieve roominess and user-friendliness in any setting.

1. Introduction

During the initial stages of development, members of the development team pondered the relationship between the customer and the CR-V that has continued since the first generation, and deeply considered what role the vehicle should play in customers' lives.

Speaking figuratively, the team wanted the vehicle to be like the slice of bread or the bowl of rice one has every morning. People eat such food every day, but it always tastes good and never gets boring. The team wanted the CR-V to be the vehicle that customers would choose, enjoy driving for many years, and feel it had become an indispensable part of their lives not because it is particularly luxurious but because it was built to the highest standards of quality and safety.

The value offered by this vehicle is that its functions are so closely aligned to customers' lifestyles at all times and that it brings joy to customers who use them day to day. The team was mindful of the fact that creating such joy is the starting point of development and the motivation for bringing the new CR-V into being.

This CR-V, the fourth generation of the model, came with a mission to meet the varied needs of Honda's many customers around the world, and the CR-V is now, along with the ACCORD and CIVIC, one of Honda's core global models.

The development team's aim was to accurately determine the current needs of customers around the world and boldly but carefully build the new CR-V to surpass the previous CR-V generations.

Making the latest CR-V the best CR-V is a natural goal but difficult to achieve in practice. To do so, it would be important to have a strong awareness of the CR-V's identity, to polish it up and to bring a proactive approach and a consistency that clearly encompasses new value. In addition, what customers want from a vehicle like the CR-V varies depending on where they are in the world. In North America, for example, customers want the CR-V to evolve into a compact crossover vehicle for safe and convenient daily transportation, while customers in Europe and Asia are looking for it to become an upgraded passenger car with premium value.

Customers looking for an expression of an energetic and rich lifestyle could use the CR-V actively. Use of the CR-V should be stress-free in daily life, formal situations and all types of settings. And finally, the CR-V aims to be smart and easy to use, so that customers could use it for many years as they go through various life stages. This is the SUPER CR-V grand concept for surpassing the expectations of customers around the world (Figs. 1, 2).

* Automobile R&D Center



Fig. 1 Grand concept

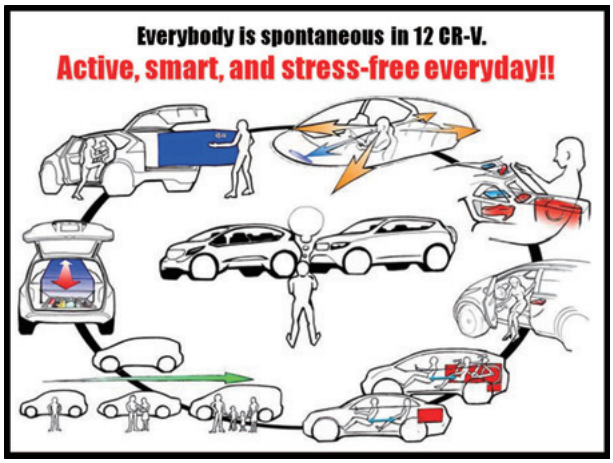


Fig. 2 Concept of customer demand

2. Package layout

One characteristic of the CR-V that has remained consistent since the first generation is the wheelbase, which is the key to the vehicle's external dimensions and interior space. The overall width, overall height and overall length have changed owing to, for example, revisions in the crash safety standards of the time and how the spare tire is loaded, as well as by the choice of a suitable platform, but this generation continues the tradition of not increasing the wheelbase to increase interior space.

Additionally, though the CR-V has been downsized compared to the previous generation, the core value of the fourth-generation CR-V was the evolution of Honda's proactive approach with its "man maximum, mechanism minimum" (MM) concept, which is to enhance comfort and user-friendliness. The development team decided that the best size for the new CR-V is one that lets customers all over the world enjoy stress-free use in their daily lives and user-friendliness for any setting in which they find themselves.

ADVANCED SYNERGY PACKAGE was taken as the theme to embody the SUPER CR-V synergy of EFFICIENT, FUNCTIONAL and CONFIDENT as the development team aimed to enhance the CR-V's convenience in a more compact size (Fig. 3).

2.1. EFFICIENT PACKAGE

To achieve vehicle efficiency and comfort, the development team pursued a lower CdA (a coefficient indicating the degree of aerodynamic drag, divided by dynamic pressure, found by multiplying Cd, a dimensionless number indicating the degree of aerodynamic drag, with A, the vehicle's frontal projected area), high-efficiency proportions, and a comfortable on-board position.

First, concerning a lower CdA, the frontal projected area was shrunk by reducing the overall height exclusive of antenna by 30 mm (or 40 mm in the North American 2WD version only), and aerodynamic performance was enhanced by extending the tail end of the roof.

Next, concerning high-efficiency proportions, everyday maneuvering was made easier by shortening body overhang by 10 mm in the front and 15 mm in the rear for North America (15 mm in both the front and rear in Japan) as compared to the final form of the previous generation, while still providing for safety performance in collisions. The cabin offers a comfortably expanded space for people by pushing the lower end of the front window forward and extending the tail end of the roof. The compact body and comfortable cabin embody high-efficiency proportions with strong individuality.

Moreover, the development team aimed to provide the on-board position of a passenger car for comfortable travel even over long distances, so the steering wheel was made the same diameter as that of a passenger car, and the seat height adjustment range was increased 15 mm downward. In the rear, foot height was left the same, while the hip point

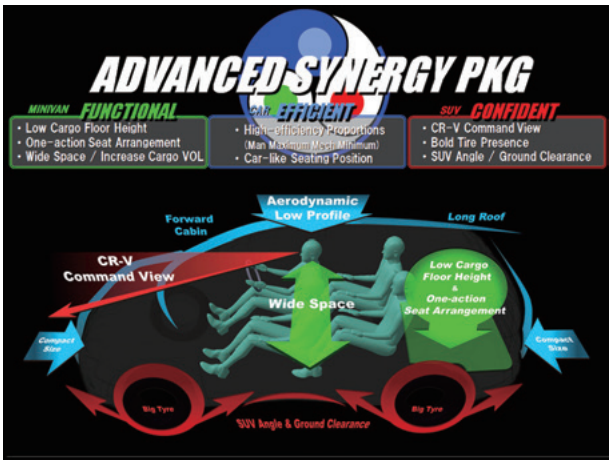


Fig. 3 Package layout concept

was lowered, making the on-board position close to that of a passenger car (Fig. 4).

2.2. FUNCTIONAL USABILITY

First, the development team pursued wide space indicative of the status of an automobile one class higher and an intuitively usable low-floor, high-volume luggage compartment to make the minivan's functionality intuitively understandable and usable.

The seating positions in the first-generation CR-V were arranged with a wider space between the right and left passenger seats in the front to allow a walk-through space between the front and rear seats. The second and third generations retained these positions, but users of the third-generation CR-V indicated that those seating positions expressed the status of an automobile one class higher. Thus, in addition to these seating positions, the development team pursued a wider lateral dimension to let the CR-V evolve into the status of an automobile one class higher. The usual design techniques to achieve this goal are to increase the overall width and move the side window outward, thus increasing frontal projected area and negatively impacting fuel economy. So instead, the new CR-V doors were made thinner in cross-section (while still providing for good performance in collisions), thus achieving 45 mm more space laterally compared to the previous generation.

A seat arrangement was designed that lets the user open up a flat luggage compartment with one action, changing the complicated seat arrangement of the previous generation. Additionally, the excellent low floor of the previous generation was lowered another 20 mm and the height of the tailgate opening lowered 25 mm, thus achieving intuitive user-friendliness. The comfortable cabin and lower floor achieved 65 L greater capacity than the previous generation despite the downsized body (Fig. 5).

2.3. CONFIDENT APPEARANCES

To provide the confidence of an SUV, the development team studied how to balance a confident appearance with enhanced fuel economy.

First, the new CR-V retained the commanding view and high sight line that has come down from the first generation in order to provide a sense of confidence and maneuverability in spite of the downsized body.

Next, the team increased the ratio of tire size to body as they worked to achieve a sense of confidence. Successive generations of the CR-V have advanced such a sense of confidence by increasing tire size, so the tire size of the previous generation was retained but the ratio of tire size to body was increased by downsizing the body, thus achieving a sense of confidence (Fig. 6).

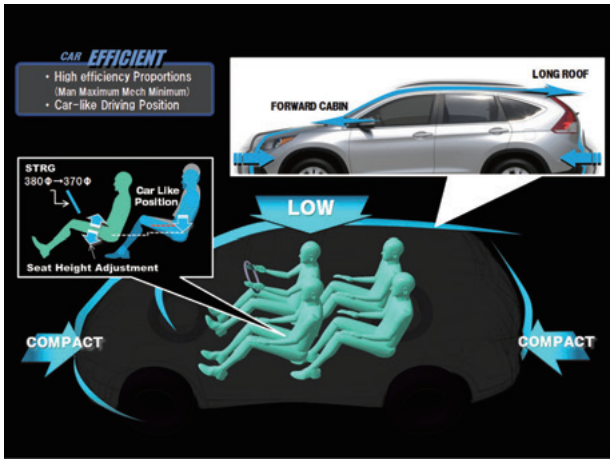


Fig. 4 Concept of efficient package

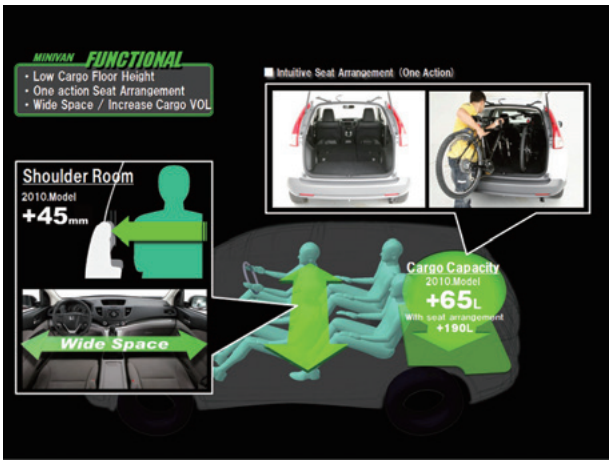


Fig. 5 Concept of functional usability

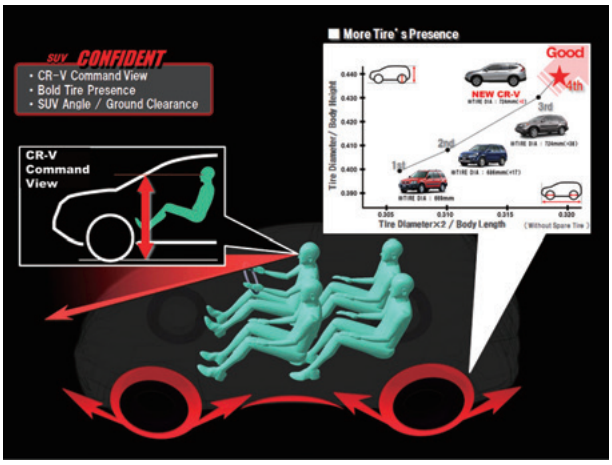


Fig. 6 Concept of confident appearances

3. Exterior Design

The exterior design aimed to express the themes BOLD (i.e., a bold, strong sense of status) and ADVANCE (high efficiency and sense of new functionality) (Fig. 7).

The side view is characterized by a low overall height

and a window slope made sharper by pushing the lower end of the front window forward. The back of the vehicle was given a silhouette reminiscent of a coupe by using highly curved rear glass. The result is a passenger car-like impression flowing sleekly from front to back. The cabin has a low roof, but the side window has been stretched as far as possible from front to back and the belt line lowered, expressing a comfortable look with a large glass area and creating a sharp impression. Unlike the rugged look used in the past, the side sill and tire area have a refined form suited to the smooth silhouette of a new crossover vehicle.

The front is a voluminous-looking mass with an engine hood that is short relative to the overall body, expressing a sense of confidence and a sense that the engine is efficiently enclosed in the compact form. Also, the simply integrated headlights and grill intertwine with each other, while the wide grill's plated insert garnish asserts the classy feel of a higher rank.

In the rear, the combination lamp is arranged vertically, which expresses the CR-V identity. The high curvature of the tailgate glass gives it a three-dimensional shape, which increases luggage compartment capacity. This, along with the sharp-lined rear combination lamp, creates a distinguishing form.

The development team aimed to achieve synergy of styling and aerodynamic performance. For example, the confidence-inspiring form of the body projects steadily outward from the front bumper corner and along the side, which achieves the desired dimensions and allows the optimal air flow, and the form of the rear combination lamps is put to use to optimize air flow at the corners (Fig. 8).

The team carefully considered the grounds for and appropriateness of the modeling of all of these parts to ensure that they were consistent with the concept. Thanks to these techniques, the vehicle projects not so much its actual downsized dimensions, but an impression of being upscale while giving a sense of status and functionality that will be convenient and useful for many years. It clearly expresses that this is the next-generation CR-V (Figs. 9, 10).



Fig. 8 Aerodynamics design



Fig. 9 Final rendering

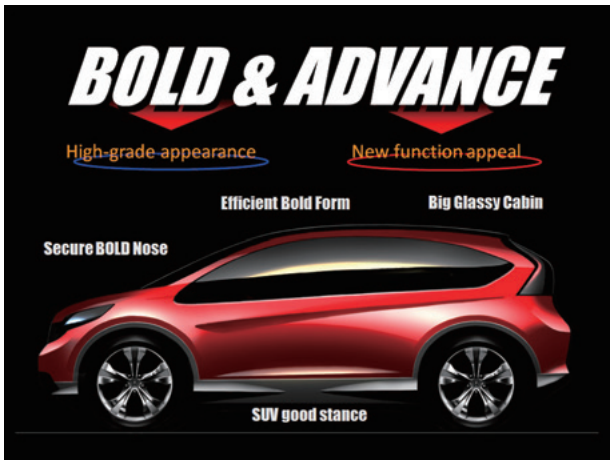


Fig. 7 Exterior design concept



Fig. 10 Final rendering

4. Interior Design

The interior design was developed under the theme of CROSS CONSTRUCTION, fusing a sense of upscale-looking status with advanced functionality.

A value that has been handed down since the first-generation CR-V is to build a space that is roomy, refreshing and pleasant to drive in. The new CR-V retains that idea and seeks to take it further, aiming to raise the sense of status to a new level (Fig. 11). Specifically, the area around the instrument panel was designed to flow openly in a horizontal layout. The end is formed to spread so far that it nestles right into the door lining, expressing a rich-looking driver's space that seems larger than its actual dimensions. Additionally, the wide decorative insert garnish panel that conforms to the tone is arranged around the driver's and passenger's seats, thus raising the sense of quality (Fig. 12).

The form of the center console makes full use of the dimensions to create the largest possible console, contributing to the excellent utility, magnificent look and sense of status. Functionally, it has box dimensions that can neatly contain A4-size documents, and side pocket dimensions that can hold a 500 ml PET bottle (Fig. 13).

Advanced functions include, for the first time on a CR-V, a center display capable of displaying music sources, wallpaper, etc. The display is located in the center of the instrument panel and displays a variety of content that may be controlled through the steering wheel switch, all adding to driving enjoyment. The all-important speedometer is located in the center of the meters and was made as large as possible to ensure instant recognition and intuitive operation. To help drivers intuitively understand switch locations, the audio panel and heater control panel are clearly zoned.

The advanced-function center display is located front and center, which minimizes movement of the driver's line of sight during cruising, and enhances instant recognition (Fig. 14).

Seats are designed with a form that strikes a high degree of balance among optimal embarking and disembarking, passenger hold, and riding comfort as an SUV.

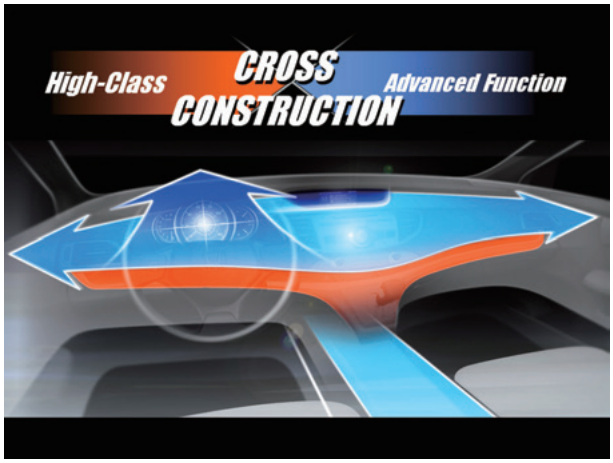


Fig. 11 Interior design concept

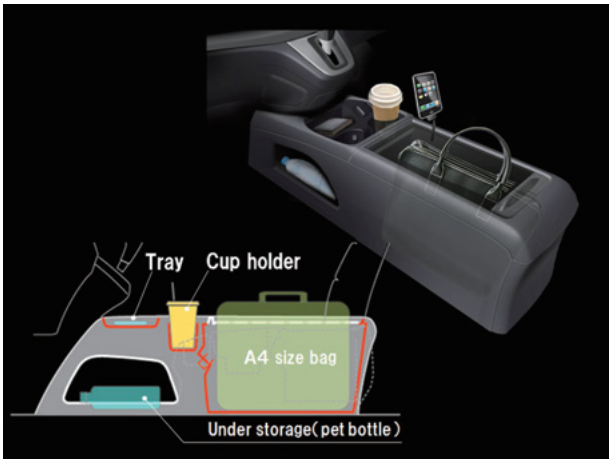


Fig. 13 Console utility



Fig. 12 Final rendering

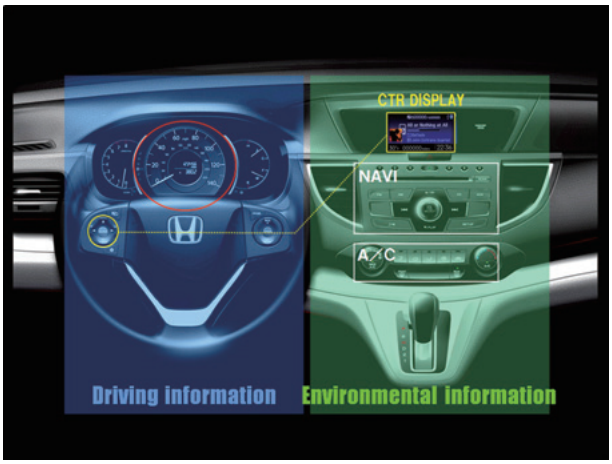


Fig. 14 Instrument panel

The luggage compartment aimed to enhance user-friendliness. It offers a one-touch seat arrangement for easy operation, uses a tonneau cover, and has net side pockets among other features meeting the need to load large items with ease and hold cargo securely.

5. Color and Fabric Design

As noted above, it was assumed that what customers want from the CR-V varies considerably, and therefore the team explored commonalities among customer needs for color and fabric.

Customers' candid opinions led the team to conclude that one necessity in common for the CR-V all over the world was more "high-class and fine-quality" colors and fabrics than in the previous generation. The team regarded this as a "compulsory exercise," and moreover set its sights on the advanced image that is always at the heart of any proposal at Honda.

The theme PREMIUM & ADVANCED was chosen with the aim of helping our customers live joyfully, youthfully and vigorously through the synergy of ADVANCED expression and PREMIUM coordination (Fig. 15).

For the exterior colors, the developers continued to use white, black, silver and dark silver as global standard colors. They also developed TWILIGHT BLUE M as a new global color. It is a good balance of PREMIUM and ADVANCED since it fuses dark blue (with the depth that is suited to a sedan and thus gives an upgraded impression) and a metallic texture (for a bright, sporty and functional look).

Additionally, given differences in customer taste in each part of the world, Honda uses the most suitable colors for each region. In North America, that includes a vivid red for Generation Y and a green metallic color that continues to be popular among a wide range of age groups. In Japan, black was chosen for an upgraded feel. In China and other parts of Asia, it is a deep red that balances sportiness with a fine-quality feel (Fig. 16).

Interior colors were coordinated using colors and materials that emphasize a high-quality feel while accounting for soiling so customers can use the vehicle comfortably in everyday life for many years. Since many customers say that soiling is a concern particularly with beige interiors, the team coordinated colors in a new way that accounts for both soiling and quality feel. The whole interior is unified in a dark brown color that does not show dirt, while seats are in high-quality bright beige. Three interior colors are available. In addition to beige, there is a black interior that has grown popular worldwide and a gray interior that is continuously popular in North America. Suitable colors will be offered in each region based on differences in taste (Fig. 17).

To enhance the fine-quality feel and the overall interior material feel, most of the interior (including the instrument panel and doors) received a unified leather texture with deep natural expression to create a sense of consistency in color and material feel, thus achieving a more comfortable fine-quality space.



Fig. 16 Exterior color line-up



Fig. 15 Color design concept

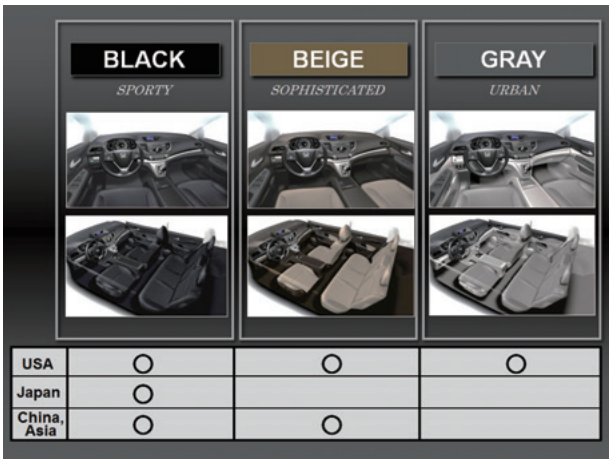


Fig. 17 Interior color line-up

The decorative panel (insert garnish) at the border between the top and bottom of the instrument panel for the high-grade model fuses a wood-grain look and silver. This is a new technique in garnish expression that fuses the natural fine-quality pattern of wood with a metallic texture showing strength and an advanced feel, thus symbolizing PREMIUM & ADVANCED. Other grades use silver insert garnish (Fig. 18).

Highly textured suede-like material, with a sporty image but at the same time a moderate sheen, was used as the seat fabric for the main seat parts. Seat sides, since these are the parts often touched by the hand, used a velour tricot material that is soft to the touch, thus creating a contrast in material feel of the main and side parts. A velour tricot material using surface unevenness to form a pattern was used as the main material for the lower grade. The pattern for both the high and low grades is an advanced, geometric-looking rectangular uneven-surface pattern, but a natural wave pattern is added so that the impression is not too rigid. It imparts an advanced expression that is easy on people. For the highest grade, leather is used (Fig. 19).

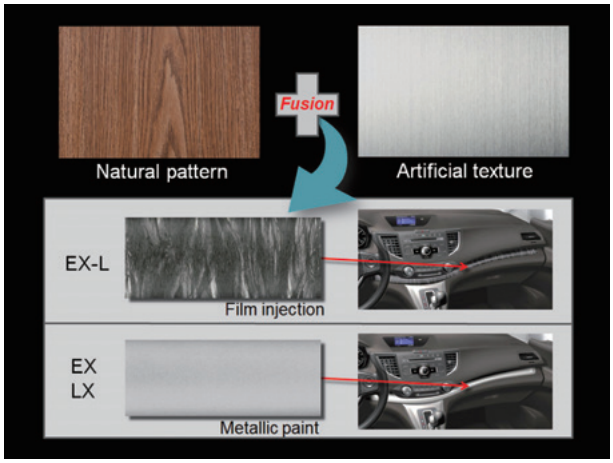


Fig. 18 Interior materials

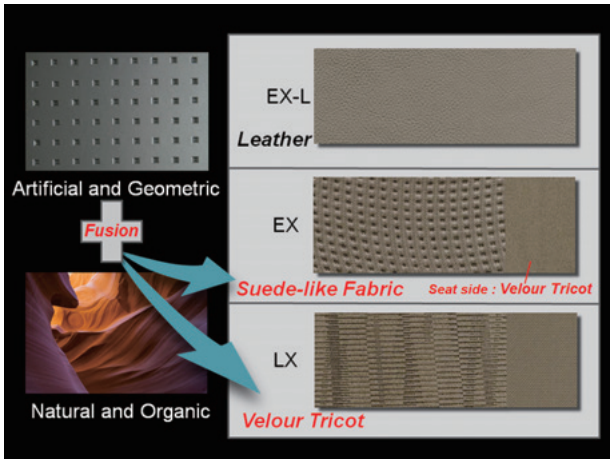


Fig. 19 Seat materials

6. Conclusion

The fourth-generation CR-V has the package of a compact crossover vehicle that has been handed down since the first generation, but this package has evolved to better meet the needs of customers around the world. The core elements of its styling have all been born and given form in this package.

Honda offers its design to customers by embodying the “man maximum, mechanism minimum” (MM) concept with a new framework based on package evolution and the technology to achieve it.

This vehicle was positively conceptualized from Honda’s strong automobile manufacturing ideas. The development team believes that its intentions will be communicated, and the CR-V will show its true worth, when customers sense that this vehicle will help make it possible for them to live comfortable lives.

The team is confident that it has built the fourth-generation CR-V into a vehicle that customers will value and keep close to them in their lives.

■ Author ■


Manabu KONAKA


Takehiro ISHIBASHI


Daisuke MORISHITA


Hiroaki RYU

Styling Design of NC700 Series

Kazuhiro KUDO*

ABSTRACT

The NC700 series was developed based on the concept to offer user-friendliness and convenience focused on daily uses, i.e. offering the enjoyment of maneuvering a motorcycle, consideration to the environmental issues and a good fuel efficiency with a reasonable price as well. While using the same shared platform, by applying the styling techniques on these series of motorcycles, it is realized to differentiate three forms: “Naked Sports,” “Crossover Concept,” and “Scooting Motorcycle.”

1. Introduction

In the motorcycle market in developed countries, while absolute performance in terms of factors such as top speed and acceleration is prioritized, the desire for low-cost models with effortless maneuvering and a relaxed riding experience is also increasing. The project discussed here set out to respond to this diversification of customer desires not with a single motorcycle, but with three different types of motorcycle based on a single platform. However, this demanded the realization of differing concepts and styling while sharing major components including the framework and the engine, a bold concept without precedent in previous motorcycle developments. The designers wished to create a motorcycle that could be used comfortably in a variety of scenarios. The NC700 series emerges from styling design development efforts based on this way of thinking.

Embodying a totally new concept without comparable former examples (including the development methods employed), packaging, and sense of what is important in a motorcycle necessitated the creation of a design method from zero, and represented a considerable challenge for the designers.

2. Styling Concept

The development target was to offer motorcycles with a user-friendliness for daily use that made it possible for anyone to use them, possessing a new level of lightness and comfort and offering a rich and pleasurable experience, but with good fuel efficiency and at an affordable price. The shared styling theme for the three models was to give form to rider-friendliness and the essential pleasure of using a motorcycle in the domain of daily life. By contrast with the mindset so often associated with sport motorcycles, which prioritizes performance above all else and seeks high speed and high power, this approach focused on elements including relaxation, safety, smart features and environmental friendliness.

Styling design for the three models based on different concepts was realized (Figs. 1, 2 and 3) in order to



Fig. 1 Concept sketch and clay model of NC700S

* Motorcycle R&D Center





Fig. 2 Concept sketch and clay model of NC700X





Fig. 3 Concept sketch and clay model of INTEGRA

offer user-friendliness to a broader range of customers and respond to their preferences, including customers who sought a style different to that of edgy, high-priced motorcycles, customers who had enjoyed riding motorcycles in the past, beginning riders, and customers seeking a convenient mode of transport around town.

In proceeding with the styling design, the following six items were established as shared points for the three models:

(1) To be a creation uniquely by Honda.
(2) A global design that could be appreciated anywhere in the world, based on the conviction that good design has no borders.
(3) Accurate communication to customers of the designers' message and commitment to quality.
(4) Expression of a well-organized, modern image motorcycle that stands out clearly yet fitting perfectly in urban areas.
(5) Expression of a sense of value that is not obsessed with hierarchies based on performance or displacement.
(6) Realization of an affordable price, but appealing to customers with a sense of quality in excess of the price.

3. Design Method for Realization of Three Models using a Shared Platform

In designing the motorcycles, the main point of focus was the attempt to prevent customers being aware that a shared platform was used.

What was necessary was to make the differences between the concepts of the "Naked Sports" NC700S, the "Crossover Concept" NC700X, and the "Scooting Motorcycle" INTEGRA clear by means of the styling.

Using a shared platform for three models for which the needs in terms of layout, including the silhouette of the vehicle as a whole, the shape of the frame, and the type of engine, would normally have been entirely different, represented a considerable challenge. The points of the design procedure were to create three different concepts and realize them in styling shapes without creating each individual base design separately as in conventional design approach.

3.1. Body Frame

In sharing a platform between the NC700S and the NC700X, which have a standard motorcycle shape in which the tank is sandwiched between the knees, and the INTEGRA, which has no tank section, the first element for which a breakthrough was needed was the body frame (Fig. 4).

For the NC700S and the NC700X, to help ensure the stiffness of the frame, the head pipe and the swing arm pivot would be connected in a straight line by a main pipe, as in standard sports models. Exposing this main pipe to allow it to be seen would also, from the design perspective, express a mechanical feel. In the case of the INTEGRA,



Fig. 4 Perspective drawing of three NC700 series models

however, designers sought to make the floor tunnel as low as possible, and it was therefore necessary for the layout to position the main pipe as low as possible.

In this model, the use of a diamond frame in combination with an engine unit with a low total height helped to ensure frame stiffness and made it possible to position the main pipe at a lower level than in a conventional motorcycle. The layout was designed to optimize the fitting of the main pipe around the engine, the points at which the pipe curves, and the positions of welds from both functional and visual perspectives, making it possible to produce a body frame that would function as a key element of the shared platform for the three models.

4. External Structural Parts and Differing Proportioning of Three Models

"External structural parts" refers to functional parts designed to clearly differentiate the styling concepts of the three models.

The NC700S and NC700X share the basic silhouette of a standard motorcycle as a common point. However, for the NC700S, designers sought to proportion the motorcycle to offer a simple, slightly forward-tilting, sporty basic feel characteristic of a sports motorcycle, with a relatively low frontal area. In the case of the NC700X, by contrast, the proportioning sought to create an upright feel, with a slightly raised frontal area, in order to express the concept of a "crossover," a fusion between on-road and off-road.

With its wide seating-position tolerance, the INTEGRA was given a scooter-like basic silhouette that emphasizes its user-friendliness in around-town riding.

The realization of very different proportioning for each motorcycle by means of external structural parts in this way represented both the challenge and the excitement of the styling design of the NC700 series.

4.1. Styling of NC700S

The NC700S offers the rider easy access to the exhilaration, mobility, and comfort inherent to "naked sports."

"Modern Fluid Form" was set as the styling theme to express the appeal of this concept. Elements suggestive of sports gear were modeled solidly and simply, expressing a modern feel and a distinct uniqueness, even as the motorcycle remains a standard model. The simplicity of the area around the headlight and the motorcycle's slim and compact exterior, fashioned using only the minimum necessary parts, are also significant features of this model.

The readily apparent and broadly appealing "Naked

Sports" styling of the motorcycle will appeal to both beginner and veteran riders with no sense of discord (Fig. 5).

4.2. Styling of NC700X

The "Crossover Concept" for the NC700X sought to embody a new way of thinking through the fusion of the different appeal factors of on-road and off-road. "Smart, Tough Body" was set as the styling theme in order to express the appeal of this concept. Smart but tough images are fittingly fused into crossover design through the characteristics created by the combination of parts painted with main body color, which feature the streamline design of the body, and parts made of pre-colored materials, whose tough-image shapes are designed to function as protectors as well (Fig. 6).

4.3. Styling of INTEGRA

The "Scooting Motorcycle" concept developed for the INTEGRA fused the pleasure of riding a motorcycle with comfort and convenience for commuting (Fig. 7).

With "Energetic Elegance" as the styling theme, the antagonistic elements of sporty/powerful and elegant/aesthetically pleasing were re-envisioned and fused at a high level to produce a novel styling. This model presents an entirely new, unprecedented concept.



Fig. 6 Image sketches of NC700X



Fig. 5 Image sketches of NC700S



Fig. 7 Image sketches of INTEGRA

5. Shared External Structural Parts

The platform concept and packaging were the absolute foundations of this development.

For the major parts shared by each model in the series, including the engine, intake and exhaust system, cooling system, body frame, chassis components such as suspensions, wheels, brakes, and lighting devices, high-quality, modern and clean design that would not interfere with the individuality of each model was employed.

5.1. Engine Design

In order to realize overall layouts for the NC700S, NC700X, and INTEGRA emerging from the entirely different concepts, it was necessary to use an engine with an extreme forward-incline cylinder configuration. Designers sought to utilize this characteristic, quite exceptional for a sports motorcycle, to realize a unique and individual engine design.

In order to effectively express the design themes "Clean" and "Modern," shared between the three models, both the left and right crankcase covers were given a modern, sculpted form. In combination with the unique inclined silhouette, the engine design imparts a sense of the functionally featured beauty of the motorcycles (Figs. 8, 9 and 10).

5.2. Design of lighting devices

The design needs in relation to the headlights of the three models clearly differed due to the differences between the concepts for each. This is because the headlight and surrounds represents the "face" of a motorcycle, and is therefore one of the most important iconic elements of the vehicle. This made it essential to realize entirely individual expressions while sharing the headlight units.

Taking into consideration the fact that there should be no design discord for any of the three models, the core element, the basic shape of the headlight unit, was designed as a simple V shape.

In the NC700S, the shared headlight unit is inserted in handle-mounted aluminum headlight stays in a parts configuration that also features a mini visor, creating a sporty and modern front area (Fig. 11).

In the NC700X, the shared headlight unit is built into the front cowl, which forms a nose as a feature of the "Crossover Concept"; the image created is one in which the colored plastic elements are guarding the headlight unit surrounds. Aluminum meter stays also serve as an element composing the external appearance of this section, helping to express a

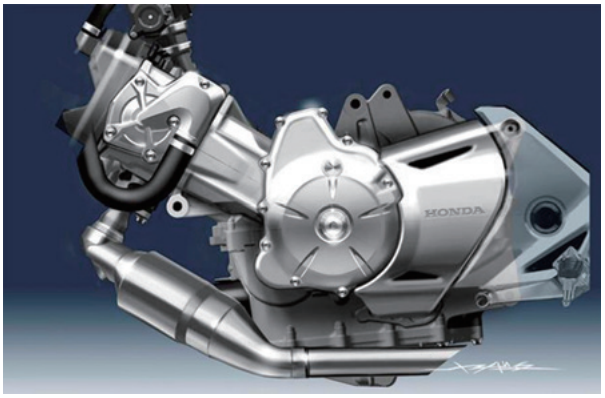


Fig. 9 Engine sketch (Left side)



Fig. 10 Engine sketch for dual clutch transmission model

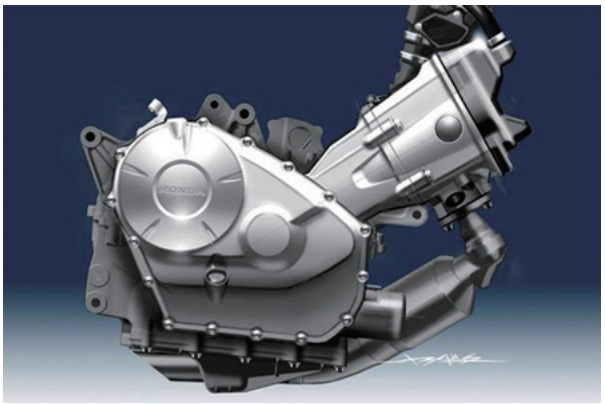


Fig. 8 Engine sketch (Right side)



Fig. 11 Front view of NC700S

"face" that reconciles tough and smart (Fig. 12).

In order to realize a luxurious and dynamic feel in the INTEGRA, the shared headlight unit, which is built into the body, is inserted in a sub-headlight unit that is incorporated with the combined function of turn signal and position lamp. The combination of a headlight incorporating a sub-headlight and texturized with metallic screen stays realizes a vigorous and elegant "face" (Fig. 13).

In the complete vehicles, the differing individuality and expression of the three models is realized without compromise.

5.3. Meter Unit Design

Because the meter display is immediately captured by the rider's eyes, it is considered to be the most important functional unit in the cockpit.

The shared meter unit for the NC700 series offers a full liquid crystal display, and is designed to express the modern feel of a meter used on the very latest model of motorcycle, simple with no idiosyncrasies. The design of variations for the three models took into consideration variation of the meters' expression through combination with the shaping of the surrounding area.



Fig. 12 Front view of NC700X



Fig. 13 Front view of INTEGRA

In the NC700S, a simple and sporty handle-mounted meter emphasizes a feeling of lightness and nimbleness (Fig. 14).

In the NC700X, body-mounted aluminum stays are used to give the meter unit a floating mount, making it easy to see in an upright riding position and offering a styling that stimulates the spirit of adventure associated with the "crossover" between on- and off-road (Fig. 15).

In the INTEGRA, the shared meter unit is arranged in an instrument panel designed on the basis of an image of the cockpit of a four-wheeled vehicle, realizing a luxury vehicle feel. In the rider's eyes, it appears to be a cozy and comfortable environment (Fig. 16).



Fig. 14 Meter display unit of NC700S



Fig. 15 Meter display unit of NC700X



Fig. 16 Meter display unit of INTEGRA

5.4. Design of chassis components and Muffler

The configuration of the chassis components was basically shared between the three models, with the longitudinal length of the suspension being extended by 30 mm in the case of the "Crossover Concept" NC700X only.

A light and modern design realizing good compatibility with both the standard and "scooting" motorcycles was employed for the wheels (Fig. 17).

The muffler is made of stainless steel and is designed to maintain a standard shape while emphasizing the shape of the body as well as creating a graceful appearance around the rear of the vehicle. This same muffler is basically shared between the three models, with only the INTEGRA employing a muffler end cap for a feeling of luxury (Fig. 18).



Fig. 17 Front wheel of INTEGRA



Fig. 18 Muffler of INTEGRA

6. Utility Space and Riding Style

In the concept established for the NC700 series, the existence of a utility space was an important appeal factor of the motorcycle.

Conventional motorcycles do not usually offer a storage space, and riders have to place anything they desire to carry in a backpack that is then either worn or attached to the rear seat or other part of the body, even if the rider is only making a short trip. Regular carrying of luggage on the motorcycle necessitates the attachment of a top box, panniers, or similar accessories to the body.

The provision of the NC700S and the NC700X with 21 L storage spaces frees riders from the nuisance involved in carrying luggage.

This utility box provides another benefit with its visually sharp appearance, since the baggage is concealed within the vehicle body. We believe that the total beauty of motorcycle styling can only be considered when it includes the rider sitting astride it as well. The provision of a utility space therefore has considerable merit.

As Fig. 19 shows, the NC700S and NC700X feature utility spaces able to hold an extra-large full-face helmet in the shelter area in front of the seat, corresponding with the position at which the knees grip when a rider is sitting on the seat. Trimming back the layout to the limit in this way has made it possible to realize a sculpting with no sense of discord, either functionally or aesthetically. In concrete terms, the design process optimized elements such as the orientation and angle of helmet storage, the thickness of its exterior walls, the cut-line of the lid, and the lock mechanism in units of millimeters, crafting the configuration down to fine details.

This has resulted in the achievement of a slim and natural profile fusing styling and function (Fig. 20).



Fig. 19 Utility space of NC700X



Fig. 20 Shelter and seat of NC700X

In case of the INTEGRA, which does not have a shelter, a 15 L storage space has been provided under the seat (Fig. 21).



Fig. 21 Utility space of INTEGRA

7. Conclusion

The vision for the shared styling design of three models of motorcycle was to take a further step in the evolution of the motorcycle, expressing in form the essence of the pleasure of using a motorcycle in daily life.

Three models were created on the basis of entirely different concepts: the "Naked Sports" NC700S, incorporating an image of sports gear and designed to realize both a sporty and a modern, urban feel; the NC700X, in which, based on the "Crossover Concept" between on-road style and off-road styling, two contradictory design elements of rough and sporty are harmonized without perception discrepancies; and the INTEGRA, featuring an unprecedented proportioning that fuses the convenience of a scooter and the sportiness of a motorcycle.

The designers of the NC700 series hope that it will serve as a benchmark for one orientation in the future of the motorcycle.

■ Author ■



Kazuhiro KUDO

Development of NC700 Series

Koki KOBAYASHI* Masaaki NEGORO* Takanori OSUKA*
Toshimasa MITSUBORI* Tadashi OSHIMA*

ABSTRACT

The NC700 series (NC700S, NC700X and INTEGRA) was developed with the aim of realizing a well-balanced fusion of the enjoyment of riding with the convenience of a commuter-type motorcycle. Each of the three model types has a distinctive character, while utilizing the common technology such as a shared platform, a liquid-cooled in-line 2-cylinder 670 cm^3 engine, that emphasizes the torque in low-to-mid speed range and has its center of gravity in lower position to increase the degree of freedom in the exterior designing, and a next-generation dual- clutch transmission which is light weighted and compact. The models created in this development offer unprecedented values not available in former models, such as combined benefits of both excellent fuel economy and the pleasant riding quality at the same time, together with values in utilities realized by equipping a larger utility compartment.

1. Introduction

The needs for middle-class motorcycles with displacement between approximately 500 and 750 cm^3 in Europe and the U.S. are diversified more.

Market surveys were conducted regarding the usage and requests for motorcycles, including commuter types such as scooters, in advanced nations. The results showed that users are broadly divided into two types.

One is the familiar type of user who enjoys super-sport category motorcycles that emphasize absolute performance. These users demand enhanced power performance in the high-speed range and cornering performance on winding roads.

The other type of user is not particular about performance and displacement hierarchy, and was the motivation for developing these models. These users place the highest priority on easy handling and convenience in everyday life. They own middle class motorcycles in a reasonable price range, and enjoy relaxed, leisurely driving that also takes into account environmental performance, and riding such as touring through suburban areas. In addition, some users of scooters and other commuter types also expressed the desire to sometimes enjoy riding like on a sporty motorcycle, while still keeping the comfort and convenience of a commuter-type motorcycle. Customer's needs have become mixed and are no longer bound by traditional motorcycle or commuter categories.

This paper introduces the NC700 series, which deploys three different model types using a shared platform to meet these needs and respond to a wide range of user demands (Fig. 1, Fig. 2, Fig. 3).



Fig. 1 NC700S



Fig. 2 NC700X

* Motorcycle R&D Center



Fig. 3 INTEGRA

2. Overview

2.1. Development Target

The development target was set as providing affordable, fuel-efficient motorcycles that are easy to handle in everyday use, and also nimble and comfortable for deeper enjoyment.

Specifically, the aim was to realize the following:

- A package that realizes nimble handling, reliable controllability and comfortable cruising
- Deployment of a three-model series to meet a wide range of customer needs, with individualistic next-generation styling designs that satisfy pride of ownership
- Amenities and an abundance of option settings that further enhance the convenience of FUN models
- Dual-clutch transmission type settings

2.2. Simultaneous Development of Three Models

In previous FUN model development, there were cases where first a core model was developed and mass produced, and then variation models with a shared platform were developed. However, there were also cases where a post-mass-production model was used as the base, but sharing was lost due to changes made to the platform to realize specifications required by later models, or other reasons.

By simultaneously developing the three NC700 series models in parallel, the specifications required to provide the performances of each type could be reflected to the platform as much as possible. As a result, the parts sharing rate could also be maximized.

2.3. Development Goals

2.3.1. Platform Concept and Packaging

Simultaneous development of three models enabled the series to share the engine, frame body, suspension, air intake, exhaust, cooling, lights and other major parts. In addition, the design enabled support of the prerequisite of a dual-clutch transmission type setting for all three models simply by changing some parts from the base normal manual transmission (MT) type. The photographs below show cutaway models of both engine types (Fig. 4, Fig. 5).

The engine also contributes greatly to efficient packaging. Increasing the fuel efficiency enabled reducing the fuel tank size and locating the fuel tank under the seat. In addition, tilting the cylinders forward by 62° reduced the engine height and secured space above the engine. In addition, a Pro-Link type rear suspension is used and mounted in the lowest position possible.

These layout measures enabled the platform to realize both a luggage space that can accommodate a full-face helmet (NC700S/X) and a scooter-like appearance (INTEGRA) (Fig. 6).

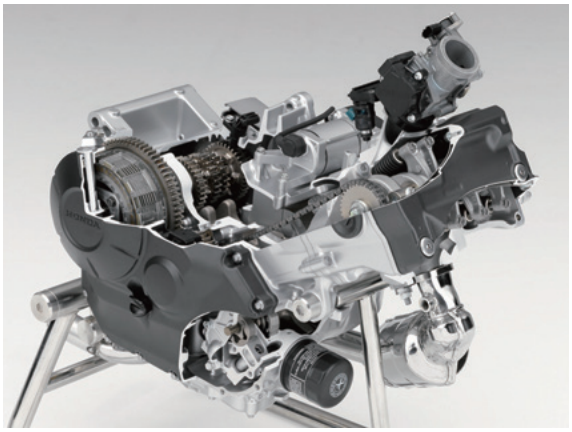


Fig. 4 Cutaway model of engine (manual transmission)

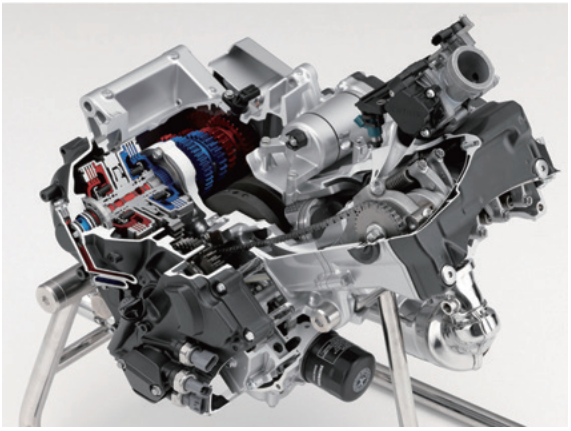


Fig. 5 Cutaway model of engine (dual clutch transmission)

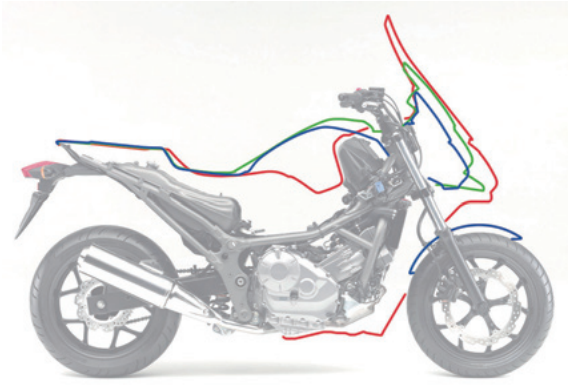


Fig. 6 NC700 platform

2.3.2. Overview of NC700S model

The NC700S aimed for a user-friendly "Neo-FUNctional Motorcycle" that lets users more easily enjoy the exhilaration and maneuverability of FUN riding while also providing comfort.

The NC700S fuses a dynamic, powerful design based on the modern and simple silhouette of a naked sporty model, with natural handling characteristics that enable users to experience the pleasure of riding inherent to motorcycles. This model combines a slightly forward-leaning riding position and a low seat height that provides good ground reach and a sense of security with an agile naked style. This enables users to enjoy relaxed, stress-free riding while still maintaining a sporty ambience.

In addition, even though the NC700S has a 21 L luggage compartment that can hold a full-face helmet, the fit between the rider and the motorcycle, as represented by knee grip, is the same level as that of a conventional model.

2.3.3. Overview of NC700X model

The NC700X aimed for a New Crossover Motorcycle that provides new value by fusing different types of attractiveness.

The NC700X has longer front and rear suspensions compared to the NC700S, and combines a dynamic, powerful and sophisticated design that looks attractive in both the city and the countryside, an upright riding position that provides good visibility and on-road comfort, and maneuverability that expands the sphere of activities.

A frame-mounted fairing and small windscreen that do not interfere with handling in the city realize freedom and broad usability that provide mobility for commuting to work or school in urban areas, while also enabling users to enjoy occasional long-distance touring.

In addition, the NC700X also has luggage space equal to that of the NC700S in consideration of everyday convenience.

2.3.4. Overview of INTEGRA model

The INTEGRA aimed for a Scooting Motorcycle that fuses the enjoyment of riding a motorcycle with the comfort and convenience of a commuter type.

Good handling characteristics provide the enjoyment of maneuverability inherent to motorcycles, and the second-generation dual-clutch transmission realizes an exhilarating ride with a powerful, direct feel even in automatic mode.

Passenger comfort was pursued in addition to cutting-edge styling. These measurement make the INTEGRA model attractive to even more customers by simultaneously providing the exhilaration and maneuverability of a motorcycle with the convenience of a commuter type, and also letting users discover new ways of enjoyment based on a free concept unbounded by any category to date.

3. Overview of Engine

The engine development goals were set as follows.

- An easy-to-handle, fuel-efficient engine that combines powerful torque characteristics in the normal engine speed range with a wide gear ratio
- A lightweight, compact engine that can be shared by three models in different categories

To achieve these goals, the NC700 series uses a 670 cm^3 liquid-cooled OHC in-line 2-cylinder engine, helping to increase the degree of freedom in body layout.

The engine specifications use a long stroke with a ø73 x 80 mm bore and stroke. In addition, optimization of the combustion chamber shape and valve timing, friction reduction, and other measures achieved a fuel efficiency of 27.9 km/L (WMTC mode) while pursuing riding enjoyment in the normal engine speed range.

Furthermore, as mentioned previously, both MT and dual-clutch transmission can be set simply by changing some parts (Fig. 4, Fig. 5).

4. Engine Details

4.1. Engine Layout

The demands on engine layout shared by the three models were as follows.

- A layout that can provide luggage space above the engine
- A narrow engine width that provides space for the rider to position their feet like a scooter

To meet these demands that contribute to body layout, an in-line 2-cylinder engine with the cylinders tilted forward by 62° (engine mounting angle) was selected.

4.2. Provision of Riding Enjoyment in the Normal Engine Speed Range

4.2.1. Power characteristics

The power characteristics emphasize performance in the normal engine speed range rather than absolute performance. For this reason, lower engine speed power characteristics are used compared to the conventional sports type engine, which realizes powerful torque characteristics in the normal engine speed range (Fig. 7). In addition, the gear ratio is also higher than that of the conventional engine, which lowered the normal engine speed.

4.2.2. 270° phase crankshaft

To realize the pulsating engine feel that is one of the attractions of motorcycles, an in-line 2-cylinder engine with a 270° phase crankshaft that results in uneven-interval combustion (Fig. 8) and cylinder head branched intake ports (Fig. 9) were used. As a result of this combination, the second cylinder, which has a short firing interval following the first cylinder, receives the effects of the intake negative pressure of the first cylinder during low-load operation, so the pressure inside the intake start port is lower than that of the first cylinder. This means that the second cylinder

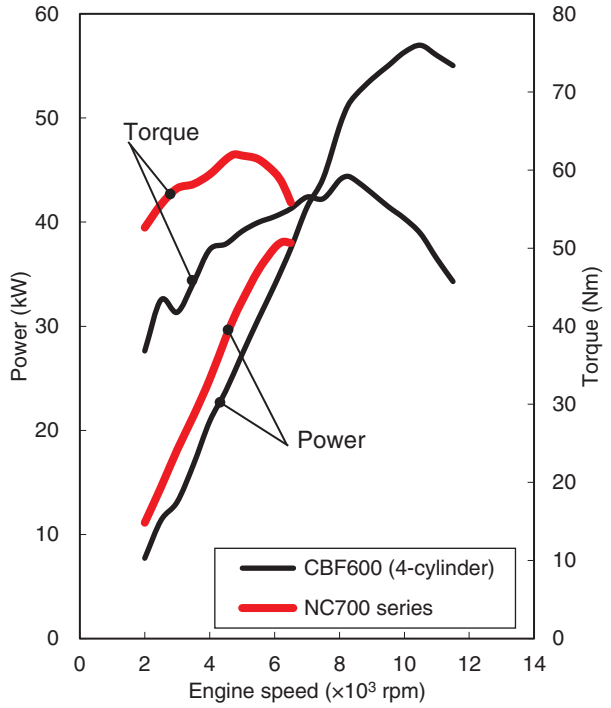


Fig. 7 Engine performance

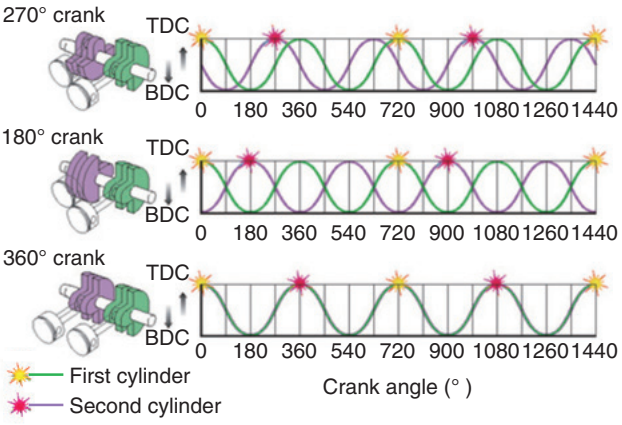


Fig. 8 Comparison of ignition timings



Fig. 9 Branched intake port

has a lower charging efficiency compared to the first cylinder, which produces a difference in the amount of work performed between the cylinders. This action plus the torque fluctuation with a 90° phase difference gives this engine a pulsating feel close to that of a V-shaped 2-cylinder engine.

4.3. Environmental Performance

A fuel efficiency performance of 27.9 km/L (WMTC mode), which is an increase of 40% or more compared to a conventional motorcycle in the same class (XL700V TRANSALP), was achieved by measures such as enhancement of combustion efficiency, friction reduction, and use of a wide gear ratio. Figure 10 shows the position of the fuel efficiency performance.

4.3.1. Enhancement of combustion efficiency

In a conventional middle-class engine, combustion becomes unstable (large combustion coefficient of variance (COV)) during low engine speed, low-load operation such as idling, so combustion was stabilized by richening the air-fuel ratio to around 13. To achieve the target fuel efficiency, this engine adopted the following measures, enabling realization of combustion stability equal to or better than that of the conventional engine, even at the theoretical air-fuel ratio (A/F14.7) (Fig. 11).

- ø73 x 80 mm long stroke
- Optimization of the valve timing
- Use of wide-gap spark plugs

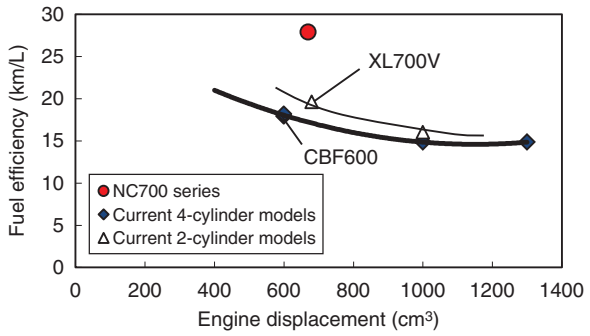


Fig. 10 Comparison of fuel efficiencies

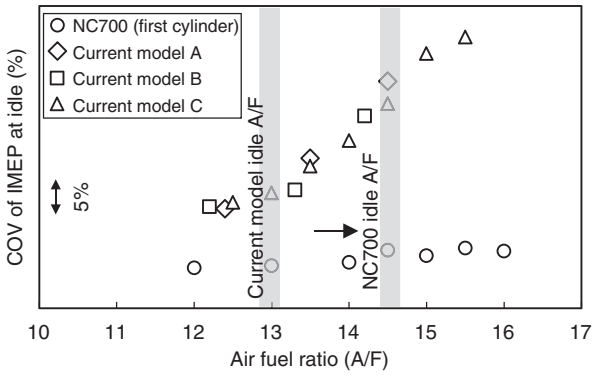


Fig. 11 Comparison of coefficients of variance (COV)

4.3.2. Friction reduction

Friction reduction technology that helped to enhance fuel efficiency included coating the pistons with resin and reducing the piston ring tension to 40% of that of a conventional motorcycle in the same class (XL700V TRANSALP). In addition, the rocker arm is a roller type that uses aluminum materials for the first known time in a motorcycle (as investigated by Honda).

Furthermore, the reduction of the auxiliary driving loss and the reduction of the number of parts were realized by functional concentration such as driving the oil pump using the balancer shaft and the water pump using the camshaft. (Fig. 12, Fig. 13).

As a result of these measures, friction loss was reduced by 20% at an engine speed of 3000 rpm in terms of friction mean effective pressure Pmf compared to a conventional motorcycle in the same class (Fig. 14).

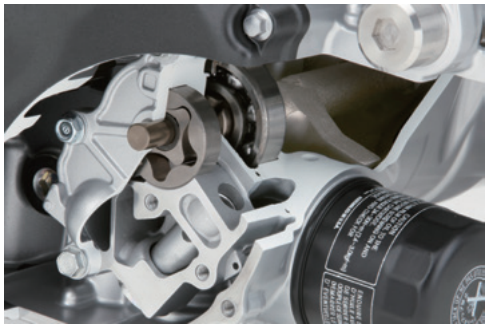


Fig. 12 Oil pump driven via balancer shaft



Fig. 13 Water pump driven via camshaft

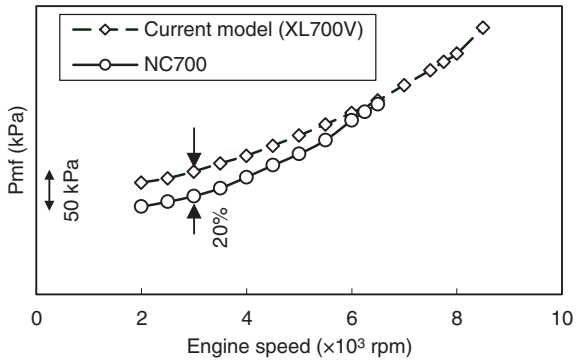


Fig. 14 Comparison of friction loss

4.4. Dual-Clutch Transmission Type Setting

In addition to the normal manual transmission type, a dual-clutch transmission type was also set for the NC700 series engine. Figure 15 shows this configuration.

The weight and size were reduced without a loss of the direct feel, powerfulness and other performances compared to the VFR1200FD (motorcycle equipped with dual-clutch transmission)[(1)] released in 2010. Furthermore, 85% of the engine parts are shared with the manual transmission type, which also reduced cost.

4.5. Evolution of Dual-Clutch Transmission

4.5.1. Hardware

Hardware evolution focused on the hydraulic circuit that is important for dual-clutch transmission control.

The linear solenoid valve position was changed from outside the engine right side cover to inside the cover. This shortened the hydraulic circuit by approximately 40% compared to the VFR1200FD, enhanced responsiveness, and realized seamless shift characteristics. In addition, changing the solenoid valve position also helped to reduce cost and size.

Furthermore, elimination of the oil feed pump and other measures enabled reducing the number of transmission parts by approximately 20% compared to the VFR1200FD (Fig. 16).

4.5.2. Software

Software evolution focused on modification of shift control, which is directly linked to riding enjoyment.

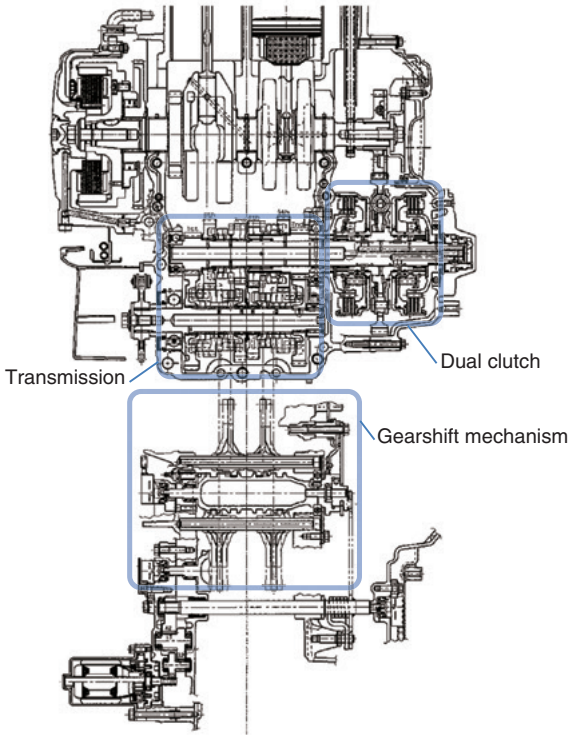


Fig. 15 Cross-sectional drawing of engine

The dual-clutch transmission enables selection of two different AT modes: D mode that also takes into account fuel efficiency when driving in urban areas, and S mode that takes into account sporty riding on winding roads. In addition, there is also an MT mode that enables riders to manually shift to select an arbitrary gear position using the Up/Down switch built into the left grip, for a total of three modes that can be selected.

NC700 series development focused in particular on differences between various driving environments and rider driving styles in D mode, and expanded the D range coverage to support a wider range of driving styles. That is to say, when D mode is selected, the optimal shift control is automatically performed in accordance with the rider's driving style, enabling support of a wide range of driving styles, from relaxed riding in urban and suburban areas to brisk FUN riding (Fig. 17, Fig. 18).

In addition, manual shifting can be performed using the Up/Down switch even when AT mode is selected, and control was incorporated that uses an auto return function to return to AT mode at the optimal timing according to the running status after manual shifting.

The addition of these control functions enabled more comfortable riding (Fig. 19, Fig. 20).

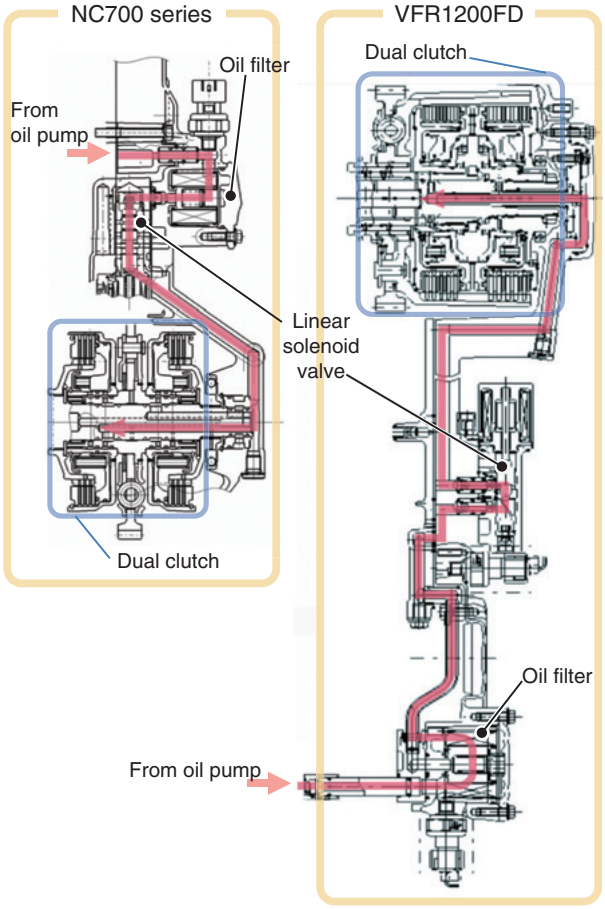


Fig. 16 Comparison of clutch oil lines

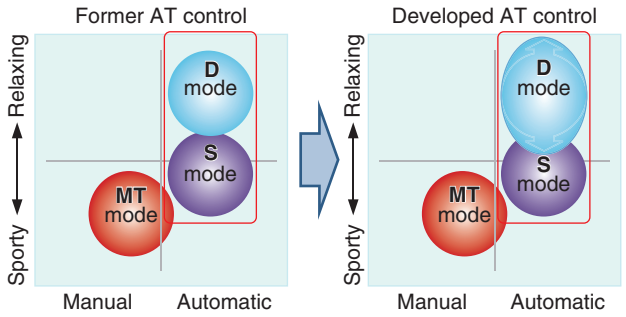


Fig. 17 Expanded D mode coverage

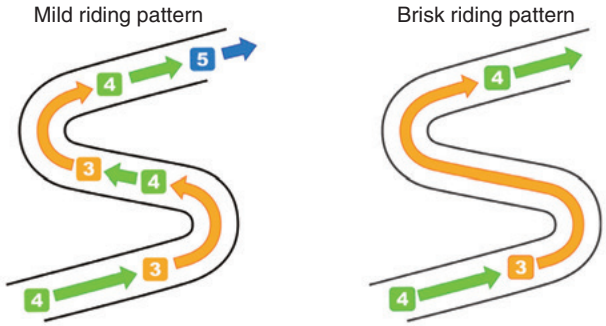


Fig. 18 Gear shifting patterns with driving inclination detection

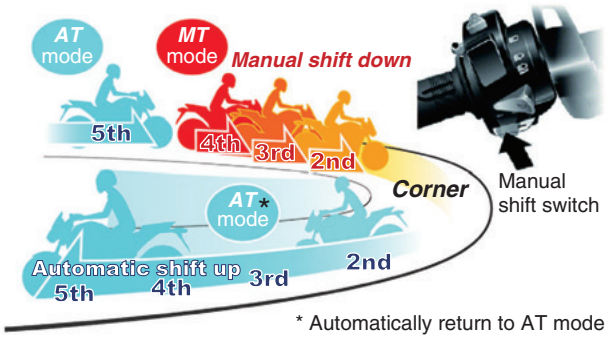


Fig. 19 Automatic return to AT mode function

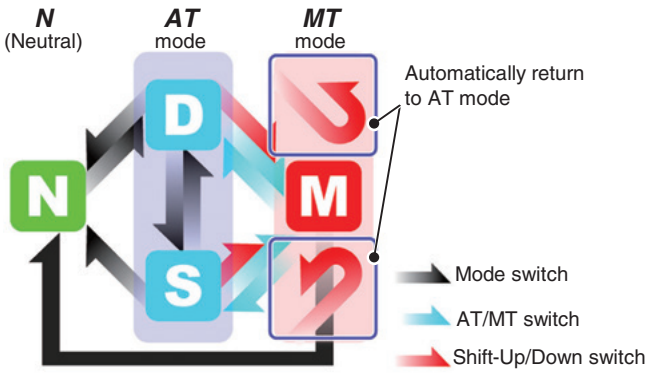


Fig. 20 Shift mode management

5. Establishment of a Frame Platform and Shared Packages

The frame body shapes of straddle riding type motorcycles and scooters differ greatly as shown in Fig. 21 and Fig. 22. In addition, due to the differences in these silhouettes, the shapes and placement of various parts also differ greatly. The greatest issue for body design in this development was to establish a frame body platform and a shared package for various parts that can be used by three different model types.

To address this issue, the engine, air cleaner and fuel tank layout and other elements were fundamentally revised, and an unconventional new frame body structure was investigated.

5.1. Engine Mounting Position

The engine mounting position in a motorcycle is an important factor determining the longitudinal weight balance, which contributes in particular to handling and stability. The engine with 62° forward-tilting cylinders mounted in the NC700 series has a low overall height but a long longitudinal length, so the degree of freedom in mounting position in the longitudinal direction is limited.

Therefore, the cylinder head cover was set to a concave shape that matches the radiator shape. This enabled securing of clearance between the front fender and the radiator when the front suspension is fully bottomed, while at the same time positioning the engine toward the front of the body (Fig. 23).



Fig. 21 Example of frame body for ride on type motorcycle



Fig. 22 Example of frame body for scooter

5.2. Air Cleaner Case

The air cleaner case is located directly above the forward-tilting cylinder head while still securing sufficient handlebar turning space, luggage space (NC700S, NC700X) and seat opening and closing space (INTEGRA). The total air cleaner capacity was set at 5.8 L, which helped to achieve power, driving, noise and other performances. Figures 24 and 25 show the layout around the air cleaner case.

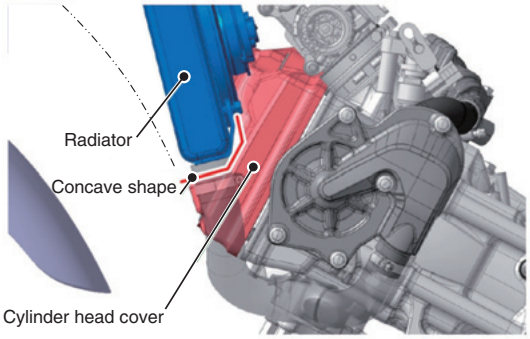


Fig. 23 Cylinder head cover shape that does not interference with radiator

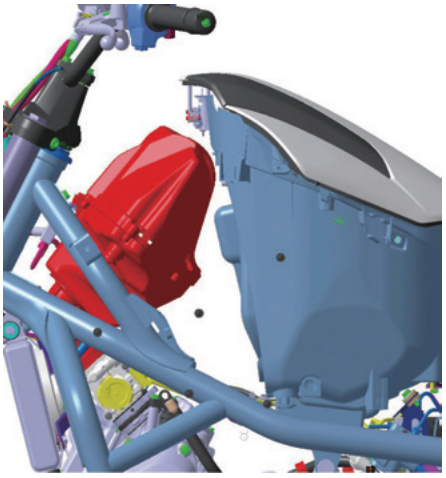


Fig. 24 Layout around air cleaner case (for NC700X)



Fig. 25 Layout around air cleaner case (for INTEGRA)

In addition, to make effective use of space, the air filter is placed so that it protrudes above the packing surface of the air cleaner case. This increases the clean side capacity downstream from the air filter, which realizes a powerful torque feel (Fig. 26).

5.3. Frame Body

The frame body uses normal steel instead of high tensile strength steel in consideration of enabling procurement and manufacture in various countries around the world in the future.

In addition, a shape that satisfies the requirements of each of the three models was investigated, and the main pipe was given a diamond type and positioned lower than that of a conventional model. Figure 27 compares the new frame body piping with that of a conventional model.

CAE analysis was performed on the frame body, and the pipe size, metal thickness, and pipe bending positions were determined to simultaneously achieve both rigidity and flexibility. Figure 28 shows an example of CAE analysis.

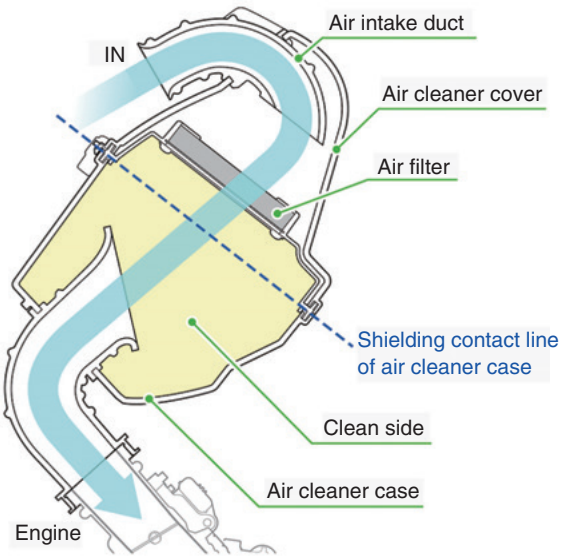


Fig. 26 Layout of air filter

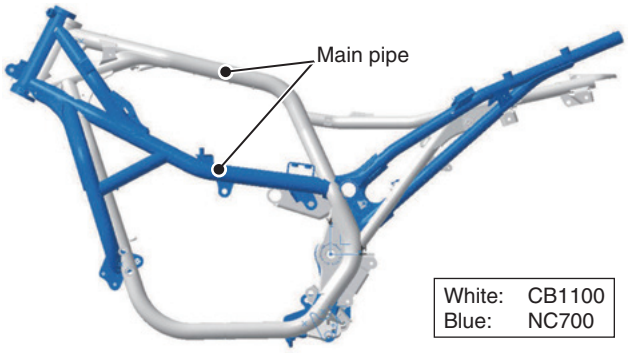


Fig. 27 Comparison of frame body pipings of CB1100 and NC700

5.4. Fuel Tank

The fuel tank is located below the seat, and uses a steel plate two-piece structure that is advantageous for securing sufficient capacity with a thin shape.

The rear frame pipes are located below the fuel tank, and the cross plate, luggage compartment stay and rear grab rail are effectively positioned so that the seat load is not directly applied to the fuel tank (Fig. 29). This structure enables the use of thinner steel plates for the fuel tank, which helps to reduce the body weight.

In addition, the new, fuel-efficient engine enables the use of a smaller fuel tank, so the fuel tank capacity was set at 14 L. This provides a cruising range of approximately 380 km per fill-up, which is the same level or better than that of the conventional model.

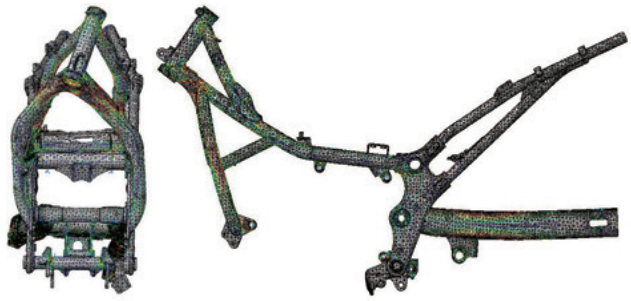


Fig. 28 Example of CAE analysis for frame body

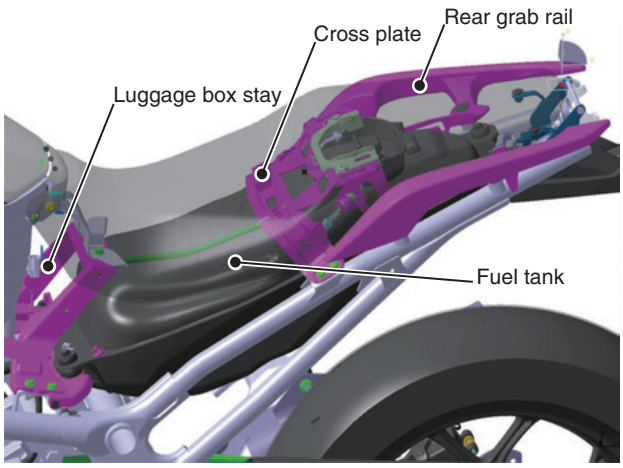


Fig. 29 Layout around fuel tank

6. Conclusion

The NC700 series was developed with the target of "providing affordable, fuel-efficient motorcycles that are easy to handle in everyday use and also nimble and comfortable for deeper enjoyment." Three new models of motorcycle, each with its own distinctive character, were realized while using shared technology such as a platform common to all three models, emphasis on low- to mid-speed torque, a liquid-cooled in-line 2-cylinder 670 cm^3

engine with a low center of gravity that helps increase both convenience and the degree of freedom in design, and a dual-clutch transmission that has the same high transmission efficiency as the conventional model, but is lightweight and compact.

This series is expected to pioneer the creation of a new motorcycle domain.

Reference

(1) Tanaka, M., Arai, D., Watanabe, J., Fukaya, K., Kittaka, E., Tsuchiya, M.: Development of Dual Clutch Transmission for VFR1200F, Honda R&D Technical Review, Vol. 23, No. 1, p. 9-17

■ Author ■


Koki KOBAYASHI


Masaaki NEGORO


Takanori OSUKA


Toshimasa MITSUBORI


Tadashi OSHIMA

Development of NSF250R Commercial Road Racer with 4-stroke Engine

Tomio ONOSATO* Yoshiyuki KURAYOSHI*

ABSTRACT

A Moto3 category that uses 4-stroke 250 cm^3 engines has been established for Grand Prix motorcycle racing from 2012. Due to this new category, Honda has developed the NSF250R, which is equipped with a newly developed 4-stroke single-cylinder 249 cm^3 engine. The new engine features an intake-from-front, exhaust-to-rear layout to increase charging efficiency, and a 15° rearward tilted cylinder to concentrate mass. A thinner lightweight piston and nut-less connecting rod are used to reduce weight, an offset cylinder and a closed crankcase with scavenging pump are used to reduce friction, and a midship muffler is used to concentrate mass. These and other measures realize engine performance and maneuverability suitable for a commercial racing machine in the Moto3 category, which is the gateway to road racing.

1. Introduction

Honda produced and sold 2-stroke 125 cm^3 racing machines for entry-level road racing starting from the MT125R in 1976 to the RS125R, which ended production with the 2009 year model. These machines broadened the base of motorcycle sports both in Japan and overseas, and raised many racing riders.

On the other hand, the need for environmental measures for general commercial vehicles is increasing on a global level, and motorcycle racing machines are also changing to 4-stroke engines. In 2002, the premier class of Grand Prix motorcycle racing changed from GP500 (500 cm^3 2-strokes) to MotoGP (currently 1000 cm^3 4-strokes), and the GP250 category (250 cm^3 2-strokes) changed to Moto2 (600 cm^3 4-strokes) from 2010. In addition, a new Moto3 category that uses 4-stroke 250 cm^3 engines has been created to replace the GP125 category (125 cm^3 2-strokes) from 2012. In conjunction with this change, the NSF250R has been newly developed as a machine for entry-level riders.

The NSF250R carries on the aim of broadening the base of motorcycle sports fostered by the RS125R, and was developed as a high-performance, compact, lightweight racing machine that feels familiar to RS125R users and can be used to learn the riding basics required to step up from the entry-level class to the premier class.

* Motorcycle R&D Center

2. Development Goals

Two-stroke GP125 class races currently held around the world are the gateway to road racing, and support a wide range of road racing, from young riders to veterans, and from local races to the Grand Prix Championships. The characteristic of GP125 class machines is a vehicle size class that enables easy machine control even by younger entry-level riders. In addition, these machines feature good engine and body responsiveness with a direct feeling, and have a wide range of setting functions to display the maximum machine performance. The basic concept of the NSF250R inherits these elements, and the development goals were to realize high maneuverability as a racing machine with the easy handling of a 4-stroke engine; that is to say, “lightweight, compact, high output, and high efficiency.”

3. Overview of Model

Figure 1 shows an external view of the NSF250R, and Table 1 lists the basic specifications. To pursue speed as a racing machine and as a result of aiming for “lightweight, compact, high output, and high efficiency,” it was determined that a specially designed engine and a compact body equivalent to the RS125R should be selected.

A DOHC single-cylinder engine equipped with an

Table 1 Major specifications

Model name		NSF250R
Dimensions (L x W x H) (m)		1.809 x 0.560 x 1.037
Wheelbase (m)		1.219
Ground clearance (m)		0.107
Seat height (m)		0.729
Caster angle (deg)		22° 36’
Curb mass (kg)		84
Tire size	Front	90/580R17
	Rear	120/600R17
Brake type	Front	Hydraulic disk ϕ296
	Rear	Hydraulic disk ϕ186
Suspension type	Front	Inverted telescopic
	Rear	Pro-link suspension system
Frame type		Aluminum twin tube



Fig. 1 NSF250R external view

intake-from-front, exhaust-to-rear layout, an integrated crankshaft, and a closed crank chamber with scavenging pump was newly developed to realize these goals. In addition, the motorcycle mass was concentrated by adopting a midship muffler, placing the throttle body inside the air box, and other measures.

4. Power Unit (Engine)

4.1. Engine Major Specifications and Development Targets

Figure 2 shows an external view of the NSF250R engine, and Table 2 compares the major specifications with those of the RS125R.

The motorcycle development goals were to realize the high maneuverability of the lightweight, compact RS125R with the easy handling of a 4-stroke engine, so the engine development targets were set as follows.

(1) Thorough concentration of engine mass including the intake and exhaust systems to realize a motorcycle frontal projected area roughly equivalent to that of the RS125R, even though using a 4-stroke engine with twice the displacement.

(2) Setting the power-to-weight ratio equal to that of the RS125R, and achieving maximum power of 34 kW or more.

(3) Adoption of a battery-less electronic controlled fuel injection system (hereafter, PGM-FI system) to enhance drivability and help ensure advantages in terms of circuit time, acceleration performance, and maximum speed.

(4) Adoption of a cam-type auto decompression system that enables push start without the use of a self-starter, kick-starter or other starting device, in order to secure the same push startability as the 2-stroke RS125R while reducing weight and simplifying the mechanism.

(5) Each part has a limited guarantee with the aim of maintaining high competitiveness as a dedicated racing engine. However, all parts require durability of 2000 km or more, and durability of 4000 km should be guaranteed for major parts, assuming periodic maintenance.

4.2. Basic Layout

The engine is based on the CRF250R commercial motocrosser, which is also a competition machine. However, all parts were reviewed including major changes to the valve train, crankcase and other areas in order to realize a dedicated road racing design that secures the qualities required of road racers while also providing advantages for future potential upgrades.



Fig. 2 Engine external view

Table 2 Comparison of engine major specifications

	NSF250R	RS125R
Engine type	Liquid cooled 4-stroke DOHC 4-valve single cylinder	Liquid cooled 2-stroke single cylinder
Displacement (cm^3)	249.4	124.8
Bore x stroke (mm)	78 x 52.2	54 x 54.5
Compression ratio	12.3	7.98
Maximum power (kW/rpm)	35.5 / 13000	32.6 / 12250
Maximum torque (Nm/rpm)	28.0 / 11000	25.9 / 11500
Fuel supply system	Battery-less PGM-FI, GQD1A φ50	Carburetor, PJ38
Starting type / starting assist system	Push start / auto-decompression system	Push start / none
Ignition system	Full-transistor	Digital C.D.I.

Figure 3 shows an overview of the engine layout. The basic engine layout aims to realize the development concept of "lightweight, compact, high output, and high efficiency." First, an intake-from-front, exhaust-to-rear layout was selected and a ram-air intake system was equipped as standard to increase the charging efficiency. The cylinder which has a relatively shallow water jacket was tilted rearward by 15° to secure the space required for intake-from-front and to concentrate mass.

In addition, a DOHC-type valve train was adopted as suitable for a small displacement road racer that is frequently used in the high-engine-speed range, and titanium materials were used in both the intake and exhaust vales for the first time in a Honda mass-production vehicle.

The shaft layout places the balancer shaft above the crankshaft in order to shorten the engine longitudinal length and concentrate mass.

Furthermore, a semi-dry sump system was adopted that uses the space comprising the bottom of the left side cover and the right and left crankcase as an oil tank inside the case, and a scavenging pump was added inside the closed crank chamber to reduce friction by reducing pumping loss.

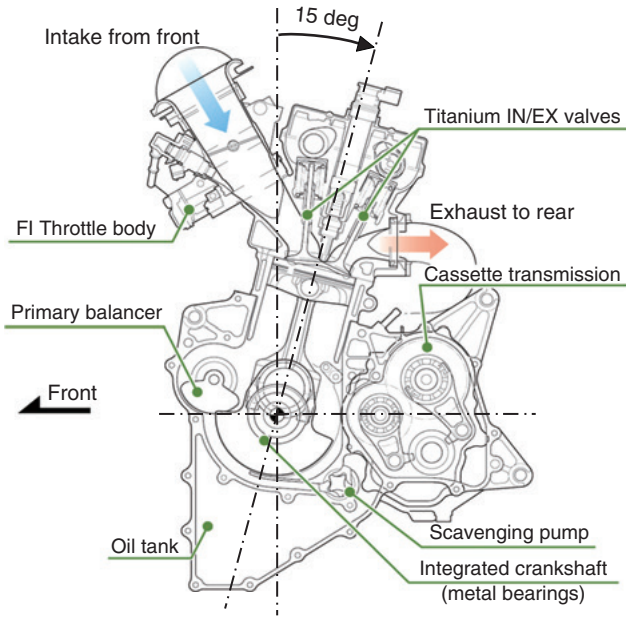


Fig. 3 Engine layout

4.3. Output Characteristics

Figure 4 compares the output characteristics of the RS125R (2-stroke) and the NSF250R (4-stroke). The port shapes, valve timings, and intake and exhaust systems were optimized and friction loss was reduced to obtain the easy-to-handle output characteristics of a 4-stroke engine with flat torque characteristics, enabling simultaneous achievement of the target maximum power. This resulted in performance enhancement of approximately 9% in terms of maximum power and approximately 8% in terms of maximum torque.

Friction loss was reduced by approximately 21% at the

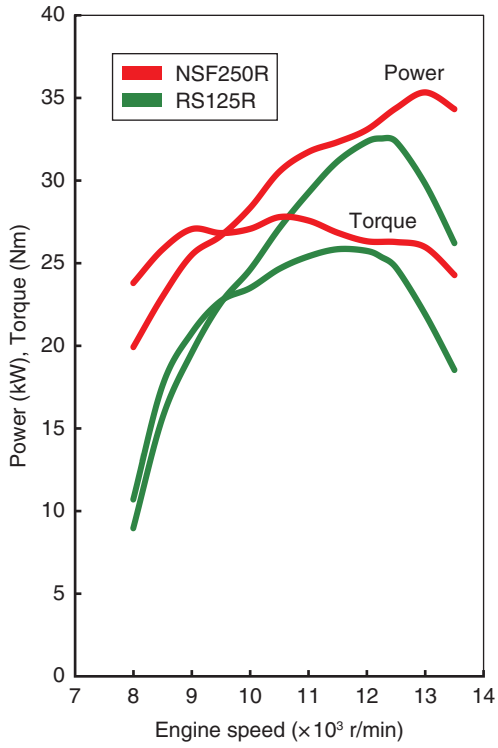


Fig. 4 Comparison of output characteristics

maximum output engine speed of 13000 r/min compared to the CRF250R (2009 year model), which has the same bore-stroke. Figure 5 compares the friction loss under the same oil temperature conditions, as measured by the motoring method.

The main technologies introduced to the engine to realize these results are described below.

4.4. Thinner Lightweight Forged Piston

Figure 6 shows the structure around the piston. A thin, lightweight piston with a bore diameter of 78 mm and a total height of 31.5 mm is used. The piston is hot-forged using A2618 materials with good high-temperature strength, and the piston head that forms the combustion chamber is finished by full machining. In addition, T6 treatment is performed as the piston heat treatment to increase strength for racing.

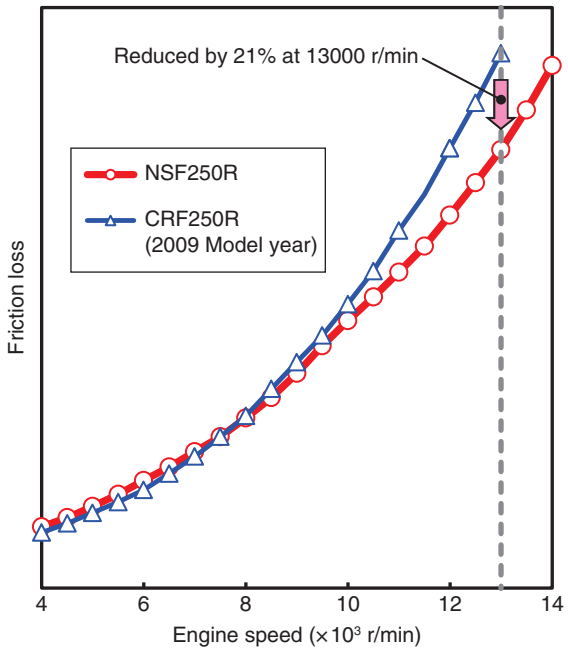


Fig. 5 Comparison of friction loss

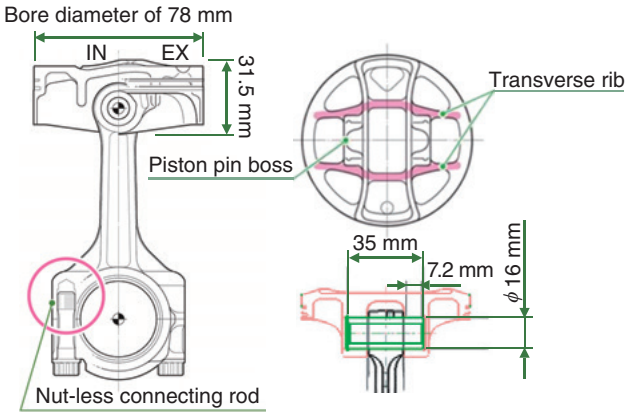


Fig. 6 Structure of piston and connecting rod

The shape was investigated and verified by CAE analysis. Based on these results, two transverse ribs connecting the pin bosses were added to the piston rear surface, and the transverse rib height decreases towards the piston peripheral wall. This enabled simultaneously increasing rigidity and reducing mass.

The top ring groove and the piston pin clip groove are plated with a nickel-phosphorous (Ni-P) alloy to increase wear resistance. This enables maintaining high performance while enhancing durability.

The piston pin is short with an overall length of 35 mm relative to an outer diameter of ø16 mm, and the contact surface width between the pin boss and the piston pin is narrow at 7.2 mm per side, which is disadvantageous in terms of resistance to surface contact pressure. Therefore, wear resistance is increased and friction is reduced by applying a diamond-like carbon (DLC) coating as surface treatment. In addition, heat-resistant case hardening steel with an increased molybdenum blending ratio is used as the piston pin material.

The specifications use only the two piston rings of the top ring and the oil ring. The top ring surface treatment consists of a nitriding base with ion plating on the sliding surface around the circumference to increase wear resistance and reduce friction.

These reductions in size and weight around the piston reduced the reciprocating motion mass by approximately 4% compared to the CRF250R (2009 year model).

4.5. Forged Integrated Crankshaft and Nut-less Connecting Rod

Figure 7 shows a sectional view of the area around the crankshaft.

The forged crankshaft has an integrated structure and uses originally developed high-strength nitriding steel[(1)], with low-temperature carbonitriding (LCN) applied as surface treatment, and high frequency induction hardening applied to the timing sprocket and oil pump drive sprocket

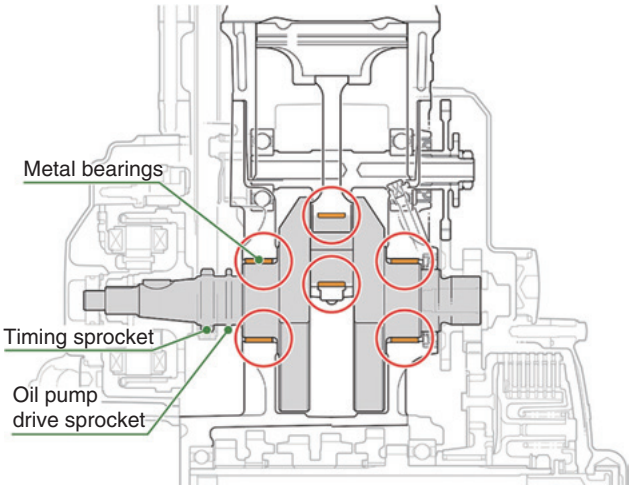


Fig. 7 Sectional view of crankshaft unit

areas. With these techniques, it was made possible to realize the high rigidity and high accuracy required for a high-speed, high-power racing engine while also increasing the strength of the sprocket area.

The connecting rod uses a lightweight nut-less system (Fig. 6). The simple structure is fastened by screwing a bolt into a hole cut directly into the rod side, which reduces the mass compared to the conventional type.

Metal bearings are used for the connecting rod big end bearings and crankshaft journal bearings to support higher power and reduced friction as well as to reduce the engine mass and size.

4.6. Cylinder Head, Cylinder and Valve Train System

Figure 8 shows a sectional view of the intake and exhaust port shapes and an overview of the offset cylinder and the valve train system.

The intake-from-front, exhaust-to-rear layout makes it easier to straighten the ports. In particular, the position of the injector mounted on the throttle body built into the air cleaner box is shifted forward (toward the front of the motorcycle). This enables the inlet port to rise more directly upward, which realizes a high-efficiency downdraft-type straight port.

The cylinder is made from a lightweight aluminum alloy with nickel silicon carbide (Ni-SiC) surface treatment applied to the bore surface. In addition, the cylinder axis is offset by 2 mm to the inlet side, which reduces the thrust load between the piston and the cylinder, reducing friction loss.

In contrast to the piston bore diameter of 78 mm, four valves consisting of two IN valves with a diameter of 32.5 mm and two EX valves with a diameter of 26 mm are set for the valve train, and lightweight titanium valves are used for all valves. The IN valves use a Ti-6Al-4V based titanium alloy that uses off-grade sponge titanium with a large iron component[(2)]. The EX valves use a heat-resistant titanium alloy that is a modification of Ti-6Al-2Sn-4Zr-2Mo, and marks the first titanium EX valves in a Honda mass-production vehicle.

In addition, a compact combustion chamber with the ideal shape was realized by setting a narrow angle of 21.5° between the valves and using a flat shape for the combustion chamber surfaces of both valves.

The cam chain uses a BorgWarner 96 type chain to simultaneously increase strength and reduce friction, and to secure the required crank timing sprocket strength. The specifications also support future potential upgrades such as even higher rotation speeds and enhanced performance.

The cam chain tensioner uses a double tensioner system that provides an auto tensioner lifter in the cylinder area and a manual tensioner in the head area. This realizes stable cam chain driving under the operating conditions of road racers that are frequently used at high engine speeds, and is also an effective means of suppressing irregular vibration of cam chain behavior due to sudden crankshaft rotation speed fluctuation produced by gear shifting and other conditions during actual operation.

4.7. Dual-Channel Lubrication System and Closed Crank Chamber with Scavenging Pump

Figure 9 shows an overview of the dual-channel lubrication system.

A dual-channel type lubrication system is used that places an oil seal on the right side of the crankshaft and balancer shaft, and divides the lubrication methods for the crankshaft and piston side (internal-combustion engine side) and for the transmission and clutch side (drive system side) into two separate channels. The internal-combustion engine side adopts a force feed-type lubrication system using a trochoid-type feed pump, and the drive system side adopts the same oil bath-type lubrication system as that used in 2-stroke engines.

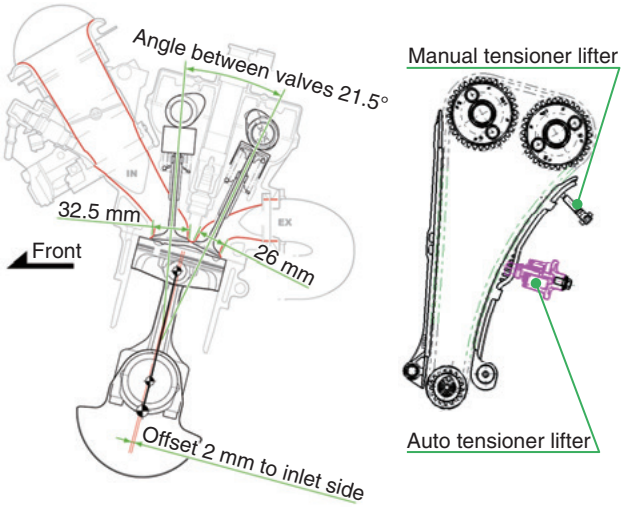


Fig. 8 Engine sectional view and valve train system

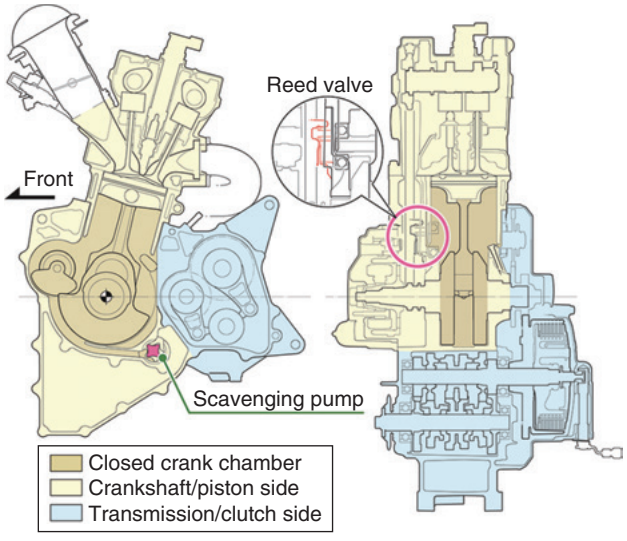


Fig. 9 Dual-channel lubrication system

The merits of a dual-channel lubrication system are that the drive system side oil does not directly receive the combustion heat from the internal-combustion engine, which suppresses the rise in oil temperature, and the size can be reduced due to the smaller clutch capacity. This enables use of the same clutch capacity, transmission and other specifications as those of the RS125R.

An additional merit is that mixing of wear debris produced by sliding of the transmission gears and other parts into the internal-combustion engine side oil is suppressed, enabling use of a smaller oil filter. Furthermore, molybdenum and other additives can be used on only the internal-combustion engine side, enabling reduced friction loss without lowering clutch performance.

Regarding the crankcase, the area housing the crankshaft, balancer shaft, connecting rod and piston unit has a closed structure. Pumping loss and friction are reduced by using a scavenging pump located on the same axis as the oil feed pump to forcibly discharge the oil inside this closed crank chamber and generate a negative pressure.

In addition, a reed valve was added to the upper left of the closed crank chamber (the balancer bearing housing area). When push-starting the engine, the rotational speed is low so the scavenging pump is unable to operate effectively, and a positive pressure is generated inside the closed crank chamber. In these cases, the reed valve opens to help prevent a rise in the pumping pressure, providing the stable crankshaft rotation speed required for starting.

4.8. Auto Decompression System

An auto decompression system is mounted to help start the engine by push-start. This system uses a lightweight, simple cam-type decompression system with a centrifugal weight as shown in Fig. 10. By reducing the compression pressure inside the cylinder during engine start and securing sufficient crankshaft rotation speed even during push start, the required power generation level can be obtained from the ACG. This enables ECU start-up even with a battery-less system.

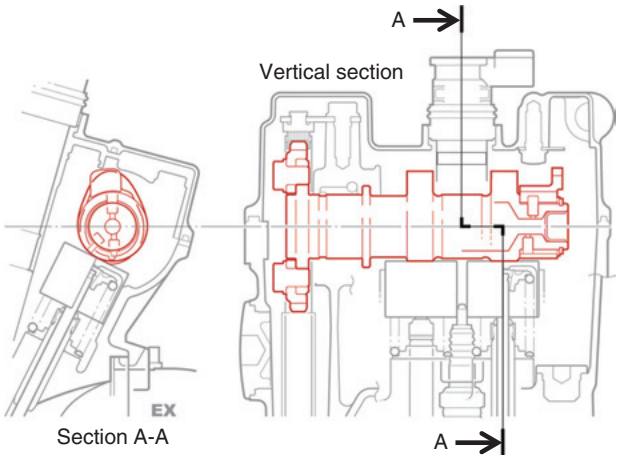


Fig. 10 Auto decompression system

The two important points for the decompression system settings are optimization of the valve open timings and lift amounts, and setting the proper decompression OFF engine speed in combination with the centrifugal weight and set spring settings. In addition, push-startability equivalent to that of the 2-stroke RS125R is provided by optimizing the fuel injection settings.

4.9. Cassette-Type Transmission

An easily replaceable cassette-type transmission is used to enable the optimal gear selection in accordance with the characteristics of each circuit (Fig. 11).

This cassette-type transmission enables maintenance and gear ratio changes in a short time without the need to remove and remount the engine or disassemble the crankcase. In addition, the RS125R transmission can also be used in consideration of convenience for RS125R users.

4.10. Fuel Supply System and Induction System

Figure 12 shows an overview of the throttle body, and Fig. 13 shows an overview of the induction system.

The throttle body uses an intake air control valve (IACV), and the amount of intake air in the throttle closed state is controlled by regulating the throttle opening with the PGM-FI system. This reduces the strong engine braking in a 4-stroke single-cylinder engine, enabling the deceleration



Fig. 11 Cassette type transmission

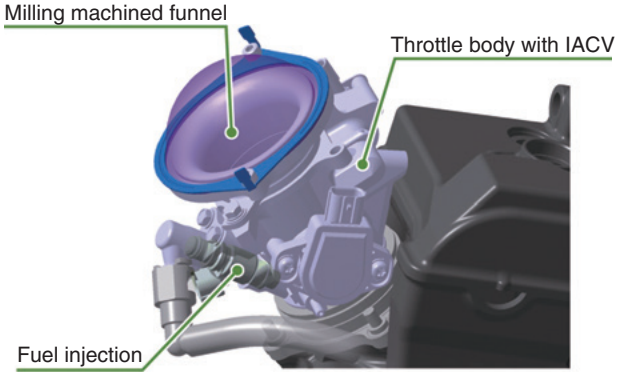


Fig. 12 Throttle body external view

feeling to be set in accordance with the rider's preferences.

The air funnel is a short type with an overall length of 26 mm to optimize the output characteristics and response, and is made of machine-processed aluminum for increased accuracy.

The throttle body unit is housed inside the air cleaner box like a MotoGP machine, and the layout places the air cleaner box between the cylinder and the radiator. This makes the most of the limited motorcycle body space while concentrating mass, enabling realization of a large-capacity 5L air box.

Regarding the induction system, a ram-air intake system not mounted in the RS125R is equipped as standard, and the air passing below the bottom bridge passes through an air duct with a large opening and is led straight to the air box. This active use of ram-air intake increases the power.

4.11. Exhaust System

The exhaust pipe uses stainless steel with good heat resistance. A diffuser shape with pipe diameter that expands gradually as it approaches the muffler for good exhaust efficiency was adopted and the output characteristics were optimized with the aim of simultaneously achieving both the flat torque characteristics of a 4-stroke engine and the target maximum power (34 kW or more).

In addition, the exhaust system layout uses a "midship muffler layout" in which the exhaust pipe leads from the back of the rearward tilted cylinder in a large reverse "S" shape to the muffler located under the engine. Placing the muffler, which is a heavy object, close to the center of gravity of the motorcycle body concentrates the mass and realizes handling that does not convey the effects of the increase in mass due to the change to a 4-stroke engine. Furthermore, placing the muffler, which has a large volume, inside the cowl also helps to reduce air resistance.

Figure 14 shows an overview of the exhaust system layout.

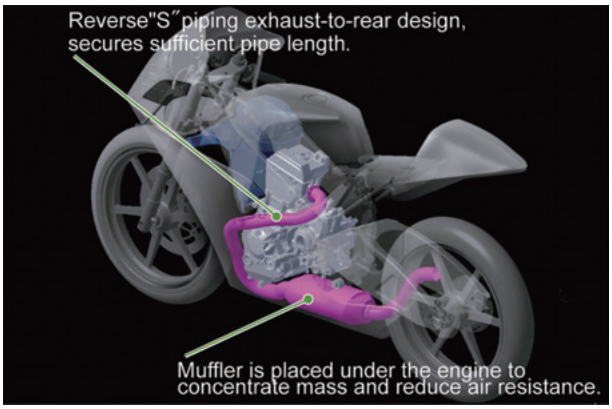


Fig. 14 Exhaust system layout

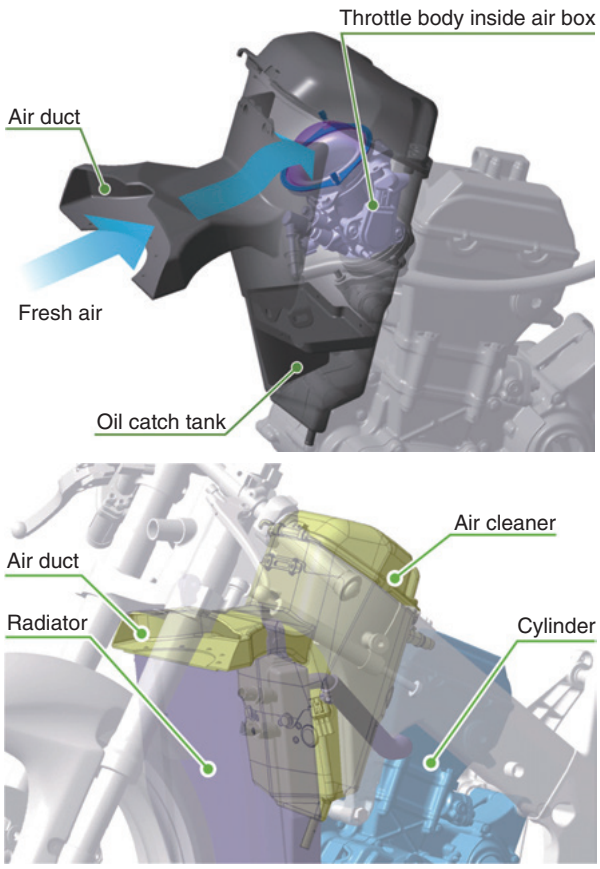


Fig. 13 Induction system

5. Motorcycle Body Layout

The following technical means were adopted to realize a package that carries on the compact body of the RS125R with a 4-stroke 250 cm^3 engine.

(1) Rearward tilted cylinder engine with intake-from-front and exhaust-to-rear
(2) Throttle body inside the air box
(3) Reverse "S" piping exhaust pipe
(4) Midship muffler

This motorcycle packaging helped to reduce both weight and size. Figure 15 shows the major dimensions and riding position.

In terms of dimensions, the wheelbase is the same as that of the RS125R, but the crankshaft center in the engine-mounted condition was set 27.4 mm to the front and 51.5 mm below that of the RS125R. As a result, the front shared load ratio was able to increase 0.7 percentage points while keeping the same center of gravity height as that of the RS125R. In addition, the motorcycle mass increased by approximately 9.2 kg, but increasing the degree of mass concentration achieved a yaw moment of inertia equivalent to that of the RS125R. Optimizing the mass distribution and center of gravity height in this manner enabled simultaneous achievement of a high degree of controllability and stability, which realized the cornering performance demanded by the lightweight class.

Figure 16 compares the yaw rate at cornering when the RS125R and NSF250R are driven by the same driver over the same circuit. This shows that the yaw rate at cornering is the same in the high-speed range, and is enhanced by approximately 5% in the low-speed range.

The frame body is based on the RS125R, and the optimal rigidity balance required for the NSF250R was achieved by changing the front engine hanger shape and the main pipe sectional shape to increase torsional rigidity while maintaining lateral rigidity compared to the RS125R (Fig. 17).

The newly designed swing arm was optimized by a similar rigidity balance technique as that used for the frame body with the aim of increasing stability and the sense of integration with the frame. In addition, the center of gravity of the standalone swing arm was shifted toward the front to concentrate mass. Furthermore, both the swing arm and the frame body have skeletal shapes that enable them to twist flexibly.

These measures increase stability when braking and provide a degree of cornering freedom and nimbleness equal to or greater than that of the RS125R. This realizes handling that does not convey the increase in mass due to the change to a 4-stroke engine, even when approaching corners.

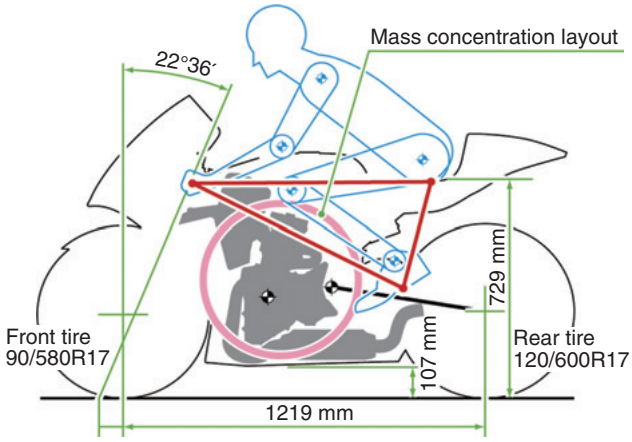


Fig. 15 Major dimensions and riding position

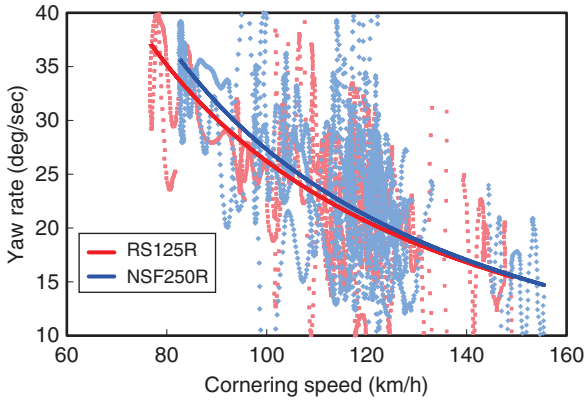


Fig. 16 Comparison of yaw rate at cornering

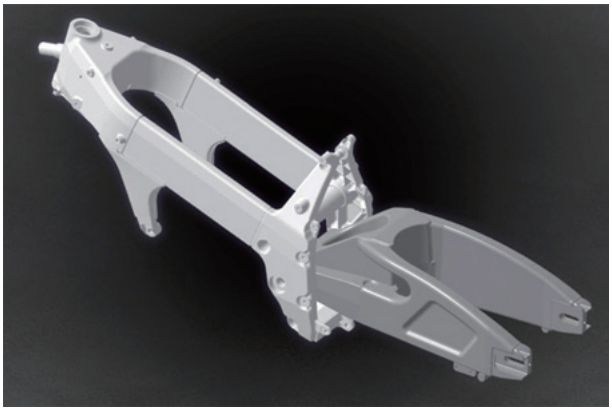


Fig. 17 Frame body and swing arm

6. Conclusion

The NSF250R utilizing the technology introduced in this paper not only manifests the stable, high performance befitting a top-end machine, but also makes this performance easily available to almost anyone, and Honda is confident that it can meet the demands of all riders.

Like the RS125R, it is hoped that the NSF250R will vitalize the Moto3 class, thereby broadening the base of motorcycle sports, sharing dreams and emotion with spectators, and creating the chance for riders to become future MotoGP champions.

References

(1) Suwa, S., Kawaguchi, D., Murakami, A., Kimura, K., Tada, M.: Development of Nitrocarburized High Strength Crankshaft Through Controlling Vanadium Carbonitride Precipitation by Normalizing, SAE Paper, 2009-32-0076 / SETC2009, 20097076 (2009)

(2) Marui, Y., Kinoshita, T., Takahashi, K.: Development of a Titanium Material by Utilizing Off-Grade Titanium Sponge, SAE Paper, 2002-32-1816 / SETC2002, 20024309 (2002)

■ Author ■



Tomio ONOSATO



Yoshiyuki KURAYOSHI

Development of BF250 Flagship Outboard Motor

Yoshihiro HARADA* Kazuhiro ISHIZAKA* Go TANAKA*
Kunihiko ISHIZUKA* Fumiya ISONO*

ABSTRACT

The BF250 large outboard motor was developed to achieve higher engine output using the first direct air intake system to be adopted for an outboard motor.

The conventional structure had the air intake inside the engine cover in order to prevent water infiltration into the engine combustion chamber. By contrast, the developed engine, which is the first in the world to incorporate a direct intake system, is formed with an intake duct that has drainage functionality inside the engine cover so that water is separated as outside air is inducted directly into the engine. This lowers the intake air temperature more than in the conventional structure and, in combination with other specification changes, it achieved 184 kW (250 HP) with a basic structure that is used in common with the current mass production model BF225. Revision of the lean burn control yielded a maximum 30% enhancement of fuel consumption in cruising speed range relative to outboard motors of the same class. In other respects, adoption of a high durability gear case at the top of its class, adjustable idle charge system, and shifting load reduction control system heightened both durability and convenience.

In order to accentuate the appeal of the BF250, a power intake form that achieves a high level balance of functionality and design was adopted. This raises the outboard motor to the level of a finished product well suited to be Honda's flagship model.

1. Introduction

Recent years have seen a trend to increase the horsepower of the boat type capable of coastal cruising that is known as an offshore boat, particular for those manufactured in North America and Europe. A large percentage of these outboard motors of the large class, which have output of 147 kW (200 HP) or more, are installed on boat types for commercial use that are used in long-term heavy duty environments. Durability and reliability are therefore demanded.

The flagship BF250 large outboard motor was developed in light of these requirements, and the technology adopted in the BF250 is introduced here. Figure 1 shows an external view of the BF250.



Fig. 1 External view of BF250

2. Large Outboard Motor Market Environment and Demands

2.1. Market Environment of the Large Outboard Motor

The main market is in North America. Figure 2 shows the changes in that market in maximum horsepower capacity of offshore boats capable of mounting large outboard motors.

Outboard motor manufacturers have continued to fill out their lineup of large models of 184 kW (250 HP) or more. At the same time, boat manufacturers have also been concentrating on their lineup of large boats (Fig. 2). For the outboard motors mounted on those large boats, there is a trend toward choice of 184 kW (250 HP) engines for their balance of price and performance.

In addition to general leisure use, a large percentage of this class of outboard motor boat has professional uses such as commercial and government. At approximately 30%,

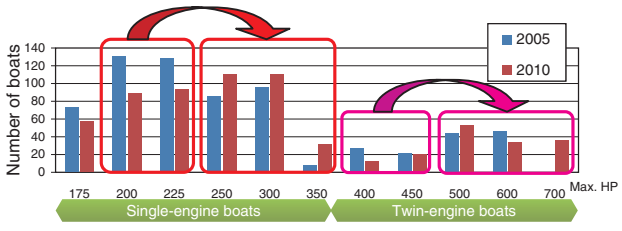


Fig. 2 Number of offshore boats by maximum mountable horsepower

* Power Products R&D Center

this figure is higher than will be found in other horsepower segments (Fig. 3).

2.2. Demands for Performance

As discussed above, there is a preference on the market for engines with 184 kW (250 HP) output. Furthermore, there is demand for high durability and reliability to withstand the harsh conditions of long-term, heavy-duty operation envisioned for professional uses. (As an example of use, Fig. 4 shows a boat type that is used in coastal patrol and other such work.)

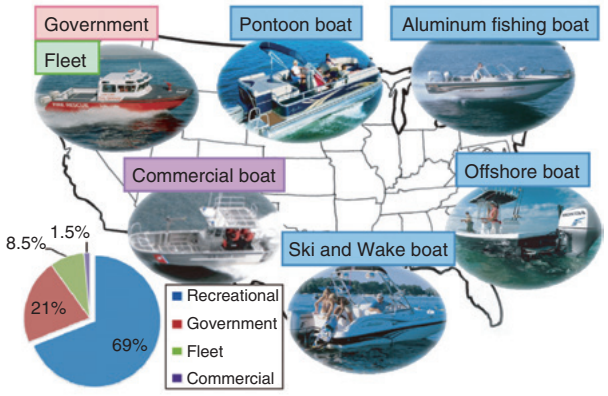


Fig. 3 Variety and percentage of large boat in the market



Fig. 4 Coastal patrol boat

3. Development Concept

In Customer Satisfaction Index (CSI) surveys conducted by J. D. Power and Associates from 2005 to 2009, the current mass production model BF225[(1)] won first place four times during the five-year period. With this kind of established reputation for performance and reliability, the BF225 was taken as the base for development of a product aimed to be appropriate as the flagship model in the Honda outboard motor series. Making minimal changes to the base engine specifications while raising the efficiency of the intake system to achieve 184 kw (250 HP), this development adopted a highly advanced design and achieved further enhanced reliability as well as power performance, fuel consumption, and utility at the top of its class.

Table 1 Specifications

Code name	BF250A X-type
Overall length (mm)	920
Overall width (mm)	625
Overall height (mm)	1887
Transom height (mm)	635
Dry mass (kg)	284
Engine type	4 stroke 60˚ V-Type 6 cylinder
Displacement (cm^3)	3583
Bore (mm) × Stroke (mm)	89 X 96
Compression ratio	10.0 : 1
Valve train	SOHC VTEC 24 valves
Maximum power (kW/rpm)	183.9/ 5800
Maximum torque (N·m)	320
Recommended engine speed range (rpm)	5300 - 6300
Fuel supply system	Programmed Fuel Injection
Ignition system	Programmed Ignition
Charge output (A)	60
Exhaust system	Through propeller hub
Gear ratio	2.00 : 1 (24/12)

4. Major Specifications and Overview

Table 1 shows the major specifications for the BF250.

Based on the BF225's 3.5-liter, 60° V6 engine, the Legend crankshaft was combined with connecting rods to extend the stroke by 3 mm, and the engine displacement was set at 3.6 liters. Furthermore, by changing the compression ratio from 9.4 (BF225) to 10.0, both high output and high efficiency were achieved.

5. Main Technology

5.1. Direct Air Intake System

Following the above concept, this direct air intake system is the technology adopted to achieve an increase in output with minimal changes to specifications of the base mass production model BF225.

The present system completely separates the engine intake and exhaust heat as a means of lowering the intake air temperature. It is structured with a separate duct through which exhaust heat is evacuated by a cooling fan.

This was done making the minimum necessary changes to the base model in the engine cover, cooling fan, and fan cover.

In order to minimize the increase in overall height relative to the base model, maximum use was made of the space inside the engine cover by optimal placement of the intake duct, exhaust heat duct, drain duct, and silencer system (Fig. 5).

The following will explain details of the various element technologies.

5.1.1. Intake air cooling and water separation system

Figure 6 shows the engine intake system of the BF225 base model. The structure not just of the BF225 but also of conventional outboard motors from other manufacturers brings outside air inside the engine cover and causes it to circulate within the cover to prevent water intrusion into the engine combustion chamber, perform auxiliary machine cooling, and reduce noise values. After that, it is taken into the throttle body. Consequently, the difference Δt between the outside air temperature and the throttle body intake air temperature is large. This is a factor that lowers engine output.

Figure 5 shows the BF250 direct air intake system. Here, by contrast, air inlets placed on both sides of the engine cover take in outside air that passes through an intake duct made up of an air guide and rear air duct inside the engine cover and then is guided directly into the throttle body. The air inducted by this direct air intake system is less likely to be affected by heat generated by the engine. Therefore, the Δt can be reduced by 14°C compared with the conventional construction, contributing significantly to increased engine output.

Adoption of the direct air intake was also accompanied by the addition of a water separation and drain structure. This was added on the assumption that bringing outside air directly in would cause water intrusion inside the intake duct.

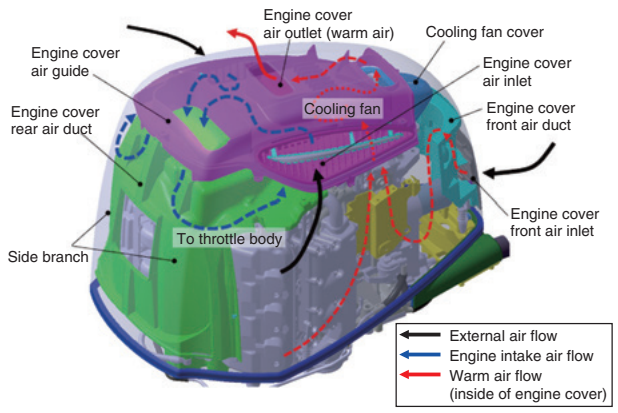


Fig. 5 Direct air intake system (BF250)

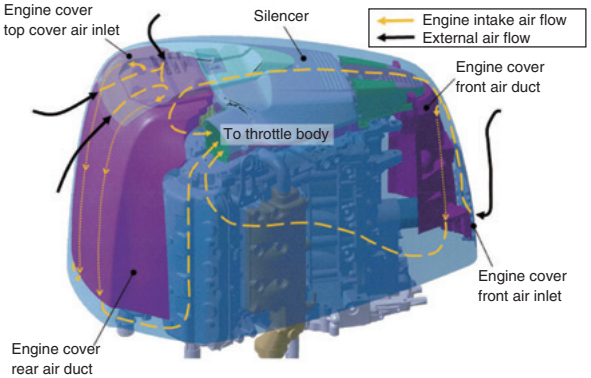


Fig. 6 Conventional air intake system (BF225)

Structures are set up to handle both large and small droplets of water carried along by the flow velocity from the intake. This prevents their intrusion into the throttle body side (Fig. 7). The large water droplets are prevented from intruding by means of a chimney shaped rib placed immediately behind the inlets on both sides. The small water droplets that are carried past this rib by the intake flow velocity pass through an intake duct that turns back 180°. In this arrangement, they are made to adhere to the inside wall of the engine cover while passing through the intake duct. There they are guided downward by vertical ribs in the inside cover wall (Fig. 8) and evacuated through a water drain at the bottom end of the air duct.

In addition to its function as a water drain passage, the side branch portion has the function of decreasing noise (Fig. 7). There, the intake pulsation is used to create a condition whereby the pressure at point B is lower than at point A. This moves water to point B where the pressure is lower, heightening drain performance at wide open throttle (WOT).

5.1.2. Auxiliary machine cooling structure

In adopting the direct air intake system for the BF250, it also became necessary to have a cooling passage independent from the intake duct to perform auxiliary machine cooling inside the engine cover. The BF250

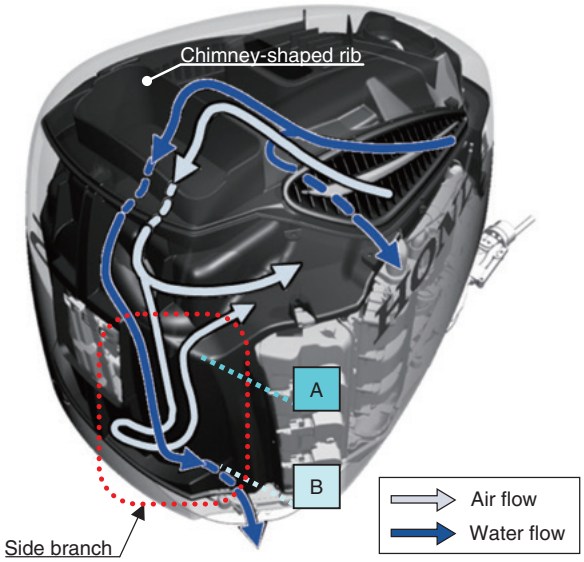


Fig. 7 Separation system of air and water

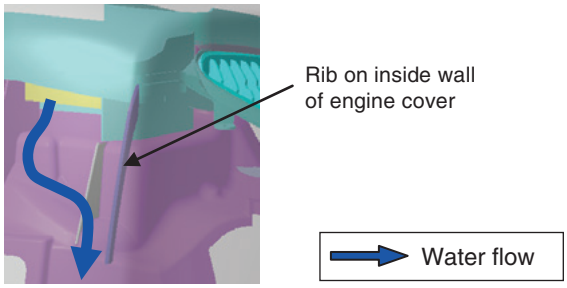


Fig. 8 Rib on inside wall of engine cover

therefore has newly included a fan cover consisting of a cooling fan directly coupled to the crankshaft and a scroll-shaped chamber that covers the cooling fan. Figure 9 shows a simplified diagram of the cooling system inside the engine cover. Figure 10 shows the form of the scroll-shaped chamber in the fan cover. The scroll-shaped chamber is made up of fan covers A and B, and is made as a form that is independent of the forms of the engine parts around it. This suppresses the turbulence around the cooling fan, separates the cooling fan from the high-temperature engine parts, and can suppress the thermal expansion of the air surrounding the cooling fan, thus achieving higher fan efficiency. The result enabled creation of a cooling system capable of efficiently exhausting the heated air inside the engine cover to the outside, allowing stable auxiliary machine cooling.

5.1.3. Structure to decrease noise

Adoption of the direct air intake system involved placement of intake and exhaust heat ducts. The result was an inability to place an intake silencer chamber with adequate capacity. Directly linking the throttle body to the outside of the engine cover with an intake duct made for a structure that discharges intake noise to the engine cover exterior. In order to reduce the intake noise, therefore, a side branch structure was adopted for the BF250. As shown in Fig. 11, this is a silencer that works by interference of acoustic waves.

A side branch of length L is located on either side partway along the intake duct that is composed of the engine cover and rear air duct. The purpose of this is to cause acoustic wave interference in order to reduce the intake noise of intake pulsation at the frequency of approximately 300 Hz at WOT.

The adoption of the direct intake structure for the BF250 resulted in an increase in WOT pass by noise[(2)] of 4 dBA compared to the conventional model. However, the addition of the side branch structure to deal with intake noise, which is a factor in the increase in sound pressure, and measures to optimize the length of the intake duct to avoid resonance with the intake noise. This reduced intake noise by 10 dBA. This enabled the pass by noise to be suppressed to a level that does not exceed the limit value (≤ 75 dBA) (Fig. 12).

5.1.4. Effectiveness (power and fuel consumption)

Adoption of the direct intake structure enabled a 14°C reduction in the difference Δt between the outside air temperature and the throttle body intake air temperature compared to the conventional structure. As a result, the synergistic effect of the enhanced volumetric efficiency (ηv) due to increased density of intake air and the ignition timing advance due to the raised knocking limit yielded an increase of 6.6 kW (9 HP) in peak output (Fig. 13).

In addition, the stroke was made longer, increasing the displacement; the compression ratio was raised; the

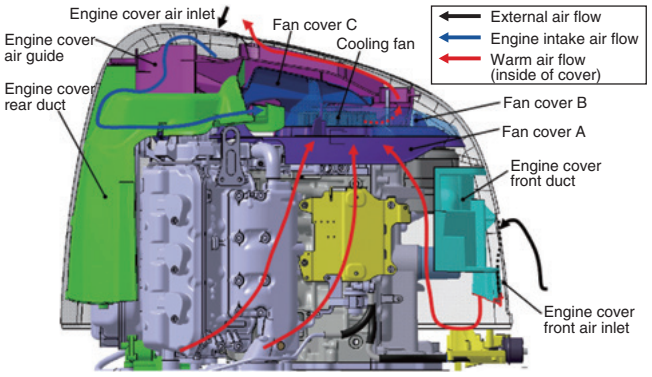


Fig. 9 Cooling fan system

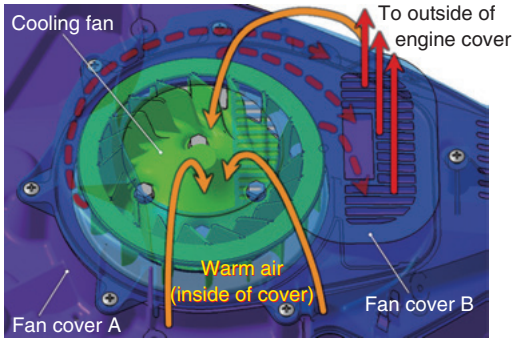


Fig. 10 Scroll shape of fan cover

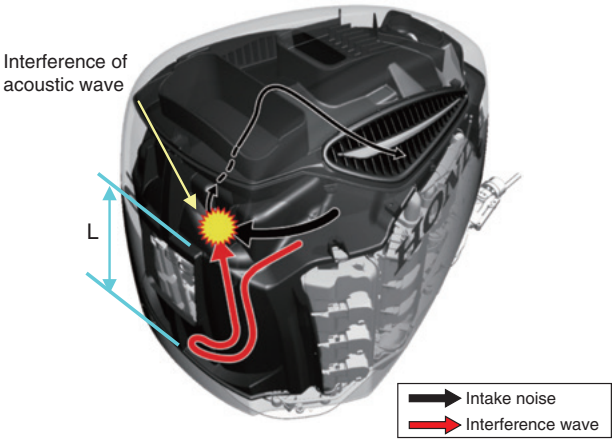


Fig. 11 Side branch system for noise reduction

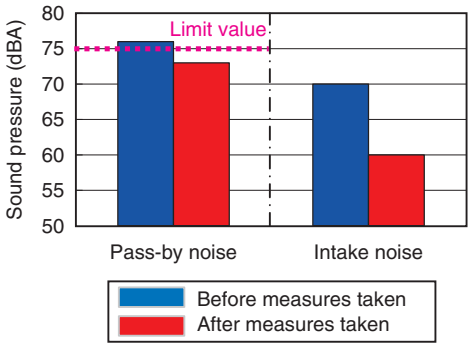


Fig. 12 Pass-by noise and intake noise

valve timing was optimized; the intake valve diameter was increased to heighten ηv; the adoption of a large diameter thermostat and piston cooling oil jet raised the engine cooling capacity; and the rated speed was increased. By these and other such effects, the developed motor achieved a peak output of 184 kW (250 HP) while sharing the basic structure of the BF225.

In addition to the increase in engine output, a revision of lean burn control[3] achieved a maximum 30% enhancement of fuel consumption in cruising speed range relative to outboard motors of the same class (Fig. 14).

5.2. High Durability Gear Case

Figure 15 shows a structural drawing of the BF250 gear case assembly. Generally, every effort is made to reduce the size of the shell shaped section that contains the bevel gear of the outboard motor gear case in order to reduce the water resistance. However, reducing the diameter of that section is disadvantageous in terms of gear strength design. As this indicates, power performance and strength are mutually antagonistic. In order to enhance the durability of the BF250, the diameter of the bevel gear was increased by 10% over that of the BF225.

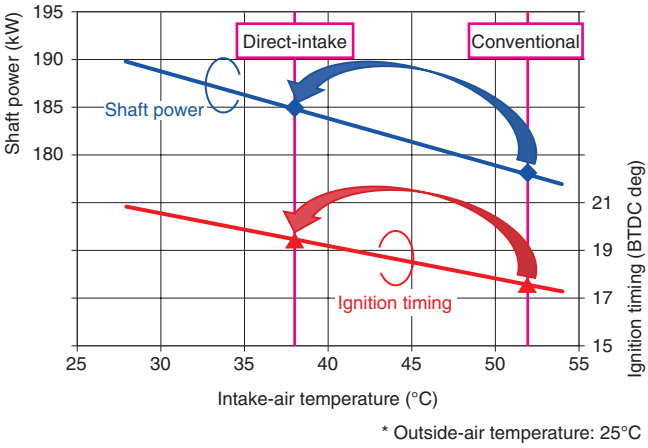


Fig. 13 Intake-air temp-shaft power/ignition timing

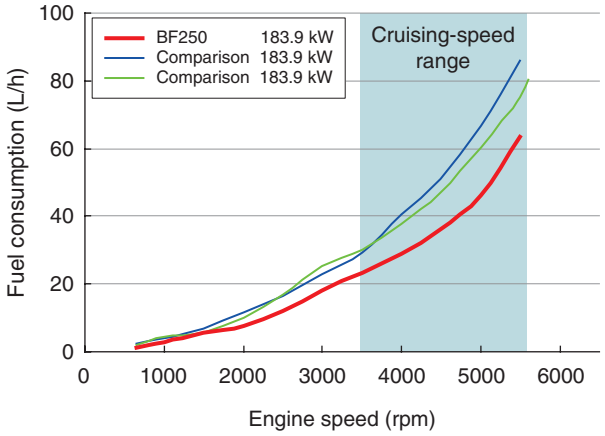


Fig. 14 Fuel consumption at cruising speed

The increase in water resistance resulting from the increased size of the bevel gear was addressed by performing a computer fluid analysis (Fig. 16) to find the optimal case shape. This yielded a 5% decrease in the Cd value, and the steps taken to reduce the water resistance secured power performance that yields nothing to the competition.

For the gear material, a modified material with superior durability was adopted. This is a nickel-chrome-molybdenum steel material refined to remove impurities to the utmost degree. This also enhanced the machining precision of the tooth surfaces, reducing the deviation in gear engagement and thus realizing higher durability.

5.3. Adjustable Idle Charge System

The electronic control unit (ECU) detects the charge output from the AC generator during idling. When it detects the connection of a load exceeding the charge output at the normal idling speed of 650 rpm, the system can raise the engine speed in 100 rpm, thus increasing the charge output by 29%.

5.4. Shifting Load Reduction Control System

Unlike the conventional control, this system adds ignition timing variable control at deceleration to generate engine torque fluctuation and so reduce shifting operation load.

As shown in Fig. 17, changes in engine speed and throttle opening detected by the ECU are used to predict the operator's shifting operation. The ignition timing of cylinders 4, 5, and 6 is retarded to cause fluctuation in the engine torque. This causes variable of transmission



Fig. 15 High durability gear case assembly

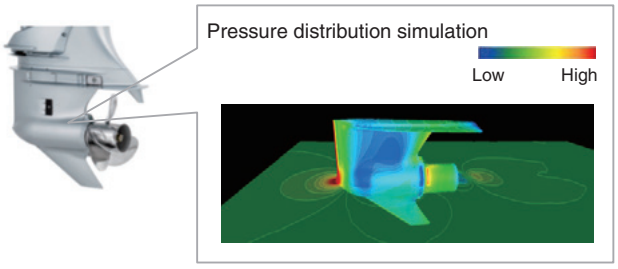


Fig. 16 Fluid analysis simulation

torque in the dog clutch that connects the engine side and the propeller shaft side, reducing the pull-out load on the dog engagement part. This has enabled a 30% reduction in shifting operation load, as shown in Fig. 18.

This does not detect the operator's shifting operation by using a dedicated sensor. Rather, a new control method was developed to make predictions based on changes in the engine speed and throttle opening and reduce the operation load accordingly.

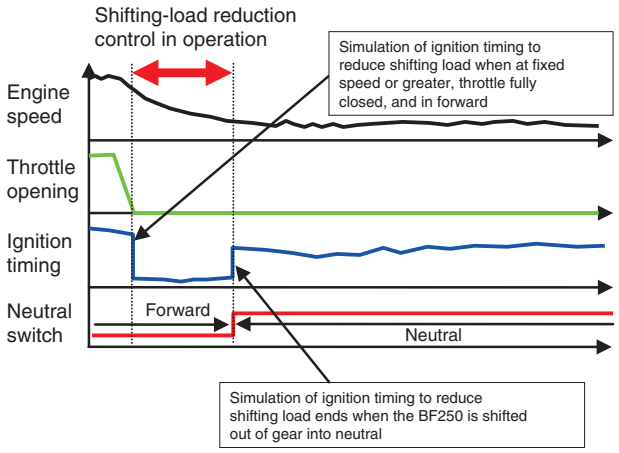


Fig. 17 Shifting-load reduction control

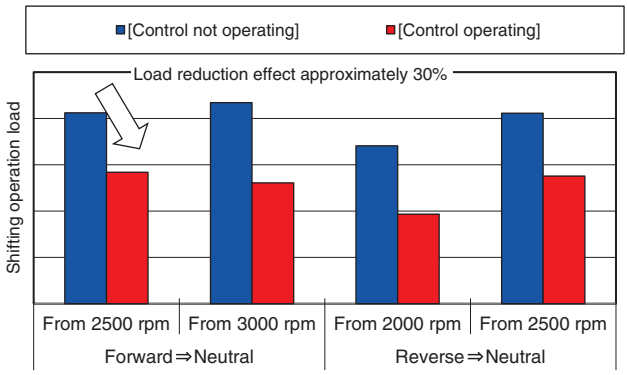


Fig. 18 Shifting-load test results

6. New Design

6.1. Power Intake Form

The direct air intake system is a major feature of the BF250. In order to highlight the appeal of this engine, the "power intake form" was taken as the concept and the following methods were incorporated to realize the design in concrete form.

The intake ports on both sides of the outboard motor top cover, as seen from the operator's point of view, tighten up the bulky appearance of the top cover. This presents a sense of sharpness as an element of appeal (Fig. 19).

A chrome part with a Japanese sword motif was placed in the central part of the intake sections. This underscores the sense of speed while also adding an expressive element never used before. The fin shape in the intake helps prevent the intrusion of splash water from the front while also directing the intake noise toward the rear where it will have less impact on the operator and the surrounding area. It also takes in fresh air from the rear. This achieves a high-level balance of functionality and design (Fig. 20).

6.2. Color Graphic

The color is not the previous silver from a warm color group, but rather a silver with a strong feeling of transparency that gives a sense of depth. This highlights the higher quality and sharper appearance of the engine. The font was also upgraded, and a new typeface with a sense of speed and heightened visibility was adopted (Fig. 21).

The new BF250 design concentrates these elements and qualities, enabling it to convey a powerful image suitable to the flagship model of Honda's BF series.



Fig. 19 Design concept of BF250



Fig. 20 Power intake design

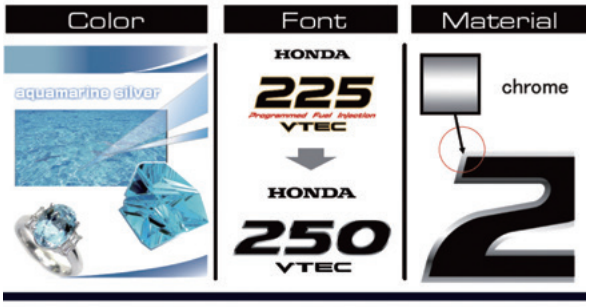


Fig. 21 Color graphic design

7. Conclusion

In development of the BF250, the basic structure of the base model was borrowed while the output power was raised. The durability and reliability were also increased to enable the engine to fully withstand harsh conditions of use while advances were made in utility and design. Development carried out with these aims yielded the following results.

(1) The adoption of a direct air intake structure reduced the difference Δt between the outside air temperature and the throttle body intake air temperature by 14°C and raised output by 6.6 kW. Revision of the lean burn control achieved a maximum 30% enhancement of fuel consumption in cruising speed range relative to outboard motors of the same class.
(2) Adoption of a high durability gear case supported the increase in power output while achieving durability at the top of its class.
(3) Adoption of charge output variable control during idling increased the charge output by 29%.
(4) Adoption of a shifting load reduction control system reduced shifting operation load by 30%.
(5) Adoption of a new power intake form as the flagship model of the BF series clarified the differences from other manufacturers and realized the expression of a "new identity."

These results were very well received. At IBEX 2011 (The International Boat Builders' Exhibition & Conference) held in Louisville, Kentucky, in the United States on October 17-19, 2011, the BF250 received an IBEX 2011 Innovation Award in the outboard motor category from the National Marine Manufacturers Association (NMMA).

References

(1) Tsunoda, M., Furuya, K., Ohsumi, M., Shidara, S., Yonezawa, M., Kimata, R.: Development of Honda Flagship Outboard Motor "BF225/200", Honda R&D Technical Review, Vol. 14, No. 1, p. 11-20
(2) DIRECTIVE 2003/44/EC OF THE EUROPEAN PARLIAMENT AND OF THE COUNCIL of 16 June 2003: ANNEX. I. C. 1 Noise emission levels
(3) Tanaka, M., Shimizu, N., Yamamoto, H., Sakata, S., Yasuda, K., Yamagishi, M.: Development of Midrange Outboard Motor BF60 with Equipment for User Comfort, Honda R&D Technical Review, Vol. 23, No. 2, p. 22-29

■ Author ■


Yoshihiro HARADA


Kazuhiro ISHIZAKA


Go TANAKA


Kunihiko ISHIZUKA


Fumiya ISONO

Development of New CVT for Midsize Vehicle

Koichiro INUKAI* Akihiro SHIBAHARA* Yasunori MURAKAMI*
Takeshi UCHINO* Michio KOJIMA* Keiichi NISHIYAMA*

ABSTRACT

A CVT for midsize vehicles was developed that simultaneously achieves high levels of fuel efficiency performance and driving enjoyment, reliability and marketability enabling deployment to global markets, and support for high-power direct injection engines. This was done by modifying the CVT for 2.4 L-class vehicles sold in Japan, expanding the ratio range, using CVTF with a high friction coefficient that simultaneously realizes both high efficiency and a high transmission capacity, and adopting protective control such as constant control of the clutch pressure. This enabled achievement of an overall length of 386.5 mm, total weight of 96.1 kg, and maximum transmission torque of 270 Nm, and also enhanced fuel efficiency by approximately 10% (CAFE Comb.) compared to the 2008 model year Accord 5AT and approximately 5% (JC08) compared to the 2010 model year STEP WGN CVT. Thus, CVT performance was obtained that can simultaneously realize high levels of both fuel efficiency and driving enjoyment. This CVT is applied from the 2012 model year STEP WGN and the 2013 model year Accord.

1. Introduction

Recently, high environmental performance is demanded of automobiles, and transmissions (T/M) are playing an extremely important role. Adoption of Dual clutch transmission, CVT, and multi-gear AT with more gears than conventional 4AT and 5AT is also increasing around the world. Honda adopted starter clutch-type CVT from the 1996 model year CIVIC[(1)], and has expanded application mainly to compact vehicles and hybrid vehicles[(2), (3)]. For midsize vehicles, a CVT with a torque converter was used in the 2004 model year Odyssey[(4)], and has been applied to minivans for the Japanese market. To meet global demands for even higher fuel efficiency in the future, there have been requests to apply CVT for midsize vehicles of this class not just to minivans for the Japanese market, but also sedans and SUVs around the world. Against this background, the transmission efficiency of the newly developed CVT was increased while also expanding the torque capacity and ratio range, with the aim of simultaneously realizing the high levels of driving performance and fuel efficiency performance required of midsize vehicles. In addition, an exhilarating and sporty shift feeling was realized so that AT users around the world can switch to the new CVT without a feeling of unnaturalness. This paper describes the development goals, basic structure, and key technologies of this new CVT.

2. Development Goals

The following three items were set as development goals to develop a CVT for midsize vehicles with world-class performance.

(1) High fuel efficiency performance to achieve the year 2020 fuel efficiency standard established by the U.S.
(2) Reliability to support next-generation high-power direct injection (DI) engines and various usage formats around the world
(3) Driving performance marketability that enables worldwide deployment

3. Main Section and Key Specifications

Figures 1 and 2 show the main section and external view of the new CVT for middle-size vehicles (hereafter "this CVT"), and Table 1 lists the key specifications.

The basic layout of this CVT has the following features.

(1) Expansion of the ratio range to 6.54 to simultaneously achieve high levels of fuel efficiency and driving performance
(2) Advanced control of a vane-type oil pump with half-feed switching mechanism, and expansion of the half-feed operation area
(3) Adoption of an electric oil pump to support an idling-stop system

* Automobile R&D Center

Table 1 CVT specifications

		2013 model year Accord	2012 model year STEP WGN	2008 model year Accord (5AT)	2004 model year Odyssey
Engine specification	Type	2.4L DOHC DI	2.0L SOHC i-VTEC Idle Stop	2.4L SOHC i-VTEC	2.4L SOHC i-VTEC
	Max power (kW/rpm)	137/6400	110/6200	150/7000 135/6500	118/5500
	Max torque (Nm/rpm)	243/4000	193/4200	230/4500 225/4500	218/4500
Ratio	Low OD	2.645 0.405	2.645 0.405	1st: 2.651 5th: 0.566	2.470 0.450
	Ratio range	6.54	6.54	4.68	5.48
	Secondary	1.558	1.558	-	1.514
	Final	3.238	3.238	4.437	3.350
	Reverse	0.703	0.703	2.000	1.735
	Transfer (4WD)	-	0.279/1.411	-	-
Dimensions	Overall length (mm)	386.5	386.5	379	385
	Pulley axis distance (mm)	180	180	-	170
	Weight (kg)	96.1 (Wet)	97.3 (Wet)	92.6 (Wet)	95.3 (Wet)

(4) Use of CVT fluid (CVTF) that simultaneously realizes both high efficiency and a high metal friction coefficient
(5) Optimization of the surface properties of the pulley V-surface
(6) Adoption of a hydraulic circuit that enables constant control of the clutch pressure using a dedicated linear solenoid, and protective control that cooperates effectively with the throttle and other systems

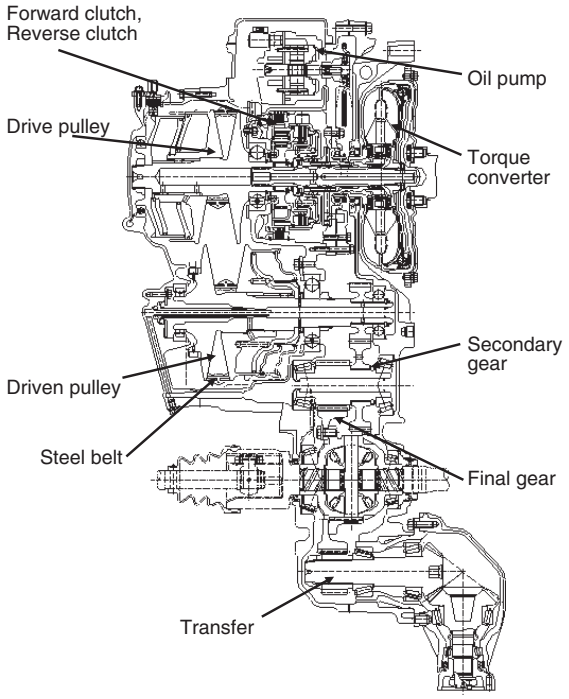


Fig. 1 Main section of CVT



Fig. 2 External view of CVT for STEP WGN

4. Key Technologies

4.1. Expanded Ratio Range

The distance between the drive (Dr) pulley and driven (Dn) pulley axes was increased from 170 mm for the conventional CVT to 180 mm and the ratio range was expanded to simultaneously achieve high levels of the contrary characteristics of fuel efficiency performance and sufficient driving force (Fig. 3).

4.1.1. Fuel efficiency performance

In order to optimize fuel efficiency over the entire

operating range, a high ratio was secured to enable active use of the range with good engine fuel efficiency.

4.1.2. Sufficient driving force

A low ratio is secured to obtain sufficient driving force in consideration of the various models in which the new CVT may be used and the operating conditions in each destination.

The distance between axes, shaft diameters, pulley diameters, belt-line alignment between the drive and driven pulleys, and other settings were optimized based on the above two main points, and assuming use of a conventional 30 mm-wide metal belt with proven results. This greatly expanded the ratio range to 6.54 compared to 4.68 for the 2008 model year Accord 5AT and 5.48 for the conventional CVT.

In addition, a basic framework was constructed that realizes good fuel efficiency performance, powerful acceleration performance, and a smooth drive feeling.

4.2. Expanded Oil Pump Half-Feed Operation Area

The feed flow rate of a displacement pump such as the vane-type pump used in this CVT is proportional to the engine speed, so when set to secure the feed flow rate required to drive the T/M in the low engine speed range, the feed flow rate becomes excessive in the high engine speed range. As a result, unnecessary motive power is consumed to drive the pump, which is an issue reducing fuel efficiency.

Therefore, the developed control works to enhance fuel efficiency while driving by constantly calculating the excess flow, which is the difference between the estimated half-feed operation flow rate and the flow rate required to drive the T/M (sum total of the shift flow rate, leak flow rate from the hydraulic circuit, and lubrication flow rate) in the current operating state (Fig. 4). The variable capacity pump is then operated in the full-feed state when the excess flow value is less than the prescribed value, and switched to the half-feed operation state when the excess flow value is the prescribed value or more. This control enabled expansion of the half-feed operation area compared to the conventional CVT (Fig. 5).

On the other hand, the excess flow rate used as the judgment parameter for switching to the half-feed operation state is calculated from various parameters in consideration of the effects of variance with respect to the design specifications and test results. However, this does not necessarily match the operating state of each vehicle, so reliability of control is provided by simultaneously applying control to return from the half-feed operation state to the full- feed operation state when the calculation results deviate from the actual vehicle conditions.

4.3. Idling-Stop System

Fuel efficiency performance was enhanced by basically using the high-efficiency, compact electric oil pump also used in CVT for K-cars, and by stopping the engine when the vehicle is stationary with the transmission in the D range. In addition, the ring gear driven by the starter motor uses a helical ring gear to enhance NV performance (reduce ring gear meshing sound) during engine restart. When the electric oil pump is positioned above the static oil level while the engine is stopped in consideration of environments where the engine may be exposed to water, air accumulates in the suction circuit, which may give rise to the issue of delayed response and abnormal noise due

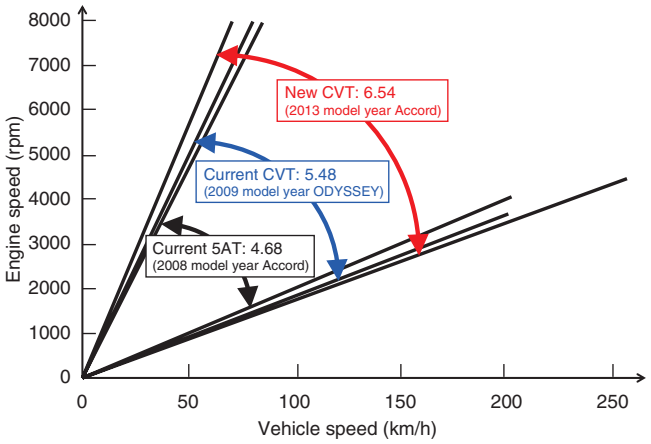


Fig. 3 Ratio coverage comparison

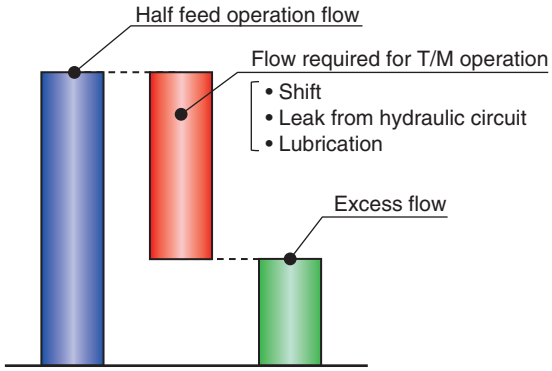


Fig. 4 Detail of half feed operation

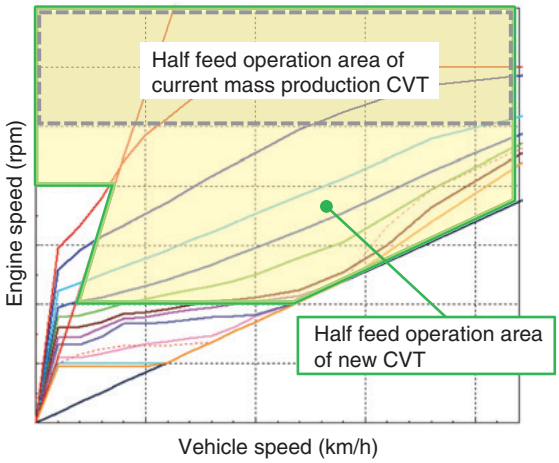


Fig. 5 Expanded half feed operation area

to trapped air at pump startup. To address this issue, the structure introduces a hydraulic circuit drain to the suction circuit so that the circuit is constantly filled with CVTF. This enabled the electric oil pump to be positioned above the oil level (Fig. 6).

4.4. CVTF with High Metal Friction Coefficient

One performance characteristic demanded of CVTF is enhancement of mechanical efficiency. Methods of enhancing this characteristic using CVTF include the following:

(1) Reduction of CVTF mixing resistance by lowering viscosity

(2) Reduction of the required pulley hydraulic pressure by increasing the coefficient of friction between the metal belt and pulleys

The developed CVTF (name: HCF2) secured good normal range viscosity and shear stability by the addition and blending of the optimal amounts of multiple viscosity modifiers (Fig. 7).

In addition, the coefficient of friction of the metal belt was increased by 10% or more compared to the mass-production CVTF (name: HMMF) by use of a new blend of friction modifiers and a Ca-based additive. At the same time, the contrary characteristic of wear resistance was also enhanced and wear was reduced by use of a new S-based extreme pressure agent (Fig. 8).

As a result of the above measures, HCF2 achieved high performance that is among the top level in the industry, and contributed greatly to increasing the transmission capacity of the CVT mechanism and reducing fuel consumption.

The above fuel efficiency enhancing technologies successfully enhanced fuel efficiency by approximately 10% (CAFE Comb.) compared to the 2008 model year Accord 5AT and 5% (JC08) compared to the 2010 model year STEP WGN CVT.

4.5. Pulley V-surface Lapping Finish

Belt-type CVT transmits motive power by the friction force between the belt and pulleys, so a certain friction coefficient value or more is required between the belt and pulleys. In addition, CVT with this structure experience constant micro-slipping between the belt and pulleys, and this slipping produces a certain amount of belt and pulley wear.

It is known that the coefficient of friction tends to drop as this wear progresses, so in consideration of worldwide deployment, technology is needed that can maintain a certain coefficient of friction or more even after driving for long distances. Therefore, the surface properties of the pulley V-surface were optimized as an effective measure for reducing wear.

A lapping process that uses the optimum combination of lapping film granularity and machining condition parameters was added to the conventional pulley V-surface grinding

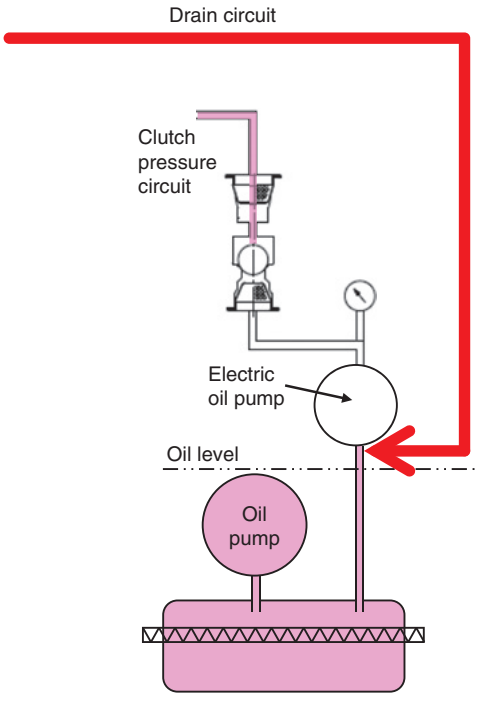


Fig. 6 Hydraulic circuit of electric oil pump

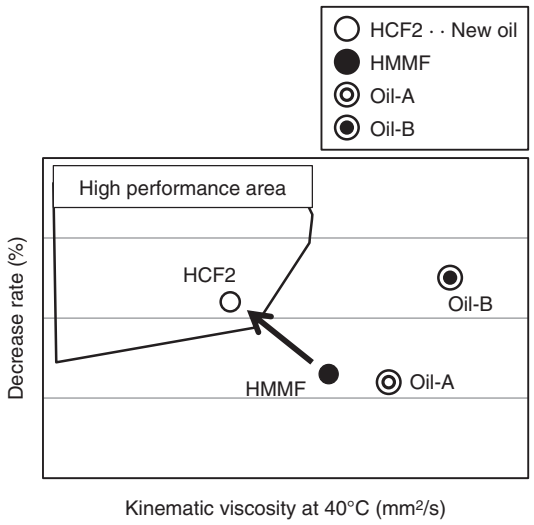


Fig. 7 New CVTF viscosity characteristics

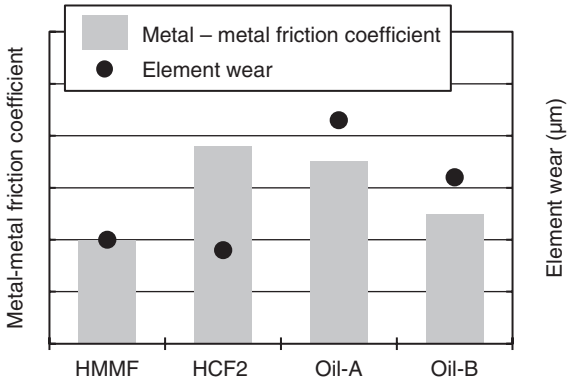


Fig. 8 HCF2 friction coefficient

process. Specifically, the surface property of peak height was reduced to lower aggressiveness towards the belt, while at the same time the valley depth was increased to enhance the oil film retention performance. By manufacturing-in these surface properties, belt wear was reduced while at the same time suppressing the drop in the coefficient of friction (Fig. 9).

4.6. Protective Control

Protective control is performed in accordance with the reliability of each part of this CVT in order to avoid the weight increase resulting from excessive strength increase to support various vehicle usage formats around the world. Figure 10 lists the protective control subjects.

4.6.1. Engine speed control

Oil pump reliability is increased by restricting the maximum engine speed in accordance with the CVTF oil temperature.

Differential gear reliability is increased by restricting the right-left rotation speed difference when single wheel slip occurs.

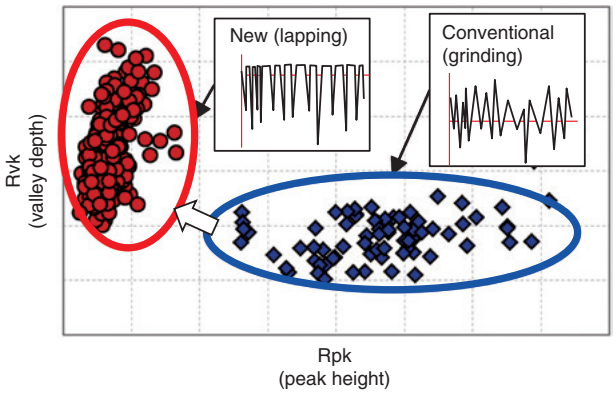


Fig. 9 Surface properties of the V-surface

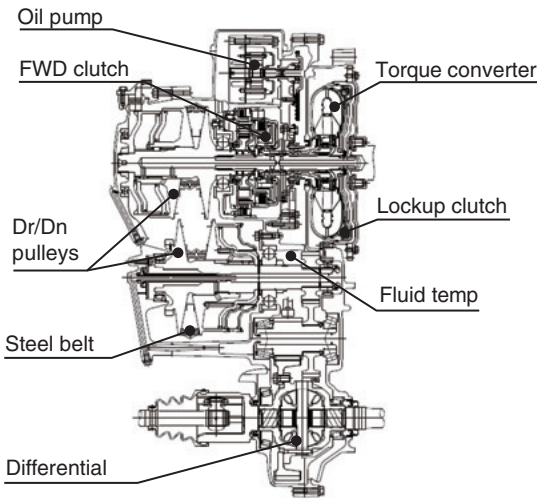


Fig. 10 Protective control subjects

4.6.2. Engine torque cooperative control

The amount of generated heat is reduced and the friction material life is extended by performing cooperative control on the engine torque when engaging the clutch.

The input torque upper limit is obtained from the required driving force, and launch torque cooperative control is performed for the Dr and Dn pulleys in accordance with the pulley input torque characteristics. This achieves control to the proper pulley hydraulic pressure and enhances reliability while at the same time realizing smooth and powerful launch characteristics.

Regarding the metal belt, dedicated linear solenoids are provided to control the clutch hydraulic pressure, and constant control is performed so that the clutch capacity is always the belt transmission capacity or less to increase toughness with respect to belt slip when the rotation speed change abruptly (Fig. 11).

4.6.3. CVTF temperature control

CVTF life is extended by constantly monitoring the oil temperature and controlling the engine upper limit speed so that the oil temperature stays below a certain value.

Torque converter reliability is enhanced by performing cooperative control on the engine torque when stalled to keep the internal CVTF temperature to the allowable value or less.

Lockup clutch life is extended by the adoption of lockup clutch protective control that estimates the friction material temperature and performs control so that the lockup clutch is used at the allowable friction material temperature or less.

These reliability enhancing technologies simultaneously realized a maximum transmission torque of 270 Nm, 4WD support, and helped ensure the reliability needed to support various usage formats around the world, while maintaining the same overall length and weight as the conventional CVT.

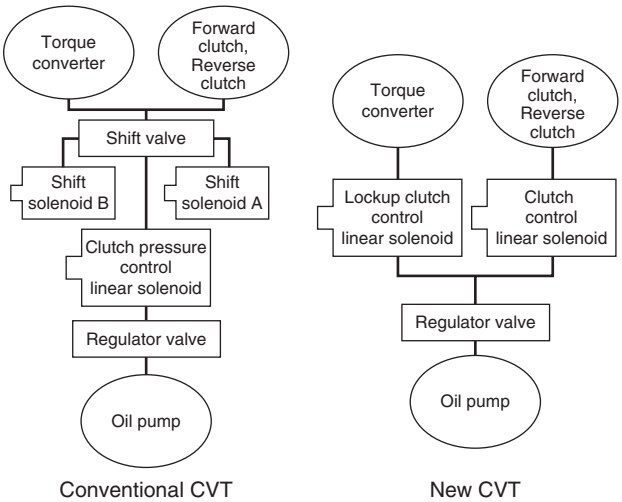


Fig. 11 Hydraulic circuit of new CVT

5. Driving Performance

The new CVT responds quickly to driver demands, provides a high continuing acceleration feeling, and realizes an exhilarating and sporty drive feeling. This enables conventional AT users to switch to the new CVT without a feeling of unnaturalness, while still making use of the smooth characteristics of a CVT.

5.1. Launch Characteristics

Launch control was enhanced and the engine speed is increased with a linear and quick response. This maintains high continuing acceleration and enhances the linear engine rev-up feeling (Fig. 12, Fig. 13).

5.2. Kick down

The step shift amount was increased, and the shift gain for step shift was set to quicken the shift response. In addition, control is performed to swiftly and linearly increase the engine speed after step shift, and to correct the target engine speed to a higher level. This increased the acceleration force, enhanced the response, clarified the acceleration response, and enhanced the smooth engine rev-up feeling (Fig. 14, Fig. 15).

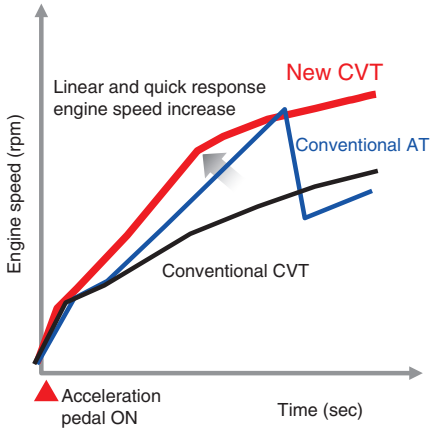


Fig. 12 Launch engine speed characteristics

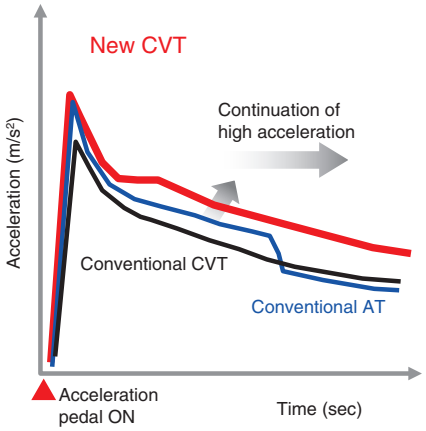


Fig. 13 Acceleration characteristics

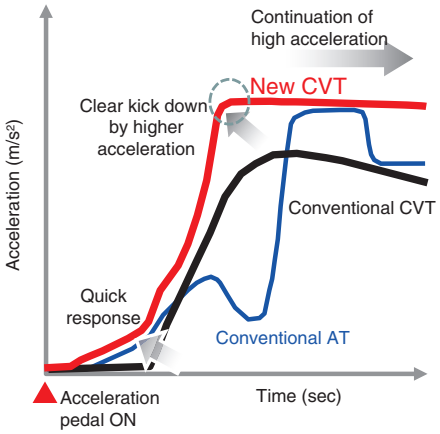


Fig. 14 Kick down characteristics

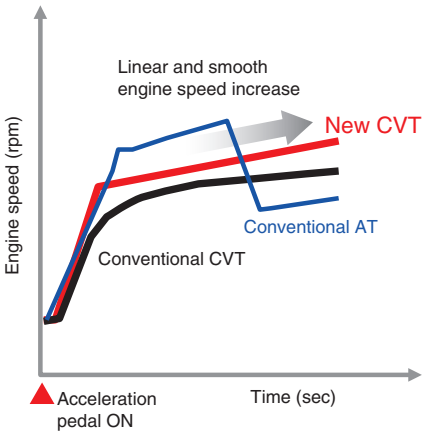


Fig. 15 Linear acceleration characteristics

6. Conclusion

A new CVT for midsize vehicles was developed, and the development goals were achieved. CVT transmission efficiency was enhanced, increasing fuel efficiency by approximately 10% compared to the conventional 5AT in the US CAFE Comb. mode and approximately 5% compared to the conventional CVT in the Japanese JC08 mode.

Reliability was achieved that can support both next-generation high-torque DI engines and various usage formats around the world.

Shift control technology was constructed that realizes appropriate driving force control and launch characteristics that provide an exhilarating and sporty drive feeling.

References

(1) Ohsono, K., Aoki, T.: Development of Full-electronic Control Metal Belt CVT, HONDA R&D Technical Review, Vol. 8, p. 21-33

(2) Ohta, S., Kunii, H., Sumi, M., Fujimoto, S., Yamaguchi, T.: Development of a Compact CVT for a Hybrid Car -

Insight, HONDA R&D Technical Review, Vol. 12, No. 2, p. 61-70
(3) Sumi, M., Kunii, H., Fujimoto, S., Ichijo, S., Hasegawa, T., Fukushima, M.: The Development of a New Compact CVT for the Fit, Honda R&D Technical Review, Vol. 14, No. 1, p. 67-76
(4) Sato, Y., Urano, J., Ohashi, A., Sakuma, S., Yamaguchi, M.: Development of CVT for 2004 Model Odyssey, Honda R&D Technical Review, Vol. 16, No. 2, p. 87-94

■ Author ■


Koichiro INUKAI


Akihiro SHIBAHARA


Yasunori MURAKAMI


Takeshi UCHINO


Michio KOJIMA


Keiichi NISHIYAMA

Development of New Manual Transmission for Middle-Torque Engine

Takashi YOKOYAMA* Keiji KUZUHARA* Masahiro HAGINIWA*
Takumi TAKAHASHI* Akira NAKAMURA*

ABSTRACT

A new 6-speed manual transmission has been developed that supports 300 Nm of maximum input torque, which corresponds to middle torque in the company's manual transmission series. This transmission supports maximum input torque of 300 Nm in the same size as the previous model used with torque of up to 235 Nm.

To improve fuel economy, it has furthermore increased transmission efficiency and thereby achieved top-level efficiency. It also uses a preceding sleeve tooth and offset gear dog to achieve a smooth and refreshing shift feeling. It uses a constant-mesh reverse system with main shaft braking system, which reduces reverse gear noise and mitigates the load when putting the shift lever into reverse.

1. Introduction

Downsizing of diesel engines continues to be the mainstream practice, and Honda also has developed a new compact diesel engine. As this engine is planned to be installed into vehicles for Europe, we need a transmission with reliable capacity of 300 Nm of torque in a size small enough to be installed into a compact vehicle, which is why the new higher-torque, lightweight and compact 6-speed manual transmission (new 6MT) was developed. This paper introduces the technical features of the transmission.

2. Development Targets

The development concept for the new 6MT was to attain higher torque capacity in a lightweight and compact transmission, along with higher efficiency and product appeal. The following development targets were established in order to achieve this.

(1) Achieve the same or smaller size as the previous 2.4 L gasoline engine 6MT so that the new 6MT, while accommodating maximum torque capacity of 300 Nm, could be mounted on a FIT-class compact automobile with the new compact engine.
(2) Achieve top-level transmission efficiency.
(3) Enhance the change feeling and product appeal in reverse.

3. Basic Construction and Specifications

The gear train was given a constant mesh-type synchromesh construction, with gears 1 through 6 always in contact, with a parallel dual-shaft configuration. To increase transmission efficiency, splashing-type lubrication was used, while ball bearings were used as differential side bearings. A constant mesh-type reverse system was used to both shorten overall length and reduce reverse gear noise, which is an element of product appeal in reverse. A helical gear was used for the reverse gear. Finally, a main shaft brake system (MBS) that uses the third-gear synchronizer when operating reverse gear was used in order to reduce load during reverse operation and reduce synchronizer drag torque. Table 1 shows the major specifications and Fig. 1 the longitudinal section.

* Automobile R&D Center

Table 1 Specifications of transmission

Transmission type		6-speed manual
Torque capacity (Nm)		300
Gear ratio	1st	3.642
	2nd	1.884
	3rd	1.179
	4th	0.869
	5th	0.705
	6th	0.592
	Reverse	3.671
	Final	3.571

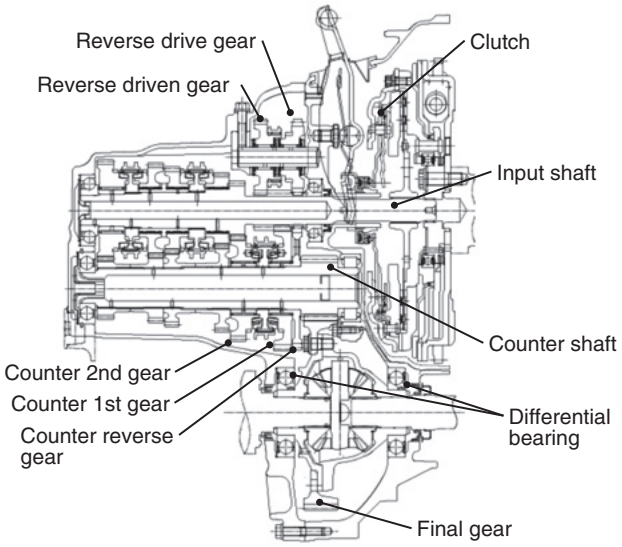


Fig. 1 Main section of transmission

4. Higher Torque Support in a Lightweight and Compact Transmission

4.1. Shortening the Overall Length

To curb the increase in weight, the following changes were made to shorten overall length while leaving the inter-shaft distance as is. This resulted in support for higher torque without changing the overall transmission length.

Figure 2 shows the relationship between transmission allowable torque and length of a transmission case with gear train inside. The case is shorter than that of the previous 6MT with the same level of torque.

(1) Using a constant-mesh reverse system with MBS resulted in the clutch gear, which was molded onto the end face of the previous gear, being brought inside the gear, reducing the overall width from first to second gear, including reverse gear (Fig. 3).

(2) With first and second gear it is necessary to deal with two issues: increasing gear tooth root strength with impact load and providing a contact ratio that would reduce gear noise. In consideration of the goal of a lightweight, compact transmission, the increase in gear width in the new 6MT was kept to a minimum by imparting higher-stress support with water-jet peening while securing the needed contact ratio through the use of small modules.

(3) To reduce gear misalignment, the main shaft and countershaft were made more rigid by increasing their inner diameter.

4.2. Higher Torque Support

In conventional development, a theoretical tooth shape is used and gears are designed for strength without accounting for gear misalignment. These designs are then evaluated in comparison to results of past durability tests of stand-alone transmissions. With this method, however, actual gear life is sometimes shorter than calculated. It is assumed this

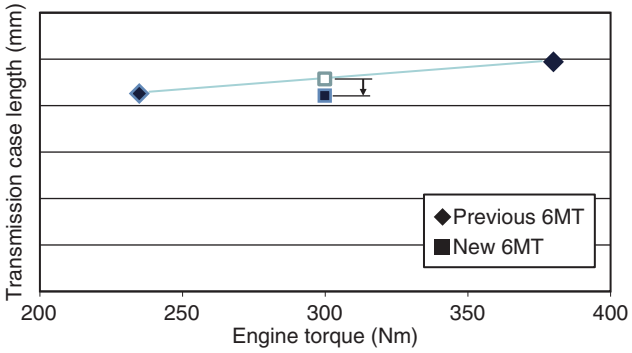


Fig. 2 Comparison of transmission case length

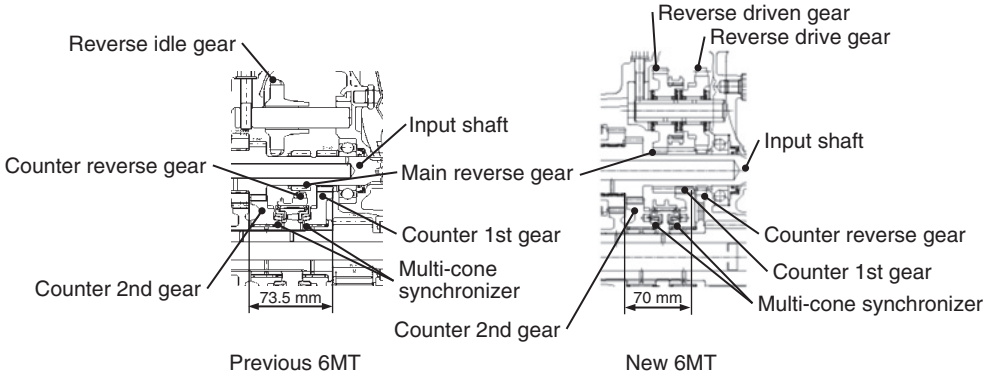


Fig. 3 Layout of 1st, 2nd and Reverse Gears

may be caused by misalignment that results in a decrease in tooth bearing ratio, but to increase a transmission's torque capacity from 235 Nm to 300 Nm without increasing its overall length, it was necessary to establish a method for more accurately predicting gear strength. Therefore, gear misalignment was calculated using Romax brand gears and gear strength was designed after predicting strength reduction based on deviation in tooth shape. Stand-alone gears were compared for tooth root stress and tooth pitting life data and the target torque capacity was provided by making the minimal necessary increase in tooth width.

Figure 4 shows a conceptual diagram of this stance on gear strength design. The vertical axis of the graph represents tooth root stress or tooth profile pressure, while the horizontal axis represents the gear working number. The intersection of the S-N line or P-N line and the target gear working number, that is, the durability cycle intersection, is the limit of tooth root stress or tooth profile pressure, and gears need to be designed so that the maximum tooth root stress or tooth profile pressure, taking tooth shape deviation into account, is within this limit.

Figure 5 uses the tooth root stress of the first gear as an example to show the degree of influence of each element making up gear strength when increasing torque support from 235 Nm to 300 Nm. The increase in gear width was kept to the minimum necessary by correctly predicting strength reduction based on misalignment and deviation in tooth shape for the gear of each speed. As a result, the width of first gear was increased by 1.5 mm, second gear by 0.5 mm and sixth gear by 1.5 mm.

4.3. Reducing Weight

Designing the transmission to support higher torque increases its weight by enlarging the external diameter of the main shaft and countershaft to reduce misalignment. However, by doing the verification previously described and enlarging the shaft inner diameter only as long as there is no impact on gear strength, and by giving each gear a form that accounts for slanting, weight was reduced. Figure 6 compares the gear and shaft weight against the previous 6MT. The weight was successfully reduced compared to the previous 6MT for the same level of torque.

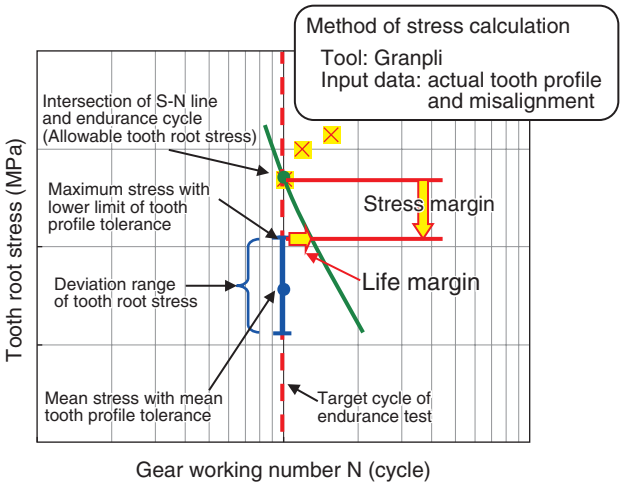


Fig. 4 Concept diagram of gear design

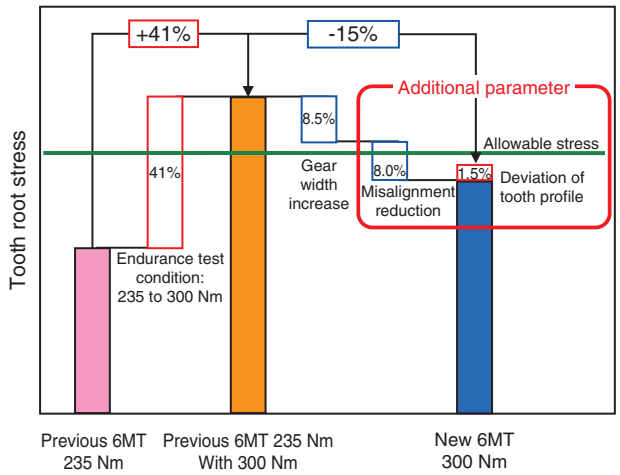


Fig. 5 Contribution to gear strength

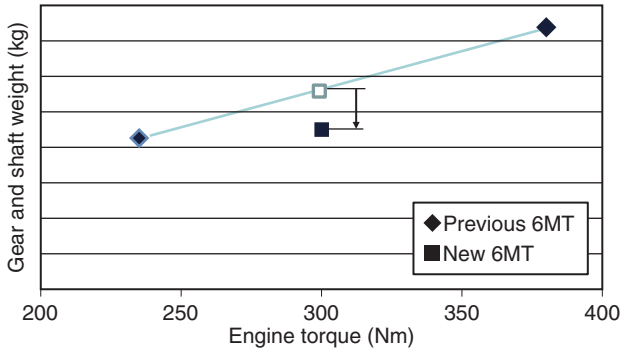


Fig. 6 Comparison of gear and shaft weight

5. Increasing Transmission Efficiency

The following techniques resulted in the transmission reducing loss torque 15% compared to the previous 6MT supporting 380 Nm and the same or greater transmission efficiency as the previous 6MT supporting 235 Nm.

(1) Using splashing-type lubrication
(2) Reducing synchronizer drag torque
(3) Using ball bearings as differential bearings

5.1. Using Splashing-type Lubrication

Though the maximum permissible torque is 300 Nm, the same gear splashing-type lubrication was used as in the previous 6MT supporting 235 Nm. With gear splashing-type lubrication there is usually the issue of reduced lubricity when the gears are rotating at lower speeds, but the lubricity at lower gear rotation speeds was enhanced by enabling gears to get splashed with oil from the rotation of the counter reverse gear. The construction is shown in Fig. 7.

5.2. Reducing Synchronizer Drag Torque

Conventionally, synchronizers have been designed with large capacity by focusing on reducing shift load when operating the engine at maximum rotation speeds. However, here a study was done on users' usage status, with the results showing that, more importantly than the value of shift load itself, users preferred small deviations in that load at each shift level in the normal zone. Thus, an effort was made to revise the target load and thereby reduce multi-cones and drag torque (Fig. 8). Additionally, the reverse synchronizer was removed due to the use of MBS.

5.3. Using Ball Bearings as Differential Bearings

A competitor's 300 Nm class transmission uses tapered roller bearings as the differential bearings. While tapered roller bearings yield higher capacity in a compact size, efficiency tends to decline because a preload is applied. The recently developed transmission increases transmission efficiency by using ball bearings similarly to the previous 6MT supporting 235 Nm.

First, the size of the ball bearings was increased, then to additionally bring out the capabilities of the bearings, a gutter plate was used so that even at lower rotation speeds bearings could be dependably lubricated with lubricating oil splashed by the final gear. The construction is shown in Fig. 9. Installing a gutter plate with two-level construction for lubrication at both lower and higher rotation speeds achieved lubrication volumes 6.6 times greater than in conventional constructions.

With these technologies, increased torque capacity and the same or greater transmission efficiency than the previous 6MT for the same level of torque were achieved (Fig. 10).

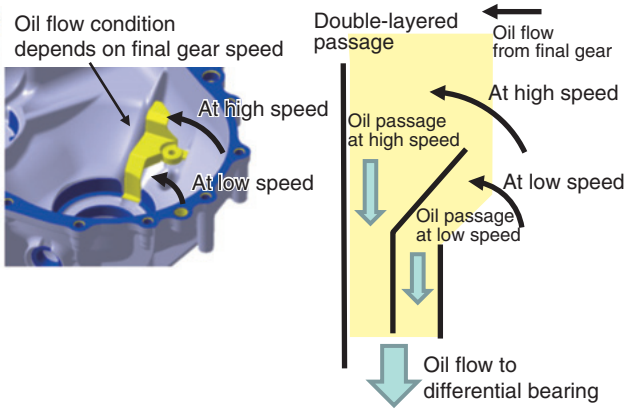


Fig. 9 Lubricating system 2
Details of gutter plate for differential bearing

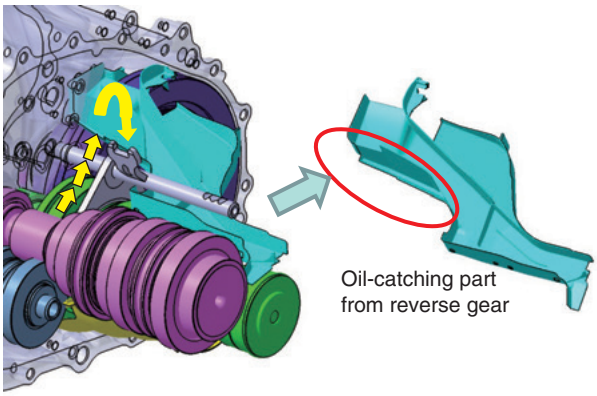


Fig. 7 Lubricating system 1
Details of main gutter plate

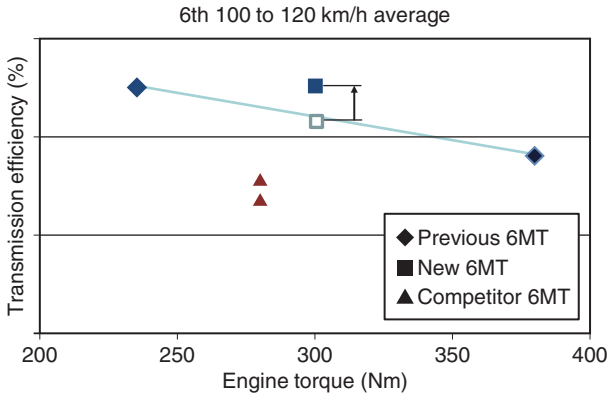


Fig. 10 Comparison of transmission efficiency

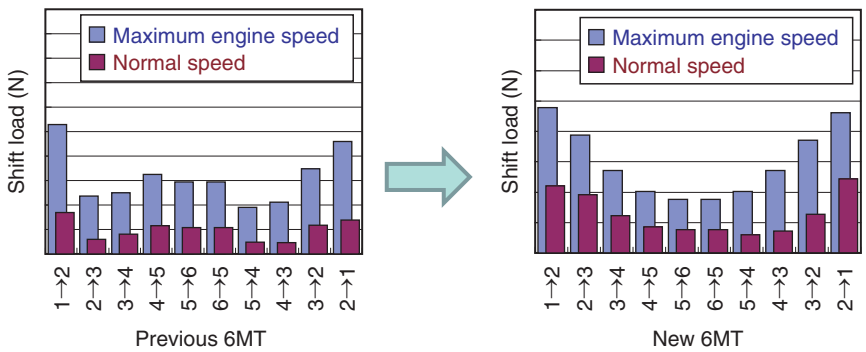


Fig. 8 Comparison of shift load

6. Technology to Increase Product Appeal

6.1. Improving Change Feel

Focusing on sensory performance when changing gears, an attempt was made to improve the feel by focusing on the following.

(1) Swallow feel
(2) Intuitive operating feel
(3) Smooth operating feel

6.1.1. Improving swallow feel

"Swallow feel" refers to the feel of gear-shifting when the shifter seems to be drawn into the in-gear position, without any feel of resistance or bumpiness. To improve this performance, the detent spring load and detent groove shape of each part of the transmission (Fig. 11) were revised to emphasize an operating feel that the load is being turned over (drawn in) when shifting. The load imparted by the shift arm detent was designed to be larger and other loads to be smaller as compared to the previous model, which shortened stroke when drawn in by 6 mm, increased drawn-in load with the same stroke by 4 N and enhanced the swallow feel as compared to the previous model (Fig. 12).

6.1.2. Intuitive operating feel

"Intuitive operating feel" refers to being able to clearly distinguish the various in-gear positions through the sense of touch with the hand and an operating feel that makes it easy to change gears. To enhance this performance, the forms of the components that make up the change operation pattern, namely the shift piece, interlock and fork (Fig. 13), were revised to reduce the select direction backlash (gate width) after getting in gear and to create a change pattern with a wider frontage (slant shift width) when shifting diagonally, such as from second to third gear. Increasing the select stroke within the transmission and making the ratio up to the knob smaller reduced the influence of the internal backlash.

As a result, gate width was reduced 3 mm and slant shift width increased 5 mm as compared to the previous model, achieving intuitive operating feel (Fig. 14).

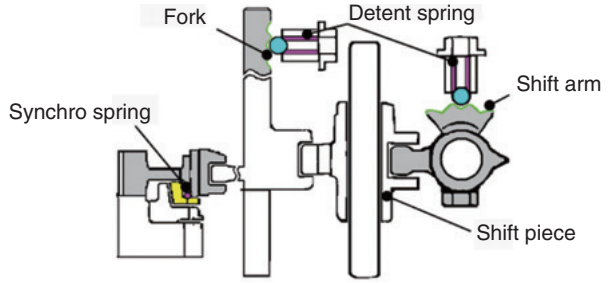


Fig. 11 Detent system

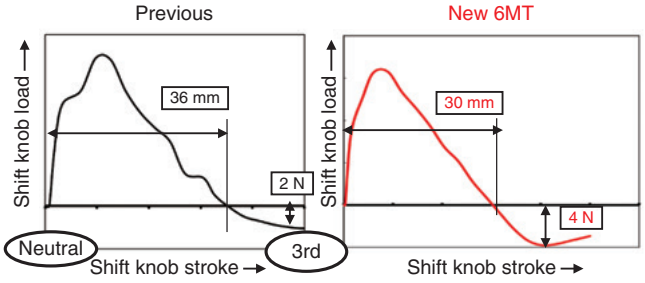


Fig. 12 Characteristic of shift feeling

6.1.3. Smooth operating feel

"Smooth operating feel" refers to an operating feel in which double-bump, a phenomenon in which the driver feels bumpiness during dynamic shifting, is inhibited. Focus points already known for inhibiting double-bump are inhibiting the drivetrain torsion amplitude and shortening the sleeve meshing time. A variety of initiatives have been tried during development of transmissions up to now[(1) - (3)]. Using the software AMESim (by LMS), the double-bump phenomenon was visualized and behavior analysis was conducted by dynamic simulation, which made it possible to quantitatively evaluate the influence of each parameter. An outline of the simulation model is given in Fig. 15 and an example of simulation output in Fig. 16. Depending on the preceding sleeve tooth and amount of gear dog offset, the double-bump load ratio, an indicator of double-bump, changes.

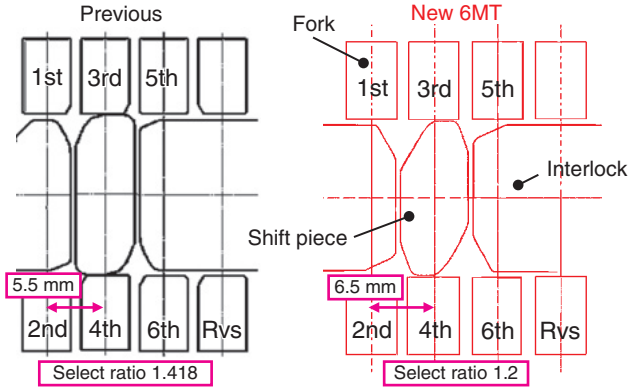


Fig. 13 Change piece layout

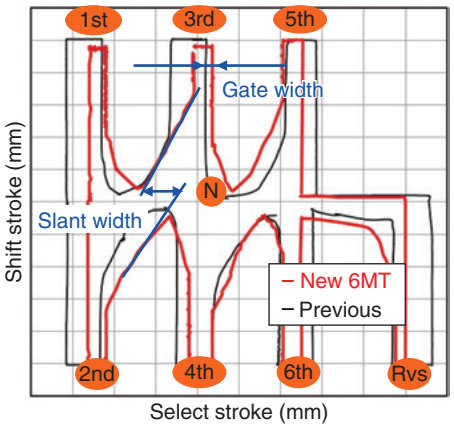


Fig. 14 Change pattern

(1) Inhibiting drivetrain torsion amplitude: Drivetrain torsion amplitude is widely known as a factor in the double-bump phenomenon, but it has been uncertain how much influence there is from synchronizer synchronization torque (below, synchronization torque) and structural components. A study was therefore done under previous model specifications, results were compared with a sensory-based evaluation, and the influence of parameter changes was confirmed. As a result, it was confirmed that there are differences in how the double-bump phenomenon occurs depending on differences in conditions, such as synchronization torque, driveshaft rigidity, gear ratio, transmission inertia and synchronization capacity, and that enhancements are needed for upshifting from first to second gear and from second to third gear (Fig. 17).

Based on these results, the following measures were taken.

(a) Adjusting synchronizer size, taking users' usage styles into account (see 5.2)

(b) Revising lever ratio within the transmission by reducing sleeve stroke. The new 6MT uses a preceding sleeve tooth (Fig. 18) among other measures, which shortened sleeve stroke by 8% as compared to the previous 6MT.

These measures inhibited excessive synchronization torque and reduced drivetrain torsion amplitude.

(2) Shortening sleeve meshing time: When synchronization torque has disappeared as a result of sleeve advancement, twisting on the output shaft side becomes undone, which results in a difference in rotation speed and a failure of synchronization. However, shortening the sleeve meshing time shortens the time of this failure of synchronization, which has the effect of reducing the frequency of double-bump[1]. Specifications were studied for the form of a chamfer that makes the timing of sleeve and gear dog meshing end early.

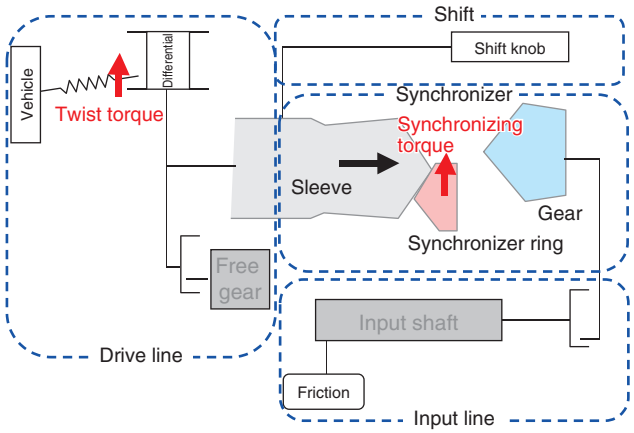


Fig. 15 Outline of dynamic simulation

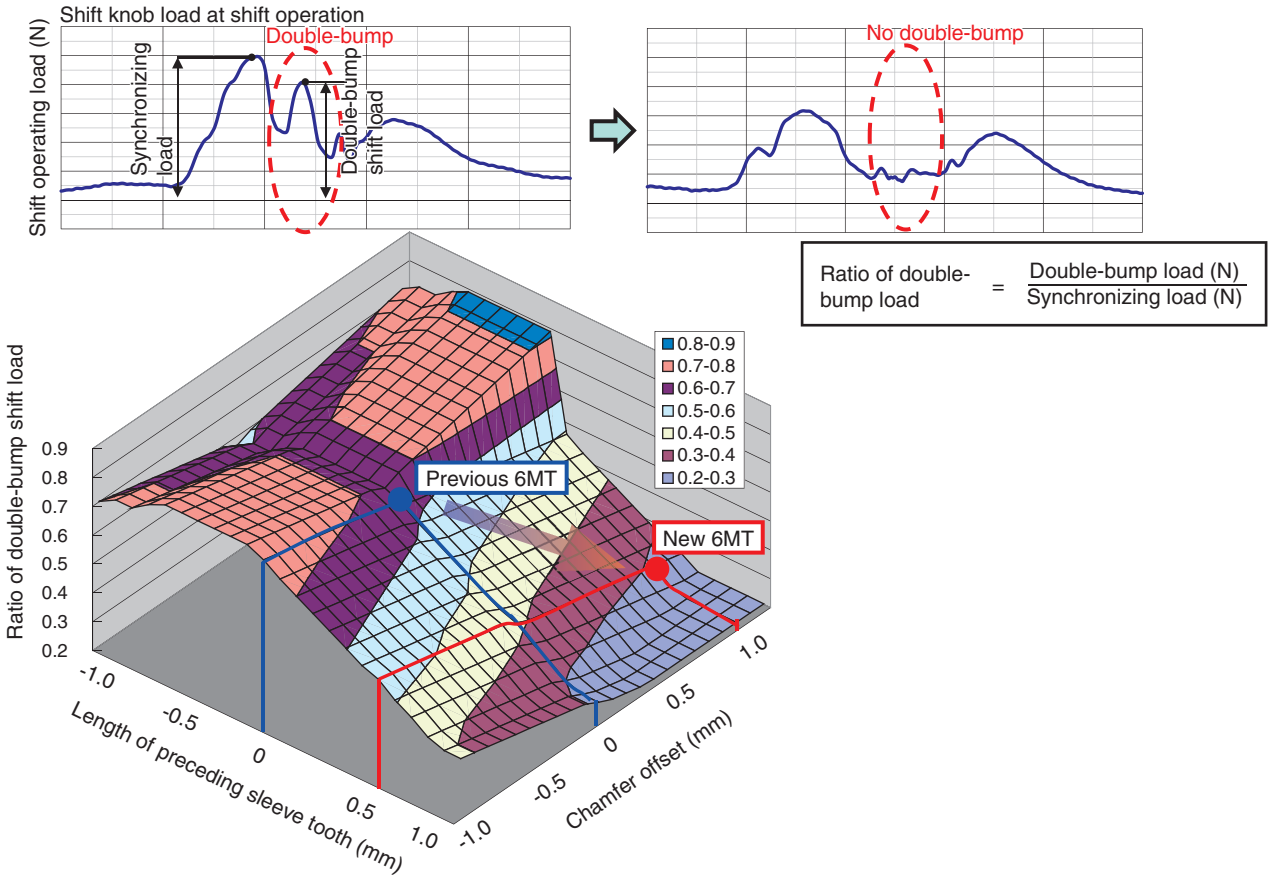


Fig. 16 Example of AMESim simulation output

Compared to the previous model, the chamfer form of the new 6MT is characterized by the second gear having a sleeve with a 0.7 mm preceding tooth and gear dog offset of 0.3 mm and the third gear having a sleeve with a 0.7 mm preceding tooth and gear dog offset of 1 mm. Since the transmission's equivalent inertial mass is particularly higher in second gear (Fig. 19), specifications were decided that took account of the dog push-through load when shifting down.

The application of these technologies reduced double-bump load to a great extent and achieved smooth shift operation. The double-bump frequency reduction effect is shown in Fig. 20.

6.2. Product appeal in reverse

Changing to a constant-mesh reverse system and using a helical gear as the reverse gear reduced gear noise.

In the previous constant-mesh reverse gear mechanism, the reverse gear silencing mechanism was a reverse-specific synchronizer (ϕ44 single) placed on the same shaft as the reverse idle gear (Fig. 21). However, since there are size restrictions in the layout, a synchronizer on the same shaft as the reverse idle gear made reverse shifting heavier.

Thus, the new 6MT uses a gear silencing mechanism that makes the third synchronizer (ϕ66 single) work during reverse shifting (Fig. 22). The result was lower reverse

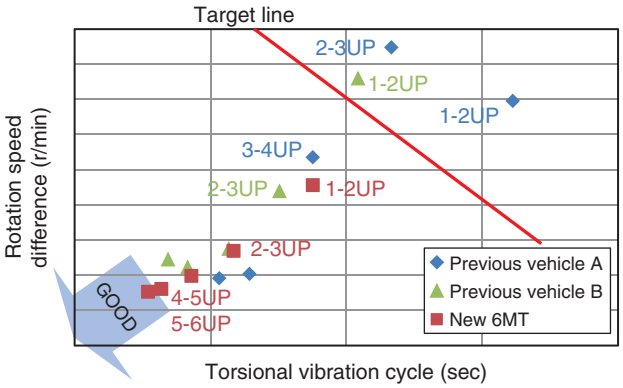


Fig. 17 Relationship of rotation speed difference and torsional vibration cycle of drivetrain

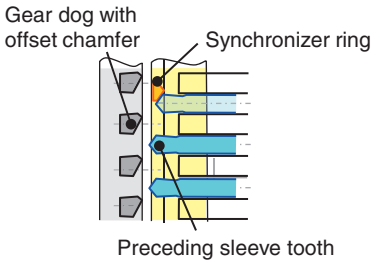


Fig. 18 Preceding sleeve tooth and gear dog with offset chamfer

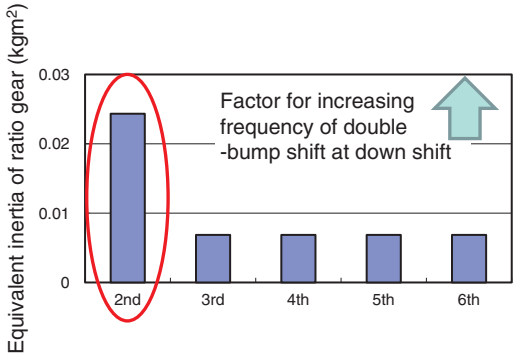


Fig. 19 Comparison of equivalent inertia of each speed ratio

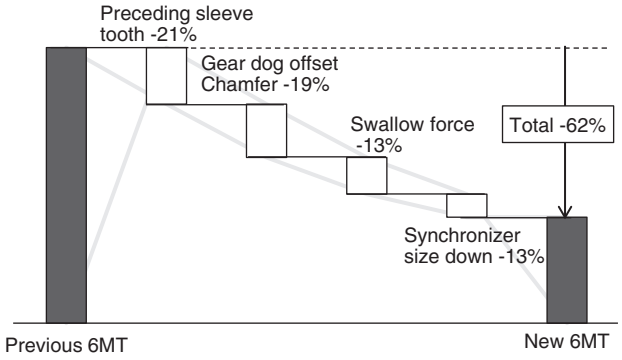


Fig. 20 Contribution to reducing frequency of double-bump shift

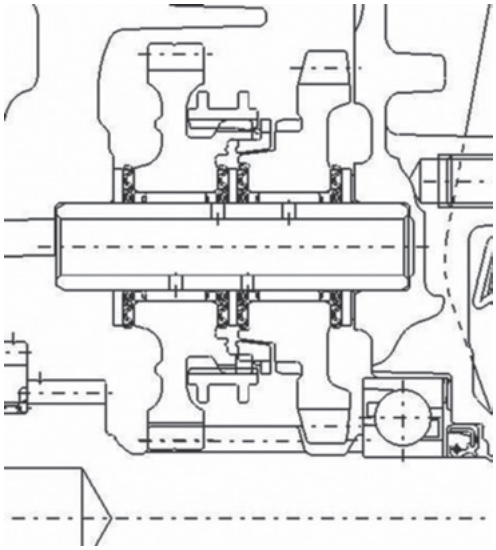


Fig. 21 Previous reverse system

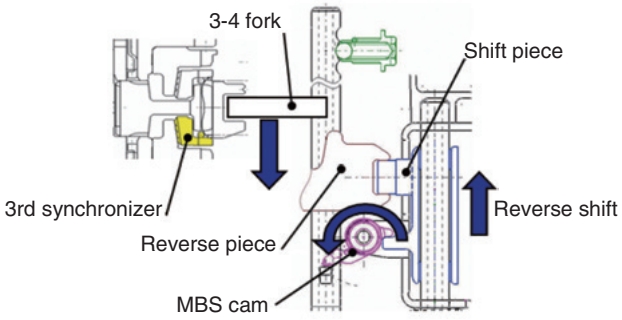


Fig. 22 Main shaft braking system

Table 2 Achievement of reverse system performance

Reverse system performance	Reverse gear noise	Reverse shift load
New 6MT	60 dB	59 N
Previous reverse system	60 dB	97 N
Previous sliding type	75 dB	63 N

gear noise and reduced shift load due to the increase in synchronizer capacity. Table 2 compares the previous and new construction.

7. Conclusion

A new manual transmission for middle-torque engines was developed with the following characteristics.

(1) Torque capacity of 300 Nm was achieved by using a new gear strength evaluation method that considers misalignment.
(2) With the help of the new gear strength evaluation method, the inner diameter of the main shaft and countershaft was enlarged and the gear form was optimized, which achieved lighter weight.
(3) The use of a splashing-type lubrication system, reduction of synchronizer drag and use of ball bearings as differential side bearings helped to achieve top-level transmission efficiency.
(4) Improving the detent mechanism and change pattern and using a preceding sleeve tooth and gear dog offset chamfer improved swallow feel, intuitive operating feel and smooth shift feel.
(5) The constant-mesh reverse mechanism reduced reverse gear noise and also reduced reverse operating load.

References

(1) Murai, A., Okazaki, K., Okuno, K.: Sporty Shifting Feel of the HONDA S2000, HONDA R&D Technical Review, Vol. 11, No. 2, p. 73-78
(2) Fujimoto, S., Udou, H., Kitajima, K., Kobayashi, S., Okazaki, K.: Development of New Manual Transmission for a 3-Liter Class Vehicle, Honda R&D Technical Review, Vol. 14, No. 2, p. 37-44
(3) Matsuda, K., Manita, M., Yokomizo, K., Iwasaki, T., Haginiwa, M.: Development of Lightweight and Compact 6-speed Manual Transmission, Honda R&D Technical Review, Vol. 18, No. 1, p. 28-33

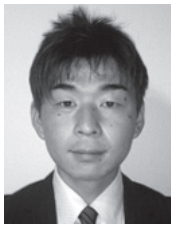
■ Author ■


Takashi YOKOYAMA


Keiji KUZUHARA


Masahiro HAGINIWA


Takumi TAKAHASHI


Akira NAKAMURA

Development of Rare Earth-saving Magnet Using Localized Diffusion Method

Takehiro MIYOSHI* Takayuki HIGASHI*
Masashi INOUE* Kojiro OHSAKI*

ABSTRACT

A magnet in which rare earth content is reduced by means of a localized diffusion method has been developed in order to reduce the volume of dysprosium used in $Nd_2Fe_{14}B$ sintered magnets employed in the drive motors of hybrid, electric and other vehicles.

Based on the fact that the distribution of the demagnetization fields to which the magnets in a motor are subject is not uniform, but rather concentrated at the corners of the magnets, the necessary coercivity distribution for the magnets was quantified using CAE, and a magnet with localized Dy diffusion was developed in order to realize this coercivity distribution. Evaluation of motor characteristics showed the developed magnet to possess identical demagnetization characteristics to a conventional magnet.

Dysprosium resources represent a particular issue among the rare earths more generally, and the technology developed in this project is able to reduce dysprosium use in magnets by 30% or more while maintaining motor performance.

1. Introduction

$Nd_2Fe_{14}B$ sintered magnets possess high magnetic flux density, and contribute to the realization of high torque and reduced size in motors. However, when used at high temperatures, the flux density of the magnets drops, resulting in a decline in motor torque. To compensate for this characteristic, dysprosium (Dy) is substituted for part of the neodymium (Nd) content of the magnets to produce Dy-containing $Nd_2Fe_{14}B$ sintered magnets. The highly anisotropic magnetic field of the Dy makes it possible to use the magnets at high temperatures.

These Dy-containing $Nd_2Fe_{14}B$ sintered magnets are used in the drive motors of hybrid and electric vehicles. This accounts for a high volume of Dy use among the substance's applications in magnets, with between 5 and 15wt% being added.

The electrification of automobiles is accelerating today as a measure to reduce CO_2 emissions, and as Fig. 1 shows, it is predicted that the demand for magnets will increase with increases in the number of electric vehicles and other vehicles fitted with motors[1]. However, rare earths such as Dy are found only in a limited range of areas, and at present China holds a more than 90% share of their production. As a result of the limited areas of production against the background of increasing demand, the price of Dy increased significantly in fiscal 2011. Figure 2 shows trends in rare earth prices[2]. While prices have most recently displayed a tendency to decline, they remain more than 20 times higher than they were five years previously. It is predicted that in future the gap between demand and supply for Dy will not be closed, and that resources will become depleted[3], making the reduction of Dy use while maintaining current levels of demagnetization performance in magnets used in automotive motors an urgent issue.

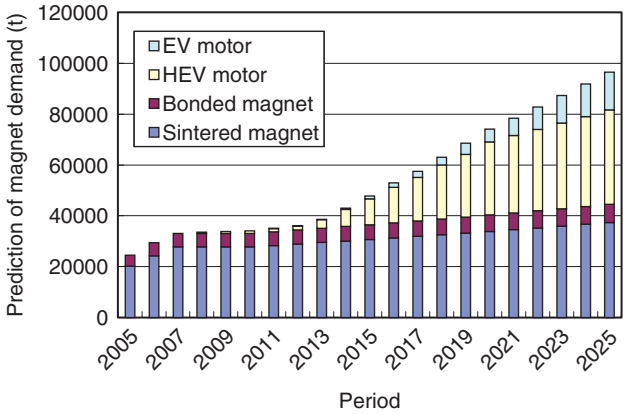


Fig. 1 Prediction of magnet demand

* Automobile R&D Center

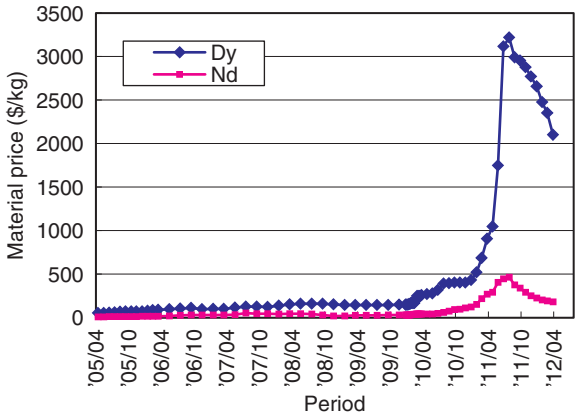


Fig. 2 Material prices for Nd and Dy

2. Issues of Reducing Dy Use

When the demagnetizing fields that magnets in motors are exposed to exceed the magnets' coercivity, the magnetic flux produced by the magnets declines, and the magnetic flux level does not return to normal despite the weakening of the demagnetizing field, resulting in a decline in torque. This phenomenon is termed demagnetization. Because $Nd_2Fe_{14}B$ sintered magnets display low coercivity at high temperatures (Fig. 3), demagnetization occurs when a specific limit temperature is exceeded. The anisotropic magnetic field strength of Dy is approximately twice that of Nd, and the addition of Dy to the magnets therefore increases coercivity and raises the temperature at which demagnetization occurs. In an automotive environment, conditions such as hill climbing and continuous high-speed driving can increase the magnet temperature from 160˚C to 200˚C. A decline in coercivity at high temperatures due to a reduction in the use of Dy would therefore render a magnet unsuitable for automotive use. This necessitates the development of a technology able to maintain the demagnetization characteristic of a magnet despite a reduction in Dy.

A technology for the diffusion of Dy at the grain boundary has been proposed as a means of reducing the volume of use of Dy in $Nd_2Fe_{14}B$ sintered magnets[4), 5)]. This grain boundary diffusion technology is a method of promoting internal diffusion of Dy coated on the surface of the magnet. However, the technology is only able to boost the demagnetization characteristic close to the surface of the magnet, and only reduces Dy use by approximately 10% to 15%. In addition, while magnets with a uniform coercivity throughout the magnet have long been in use, there are no examples of the use of magnets with differing characteristics in specific areas.

The development concept behind the research discussed in this paper was to employ the minimum amounts of Dy in only the necessary areas of the magnet in order to further reduce its use, even if only marginally. It was considered that the realization of increased coercivity only in the corner sections of the magnet, which are prone to demagnetization, using the grain boundary diffusion technology discussed above would make it possible to obtain a demagnetization characteristic equivalent to that of a conventional magnet. Figure 4 shows an image of this concept. In order to maintain the demagnetization characteristic while reducing Dy content, the issue was the realization of a technology able to locally diffuse Dy.

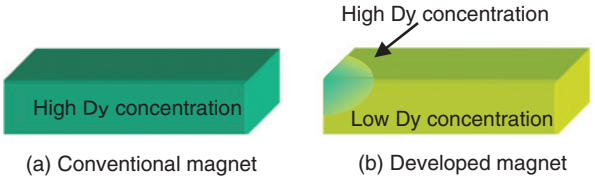


Fig. 4 Concept of reduction of Dy through localized diffusion

3. Study towards Reduction of Dy

Using the electromagnetic field analysis software JMAG, manufactured by JSOL, the demagnetization behavior of an interior permanent magnet (IPM) motor was computed, and the necessary amount of Dy for each area of the magnet was quantified.

The motor's electromagnetic field was analyzed under demagnetizing conditions, and the areas in which demagnetization occurred were identified. The results are shown in Fig. 5. Demagnetization does not occur uniformly

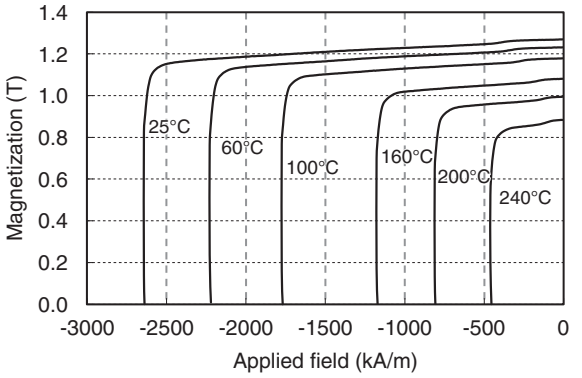


Fig. 3 Temperature-dependence of magnet property

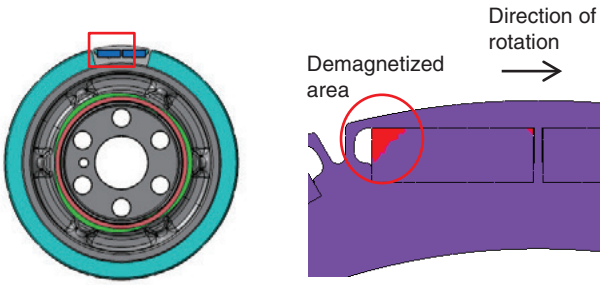


Fig. 5 Motor demagnetization area

throughout the magnet, but rather occurs from the tip of the magnetic pole on the rotor outer circumference side. This is thought to be due to the fact that the demagnetizing field to which a magnet is exposed in a motor is stronger at the corners of the magnet.

Figure 6 shows the results of quantification of the necessary coercivity in each area of the magnet by means of electromagnetic field analysis. Figure 7 shows the concept of magnet specifications. When a low-coercivity (low-Dy) magnet is used as the base magnet prior to the diffusion process, it is necessary to increase coercivity in the corner sections in order to maintain the same demagnetization characteristic as a conventional magnet, necessitating localized diffusion of Dy. Because the amount of Dy necessary at the corner sections of the magnet increases when the coercivity of the base magnet is further reduced, the total amount of Dy used takes on an extreme value. In the case of the motor studied in this project, using a magnet of 550 kA/m lower coercivity than a conventional magnet, it would be possible to reduce the amount of Dy used if coercivity was increased in areas of approximately 3 mm around the corners, realizing the same level of coercivity in the corner sections as a conventional magnet. In this case, it was estimated that Dy could be reduced by 30%.

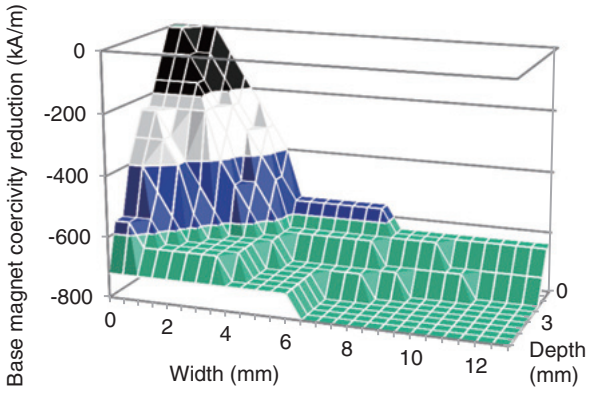


Fig. 6 Minimum Dy distribution

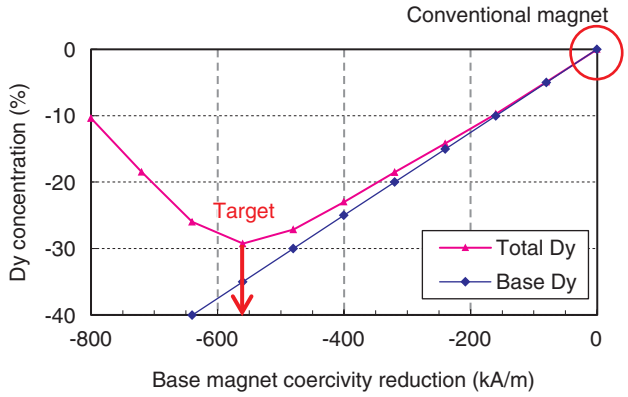


Fig. 7 Concept of base magnet

4. Manufacture of Magnet and Methods of Evaluation

4.1. Manufacture of Magnet with Localized Dy Diffusion

Diffusion conditions were set so as to diffuse Dy locally only in the areas of the magnet in which it was necessary to increase coercivity. Figure 8 illustrates the differences between the conventional magnet manufacturing process and the concept employed here. In order to diffuse Dy, the developed process adds procedures for the application of a Dy paste to the surface of the magnet and for its thermal diffusion. Figure 9 shows a model of standard diffusion[6]. The governing factors in the diffusion of Dy were studied

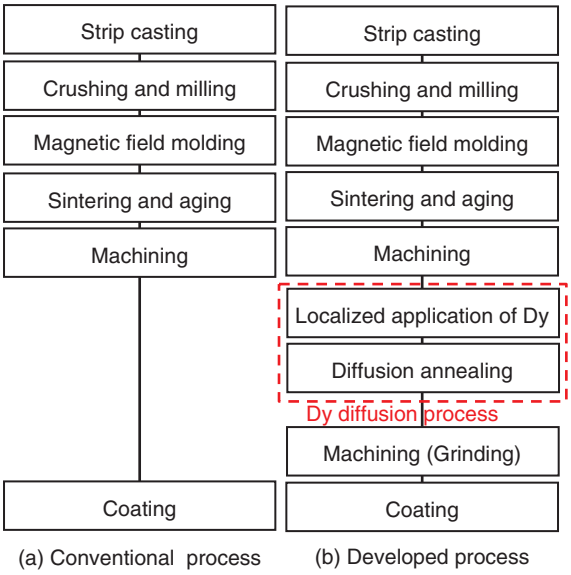
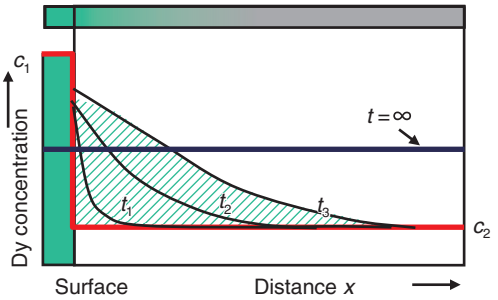


Fig. 8 Dy diffusion process



$$C = c_1 + \frac{(c_2 - c_1)}{2}\left[1 + erf\left(\frac{x}{2\sqrt{D_0 \cdot t \cdot \exp(-E/k_B T)}}\right)\right]$$

C: Dy concentration
c_1: Surface concentration
c_2: Base concentration
x: Distance
D_0: Vibration factor
t: Time
E: Activation energy
k_B: Boltzmann's constant
T: Temperature

Fig. 9 Basic diffusion model

based on the equation shown here, and optimal conditions were set for factors including the surface concentration of Dy, the temperature of the heat treatment applied during diffusion, time, and the dimensions of the magnet and the coated area.

4.2. Method of Evaluation of Magnet Characteristics

A vibrating sample magnetometer (VSM) was used to measure coercivity in each area of the magnet with localized Dy diffusion in order to determine the local distribution of the Dy. As Fig. 10 shows, the magnet was divided into 0.9 mm sections, and a VSM was used to measure coercivity for each section.

Total open flux was measured using a flux meter, and Dy distribution was measured using an electron probe microanalyzer (EPMA).

4.3. Method of Evaluation of Motor Characteristics

A motor was produced using magnets manufactured by means of the process discussed above, and its characteristics were evaluated. Figure 11 shows an external view of the motor evaluation system. In order to quantify the effect of local Dy diffusion, the same evaluation was conducted using a motor in which the magnets had not been subjected to the Dy diffusion process in order to provide a comparison.

For the torque characteristic, the torque produced by the motor when a predetermined current was impressed was measured. In the case of the demagnetization characteristic, a demagnetizing field of the maximum strength was induced in the magnets by impressing the maximum current in the motor at a predetermined temperature, following which the magnetic flux produced by the magnets was evaluated, and the changes before and after the current was impressed were measured. The demagnetization characteristic of the magnets was evaluated from the rate of decline in magnetic flux from the initial value.

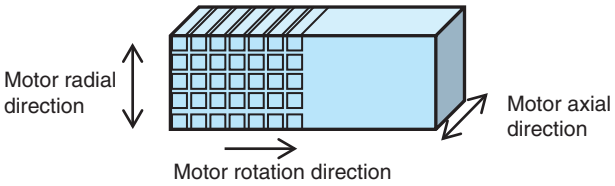


Fig. 10 Method of evaluation of coercive force distribution

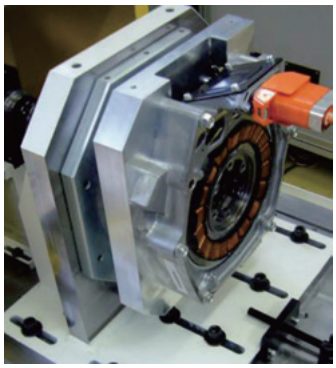


Fig. 11 Appearance of motor evaluation system

4.4. Method of Evaluation of Characteristics following Demagnetization Test

The flux density distribution on the surfaces of the magnets was measured before and after the demagnetization tests in order to determine the demagnetized areas of the magnet. It is possible to identify demagnetized areas of a magnet by means of differences in flux density before and after demagnetization tests. A magnet analyzer was used in the measurements.

5. Results and Discussion

5.1. Evaluation of Materials

5.1.1. Coercivity characteristic

Figure 12 shows the results of measurements of the distribution of coercivity in the magnet with localized Dy diffusion. The coercivity of the central section of the magnet is the same as for the magnet prior to the localized Dy diffusion process, but coercivity increases towards the corners, and reaches or exceeds the target level of 550 kA/m at the corners, where it is at its peak. These results conform to the results of the study using the Dy diffusion model, and confirm that differences in the concentration of diffused Dy result in different coercivity levels in different areas of the magnet.

Figure 13 shows a comparison between the distribution of coercivity in a magnet with localized Dy diffusion and target values. Coercivity distribution was evaluated from two planes, a cross-section from the corner parallel to the side and a 45° cross-section in which the diffusion distance is greatest. The necessary coercivity has been realized in both planes. The results also show that it was possible to control the allocation of coercivity by controlling the amount of Dy applied as a coating and heat treatment conditions.

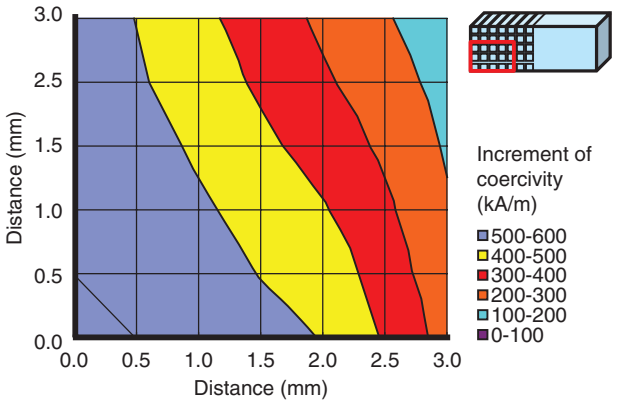


Fig. 12 Coercivity map for localized Dy diffusion process

5.1.2. Magnetic flux density

Normally, when Dy is added to a magnet to achieve high coercivity, the remanence of the magnet declines[7]. The magnetic flux density of the magnet produced in this research was compared with that of a conventional high-Dy magnet. No difference in remanence was observed due to the localized Dy diffusion process in the developed magnet. In a high-Dy magnet, Dy is dispersed throughout the $Nd_2Fe_{14}B$ phase. The magnetic fluxes of the Dy and Nd mutually cancel each other out, and total magnetic flux density declines. By contrast, in the magnet with localized Dy diffusion, Dy is concentrated at the grain boundary, where the melting point is low. It is believed that the decline in magnetic flux density with increased coercivity is controlled because of this fact.

Figure 14 shows EPMA images before and after localized diffusion of Dy. Figure 14(a), an image taken prior to the Dy diffusion process, shows that Dy is uniformly dispersed throughout the magnet, with no areas of conspicuous change in concentration. In Fig. 14(b), an image taken following the Dy diffusion process, the Dy (the white areas in the image) is concentrated in lines, and it is considered that there is no mutual cancelling of magnetic fluxes in the $Nd_2Fe_{14}B$ phase and no decline in remanence.

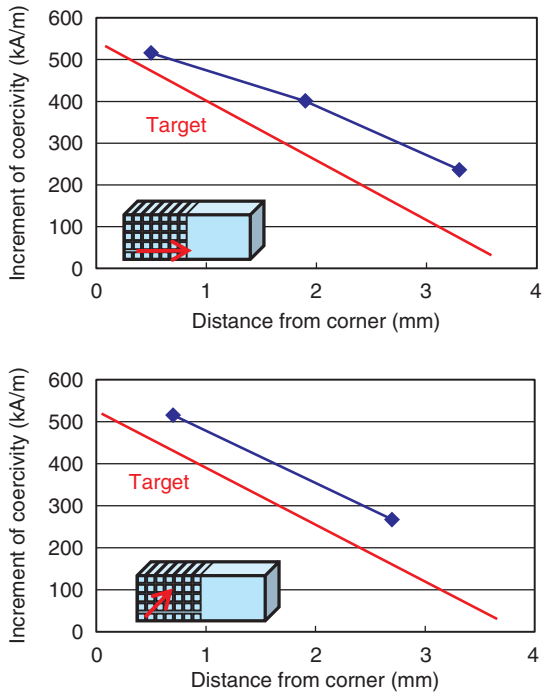
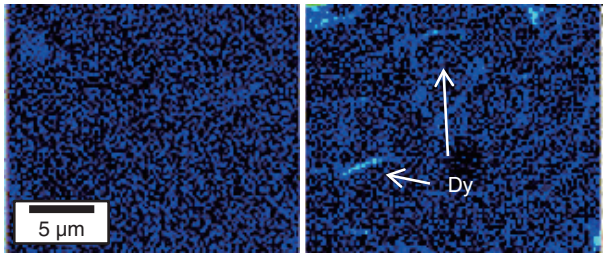


Fig. 13 Comparison of CAE analysis and magnet with localized Dy diffusion



(a) Base magnet (b) Magnet with localized Dy diffusion

Fig. 14 Cross-sectional EPMA photographs

5.2. Evaluation of Motor Characteristics

5.2.1. Torque characteristic

The torque characteristics of motors using magnets with localized Dy diffusion and conventional high-Dy magnets were compared in motor tests. The results are shown in Fig. 15. Each motor displayed identical torque characteristics, confirming that no decline in torque occurred as a result of the localized Dy diffusion process. This result accords with the fact that no decline in magnetic flux density was observed when magnets were studied in isolation.

5.2.2. Demagnetization characteristic

The demagnetization characteristics of conventional high-Dy magnets and the developed magnets with localized Dy diffusion were compared in motor tests. Figure 16 shows the results. Despite the fact that the developed magnets contain 39% less Dy, their demagnetization behavior is the same as that of the conventional magnets.

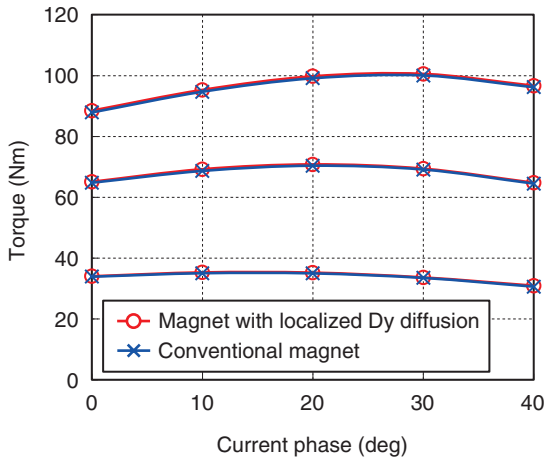


Fig. 15 Comparison of current-torque characteristics

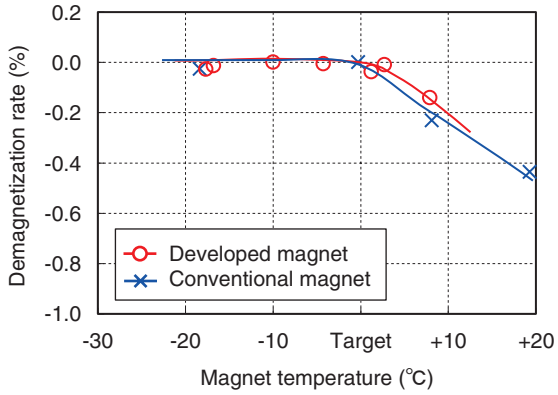


Fig. 16 Demagnetization characteristic

This is considered to be a result of the fact that the magnets with localized Dy diffusion display the same level of coercivity as the conventional magnets in their corner sections, where demagnetization commences. It is predicted that differences in demagnetization behavior would be observed at higher temperatures, when the demagnetization field acts on greater areas of the magnets, but this result indicates that in the use environment of a hybrid vehicle drive motor, the reduction in Dy content would have no effect on motor characteristics.

5.2.3. Measurement of demagnetized area

Figure 17 shows the results of measurements of the demagnetized areas of magnets following demagnetization. The results of calculations of the demagnetized areas by means of electromagnetic field analysis are also shown. The respective areas of demagnetization are shown outlined in blue. By contrast with the conventional magnet shown in Fig. 17(a), in which demagnetization commences in the corners, in the case of the magnet with localized Dy diffusion shown in Fig. 17(b), demagnetization commences in the center. This is thought to be due to the center of the magnet having become the weakest area with the realization of increased coercivity at the corners through localized Dy diffusion. In the case of the results of electromagnetic field analysis, because the calculations do not incorporate the internal temperature gradient of the magnets, there is a lack of conformity between the detailed shapes of the demagnetized areas, but the tendency towards a shift from the corners to the center of the magnet is reproduced. Taken together with the demagnetization characteristics discussed in the previous section, this indicates that the project was successful in developing a magnet conforming to its initial concept.

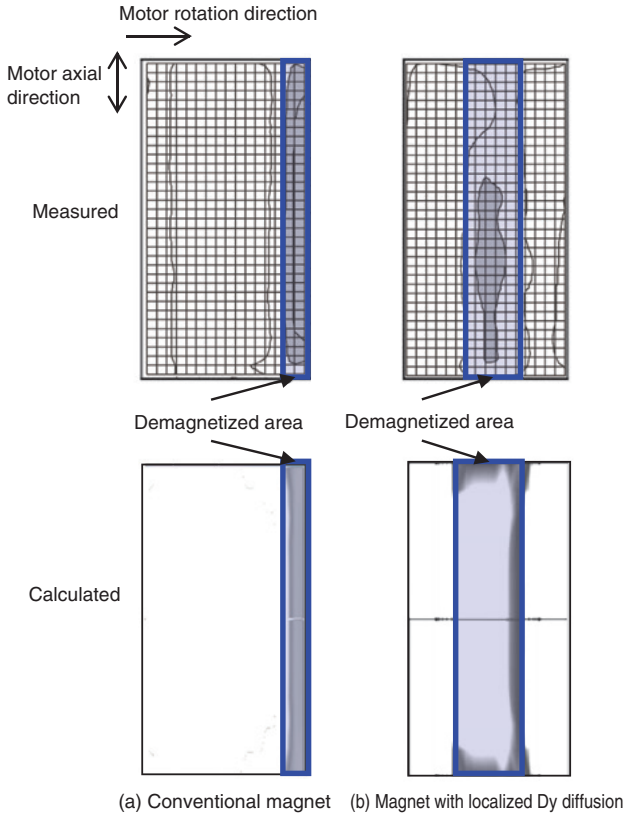


Fig. 17 Magnet flux distribution after demagnetization test

6. Effect of Application of Technology

Magnets with localized Dy diffusion at the corner sections alone produced identical motor characteristics and displayed identical demagnetization characteristics as conventional high-Dy magnets. Figure 18 shows the effect of reduction of the amount of Dy added to the magnets. A total of 47% of the Dy concentration of a conventional magnet was reduced by not adding Dy in areas in which coercivity was unnecessary, but 8% of the Dy concentration of a conventional magnet was added in the localized diffusion process, for a final Dy reduction of 39%.

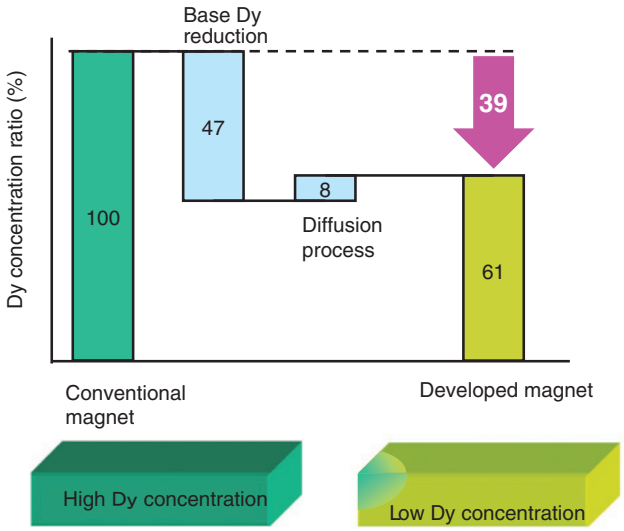


Fig. 18 Effect of application of magnet with localized Dy diffusion

7. Conclusion

Focusing on the distribution of demagnetizing fields in magnets used in automotive motors, the project discussed in this paper formulated a design concept for a magnet in which the distribution of Dy was locally varied, and established a method of manufacture for such a magnet. The developed magnet was verified as displaying identical magnetic characteristics to a conventional magnet. The reduction of the volume of use of rare earths is a long-term issue for the magnet industry, and the technology developed here was able to reduce Dy use by 39%.

The developed magnets will be employed successively

in motors used in the Integrated Motor Assist (IMA) systems of Honda hybrid vehicles.

References

(1) Yamamoto, H.: Kidoruijishakunohattentoshijodoko, Nitchu Rare-earth Koryukaigi Symposium (2009) (in Japanese)
(2) METAL-PAGES, http://www.metal-pages.com/
(3) Lifton, J.: The Consequences of Uncertainty in the Future Rare Earths Supply Chain, REPM 2010
(4) Nakamura, H.: Nd-Fe-B Sintered Magnets Produced by the Grain Boundary Diffusion Process, Bulletin of Topical Symposium of the Magnetics Society of Japan, No. 147, p. 13-18 (2006)
(5) Machida, K.: Development of High-performance Rare Earth Magnets by Grain Boundary Diffusion Techniques for the Less Amounts of Specific Rare Earth Additives, Ceramics 44, No. 5, p. 392-396 (2009)
(6) Sugimoto, K., Osamura, K.: Kakusanhoteishikinokai, Zairyososhikigaku, Asakura Publishing, p. 64-69 (1991) (in Japanese)
(7) Shimada, H., Yamada, K.: Kidoruijishaku, Jiseizairyo, Kodansha, p. 114-126 (1991) (in Japanese)

■ Author ■


Takehiro MIYOSHI


Takayuki HIGASHI


Masashi INOUE


Kojiro OHSAKI

Development of Anti-allergenic Compound for Durability of Automotive Seat Fabric

Rie HAYASHI*

ABSTRACT

Mite and cedar pollen allergens can be indicated as the main allergens that are carried into automobile passenger cabins, for example by adhering to the clothes of vehicle occupants. An allergen-reducing seat fabric has been developed that displays good deactivation performance against these allergens, and is resistant to the friction, environmental aging, and other severe conditions characteristic of automobiles.

In order to realize this performance, optimal materials were selected from among multiple anti-allergenic compounds. In addition, attention was paid to the compounding ratio, particle size, binding agent, and coating method in order to produce a seat fabric conforming to performance targets.

Tests of the efficacy of the seat fabric in relation to allergens other than cedar pollen indicated that it is effective in reducing allergens throughout the year.

1. Introduction

The incidence of allergies is increasing in Japan, and the rate of allergies affecting the eyes and nose is particularly high[(1)]. In addition, an increasing concern with health and personal comfort is also generating large numbers of proposals for value-added technologies possessing functions that consider the health and comfort of passengers in automobile cabins.

High-performance allergen-free deodorizing air conditioner filters that have already been mass-produced have the function of reducing allergens in automobile cabins. These filters are able to reduce the number of allergens entering the vehicle via air from the outside, but are unable to reduce allergens that are carried into the vehicle, for example substances adhering to occupants' clothes. The allergens entering the vehicle by this path are not restricted to pollen, but also include mite allergens, which produce eye and nose allergies. These allergens accumulate in particularly high quantities on the seats (Fig. 1).

The research discussed in this paper set out to increase occupant comfort in vehicle cabins by developing an anti-allergenic compound that would be effective in deactivating (reducing) various allergens over the course of the year, and applying this compound to automotive seat covers without affecting durability or the commercial appeal and functionality of the seat assembly itself.

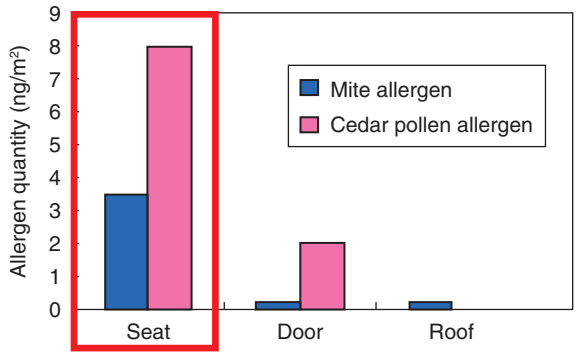


Fig. 1 Mite and cedar pollen allergen count on automotive interior fabrics

2. Anti-allergenic Compounds

In the standard mechanism of generation of allergy symptoms, contact occurs between antibodies adhering to mast cells and allergens (antigens), producing an antibody-antigen reaction (Fig. 2); this results in the release of histamines and other inflammatory substances that stimulate the nerves and blood vessels, and produce allergic symptoms[(2)].

Anti-allergenic compounds are substances that control the reaction between allergens and antibodies in the body by adsorbing allergens and denaturing them by acting on their protein structures.

* Automobile R&D Center

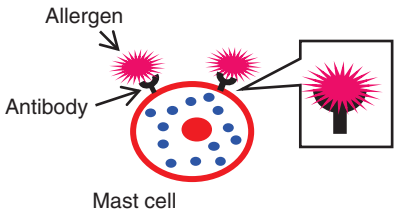


Fig. 2 Mechanism of antigen-antibody reaction

3. Development Goals

The application of conventional anti-allergenic compounds to automotive seat fabrics presents a variety of issues, including restrictions on the allergens targeted by the compound due to the effect of its coloration and other factors, decline in the performance of the compound due to the internal environment of the vehicle cabin or friction, and decline in the attractiveness of the fabric as a result of water marks or other issues during assembly.

The targets set for the allergen-reducing seat fabric developed in the research discussed here were therefore to address the issues described above while fulfilling the performance demands made on automotive fabrics.

3.1. Setting of Targets for Deactivation Performance

The research took mite and cedar pollen allergens, in relation to which there is a high general need for relief, as its target allergens, and set deactivation performance targets based on conditions assumed for a complete vehicle.

In the case of mite allergens, the WHO has established threshold values for the appearance of symptoms. The performance target for the allergen-reducing seat fabric was set as a deactivation rate (reduction rate) such that, commencing with the amount of mite allergens discovered in a complete vehicle, the amount would be below the WHO threshold value for symptoms when the fabric had been exposed overnight.

For cedar pollen allergens, the rate of 10 grains per cm^2, which has been set by Japan's Ministry of the Environment as the maximum threshold for what is considered to be low levels of pollen, was employed as a reference, and the target for the deactivation rate was set such that the amount of cedar pollen on the seat fabric would always correspond to 10 grains/cm^2 or less.

3.2. Setting of Durability Targets

The target for the allergen-reducing seat fabric was to maintain a high level of deactivation performance following automotive durability tests involving factors including severe environmental conditions and friction. Following this, the optimal treatment method, binding agent, and other elements were studied from the perspectives of durability, uniformity of coverage, and mass producibility.

3.3. Maintaining Commercial Appeal of Fabric during Seat Assembly

Specifications were examined to help ensure a uniform coverage of the entire seat fabric in order to boost the performance of the anti-allergenic compound without any reduction of the commercial appeal of the seat cover during seat assembly due to color change or whitening.

3.4. Study of Effect on Allergens other than Mite or Cedar Pollen Allergens

The effect of the allergen-reducing seat fabric in relation to cypress and ragweed pollen allergens was also tested in order to verify its year-round effectiveness in reducing allergens occurring in Japan.

4. Basic Specifications of Allergen-reducing Seat Fabric

4.1. Specifications of Anti-allergenic Compound

To produce the anti-allergenic compound used in this research, a selection was made from among some tens of candidate types that were colorless, highly water-resistant, and stable in response to heat, light and other environmental conditions. From these, an aromatic polymer with hydroxyl groups and zirconium oxide were selected for blending based on their ability to satisfy the development targets indicated in Chapter 3 for both mite and cedar pollen allergens (Fig. 3).

In addition, the specifications were set for a relatively low average particle size of between 0.8 μm to 1.0 μm in order to maintain the stiffness and stretchability of the fabric (factors that affect the commercial appeal of the seat assembly) during the fabric treatment process, and to help ensure that a high level of deactivation performance could be achieved while using a minimal amount of the compound by increasing the amount of contact between allergens and the anti-allergenic compound.

4.2. Specifications of Binding Agent with Consideration of Durability

A binding agent was added to fix the anti-allergenic compound to the seat fabric and help prevent it from being

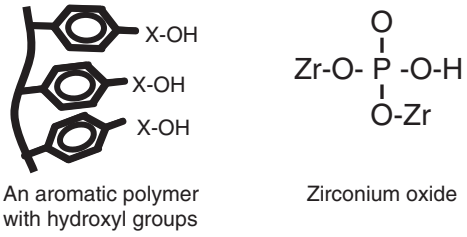


Fig. 3 Structure of anti-allergenic compounds (image)

Table 1 Test results for binder resin

Kind of binder resin	Compatibility with anti-allergenic treatment	Chalk mark resistance	Flame resistance
Polyester resin	○	○	○
Polyurethane resin	○	×	×
Acrylic resin	○	○	×
None	–	×	○

○: OK, ×: No good

rubbed off due to friction, for example from occupant entry and exit. Based on the results of a study of different types of binding agent, a polyester resin able to satisfy performance demands including flame resistance and chalk-mark resistance was selected (Table 1).

4.3. Method of Treatment of Seat Fabric

As the method of treatment, the project employed the dipping method, generally employed as a resin treatment method for automotive seat fabrics. The selection of this method made it possible to treat the entire seat fabric with the anti-allergenic compound, thus helping to enable the realization of a high level of deactivation performance; its use in combination with the binding agent also increased durability.

Figure 4 shows an image of the treatment process, and Fig. 5 shows scanning electron microscope images of the seat fabric before and after treatment.

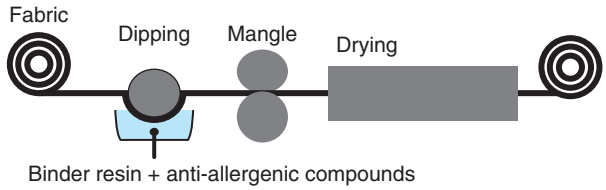


Fig. 4 Processing method for seat fabric

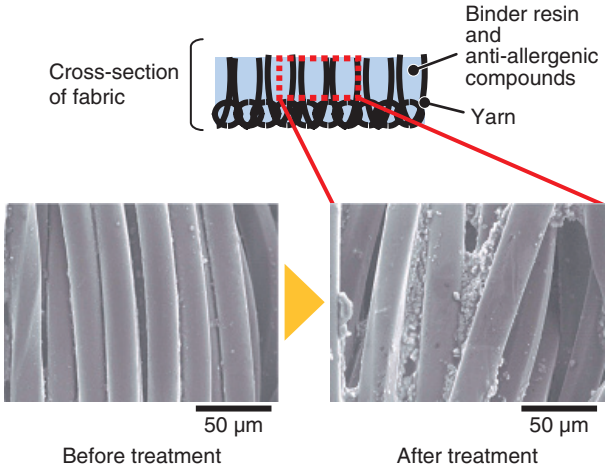


Fig. 5 SEM photograph of seat fabric

Table 2 Test conditions for ELISA

Kind of allergen	Test piece size	Allergen concentration
Mite	25 cm²	1.575 ng/ml
Cedar pollen		0.325 ng/ml

5. Results of Performance Verification

5.1. Deactivation Characteristics for Mite and Cedar Pollen Allergens

The ELISA method[2], a generally employed measurement method, was used in the evaluation of allergen deactivation performance. Measurements were conducted under the conditions shown in Table 2. The conditions were set with reference to the amounts of allergens accumulating in an actual vehicle, as shown in Fig. 1.

As Fig. 6 shows, the seat fabric achieves a high deactivation rate of 97% or more against both mite and cedar pollen allergens.

5.2. Durability as an Automotive Seat Fabric

A variety of durability tests were conducted to study the deactivation performance of the seat fabric, in order to determine whether it would lose its effectiveness under severe automotive environmental conditions (heat, humidity, light) (Figs. 7-9).

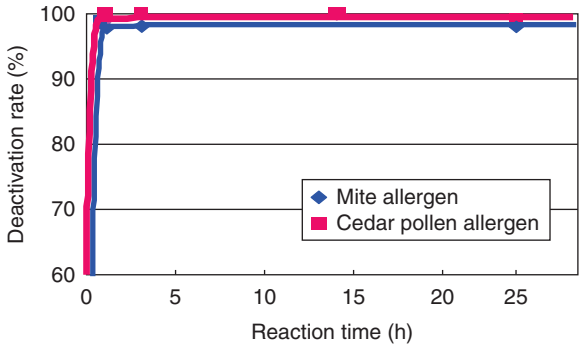


Fig. 6 Test results for deactivation rate

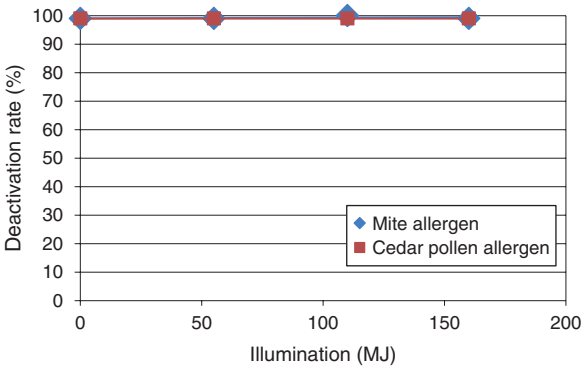


Fig. 7 Test results for deactivation rate after light resistance

It was demonstrated that the allergen-reducing seat fabric maintained an allergen deactivation performance even under severe automotive conditions. Turning attention to the usability of the seats, the allergen deactivation performance of the fabric was also tested following abrasion test using a Taber abrasion tester and durability tests focusing on entry to and exit from the seat assembly (Figs. 10 and 11).

The results of these tests indicate that the seat fabric displays good allergen deactivation performance not only initially, but also following testing under a variety of durability testing conditions set for automotive seat fabrics.

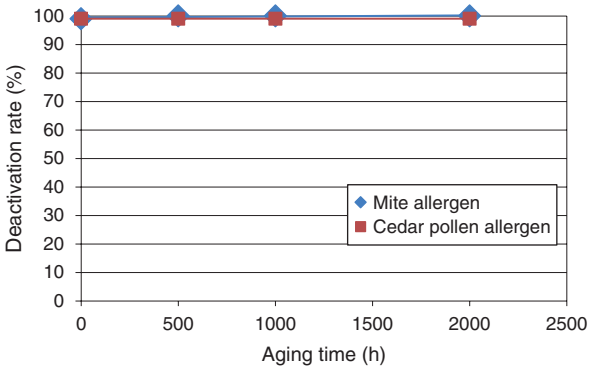


Fig. 8 Test results for deactivation rate after heat and humidity resistance

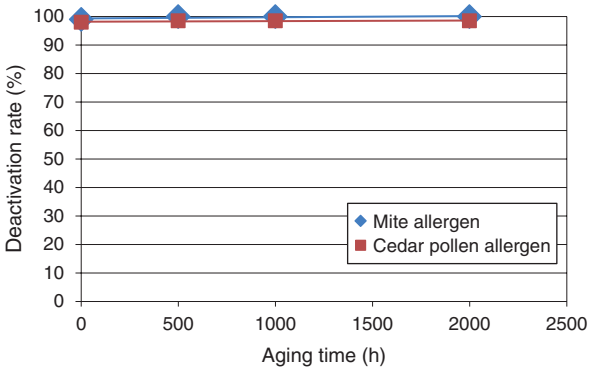


Fig. 9 Test results for deactivation rate after heat resistance (100°C)

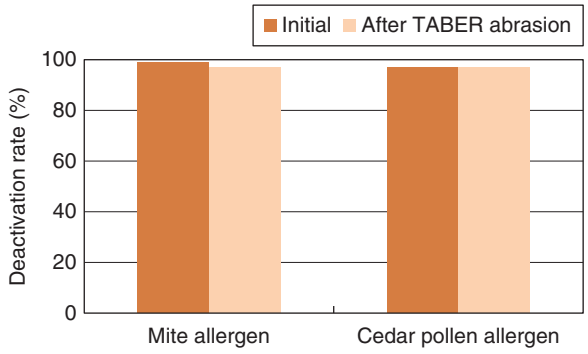


Fig. 10 Test results for deactivation rate after TABER abrasion (3000 cycles)

Table 3 Test results for seat fabric

Item	Non-process	Process
Constant elongation (%)	23/22	25/21
Tensile elongation (%)	93/108	103/106
Tearing strength (N)	218/173	188/155
Stiffness (mm)	33	39
Color fastness (grade)	4.5	4.5
Light resistance (grade: color change)	4.5	4.5
Heat resistance (grade: color change)	4.5	4.5
Heat and humidity resistance (grade: color change)	4.5	5.0

Table 4 Seat ASSY appearance

Seat ASSY appearance	Results
Chalk mark	None
Water mark	None
Wrinkle	None
Yarn breakage	None

5.3. Verification of Fabric Unit Performance and Commercial Appeal of Appearance of Seat Assembly

It remained necessary for a product with the anti-allergenic compound treatment to satisfy performance and commercial appeal demanded for the seat fabric and the seat assembly, and these factors were therefore verified.

Table 3 shows the results of tests of generally demanded automotive seat fabric performance parameters (strength characteristics, resistance to color change or fading in response to environmental factors, and others). Standard performance parameters for the treated fabric are at the same level as for untreated fabric, and there is virtually no decline in elongation or strength in the treated fabric.

With regard to the appearance of the seat assembly using the seat fabric treated with the anti-allergenic compound, as Table 4 indicates, the assembly maintains the same appearance as a seat assembly using untreated fabric, with

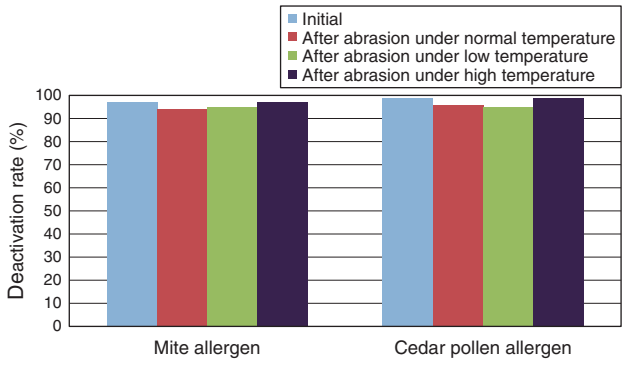


Fig. 11 Deactivation rate after ingress and egress durability

no issues such as chalk marks or water marks.

Plain black fabrics were used in this study in order to facilitate the checking of the appearance of the seat assemblies.

5.4. Verification of Effect in Relation to Allergens other than Mite and Cedar Pollen Allergens

Other than mite and cedar pollen allergens, eye and nose allergies in Japan are also produced by cypress pollen, which is spread in spring, and ragweed pollen, which is spread from summer to fall[2, 3]. The deactivation performance of the treated fabric in relation to these allergens was also tested. The results of these tests are shown in Fig. 12, and demonstrate that the developed seat fabric also displays good deactivation performance in the case of cypress and ragweed pollen. This indicates that the allergen-reducing seat fabric developed in this research will possess a high level of efficacy throughout the year (Fig. 13)[2, 4].

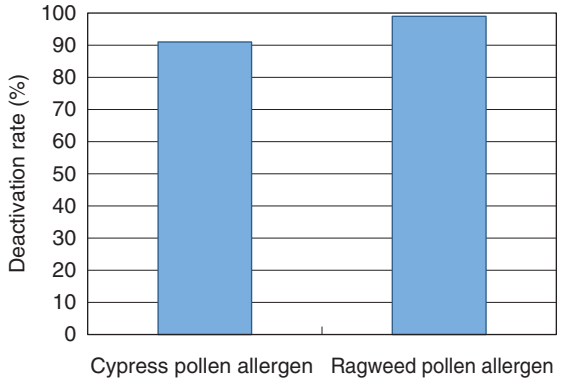


Fig. 12 Test results for deactivation rate of cypress and ragweed pollen allergens

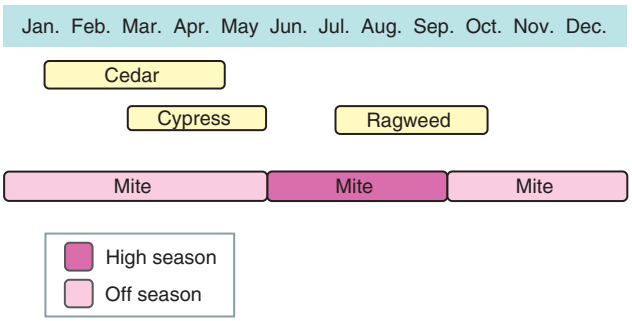


Fig. 13 Terms of pollen scatter in Japan

6. Conclusion

The research discussed in this paper developed an allergen-reducing seat cover with consideration of the durability and commercial appeal of automotive seat assemblies.

(1) A seat fabric specification that displays good deactivation performance against multiple allergens, including cypress and ragweed pollen allergens in addition to mite and cedar pollen allergens, was developed through the blending of two types of anti-allergenic compound.

(2) The selection of an optimal binding agent and treatment process resulted in a specification that maintained good deactivation performance when exposed to durability testing conditions as an automotive seat fabric.

(3) Refinement of the size of the particles in the anti-allergenic compound and the uniform treatment of the entire surface of the fabric achieved through the use of the binding agent helped enable the developed fabric to maintain the stretchability, stiffness, and resistance to chalk marks necessary from the perspective of the commercial appeal of the appearance of the seat assembly.

The allergen-reducing seat fabric developed in this research has been applied in allergy-free seats in the N BOX. This technology for realizing added functionality in seat fabrics is expected to have wide-ranging applications as a method of increasing commercial appeal.

References

(1) http://www.mhlw.go.jp/toukei/saikin/hw/hftyosa/hftyosa03/index.html

(2) Sahashi, N., Takahashi, Y., Murayama, K.: Sugi kafun no subete, Medical Journal, 117p. (1995) (in Japanese)

(3) Ministry of the Environment, Environmental Health Department, Environmental Health and Safety Division: Kafunsho kankyo hoken manual, 37p. (2009) (in Japanese)

(4) Moriya, K.: Ieno nakano dani, Shokabo Publishing, 149p. (1990) (in Japanese)

■ Author ■



Rie HAYASHI

Verification Test of High Differential Pressure Water Electrolysis-type Solar Hydrogen Station (SHS2)

Hisashi NAGAOKA* Nobuyoshi YOSHIDA* David CUN**
Ikuya YAMASHITA* Masanori OKABE*

ABSTRACT

A high differential pressure water electrolysis-type solar hydrogen station (SHS2) was developed, envisioned for household use, and verification tests were conducted for approximately one year with production of hydrogen used by fuel cell electric vehicles. This SHS2 unit is equipped with a high differential pressure water electrolysis stack that raises the pressure of the hydrogen produced by water electrolysis to 35 MPa, enabling supply of the hydrogen to fuel cell electric vehicles. This technology has obviated the need for a mechanical compressor to compress the hydrogen, and has achieved low noise, high efficiency, and compactness.

As a result of the verification tests, it was found that the amount of hydrogen produced in one year was approximately 120 kg, and the amount of electric power needed for production was fully supplied by solar cells. The initial system efficiency was 55.5%, and 6.38 kWh of electric power was consumed per 1 Nm^3 of hydrogen. Increased efficiency and other such work on the stack and device is anticipated to allow system efficiency to be raised to as much as approximately 70%. Operation simulation using data obtained in verification tests showed that the convenience for most users could be increased by installing a storage tank together with the SHS2.

1. Introduction

Honda has engaged in the development of fuel cell electric vehicles based on its understanding that fuel cells utilizing hydrogen are the ultimate next-generation powerplant in terms of providing an alternative to fossil fuels, reducing emissions, and lowering the impact on global warming.

Compressed hydrogen is the main fuel for these fuel cell electric vehicles, but the adequate infrastructure to supply compressed hydrogen is not yet in place. At the same time it is developing the vehicles, Honda is also engaging in research on methods for producing hydrogen to supply to fuel cell electric vehicles.

A normal pressure water electrolysis-type Solar Hydrogen Station 1 (SHS1) was previously installed at the Honda R&D Los Angeles Center in California in the United States in 2001, and verification tests were conducted on the continuous production and filling of vehicles with the hydrogen required by fuel cell electric vehicles. After the efficiency of this system was upgraded in 2003, verification tests were conducted for over four years[(1)]. In January 2010, the SHS1 was upgraded to the SHS2 using high differential pressure water electrolysis technology[(2)-(4)] and verification tests were conducted for a period of approximately one year. There was no precedent for long-term testing of a station using high differential pressure electrolysis technology, and the purpose of the verification tests was to confirm its acceptability in society.

This article will provide details of SHS2 system configuration and operation, after which it will present results of the one-year verification tests and initial system efficiency together with prospects for the future. The verification test results were also used in simulations that verified the convenience of the SHS2 and storage tank.

2. Detailed Explanation of the SHS2

2.1. System Concept

Figure 1 shows an overall view of the SHS2 system. This system is capable of producing compressed hydrogen that satisfies the hydrogen fuel standards for fuel cell electric vehicles without utilizing a mechanical compressor. The combination with solar cells enables hydrogen

* Automobile R&D Center
** HONDA R&D AMERICAS, INC.

production without discharging any CO_2 during the production process.

The system specifications are shown in Table 1. The SHS2 specifications were created on the assumption that the system would be installed in ordinary households in the future. On the assumption of everyday use for commuting to work, the specifications are set according to the concept of a hydrogen flow rate and so on that allow for producing and filling a fuel cell electric vehicle with enough hydrogen during the night to enable 40 miles of travel per day. The discharge pressure of the high differential pressure water electrolysis stack is set to 35 MPa, the same as the maximum filling pressure of the onboard tank.

The unit is also installed with CIGS thin-film solar cells[5] with 6 kW output manufactured by Honda Soltec Co., Ltd. These are made to connect with the unit through the electrical grid. The electric power generated by the solar cells during the day is used by the electrical grid, and then at night, after the car returns, electric power from the electrical grid is used to produce hydrogen. This concept allows for reduction of CO_2 by the electrical grid as a whole.

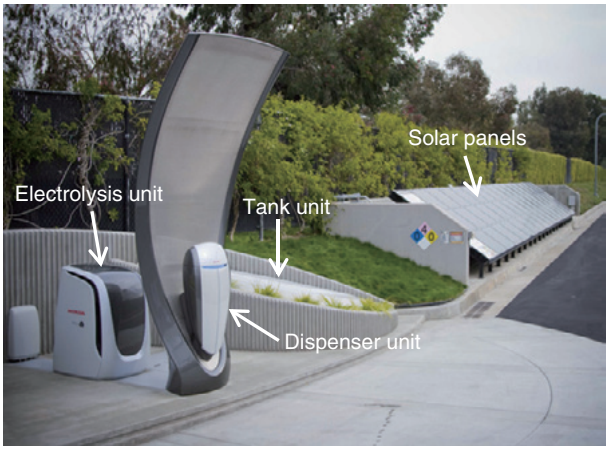


Fig. 1 External view of Solar Hydrogen Station (SHS2)

Table 1 Specifications of SHS2

Hydrogen production	Flow rate	0.7 Nm^3/hr (0.5 kg/8 hr)
	Filling pressure	35 MPa (max.) (approx. 5000 psi)
	Purity	> 99.99%
Component	Photovoltaic modules	CIGS thin-film solar cell 6 kW system (approx. 53 m^2)
	Electrolysis unit	High differential pressure electrolyzer
Utility	Electricity	240 VAC
	Water	Tap water
Unit volume		Approx. 0.33 m^3 (approx. 12 cf)

In September 2010, a hydrogen storage tank was also installed, according to the initial plan. The purpose of this was to study the increased convenience for users and the higher utilization rate of the system.

2.2. System Configuration

2.2.1. Electrolysis Unit

The electrolysis unit is a device that uses the high differential pressure water electrolysis stack to generate hydrogen from water by electrolysis. At the same time, it also boosts the pressure of the hydrogen and dehumidifies it. Figure 2 shows the internal configuration of the electrolysis unit in schematic form with the connections to peripheral devices displayed around the high-pressure water electrolysis stack. The high-pressure water electrolysis stack continuously generates hydrogen within a closed space by breaking down water through electrolysis. It boosts the hydrogen to the configured pressure and supplies it outside the unit[6].

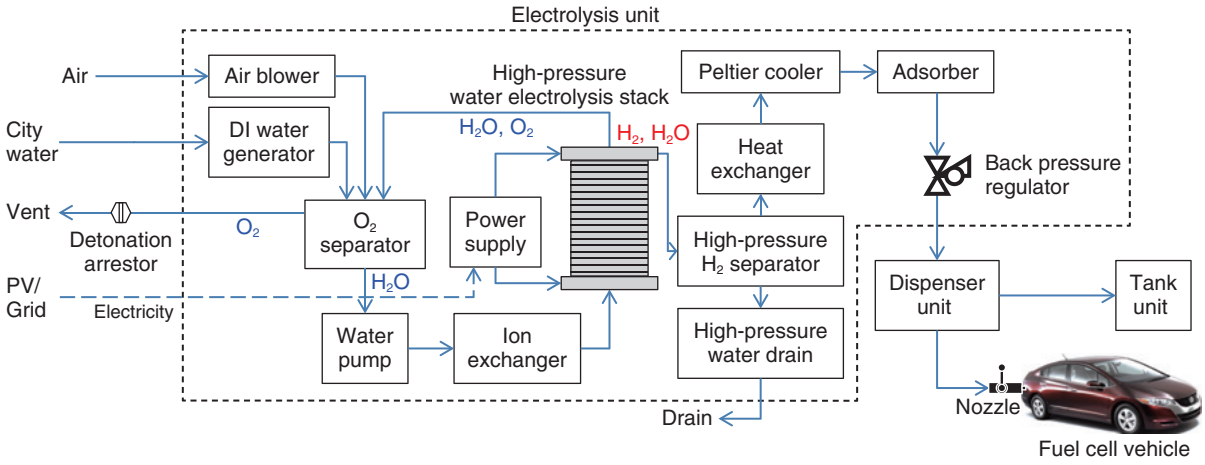


Fig. 2 Electrolysis unit configuration diagram

The deionized water required for electrolysis is produced from tap water by the deionized water generator and supplied to the deionized water circulation system. The deionized water supplied to the stack by the circulation pump passes through an ion exchanger to maintain its purity and is fed to the anode side of each cell in the stack. Inside the stack, the deionized water is electrolyzed, breaking it down into hydrogen and oxygen. The oxygen generated as a result of electrolysis is discharged from the stack together with the surplus deionized water and sent to an oxygen separator. The fluid mixture of deionized water and oxygen is separated by the oxygen separator, and the oxygen is diluted with air from the blower before being discharged through a detonation arrestor into the atmosphere. The deionized water passes through the circulation system and is again supplied to the stack.

Meanwhile, the pressure of the hydrogen that is generated by electrolysis at the cathode side of the stack continues to increase until it reaches the pressure set for a back pressure regulator (35 MPa) installed downstream. The hydrogen with boosted pressure is passed through a high-pressure hydrogen separator, a heat exchanger, a Peltier cooler, and an adsorbent that remove the water content to produce a purified dry hydrogen with a moisture concentration of 5 ppm or less. The liquid moisture in the hydrogen is eliminated by gravity in the high-pressure hydrogen separator, heat exchanger, and Peltier cooler, and that moisture is accumulated in the high-pressure separator. Consequently, when the amount of water reaches a determined level, it must be drained, and so the high-pressure drain line installed at the bottom of the high-pressure separator is opened as required to drain the water. The system operates in repeated alternation between draining water and injecting water, and this water drain cycle is shown in Fig. 3. It is apparent from Fig. 3 that variation occurs in the hydrogen flow rate of the product in linkage with the water drain cycle. While water is being

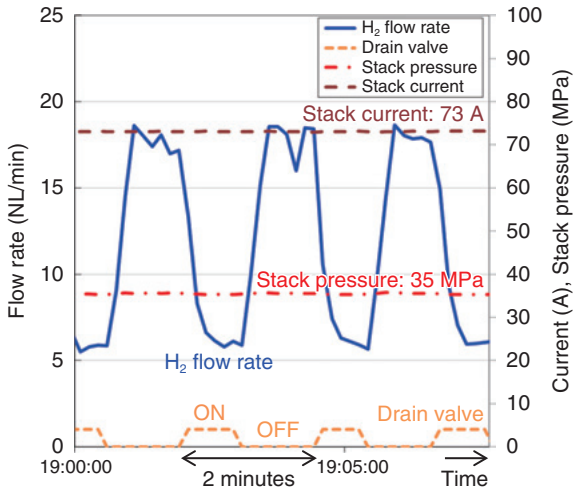


Fig. 3 High-pressure water drain cycle

Table 2 Hydrogen quality of SHS2

	ISO14687-2	SHS2
H_2	>99.99%	>99.99%
H_2O	<5 ppm	<1 ppm
Hydrocarbon	<2 ppm	<0.1 ppm
O_2	<5 ppm	1 ppm
He, Ar, N_2	<100 ppm	<16 ppm
CO_2	<1 ppm	<0.1 ppm
CO	<0.2 ppm	<0.001 ppm
Sulfur	<0.004 ppm	<0.0008 ppm
HCHO	<0.01 ppm	<0.001 ppm
HCOOH	<0.2 ppm	<0.001 ppm
NH_3	<0.1 ppm	<0.02 ppm
Halogenates	<0.05 ppm	<0.004 ppm

injected into the high-pressure separator, an amount of hydrogen corresponding to the volume of the water being accumulated is forced out, so that the apparent volume of the hydrogen product increases. On the other hand, when the water is being drained, the vapor phase hydrogen expands to a volume corresponding to that of the drained water. Therefore the pressure inside the separator diminishes, so that the hydrogen produced is used to replace the amount by which the pressure was diminished and the hydrogen product discharge volume drops or even disappears completely. This makes it appear that the production of hydrogen goes on and off in conjunction with the water drain cycle. When averaged, however, there is generation of a fixed volume of hydrogen that depends on the electric current flowing through the stack. The dehumidification performed by the adsorbent can occur using a small amount of adsorbent because the hydrogen passes through it at the high pressure of 35 MPa, where the dew point is low. The adsorbent is scheduled for replacement at approximately half-year intervals.

With normal-pressure water electrolysis, the oxygen generated at the anode side becomes mixed with the hydrogen at the cathode side as an impurity. With high differential pressure water electrolysis, however, it has been confirmed that the concentration of oxygen in the hydrogen can be held down to 5 ppm or lower when there is a pressure differential of 1 MPa or more between the anode and cathode. This can yield a hydrogen product with purity that satisfies the SAE J2719[7] and ISO 14687-2[8] hydrogen fuel standards for fuel cell electric vehicles. The fact that the hydrogen product satisfies the quality standards is also confirmed, as shown in Table 2, by impurity analysis.

The hydrogen produced in this way can either be supplied through a refueling nozzle to fill the tank on a fuel cell electric vehicle directly or, when there is a storage tank, the hydrogen can be placed in that tank to be stored.

2.2.2. Tank unit

The concept for this system when it was initially installed was to slowly fill vehicles at night with high-pressure hydrogen when they were not being used. This method makes a high-pressure storage tank unnecessary and allows for a simpler system that saves space. It also eliminates the need to satisfy standards and regulations related to hydrogen storage, easing installation in households.

Slow filling involves raising the pressure while filling. Although it can fill a vehicle tank completely, the long time taken for filling is a disadvantage. On the other hand, if a storage tank is present, then the pressure differential between tanks can be used for fast filling that takes a short time. This has the advantages of enhancing the user's convenience and enabling hydrogen production and storage while the vehicle is absent, which raises the utilization rate. Since this makes use of the pressure differential, there is the disadvantage that the vehicle tank cannot be filled completely full.

Installing a storage tank together with the system in this way to allow fast filling has advantages and disadvantages. In this case, an added storage tank was installed in September 2010 in order to conduct a study of user convenience and the system utilization rate. The tank has a capacity of 167 L and is capable of storing approximately 4 kg of hydrogen at 35 MPa.

2.2.3. Dispenser unit

The dispenser unit shown in Fig. 4 is equipped with a control panel by which users operate the system, an emergency stop button, a refueling nozzle, and a breakaway fitting for emergency separation of the nozzle.

When users fill a vehicle with hydrogen, they follow the display on the control panel and attach the nozzle to the vehicle, then press the start-filling button on the panel to begin filling. Figure 5 shows a schematic representation of the progress of the filling operation. When a storage tank is present, fast filling from the storage tank is implemented first, and after fast filling has ended, the system begins slow filling, which fills the vehicle tank directly with hydrogen produced by the electrolysis unit.

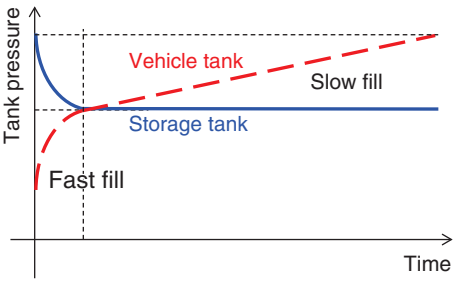


Fig. 5 Hydrogen charging sequence

3. Initial Performance

3.1. Efficiency Analysis

In order to confirm initial system performance, the unit was operated with the temperature of the stack circulation water fixed at 60°C and the system efficiency was measured. The higher heating value of the hydrogen required to calculate efficiency was set at 3.54 kWh/Nm^3. As explained in Section 2.2.1, the manufactured hydrogen flow rate varies with the water drain cycle of the high-pressure separator, so it is necessary to take an average over a sufficiently long time. In this case, the average value from 45 cycles (approximately 1 hour and 20 minutes) was sought (Fig. 6). The resulting hydrogen production in the calculation interval was 0.93 Nm^3 (=3.31 kWh), and the electric power consumption was 5.96 kWh. Therefore, system efficiency in a steady state was 55.5%. This value places efficiency generally on a par with existing large-scale hydrogen stations[(1)].



Fig. 4 Dispenser unit

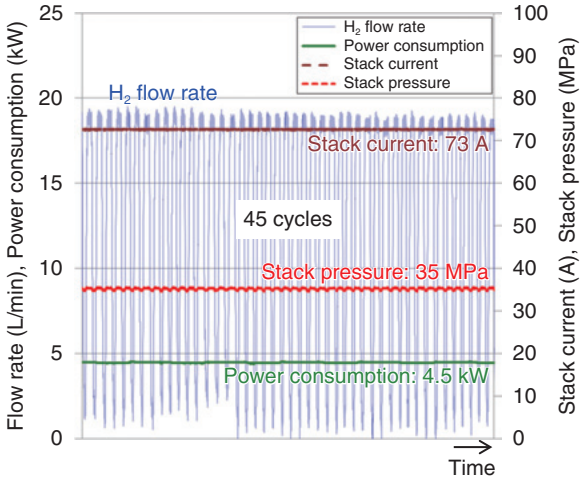


Fig. 6 Operation for efficiency analysis

Stack efficiency is of three types: the current efficiency, the voltage efficiency, and the stack efficiency (power efficiency). The current efficiency is the proportion of hydrogen obtained with respect to the theoretical hydrogen production. The voltage efficiency is the ratio of theoretical electrolysis voltage and the actual voltage. The power efficiency shows the efficiency of the stack in manufacturing hydrogen (current efficiency × voltage efficiency). Measurement and calculation results showed a current efficiency of 96.1%, a voltage efficiency of 73.6%, and a power efficiency of 70.7%. These values were confirmed to be on a par with the initial measurement values for the stack as a unit.

In high differential pressure water electrolysis, one example is that cross-permeation across the membrane occurs with the hydrogen that has been generated, therefore reducing the amount of hydrogen obtained. In the SHS2, a proton exchange membrane two times thicker than necessary to assure the strength of the membrane was used in order to be certain of maintaining functionality. This resulted in a reduced amount of cross-permeation across the membrane, and reduced the loss of hydrogen. This yielded favorable current efficiency figures. On the other hand, the greater thickness of the proton exchange membrane increased the electrical resistance component, resulting in voltage efficiency that is on the low side.

3.2. Analysis of Electric Power Consumption

Electric power consumption at the time of rating was measured when calculating system efficiency, and Fig. 7 shows a breakdown of its components. Measurement results show that producing 1 Nm^3 of hydrogen at the high pressure of 35 MPa required 6.38 kWh of electric power. Breaking that down shows that, apart from 55.5% as the amount of energy converted into hydrogen, the energy required to boost the pressure is approximately 2.7%, electric power loss in the stack is 20.2%, loss from power conversion in the electrolysis power supply is approximately 9.3%, and the total electric power consumed by auxiliary equipment is 12.2%. By item, the stack loss is considerable, followed by electrolysis power supply loss. This shows that enhancing stack efficiency and electrolysis power supply conversion efficiency would be effective in enhancing system efficiency.

3.3. Proposals for Enhancing Efficiency

The reason that stack losses are considerable, as explained in Section 3.1., can be considered to stem from increased resistance due to the use of a thicker proton exchange membrane. Basic study of efficiency enhancement relating to differences in thickness and type of proton exchange membrane has already been performed, and will be described briefly below.

Figure 8 shows the performance of a proton exchange membrane that is presently being compared with the proton exchange membrane that is currently in use. If only the thickness of the present proton exchange membrane is halved and the material is not changed, the electric resistance of the proton exchange membrane can be reduced and the voltage efficiency increased. However, reducing the thickness of the proton exchange membrane can lead to an increased amount of cross-permeation across the membrane so that the current efficiency is reduced. As a result, the apparent gain in power efficiency is slight. A proton exchange membrane made with a material that has low hydrogen penetrability to hydrogen and high strength is under study. When a proton exchange membrane with this different material is used, the amount of cross-permeation across the membrane is reduced and the current efficiency is enhanced. Since the material is stronger, the membrane can be made thinner, which enhances voltage efficiency. This has been found to yield an increase of approximately 10% in power efficiency. The proton exchange membrane with this different material has completed initial testing and results have been confirmed. At present, its durability is being confirmed.

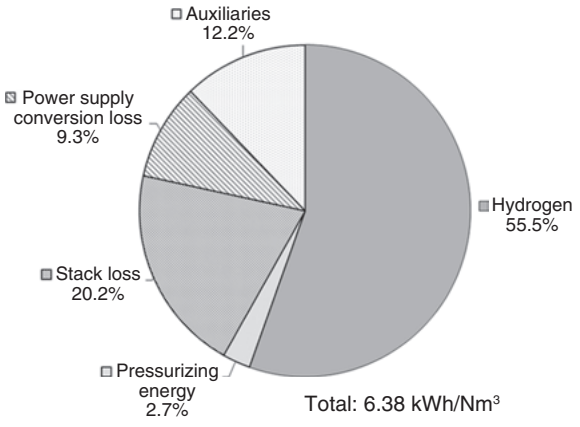


Fig. 7 Power consumption of SHS2

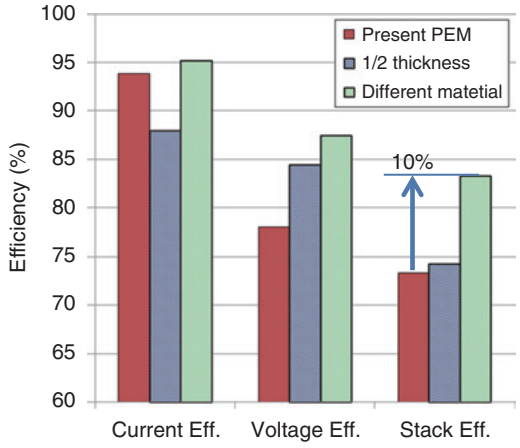


Fig. 8 Efficiency difference of alternative PEMs

Another component with considerable losses is the electrolysis power supply that performs high power conversion. It is thought that enhancement of system efficiency can be achieved most effectively by developing a power supply with greater conversion efficiency. Other measures that need to be taken include lowering the power consumption of auxiliary equipment and optimizing driving methods. These measures are anticipated to yield system efficiency of approximately 70%, as shown in Fig. 9. This figure places the unit at the highest level for compact hydrogen stations known to date[1].

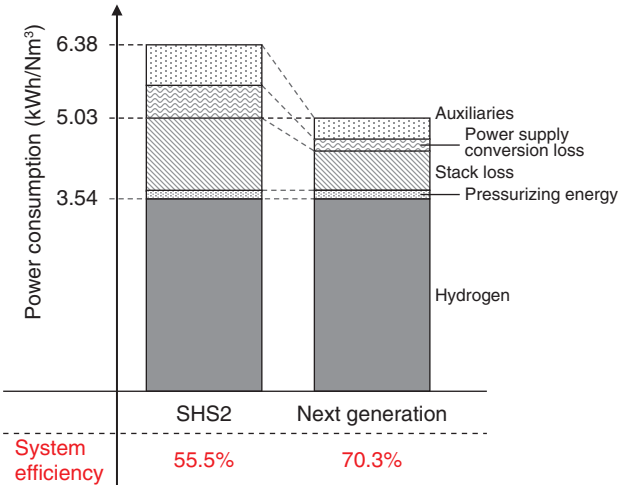


Fig. 9 Expected efficiency

4. Verification Tests

4.1. SHS2 Verification Test Results

The current verification tests used fuel cell electric vehicles operated to simulate commuting to work to test continuous manufacture of the required hydrogen and filling the vehicle with the SHS2. The testing was implemented employing local testers with fuel cell electric vehicles that they actually use to commute to work, go out, and so on.

Figure 10 shows the cumulative total of hydrogen generated by the SHS2 and electric power by the solar cells over the one-year period of operation starting in February 2010. The system is able to produce approximately 0.5 kg of hydrogen in eight hours of operation per day. An ideal line was therefore drawn in the graph for reference to represent the cumulative total of hydrogen generated if 0.5 kg of hydrogen were produced each day. In other words, if the SHS2 is operating normally, the slope of the total volume of hydrogen produced should match the slope of this line. In September 2010, a storage tank enabling 24-hour operation was installed. In other words, the unit became able to produce 1.5 kg of hydrogen per day, so the ideal line was drawn to show 1.5 kg/day from September on. It is apparent from this graph that the system operated without any major problems for a one-year period, excluding long vacations by the operating location and periods of maintenance.

As a result of operation for a one-year period, the time spent in high-pressure water electrolysis at 35 MPa amounted to 1260 hours. The system was started and stopped 267 times, and the amount of hydrogen produced came to 120 kg. Fuel cell electric vehicles were filled 268 times, and after the storage tank was installed, fast filling was performed 107 times.

The total amount of energy generated by the solar cells over the one-year period was 8.82 MWh. On the hypothesis that the system produces hydrogen with energy consumption rate of 6.38 kWh/Nm^3, the amount of electric energy required to produce the 120 kg (1344 Nm^3) over the year would be 8.57 MWh. This means that the solar cells could supply the electric energy for the total amount of hydrogen produced, verifying the system concept.

4.2. Operation Simulation Using Test Results

Under the initial SHS2 system concept, the specifications were set on the basis of night-time slow filling at home. On the other hand, installing a storage tank with the SHS2 to enable fast filling would have some disadvantages, as explained in Section 2.3., but the unit's convenience may also increase, depending on the user's circumstances of use. SHS2 operation simulation was conducted using the verification test results as the means to verify this concept. The greatest advantage to the home fueling system is thought to be the convenience of being able to fill a car with fuel at home. The indicators of user convenience were therefore taken as the fuel level at the time of departure from home; or in other words, a measure of the amount of hydrogen supplied at home, together with the SHS2 utilization rate and the number of times the vehicle was filled at outside stations.

Operating patterns were defined for the simulation

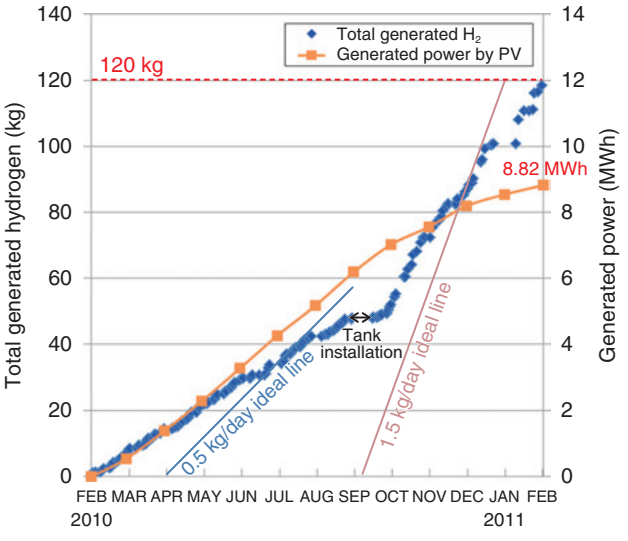


Fig. 10 Total generated hydrogen by SHS2 and power by PV

assuming low, middle, and high frequency of use of fuel cell electric vehicles. The simulation was then performed over a one-year period of operation of fuel cell electric vehicles and the SHS2 following the operating pattern for each user. The figures used for the simulation such as the fuel consumption of the vehicle, the hydrogen production efficiency of the SHS2, and so on were obtained in actual operation. Simulation was performed at first to show the impact of having the SHS2. Figure 11 and Table 3 show changes in the fuel level frequency distribution upon departure from home everyday with times filled at outside stations respectively. By having SHS2 low-frequency users (low: assuming use for commuting to work) able to maintain a high fuel level, the system was able to fully supply their required hydrogen. It is clear also from Table 3 that where the number of times the vehicle was filled outside was 61 times when there was no SHS2, this figure was reduced to 2 times when the SHS2 was present. High-frequency users were often away at night and more often travelled longer distances, so the system was not able to provide an adequate supply of hydrogen at home, and it is apparent that there was less advantage to having the SHS2.

The next simulation conducted was SHS2 with storage tanks to verify whether or not having a storage tank would have an impact on user convenience. Figure 12 shows the fuel levels obtained in the simulation, and Table 4 shows the system utilization rate, while Table 5 shows the changes in the number of times the vehicle was filled away from home. The storage tank was envisioned as having a capacity equal to the vehicle fuel tank. Table 4 shows that having a storage tank enhances the system utilization rate for all users, especially for high-frequency users. Figure 12 shows that low fuel levels could largely be eliminated. In Table 5, the number of times filled away from home could be reduced from 52 times to 15 times. This suggests that the addition of a storage tank enables adequate supply of hydrogen at home and shows that user convenience is enhanced.

Consequently, supplying the SHS2 with the storage tank as an option appears likely to meet the needs of users with various patterns of use.

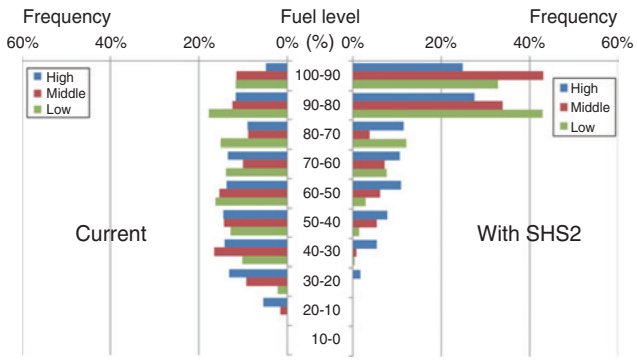


Fig. 11 SHS2 contribution for user

Table 3 Refueling frequency at public stations

	Current	With SHS2
High	111	52
Mid	101	31
Low	61	2

Table 4 System utilization rate

	No tank	With tank
High	32%	79%
Mid	44%	68%
Low	32%	52%

Table 5 Refueling frequency at public stations

	No tank	With tank
High	52	15
Mid	31	26
Low	2	0

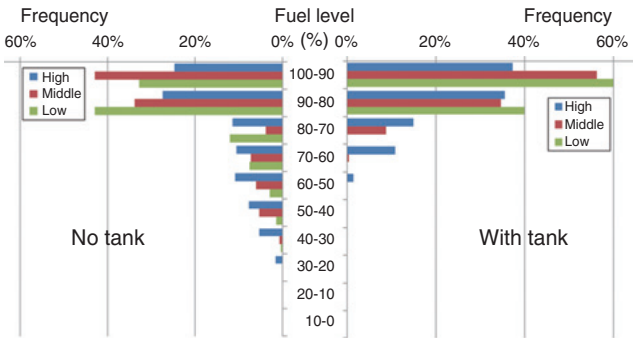


Fig. 12 Storage contribution for user

5. Conclusion

Development and installation of the SHS2 yielded the following conclusions:

(1) Verification tests of the high differential pressure water electrolysis system were implemented for a period of approximately one year. The system was able to supply hydrogen continuously to fuel cell electric vehicles. This demonstrated the endurance reliability of the system as a whole.

(2) The amount of hydrogen produced in the one-year period was 120 kg. It was found that solar cells were able to supply the entire amount of electric energy required for production. This proved the system concept.

(3) The data obtained through operation was used to define

hypothetical operating modes and perform operation simulations. The results show that having a storage tank with capacity equal to the vehicle fuel tank enabled heightened convenience for many users.

(4) The initial performance was measured when the system was first installed. The system efficiency was 55.5%, and 6.38 kWh of electric power were consumed per 1 Nm^3 of hydrogen. Future changes in the membrane material, increases in device efficiency, and other such measures are expected to yield an increase in system efficiency to approximately 70%.

Operation of the SHS2 will be continued, and plans call for accumulation of data on long-term performance and durability.

References

(1) Okabe, M., Nakazawa, K., Taruya, K., Handa, K.: Verification Test of Solar-powered Hydrogen Station (SHS) with Photovoltaic Modules, Honda R&D Technical Review, Vol. 20, No. 1, p. 72-79

(2) Nakazawa, K., Nagaoka, H., Takeuchi, J., Moburg, F., Yamashita, I., Okabe, M.: Introduction of High Differential Pressure Water Electrolysis-type Solar Hydrogen Station (SHS2), Honda R&D Technical Review, Vol. 22, No. 2, p. 28-35

(3) Okabe, M., Nakazawa, K.: Effort to Develop Honda Solar Hydrogen Station (SHS), Journal of the Hydrogen Energy Systems Society of Japan, Vol. 35, No. 3, p. 22-28 (2010)

(4) Okabe, M.: Development of Solar Hydrogen Station (SHS2) with “High differential pressure Electrolyzer”, Journal of Fuel Cell Technology, Vol. 11, No. 2, p. 30-36 (2011)

(5) http://www.honda.co.jp/soltec/cigs/index.html, 2012/5/23

(6) Haryu, E., Nakazawa, K., Taruya, K., Ishikawa, H., Okabe, M.: Mechanical Structure and Performance Evaluation of High Differential Pressure Water Electrolysis Cell, Honda R&D Technical Review, Vol. 23, No. 2, p. 97-105

(7) SAE J2719:2011. Hydrogen Fuel Quality for Fuel Cell Vehicles

(8) ISO/TS 14687-2:2008. Hydrogen fuel – Product Specification – Part 2: Proton exchange membrane (PEM) fuel cell applications for road vehicles

■ Author ■


Hisashi NAGAOKA


Nobuyoshi YOSHIDA


David CUN


Ikuya YAMASHITA


Masanori OKABE

Control Method to Reduce Degradation in Fuel Cell System at Start-up

Koichiro FURUSAWA* Kentaro NAGOSHI* Satoshi TANIMOTO*

ABSTRACT

In the fuel cell system, the anode electrode is supplied with sufficient hydrogen during generation, but when the system is stopped, the inflow of air from the exterior replaces the hydrogen with air. When the system is started with air replacing hydrogen at the anode electrode, corrosion of the catalyst at the cathode electrode occurs.

This paper proposes a method that helps to prevent corrosion of the catalyst by discharging corrosion current to external circuits at start-up. New measurement tools including measurements of electrical potential, corrosion current, and gas analysis were applied to the fuel cell system in developing the control system. Using these tools, the internal environment of the fuel cell stack was clarified, and a method of discharge at the optimal timing with consideration of hydrogen starvation was developed. The ability of the developed start-up discharge method to control corrosion at the cathode electrode was verified by measurements of potential, corrosion current, and quantity of CO_2 generated, and durability tests using an actual fuel cell system confirmed the effectiveness of the system.

1. Introduction

Today, efforts are being made to move away from fossil fuels as a result of air pollution originating in automotive exhausts, climate change due to CO_2 emissions, spiraling oil costs, and other energy-related issues. In order to resolve these issues, Honda is engaged in the development of the fuel cell electric vehicle, the ultimate environmentally responsible vehicle.

Polymer electrolyte fuel cells are the standard cells employed in fuel cell vehicles. These cells are able to operate at low temperatures, are compact, and offer a high level of energy efficiency.

Figure 1 shows a schematic diagram of the structure of a fuel cell. The cell is made up of separators to provide flow channels for gases and coolant, gas diffusion layers to diffuse gases and discharge the water produced by the reaction, catalyst layers to promote catalytic reactions, and a Proton Exchange Membrane (PEM). In the catalyst layers, several nm of platinum nano-particles are supported at high dispersion on a high-specific surface area carbon carrier of several tens of nm.

Looking at the chemical reactions taking place in a fuel cell, first, hydrogen supplied to the anode is divided into protons (H^+) and electrons by the catalyst layer. The protons migrate to the cathode through the electrolytic membrane. On the cathode side, oxygen supplied to the cathode combines with electrons that have migrated from the anode side to the exterior and protons that have crossed the electrolytic membrane, producing water. At this time, an oxygen reduction reaction occurs in the catalyst layer on the cathode side, generating electromotive force. The cathode electrode catalyst layer therefore plays an important role in fuel cell performance.

Because the catalyst layer on the anode side becomes degraded when the cell generates electricity with insufficient

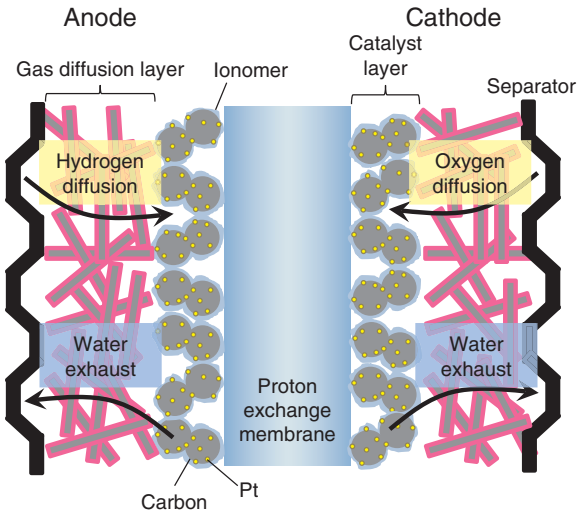


Fig. 1 Schematic of fuel cell

* Automobile R&D Center

fuel (termed "hydrogen starvation" below), it is essential to pay careful attention to the status of fuel during generation.

Figure 2 shows the gas and coolant flow in a fuel cell stack. Gases flow to the generating areas from the upper sections of the separators, and electricity is produced. Following this, the remaining unconsumed gases and the water produced by the reaction are discharged from the lower sections of the separators.

When a fuel cell system stops generating electricity, hydrogen is present on the anode side, and air is present on the cathode side. After a certain period of time has elapsed, air inflows from outside the system. Air inflows into the anode side, and ultimately air replaces the hydrogen on the anode side. When the system is started with air on both the anode and cathode sides (termed "air-air start" below), gas mixing occurs when hydrogen fuel is introduced to the anode side because of the presence of air on this side. Because variations occur in the gas supply to the electrodes, as Fig. 3 shows, in downstream areas of the flow channels, which hydrogen does not reach efficiently, the potential of the anode electrode tends not to decline, and corrosion current flows due to the difference in potential in the electrode. In addition, the potential of the opposite cathode electrode becomes prone to increase. This exposes the cathode to high potentials of 1V or more[1].

At this time, a reaction of the type described by Eq. (1) occurs downstream from the high-potential cathode. Because the electrons released in this reaction pass through the cathode due to the difference in potential, corrosion current is generated. The high potential results in a decline in generation performance due to corrosion of the carbon supporting the catalyst and reduction of the effective surface area of the catalyst through elution of the platinum[1]. In addition, the corrosion of the carbon at the electrode results in changes to its water retention ability, and the ability of the catalyst layer to discharge water declines.

This is known to result in a decline in gas diffusion performance, with a consequent decline in the generation performance of the fuel cell[2].

$$C + 2H_2O \rightarrow CO_2 + 4H^+ + 4e^- \quad (1)$$

The results of potential cycle tests indicate that the repeated exposure of the cathode catalyst to high potentials results in corrosion of the carbon support and elution of the platinum[3].

A variety of materials-based measures have been proposed as means of reducing the corrosion of cathode materials due to air-air starts[4]. Standard measures might, for example, involve increasing the corrosion resistance of the platinum-supported carbon. A system-based measure being employed is the sealing of the space around the anode and cathode in order to help prevent the inflow of air.

This paper considers a control-based approach to the reduction of corrosion, and proposes a start-up discharge control method.

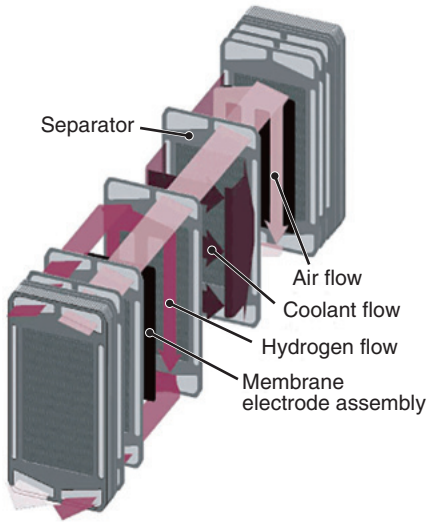


Fig. 2 Fuel cell stack configuration

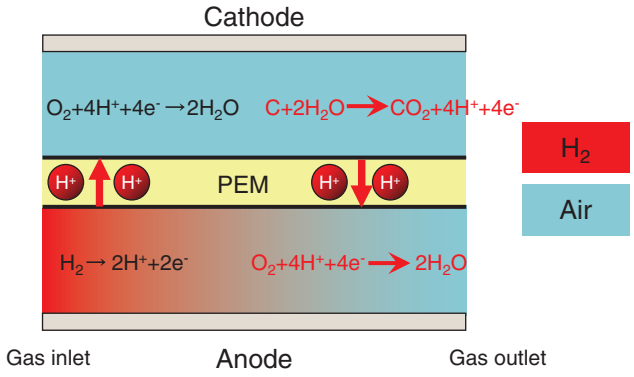


Fig. 3 Model of carbon corrosion at Air-Air start-up

2. Methods of Reducing Corrosion of Electrode Materials

"Start-up discharge" refers to the release to external circuits of the corrosion current generated downstream from the anode when gas is supplied at fuel cell start-up, as shown in Fig. 4. The electrons that flow to the external circuit would be transferred to the cathode and used in normal fuel cell reactions. This would help to prevent

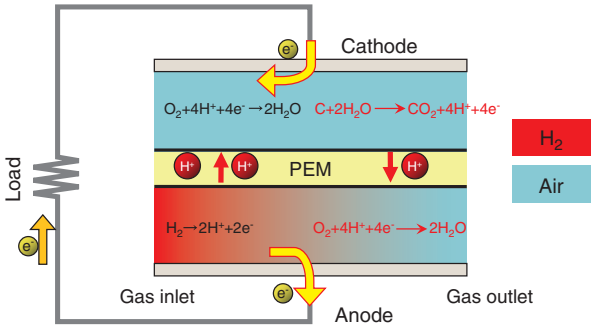


Fig. 4 Model of start-up discharge

reactions such as the one shown in Eq. (1) from occurring downstream in the flow channels. It was also considered that the discharge of electricity would reduce the voltage of the cell and lower the potential of the cathode, helping to prevent the cathode from being exposed to a high potential.

Figure 5 shows a timing chart for start-up discharge control.

Directly after the commencement of start-up of the fuel cell system, hydrogen is supplied to the anode and air is supplied to the cathode. At this time, the voltage of the fuel cell stack begins to increase. Conventional control begins discharging after open-circuit voltage has been reached, but start-up discharge control begins discharging while voltage is increasing. There is no change in the method of introducing gases at this time between the two control methods. Tests were conducted using two patterns for discharging: commencement of discharge simultaneously with the introduction of the gases (current control); and commencement of discharge after voltage had risen to a certain degree (voltage control).

One point to which it was necessary to give particular attention in constructing a system for start-up discharge control was attempting to ensure that discharge did not commence before hydrogen had been substituted at the anode. As Figure 6 shows, commencing discharge with insufficient hydrogen at the anode results in hydrogen starvation due to the reaction described by Eq. (1), leading to corrosion of the catalyst at the anode electrode[5]. Because the activation energy necessary to promote a reaction at the anode is lower than that at the cathode, the amount of catalyst material used at the anode is generally lower than that used at the cathode. This means that corrosion of the anode catalyst has a significant effect in reducing the performance of the fuel cell.

By contrast, insufficient oxygen at the cathode does not result in corrosion, but simply produces a decline in voltage.

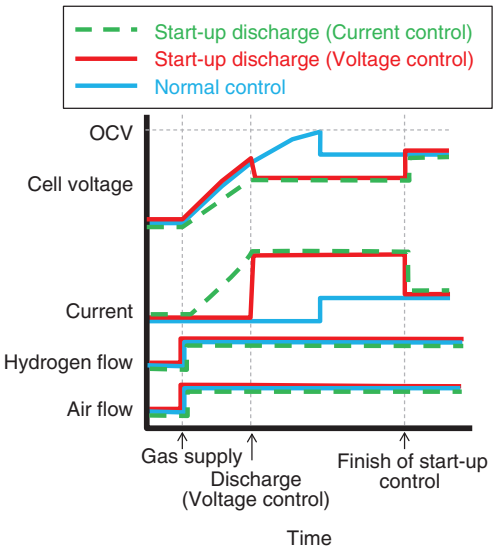


Fig. 5 Timing chart for start-up discharge

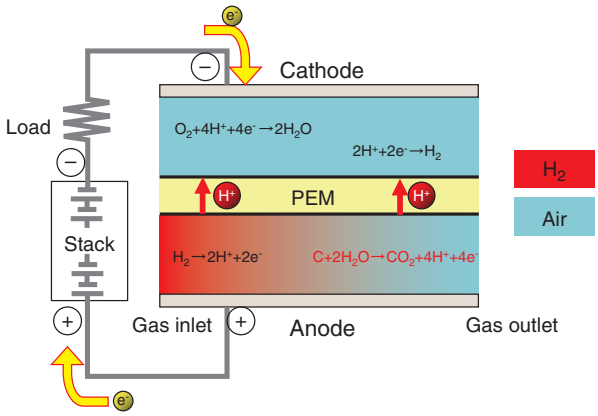


Fig. 6 Model of H_2 starvation

3. Measurement Methods

As indicated in Chapter 2, in order to implement start-up discharge control, it was necessary to obtain a detailed understanding of the reactions taking place in the fuel cells at start-up. It was necessary to conduct the measurements in a fuel cell system, because it was difficult to test transient occurring at start-up with only stack equipment. Therefore, potential and current density sensors were positioned in a fuel cell stack, and measurements of the internal environment of the cells were conducted with the stack fitted in a fuel cell system (a generating system incorporating the fuel cell stack, a gas supply system, and a cooling system).

Using the measurement methods discussed below, the internal reactions in the fuel cells were elucidated, helping to enable the development of a control system.

3.1. Measurements of Potential

Generation with insufficient hydrogen present at the anode would result in an increase in potential at the anode; in order to determine the effectiveness of the control, the study examined whether or not generation was occurring under such a condition of hydrogen starvation, and whether or not potential increase at the cathode had been controlled.

Cell voltage can be used as a parameter for understanding fuel cell performance, but the behavior of voltage alone is not sufficient to provide an accurate understanding of the reactions occurring within the cells. Cell voltage is a function of the difference in potential between the cathode and anode sides, and an accurate grasp of the reactions occurring at each electrode can be obtained by measuring the potential of each electrode. Potential measurements were therefore conducted using a small, thin-film electric potential sensor developed by Honda[6]. Figure 7 shows the positioning of the sensor. The potential sensor was a self-hydrogen-generating type. A voltage of 1.4 V was impressed in the sensor's voltage impression section, generating hydrogen at a reference electrode positioned on

the anode side. With the reference electrode providing the reference potential, the anode potential was considered as the difference between anode potential and the reference potential, and the cathode potential was considered as the difference between cathode potential and the reference potential. Using this method, it was possible to measure potential even in the case of an internal cell environment with no hydrogen present, as at air-air start.

Discharge timings were determined while conducting measurements of the potential at the anode and cathode at start-up using this sensor.

3.2. Corrosion Current Measurements

Corrosion current flowing into the electrodes at start-up was measured using a current density sensor inserted in a fuel cell stack. As shown in Fig. 8, a divided electrode was used for the anode, and oxidation-reduction current produced at start-up was measured. The corrosion current flowing through the entire electrode was calculated by integration of the figures obtained. Because corrosion of the carbon at the cathode at start-up would produce the phenomenon described by Eq. (1), the analysis was conducted with a particular focus on oxidation current.

3.3. Gas Analysis

Measurements of the CO_2 generated by corrosion of electrode materials at start-up were conducted using a mass spectrometer, Hx-07i[7](manufactured by Nohmi Bosai, Ltd.). Using the highly responsive measurement device, the gases for measurement were narrowed down to specific gas species, and the amount of gas taken in was reduced. Corrosion of the carbon that supports the platinum used as a catalyst in fuel cells generates CO_2, and measurements of this CO_2 were conducted to quantify carbon corrosion.

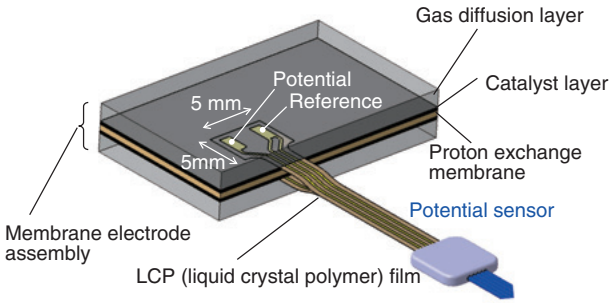


Fig. 7 Configuration of potential sensor

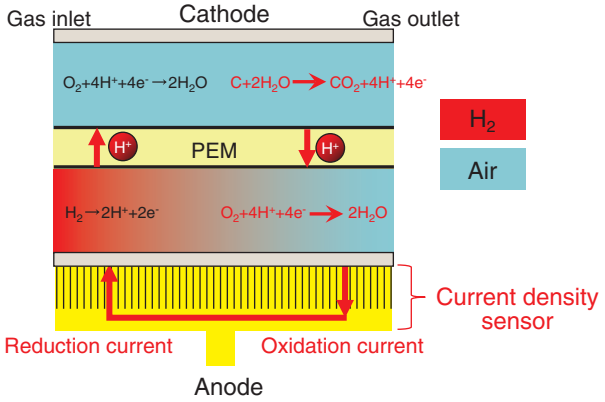


Fig. 8 Current density sensor

4. Measurement Results

4.1. Before start-up discharge

Potential and corrosion current were measured at air-air start. Results for potential are shown in Fig. 9, and results for corrosion current are shown in Fig. 10.

The image on the right-hand side of Fig. 9 shows a fuel cell seen from the orientation of the electrodes. At air-air start, the potential of both the anode and the cathode prior to start-up is 1V. At start-up, hydrogen is supplied to the electrodes, and the potential of the anode declines to 0V. The results of potential measurements show that because the anode potential does not readily decline to 0V in the vicinity of the cathode outlet (position 4), where the substitution of the gases is delayed, the opposite cathode potential increases, and the cathode is exposed to a high potential. Factors such as the speed of gas substitution and the status of corrosion of electrode materials can be confirmed from these changes in potential.

The results of measurements of the corrosion current in the electrodes, shown in Fig. 10, indicate that there is a significant flow of oxidation current downstream of the electrodes directly after start-up. These results also demonstrate that at air-air start, because the cathodes are exposed to high potentials and corrosion of the cathode

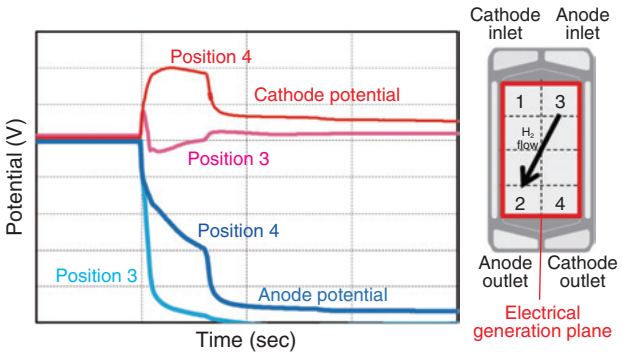


Fig. 9 Potential measurement at start-up

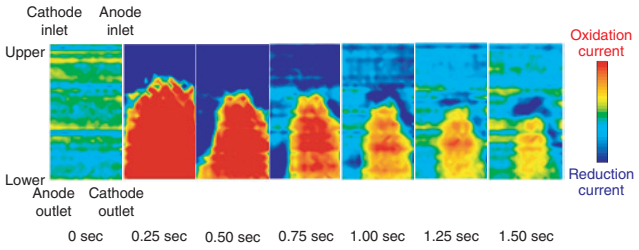


Fig. 10 Comparison of corrosion current

catalyst occurs, corrosion current flows downstream in the flow channels of the stack.

4.2. Study of Effect of Start-up Discharge

From data including potential, corrosion current, and gas concentration, the effectiveness of the start-up discharge method was confirmed. The study results for each control method are described below.

4.2.1. Current control

A fuel cell was connected to a load resistance prior to start-up in order to discharge current immediately after gas supply (current control). Figure 11 shows the results of CO_2 measurements conducted during start-up discharge under these conditions. These results show that despite the fact that CO_2 declines at the cathode, CO_2 is generated at the anode.

This indicates that because there is insufficient replacement of hydrogen at the anode electrode when discharge is commenced immediately when the gases are introduced, and reactions occur in which carbon, platinum or other substances release electrons in place of the hydrogen, the volume of CO_2 generated at the anode increases. Because CO_2 generated at the anode at start-up has a greater effect on cell performance than CO_2 generated at the cathode at start-up, the results demonstrate that current control is not sufficient to control performance declines.

In addition, with regard to the allocation of gas, the cell voltage changes polarity at points that are distant from the gas manifold because of the effect of the direction of layering. Because corrosion of the anode materials occurs when start-up discharge is conducted immediately after start-up despite the fact that the corrosion of the cathode materials is controlled, this form of control was judged as not being sufficiently effective.

4.2.2. Voltage Control

To continue the study, start-up discharge was conducted after start-up before the fuel cell reached open circuit voltage (voltage control), and potential, corrosion current, and quantity of CO_2 generated were measured.

Figure 12 shows the behavior of potential close to the cathode outlet, where potential is most prone to increase. Start-up discharge produced little effect in reducing the peak value of cathode potential, but the period for which the electrode was exposed to high potential was reduced. Based on this, it is considered that corrosion current continued to flow while the cathode was exposed to high potential, and it was possible to reduce corrosion current in areas in which the cathode potential was controlled. In addition, because no increase in anode potential was observed, it was concluded that start-up discharge did not result in hydrogen starvation, and inhibited the degradation of the anode catalyst.

Figure 13 shows the integrated values for corrosion current at the electrodes for normal control (Fig. 13(a)) and start-up discharge control (voltage control) (Fig. 13(b)). These results demonstrate that start-up discharge results in an overall reduction in the value of oxidation current. Under normal start-up conditions, a significant oxidation current flows at the cathode outlet, and the application of start-up

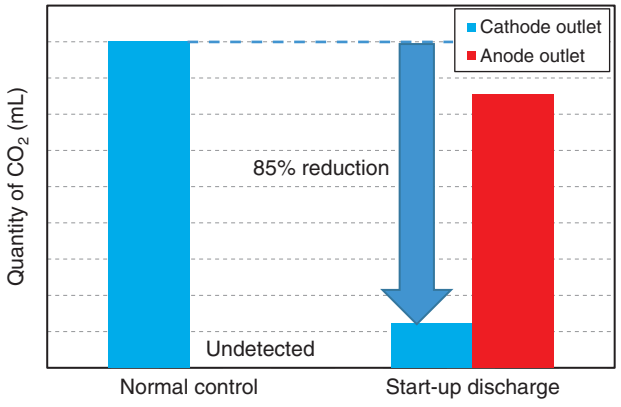


Fig. 11 Quantity of CO_2 at normal control and start-up discharge (Current control)

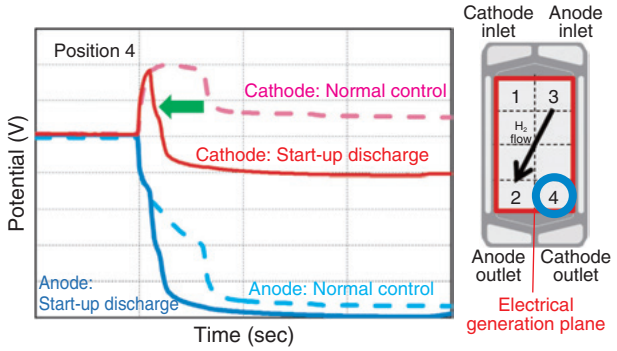


Fig. 12 Potential measurement at start-up with and without start-up discharge (Position 4)

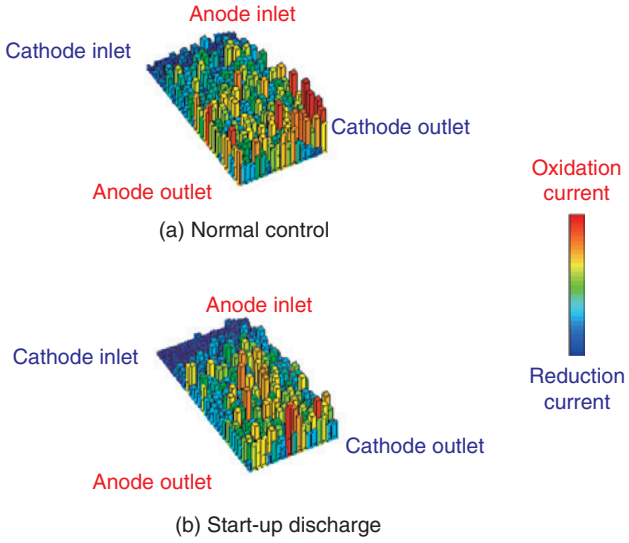


Fig. 13 Comparison of integrated oxidation current for normal control and start-up discharge (Voltage control)

discharge control (voltage control) results in a reduction of this oxidation current.

Figure 14 shows the results of measurements of CO_2 at the cathode outlet. The results show that while the overall reduction in CO_2 is lower than the reduction for current control, voltage control reduces the quantity of CO_2 generated at the cathode. The CO_2 measurements therefore also demonstrate the effectiveness of this control method, indicating a reduction in the level of corrosion of the cathode catalyst.

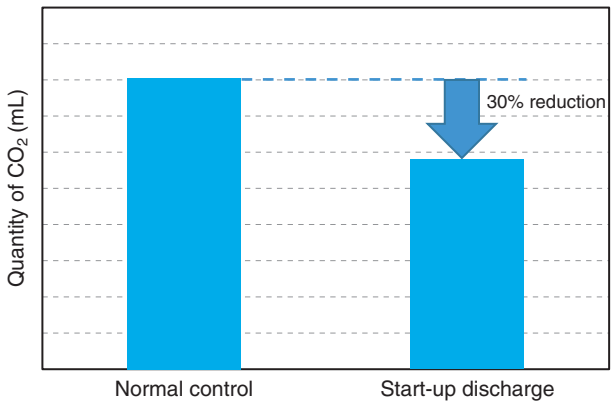


Fig. 14 Quantity of CO_2 at cathode outlet (Voltage control)

5. Verification Tests

The developed voltage control start-up discharge method was applied to an actual fuel cell stack and durability tests were conducted. The start-up durability modes were tested in the following order: soak, scavenging, air-air start, generation, and shutdown.

Figure 15 shows the level of decline in performance measured over start-up-shutdown cycles with and without start-up discharge, converted to correspond to a single cycle.

These results indicate that the use of discharge control at air-air start not only reduces the generation of CO_2 due to corrosion on the cathode side, controls potential and reduces corrosion current, but also reduces the decline in cell performance resulting from these multiple effects to less than half of previous levels, demonstrating the effectiveness of the control method.

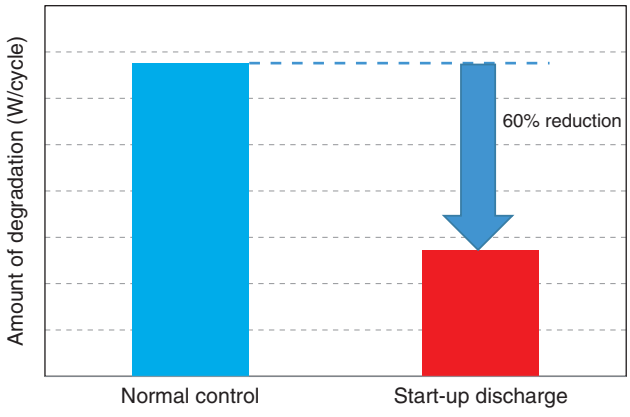


Fig. 15 Amount of degradation for normal control and start-up discharge (Voltage control)

6. Conclusion

Measurements of electrical potential and corrosion current and gas analyses were conducted in the fuel cell system, and a start-up discharge control method was developed to reduce the corrosion of electrode materials.

(1) Setting an earlier timing for start-up discharge (current control) resulted in hydrogen starvation at the anode, and the method was ineffective as an electrode corrosion control measure.

(2) Measurements of potential, corrosion current and the quantity of CO_2 generated indicated that the use of the developed start-up discharge (voltage control) method reduced the level of corrosion of the cathode, and verification tests using an actual fuel cell system confirmed the method's effectiveness.

7. Afterword

The development of the control method discussed here was made possible by advances in technologies for conducting detailed studies of the internal environment of fuel cells. Potential, corrosion current, gas analysis and other internal cell conditions measured in the course of this study will be fed back into evaluations of a fuel cell and materials, and thus assist in enhancing the development of fuel cells and materials.

The measurement methods described here has being applied to coming research for extending the long life of fuel cells, by developing optimal control methods for the power generation, shutdown, etc. while studying the actual internal environment of the cells.

In addition, the authors believe that the reduction of materials corrosion by the optimal system control will allow substitution of lower cost materials, making it possible to reduce the cost of fuel cells in the future.

References

(1) Gu, W., Carter, R. N., Yu, P. T., Gasteiger, H. A.: Start/Stop and Local H2 Starvation Mechanisms of Carbon Corrosion: Model vs. Experiment, ECS Transactions, 11(1), p. 963-973 (2007)

(2) Yamazaki, K., Nagoshi, K., Yoshida, H.: Current Status and Challenges of Fuel Cell Vehicle Development, JSAE Proceedings, No. 25-10 , p. 1-4 (2010)

(3) Takano, J., Kaji, H., Yoshida, H., Nagoshi, K.: Development of HONDA FCX, EVS24 (2009)

(4) Auer, E., Freund, A., Pietsch, J., Tacke, T.: Carbons as

supports for industrial precious metal catalysts, Appl. Catal. A. Gen. 173, p. 259-271 (1998)
(5) Taniguchi, A., Akita, T., Yasuda, K., Miyazaki, Y.: Analysis of electrocatalyst degradation in PEMFC caused by cell reversal during fuel starvation, Journal of Power Sources, 130, p. 42-49 (2004)
(6) Yoshida, H., Koiwa, N., Sato, M., Suzuki, T.: Small, Thin-film Electric Potential Sensor for In-situ Evaluation of Fuel Cell Stack, Honda R&D Technical Review, Vol. 21, No. 2, p. 162-167
(7) Nohmi, T., Maekawa, M., Mogi, T.: Suiso Ion Sensa, Suiso Enerugi Sisutemu, Vol. 33, No. 2, p. 54-59 (2008) (in Japanese)

■ Author ■


Koichiro FURUSAWA


Kentaro NAGOSHI


Satoshi TANIMOTO

Hydrogen Adsorption MOF Design and Adsorption Characteristics

Terumi FURUTA* Mitsuya HOSOE*
Izuru KANOYA* Hiroshi SAKAI*

ABSTRACT

The project discussed in this paper attempted to design and synthesize a hydrogen-adsorbing material suitable for fuel cell electric vehicles. The newly designed and synthesized Cu_2(3,5-pyridinedicarboxylate)$_2$ metal complex displayed an extremely high volumetric uptake density for a physisorption material, despite the fact that its specific surface area was only about 1,000 $m^2\ g^{-1}$. It is believed that the realization of an increased number of adsorption sites per unit area and increased adsorption energy, in addition to the optimized design of pore shapes, were major factors in the achieved uptake performance.

1. Introduction

Climate change is a major issue facing humanity today, and one which should be urgently addressed. The enormous volumes of CO_2 released as a result of the evolution of human activities is believed to be one of the main causes of climate change, strongly necessitating the reduction of CO_2 emissions. Given this, research is pushing ahead on the fuel cell electric vehicle as an advanced mode of transport able to help curb CO_2 emissions. In fuel cell electric vehicles, the motor is driven by electricity generated in a chemical reaction between hydrogen stored in a high-pressure gas tank and oxygen in the air, and the only emission is water. However, the high-pressure hydrogen storage gas tanks occupy a large amount of space, and are also heavy. The use of materials for hydrogen storage that would help to enable the vehicle bodies to be reduced in size and fuel efficiency to be increased is therefore being studied.

Hydrogen storage materials can be broadly divided into two types, and both metal hydrides, which function by chemisorption, and hydrogen-adsorbing materials (with carbon materials and zeolite as representative examples), which function by physisorption, have been the subject of study. Hydrogen-adsorbing materials offer the advantage of producing less heat than metal hydrides when adsorbing and releasing hydrogen. This does away with the need for heat management systems, which can be expected to contribute to the reduction of vehicle size and weight. The issue, however, is overcoming the low adsorption volume of these materials.

Metal-organic frameworks (MOF) have recently become the focus of attention as adsorbent materials, and numerous gas adsorption characteristics of these materials have been reported on[(1), (2)]. Metal-organic frameworks are macromolecular crystals formed from a combination of metallic cores and organic ligands known as linkers. The appropriate selection of these elements makes it possible to adjust parameters including pore size and crystal system. This high degree of freedom of design is one of the appealing points of MOF.

The research discussed in this paper attempted to design and synthesize an original MOF optimized for application in hydrogen storage for fuel cell electric vehicles. The developed MOF realizes a higher level of hydrogen adsorption performance than an existing MOF (IRMOF-1[(3)]).

2. Design of Material

From considerations of driving distance, fitting space, speed of hydrogen filling and speed of hydrogen release, hydrogen-adsorbing materials employed in fuel cell electric vehicles should reconcile high mass storage density (wt%) and volumetric storage density (vol%) with low adsorption heat (ΔH). In order to increase the volume adsorbed, it is generally necessary to increase the number of adsorption sites and attempt to ensure an appropriate level of adsorption energy. In an MOF, the number of adsorption sites can be increased by lengthening the linkers to increase the material's specific surface area. However, when long linkers are employed, an excessive number of pores are created at the same time that the specific surface area increases, and this can reduce volumetric density and increase the space necessary for fitting the hydrogen storage tank. It is, therefore, important to appropriately

* Fundamental Technology Research Center

control pore volume in order to help ensure that volumetric density does not decline. Analyses of the adsorption sites in IRMOF-1 conducted by the authors using neutron diffraction measurements and first-principle molecular dynamics calculations showed that the main adsorption sites surrounded the metallic cores[4], indicating that it would also be important to realize a high-density configuration of metallic cores.

When utilizing physisorption materials, large amounts of hydrogen can be stored by increasing adsorption energy (adsorption heat), but this results in the production of high levels of heat when the hydrogen is stored, and filling speed declines. In order to realize filling times equivalent to those for gasoline engines, hydrogen adsorption heat should be controlled to 10 kJ mol^{-1} or below. The hydrogen adsorption heat (ΔH) of IRMOF-1 is 4.8 kJ mol^{-1}[13]. Designing an MOF with a higher adsorption energy could be expected to increase adsorption volume, and methods of increasing adsorption energy were therefore investigated. The use of heterocycle linkers, in which atoms with a high electronegativity such as N, F or Cl have been partially substituted, is known to increase adsorptivity. This is supported by the analysis results shown in Fig. 1, calculated using first-principle calculations[6], [18], [19] based on density functional theory (DFT)[5], for the adsorption energy of hydrogen molecules and electron density (electrostatic potential) around adsorption sites in a benzene dicarboxylate (BDC) linker and metallic core model. It is predicted that hydrogen adsorption energy will tend to increase in areas in which electrons are localized, and the use of atoms displaying high electronegativity is therefore an effective method of increasing adsorption energy. In the metallic core, it is necessary to reduce the actual volume occupied by the atoms and to increase adsorption energy. A double-core structure known as a paddle wheel[15] represented an effective candidate given the fact that it has a comparatively low coordination number, can further reduce the actual volume occupied by the atoms in the metal cores, and is able to form high adsorption energy sites when the surface of the metal is exposed. Results for the hydrogen adsorption energy of double-core structures obtained using first-principle calculations[6], [18], [19] based on DFT indicated that hydrogen adsorption energy would be 10-12 kJ mol^{-1} in almost all cases if second-, third-, or fourth-row transition metal elements were used, and that there was no significant difference in adsorption energy between elemental species (Table 1). Cu, which is known to frequently synthesize metallic complexes with double-core structures[17], was, therefore, selected as the metallic element.

It was necessary to reconcile a high metallic core density with the formation of communicating pore spaces in creating the framework. It was also necessary to realize an arrangement of elements that would not destroy the metal exposure sites (cap sites) formed due to the paddle wheel structure[15]. The use of offset layering of monolayers formed from a combination of triangular and hexagonal pores maintained the cap sites while helping to enable the triangular sites to be maintained as communicating pores.

The bond angles between the paddle wheels[15] and the linkers were 90°, and in order to realize a triangular framework with bond angles of 60°, it was necessary to maintain the paddle wheel structure in an unstable state. It was therefore proposed that the paddle wheels should be inclined from a perpendicular alignment in order to produce a structure with minimal distortion of the bond angles. Curved linkers were employed to realize this configuration.

The MOF pore size was optimized in order to balance adsorptivity with mobility of hydrogen atoms, and was made approximately twice the size of hydrogen molecules.

Based on the above, it is considered that there are specific guidelines that should be followed in the design of

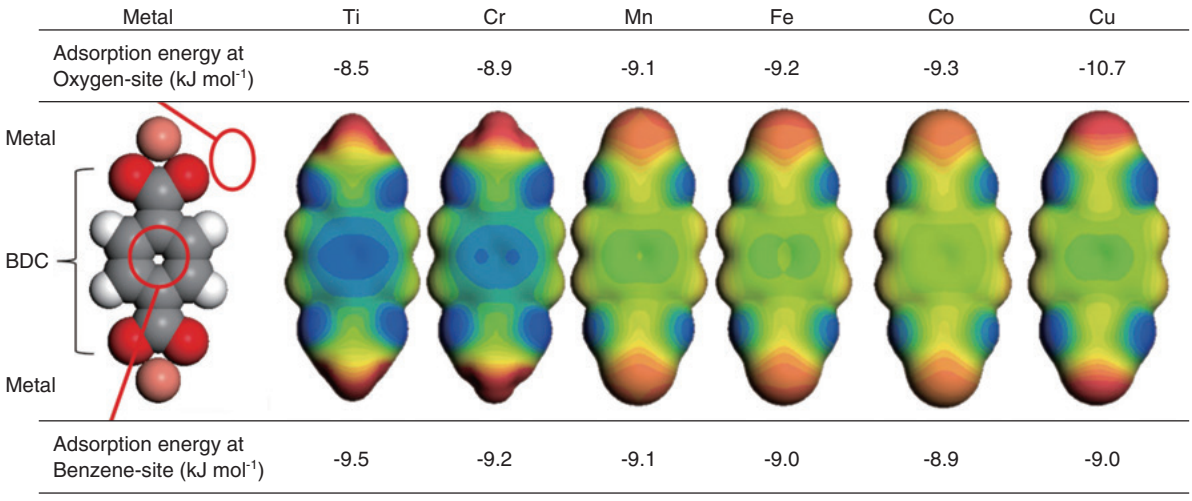


Fig. 1 Electrostatic potential and adsorption energy

* Calculated with VASP-LDA-PAW. ** The red areas correspond to positively charged areas and blue areas to negatively charged areas in the electrostatic potential map. The adsorption energy tends to be larger when there is greater negative charge, or where the electrons are localized.

Table 1 Adsorption energy of paddle wheel

Core atom	Adsorption energy (kJ mol^{-1})	Core atom	Adsorption energy (kJ mol^{-1})	Core atom	Adsorption energy (kJ mol^{-1})
Li	–11.3	V	–11.0	Zr	–11.7
Be	–10.2	Cr	–11.0	Nb	–11.7
B	–	Mn	–11.0	Mo	–10.9
Na	–11.3	Fe	–11.3	Rh	–11.4
Mg	–10.7	Co	–9.7	Pd	–11.3
Al	–12.2	Ni	–11.2	Cd	–
K	–	Cu	–11.3	La	–
Ca	–10.5	Zn	–10.9	Ce	–
Sc	–10.3	Ga	–	Pt	–12.0
Ti	–9.4	Y	–10.2		

*[-] Does not form paddle wheel structure. ** Value calculated with VASP-LDA-PAW.

an MOF hydrogen-adsorbing material produced for use in a fuel cell electric vehicle. These are:

(1) In order to increase the rate of hydrogen adsorption, it is necessary not to focus exclusively on increasing the specific surface area per unit weight, but also to increase the density of hydrogen adsorption sites as much as possible.

(2) The space occupied by the atoms forming the framework themselves (dead space) should be reduced as much as possible.

(3) In order to increase hydrogen adsorptivity, heterocycles and high-electronegativity atoms that strengthen electron localization should be employed.

(4) Space for sufficient hydrogen mobility should be created, pores that produce dead space should be reduced and the rate of diffusion should be increased.

Next, Cu_2(3,5-pyridinedicarboxylate)$_2$ (Cu_2PDC_2) was proposed and designed with comprehensive consideration of factors including the feasibility of experimental synthesis while making use of the freedom of design offered by MOF. The structure of the Cu_2PDC_2 is shown in Fig. 2(a).

This structure features a curved linker, and is formed

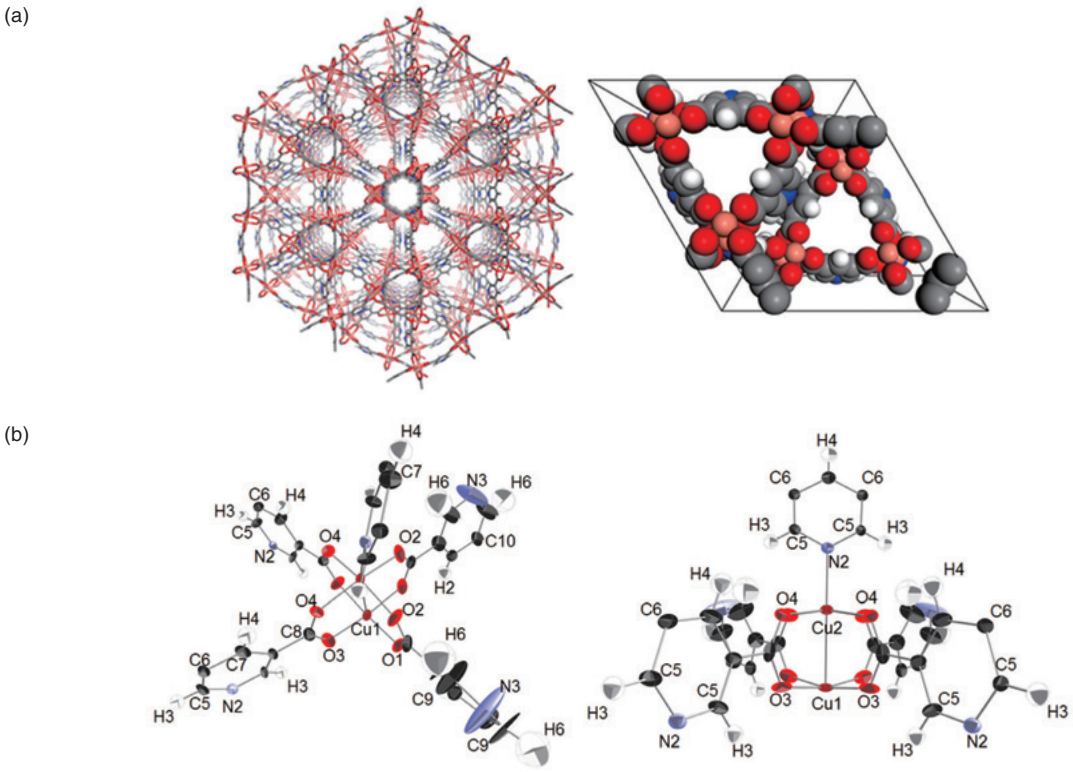


Fig. 2 (a) Overall view of Cu_2PDC_2 (left) and the unit cell (right). The space group is *P6$_3$mc* (blue: nitrogen; red: oxygen; gray: carbon; orange: copper); (b) The structure of Cu_2PDC_2. The two figures are the same structure from different angles.

Table 2 The calculated and experimentally measured density of adsorption sites, pore ratio, and adsorption energy in Cu_2PDC_2 and IRMOF-1

	Density of adsorption site (nm^{-3})	Pore ratio ($cc\ cc^{-1}$)		Adsorption energy ($kJ\ mol^{-1}$)	
	Calc.	Calc.	Exp.	Calc.	Exp.
IRMOF-1	3.8	0.77	0.86	-9.4	-4.8
Cu_2PDC_2	8.9	0.50	0.46	-16.5	-6.0

from a basic framework [Fig. 2(b)] created by the bonding of 3,5-pyridinedicarboxylate (PDC), a linker containing N, which promotes electron localization, and Cu. This basic framework forms two-dimensional sheets with pores of approximately 6 Å and approximately 11 Å through planar bonding [Fig. 3(a)], and a three-dimensional structure of ABAB stacks is created by bonding between Cu and some of the N in the PDC [Fig. 3(b)]. The space groups are $P6_3mc$. These ABAB stacks overlap in 60˚ twists centering on the c-axes, and the respective layers are characterized by continuously changing pores of sizes between 6 Å and 11 Å, as shown by A in Fig. 3(a), and communicating pores of 6 Å, as shown by B [Fig. 3(a), right].

Table 2 shows the density of adsorption sites, pore ratio, and adsorption energy as predicted from the crystal structure of Cu_2PDC_2. The adsorption energy for typical adsorption sites was calculated using first principle calculations[6), (18), (19)] based on DFT (adsorption energy tends to be overestimated by DFT[(4)]). The density of adsorption sites was calculated from the number of typical adsorption sites displaying a high level of adsorption energy. Figures calculated from Connolly surfaces (using Materials Studio manufactured by Accelrys) are used for the pore ratio. For the sake of comparison, experimental values[(13)] are also shown. The pore volume was estimated to be 0.5 cm^3g^{-1} or less, and the number of adsorption sites per unit volume to be twice that of IRMOF-1. The crystals themselves were porous, with a dense atomic arrangement. The pore occupancy ratio per unit volume was approximately 1/2. In addition, hydrogen adsorption energy was high in comparison to IRMOF-1, and overall an increase in the rate of adsorption could, therefore, be expected.

3. Synthesis of Designed Material

3.1. Study of Synthesis Conditions

For the synthesis of the proposed Cu_2PDC_2 complex, (a) the state of coordination of the metallic cores and (b) the bonding energy of the metallic cores and the ligands were focused on.

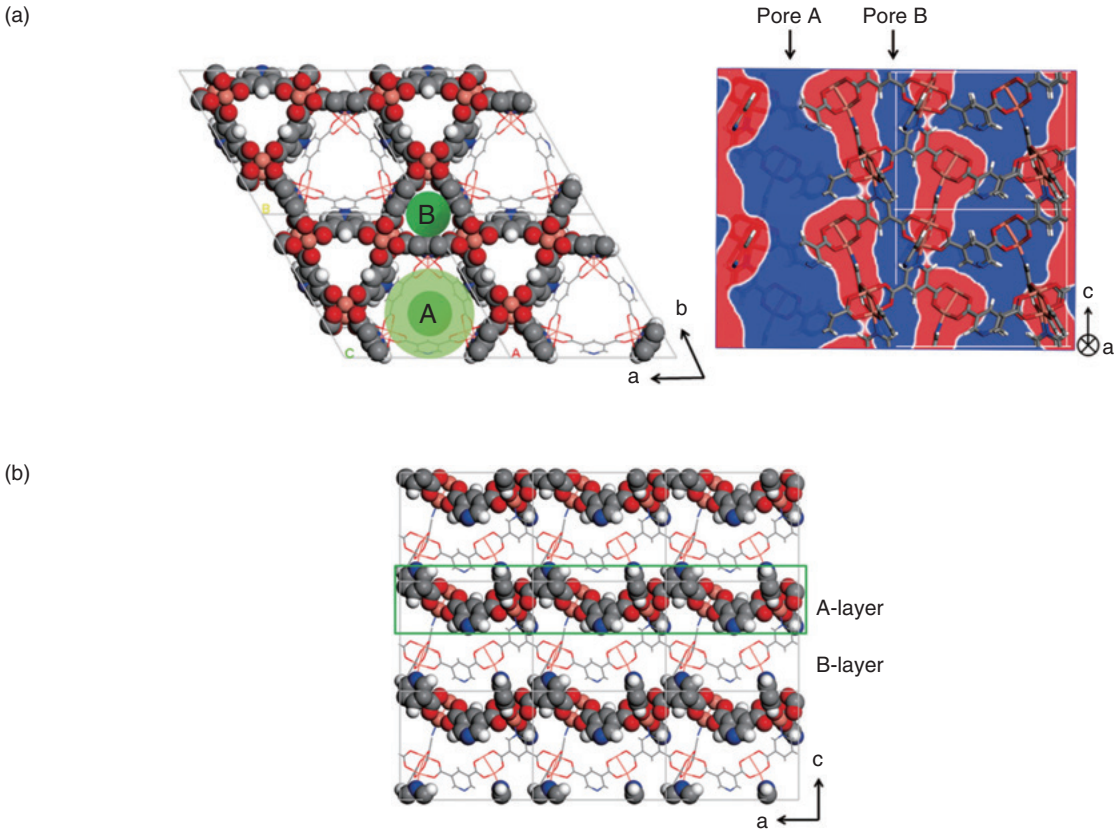


Fig. 3 (a) Pores observed from the c-axis (left) and the a-axis (right). The blue portions indicate pores in the figure to the right. Pore A consists of holes with ϕ = ~11 Å and ϕ = ~6 Å. Pore B is made up of holes with ϕ = ~6 Å; (b) The A-B stacking sequence. The rectangle shows single layer.

(a) Coordination state of metallic cores and selection of starting materials

As Fig. 4 shows, the complex has a particular coordination state, forming structures termed paddle wheels, with Cu atoms as the metallic cores. Copper(II) acetate, which has the same structure, was, therefore, selected from among the copper salts for use in synthesis. 3,5-Pyridinedicarboxylic acid (PDC acid), a precursor of PDC, was used as the linker.

The solvent forming the reactive site for the synthesis of the complex should possess the property of maintaining the paddle wheel structure of the copper(II) acetate dissolved in it. To verify this condition, the coordination state of the metal ions in the solution was measured[16] by means of Cu K-edge X-ray absorption fine structure (XAFS) measurements taken using SPring-8[14] high-brilliance X-rays. Water (H_2O), ethanol (EtOH), dimethylformamide (DMF), and diethylformamide (DEF), which are standard solvents for the synthesis of complexes, were the substances under consideration for use as the solvent. Figure 5 shows XAFS spectra for copper(II) acetate dissolved in each of the solvents. A peak occurring around 8985 eV, shown as the red broken line in the figure, reflects the paddle wheel configuration. This peak is not present in water, indicating the collapse of the paddle wheel structure. It is believed that the coordination of the acetic acid ions could not be maintained in water, which has a high polarity (water's specific permittivity is 80, while figures for EtOH and DMF are around half this). Water was, therefore, removed from the list of potential solvents. The paddle wheel structure was maintained in the other solvents, and EtOH, DMF, and DEF were therefore selected as synthesis solvents.

The selected starting materials (copper(II) acetate and PDC acid) were dissolved in each of the candidate solvents, and the status of synthesis was studied. This produced blue solutions of the type shown in Fig. 6. Scanning electron microscopy (SEM) showed the sediment precipitated out of the solution to be spherical aggregates (Fig. 6, right). Analysis indicated that these aggregates were an amorphous-like substance with an identical composition to Cu_2PDC_2 complex (see Fig. 7). It had, therefore, not been possible to obtain a Cu_2PDC_2 complex.

(b) Reexamination of conditions with focus on bonding energy between metallic cores and ligands

The bonding energy between the metallic cores and the ligands was focused on to help enable modification of the synthesis reaction conditions, and the energy diagram shown in Fig. 8 was formulated.

The energy ΔH produced by the reaction $2Cu+2PDC \rightarrow Cu_2PDC_2$ (MOF), as determined by first-principle calculations based on DFT[6), (18), (19)], was a negative figure (-46 kJ mol^{-1}), and it was predicted that the target synthesis reaction (the reaction pathway to the right in Fig. 8) could occur. At the same time, the simple bonding energy of Cu and PDC (as the energy generated by the reaction, ΔH) is also a negative figure (-5.6 kJ mol^{-1}), and it was

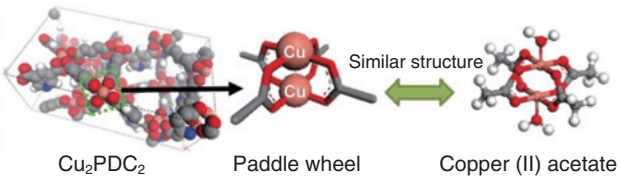


Fig. 4 Structure of Cu_2PDC_2 and coordination state of Cu

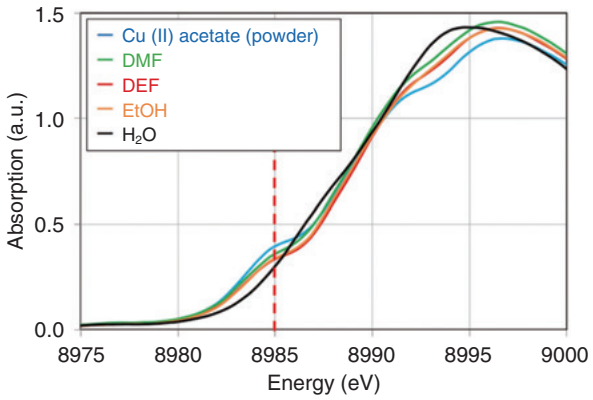


Fig. 5 XAFS spectrums of Cu acetate with solvent

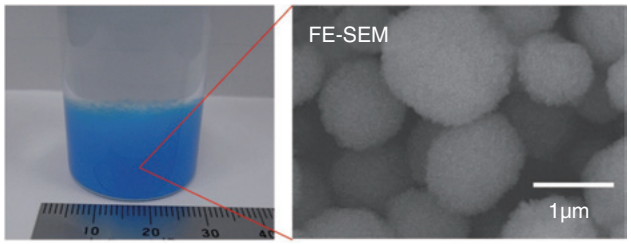


Fig. 6 SEM image of the precipitated aggregate

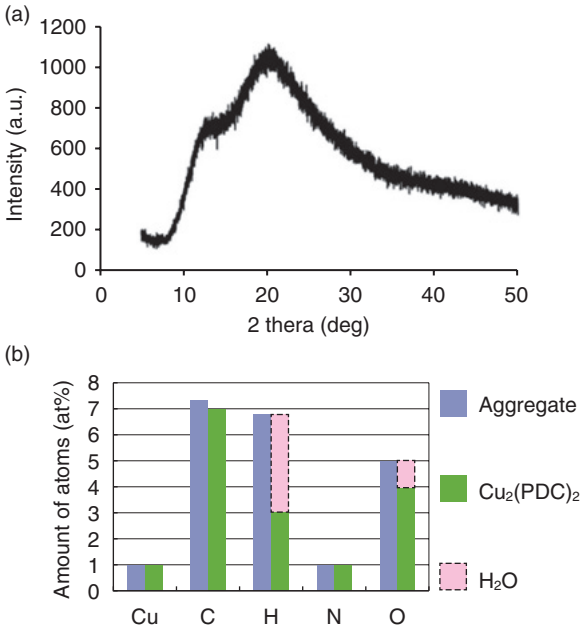


Fig. 7 Analysis results of the precipitated aggregate (a) XPRD spectrum; (b) The results of component analysis.

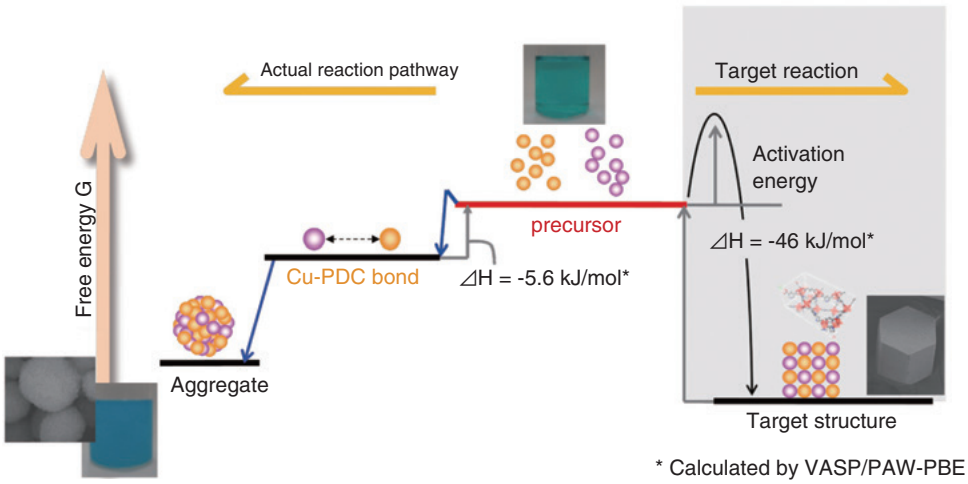


Fig. 8 Reaction pathway and energy diagram of Cu_2PDC_2

predicted that a reaction promoting simple bonds between Cu and PDC (the reaction pathway to the left in Fig. 8) might also occur. However, given the fact that aggregates were formed rather than the target structure, Cu_2PDC_2 (MOF), it was considered that the reaction activation barrier for the formation of Cu_2PDC_2 (MOF) (the reaction pathway to the right in Fig. 8) is higher than the reaction activation barrier for simple bonding between Cu and PDC (the reaction pathway to the left in Fig. 8). It is believed that as a result, the simple bonding reaction between Cu and PDC (the reaction pathway to the left in Fig. 8), for which the reaction activation barrier is lower, occurs preferentially and more rapidly, and aggregates are formed. It was, therefore, necessary to study conditions that would restrict and control the formation of aggregates by simple bonding between Cu and PDC, and promote the target Cu_2PDC_2 (MOF) synthesis reaction (the reaction pathway to the right in Fig. 8). The addition of acids and other auxiliary agents is available as a method of controlling reaction rate. The successful dissolution of aggregates and synthesis of crystalline MOF by competitively promoting a reaction between metal ions and organic ligands has been reported[17]. The acid to be used as an additive was therefore studied from the perspective of its potential for disassembling aggregates (detaching bonds between Cu and PDC) and maintaining the Cu paddle wheel structure.

Figure 9 shows the colors of the solutions produced by adding various acids to the aggregates and spectra for each solution obtained using ultraviolet absorption visible spectroscopy (UV-vis). Like XAFS results, UV-vis spectra reflect the coordination state of metal ions.

In each case, the addition of the acids resulted in the solution becoming clear, and dissolved the Cu-PDC aggregates. For the acetic acid, the fact that no changes could be observed in the UV-vis spectra indicated that the Cu paddle wheel structure was maintained. Given this, acetic acid could be considered an additive that was able to control the speed of bonding of Cu and PDC while maintaining the Cu paddle wheel structure. Based on the results discussed above, copper(II) acetate, PDC acid and acetic acid were selected as starting materials and EtOH, DMF, and DEF were selected as reaction solvents satisfying the conditions indicated in the guidelines for the synthesis of a Cu_2PDC_2 complex. The complex was synthesized by optimal adjustment of proportion, time and temperature in relation to these substances.

3.2. Method of Synthesis

With regard to the solvents, no crystals were precipitated when the candidate EtOH was employed, and crystals of low purity were obtained when DEF was employed. It was, therefore, decided to use DMF as the synthesis solution. The proposed Cu_2PDC_2 complex crystals were obtained by placing DMF (N,N-

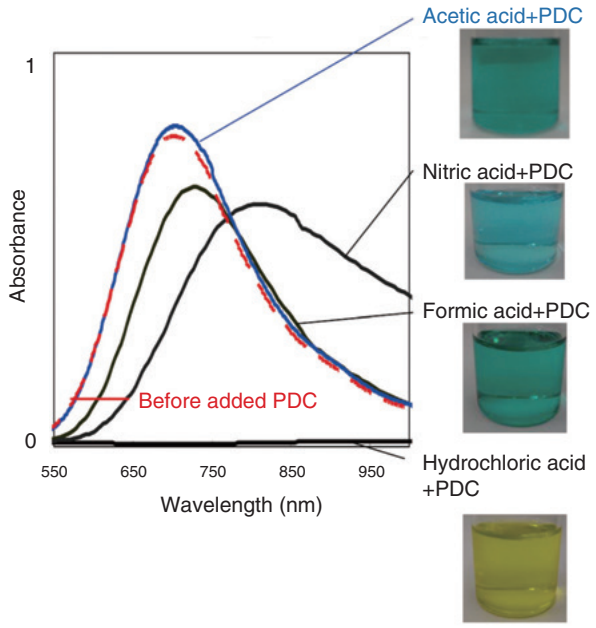


Fig. 9 Pictures and UV-vis spectrums of solution when various acids are added

dimethylformamide; CAS No. 68-12-2) 9.89 ml, copper(II) acetate monohydrate (CAS No. 6046-93-1) 51.3 mg and PDC acid (3,5-pyridinedicarboxylic acid (CAS No. 499-81-0) 85.9 mg in a vial bottle and dissolving them by ultrasound, following which acetic acid (CAS No. 64-19-7) 0.11 ml was added and the substance was stored for a week at 70˚C. Following this, the solvent was repeatedly replaced by $CHCl_3$ (trichloromethane; CAS No. 67-66-3) at room temperature in order to remove guest molecules. The crystals obtained were comparatively uniform, measuring slightly less than 100 μm in the longitudinal direction and around 50 μm in the lateral direction.

3.3. Analysis of Synthesized Material

Figure 10 shows an SEM image of the synthesized Cu_2PDC_2 crystals. These were hexagonal columnar crystals that reflected the $P6_3mc$ symmetry of the basic framework. The results of X-ray powder diffraction (XRPD) using SPring-8 high-brilliance X-rays (Fig. 11) and single crystal analysis[13] verified that the structure of the crystals was identical to that proposed in Fig. 2. In addition, there was an almost complete one-to-one correspondence between the diffraction peaks obtained using XRPD and diffraction peaks that had been optimized by calculations [Fig. 11(b)]. The synthesized Cu_2PDC_2 was, therefore, judged to be of high purity.

The results of a structural defect analysis by means of Rietveld refinement also corresponded well with a projected complete structure with no defects, suggesting that the crystals displayed an extremely low rate of defects[13]. In addition, the same analysis indicated that the difference in intensity between the values measured using XRPD and the calculated diffraction peaks was an effect of residual solvents such as DMF remaining in the pores[13].

The specific surface area of the crystals was measured at 1003 m^2g^{-1} and 1033 m^2g^{-1} by the Brunauer Emmett Teller (BET) method and the Langmuir method, respectively. The median pore size was measured at 8.9 Å by means of the Horvath-Kawazoe method[11), (12] (using a cylinder model). Because the crystal structure is porous, the value for specific surface area is comparatively high, but the figure is low in comparison to already known high specific surface area MOF[7)-(10)]. Pore sizes of 6 Å and 11 Å have been calculated, and the synthesized crystals are considered to display a value intermediate between these. (An application was made to The Cambridge Crystallographic Data Centre for registration of this Cu_2PDC_2 crystal structure, and it has been registered as CCDC 791274.)

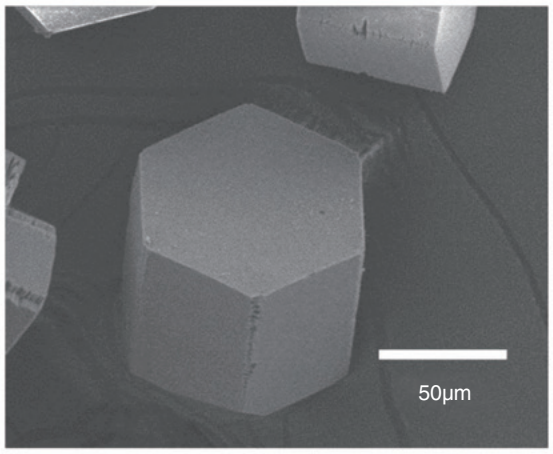


Fig. 10 SEM image of the synthesized Cu_2PDC_2 crystals

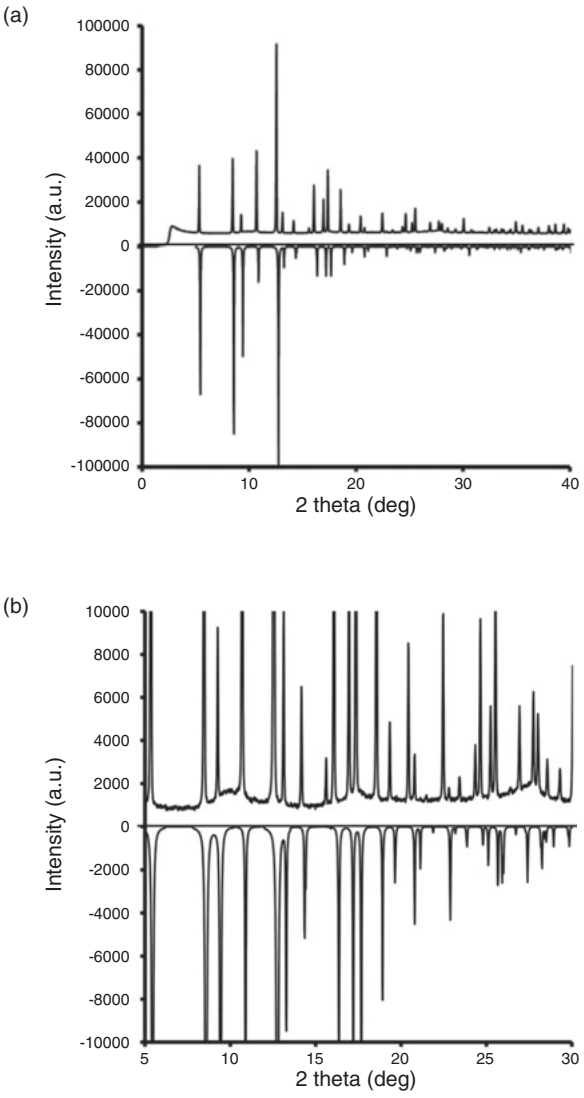


Fig. 11 XPRD spectrum of synthesized Cu_2PDC_2 crystals. (a) (Top) Diffraction pattern measured by SPring-8. (Bottom) Simulated pattern. FWHM = 0.05. λ = 1.54056 Å; (b) Highly magnified image of the low-intensity area of (a). Slight differences in peak positions are caused by differences in the lattice parameters between the actual crystal and a model crystal optimized by an LDA calculation. Measured peaks show a nearly one-to-one correspondence with the simulated peaks.

4. Hydrogen Storage Performance

The material's rate of hydrogen adsorption was measured using a pressure composition temperature (PCT) measurement apparatus. Figures 12(a) and (b) respectively show the amount of adsorbed hydrogen (wt%) at 293 K and the mass of adsorbed hydrogen (g L^{-1}) per crystal unit volume at 293 K. The amount of hydrogen adsorbed increased with increase in the pressure of the hydrogen, and was 0.77 wt% at 8.92 MPa [Fig. 12(a)]. This is a higher rate of hydrogen adsorption than IRMOF-1 (the broken line in Fig. 12), and is believed to demonstrate the validity of the design guidelines proposed by the authors. In addition, the figure of 8.66 g L^{-1} for the mass of adsorbed hydrogen per crystal unit volume at 8.92 MPa is approximately twice the figure for IRMOF-1 [Fig. 12(b)]. This is an extremely high figure for a physisorption material. In particular in the case of application in a vehicle, a high hydrogen volumetric adsorption density is able to contribute significantly to the reduction of tank volume.

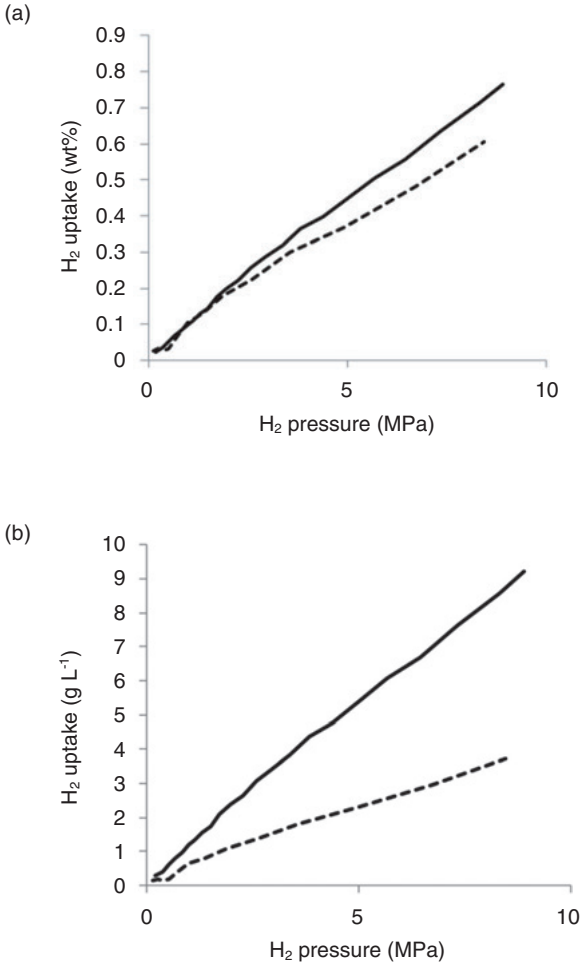


Fig. 12 Hydrogen uptake properties of synthesized Cu_2PDC_2. (a) Gravimetric uptake at 293 K, 10 MPa; (b) Volumetric uptake at 293 K, 10 MPa. Values for IRMOF-1 are shown for comparison (dashed line).

The Cu_2PDC_2 adsorption energy, calculated using a van't Hoff plot of adsorption isothermal curves at various temperatures, was 6.0 kJ mol^{-1}. This figure is approximately 1 kJ mol^{-1} higher than IRMOF-1 (Table 2). This adsorption energy figure is lower than the figure projected at the initial stage of design, but the qualitative tendency for an increase over the figure for IRMOF-1 accords with the aims established for the project.

It is believed that the factors which helped to enable the material to achieve a figure approximately twice that of IRMOF-1 for amount of adsorbed hydrogen [Fig. 12(b)] despite its specific surface area of around 1000 m^2 g^{-1} were the fact that it possesses twice the adsorption sites per unit volume, its high adsorption energy, and its effective combination of small and large pores.

5. Conclusion

The research discussed in this paper attempted to design and synthesize a hydrogen-adsorbing material optimized for use in a fuel cell electric vehicle. Despite having a specific surface area of around 1000 m^2 g^{-1}, the synthesized Cu_2PDC_2 complex achieved a figure of 8.66 g L^{-1} for maximum mass of adsorbed hydrogen, approximately twice the figure for IRMOF-1. The realization of an increased number of adsorption sites per unit volume and increased adsorption energy, in addition to a design focus on the shape of the pores, are considered to be the factors that contributed to this result. The authors believe that a focus on the micro- and nano-levels using sophisticated analytic techniques and the prediction of properties by means of computational science represent useful tools in the study of the structure of hydrogen storage materials and their design.

References

(1) Yuan, D., Zhao, D., Sun, D., Zhou, H.: An Isoreticular Series of Metal-Organic Frameworks with Dendritic Hexacarboxylate Ligands and Exceptionally High Gas-Uptake Capacity, Angew. Chem. Int. Ed., 49, p. 5357-5361 (2010)

(2) Rowsell, J. L. C., Yaghi, O. M.: Strategies for Hydrogen Storage in Metal-Organic Frameworks, Angew. Chem. Int. Ed., 44, p. 4670-4679 (2005)

(3) Eddaoudi, M., Kim, J., Rosi, N., Vodak, D., Wachter, J., O'Keeffe, M., Yaghi, O. M.: Systematic Design of Pore Size and Functionality in Isoreticular MOFs and Their Application in Methane Storage, Science, 295, p. 469-472 (2002) and Supporting Information

(4) Kanoya, I., Furuta, T., Sakamoto, R., Hosoe, M., Ichikawa, M., Itoh, K., Fukunaga, T.: Anomalous Aggregation State of Deuterium Molecules in the Nanoscale Pores of a Metal Organic Framework, J. Appl. Phys., 108, p. 074310 (2010)

(5) Kohn, W., Sham, L. J.: Self-Consistent Equations Including Exchange and Correlation Effects, Phys.

Rev., 140, p. A1133-A1138 (1965)
(6) The calculation has been performed using the ab-initio total-energy and molecular dynamics program VASP (Vienna ab-inito simulation program) developed at the Institut fur Material-physik of the Universitat Wien.
(7) Rowsell, J. L. C., Millward, A. R., Park, K. S., Yaghi, O. M.: Hydrogen Sorption in Functionalized Metal-Organic Frameworks, J. Am. Chem. Soc., 126, p. 5666-5667 (2004)
(8) Rowsell, J. L. C., Yaghi, O. M.: Effects of Functionalization, Catenation, and Variation of the Metal Oxide and Organic Linking Units on the Low-Pressure Hydrogen Adsorption Properties of Metal-Organic Frameworks, J. Am. Chem. Soc., 128, p. 1304-1315 (2006)
(9) Ferey, G., Mellot-Draznieks, C., Serre, C., Millange, F., Dutour, J., Surble, S., Margiolaki, I.: A Chromium Terephthalate-Based Solid with Unusually Large Pore Volumes and Surface Area, Science, 309, p. 2040-2042 (2005)
(10) Ma, S., Sun, D., Ambrogio, M., Fillinger, J. A., Parkin, S., Zhou, H.-C.: Framework-Catenation Isomerism in Metal-Organic Frameworks and Its Impact on Hydrogen Uptake, J. Am. Chem. Soc., 129, p. 1858-1859 (2007)
(11) Horvath, G., Kawazoe, K.: Method for the Calculation of Effective Pore Size Distribution in Molecular Sieve Carbon, J. Chem. Eng. Jpn., 16, p. 470-475 (1983)
(12) Dombrowski, R.J., Lastoskie, C.M., Hyduke, D.R.: The Horvath-Kawazoe Method Revisited, Colloids Surf., 187-188, p. 23-39 (2001)
(13) Furuta, T., Kanoya, I., Sakai, H., Hosoe, M.: Design of Improved Metal-Organic Framework (MOF) H_2 Adsorbents, Polymers, 3, p. 2133-2141 (2011) and Supporting Information
(14) URL: http://www.spring8.or.jp/
(15) Kato, M., Jonassen, H. B., Fanning, J. C.: COPPER(II) COMPLEXES WITH SUBNORMAL MAGNETIC MOMENTS, Chem. Rev., 64, p. 99-128 (1964)
(16) Dupont, L., Guillon, E., Bouanda, J., Dumonceau, J., Aplincourt, M.: SPECTROSCOPIC STUDY OF COPPER (II)-WHEAT STRAW CELL WALL RESIDUE SURFACE COMPLEX, Environ. Sci. Technol., 36, p. 5062-5066 (2002)
(17) Mori, W., Matsunaga, S.: Discovery and Development of Porous Metal Carboxylatess, Science Journal of Kanagawa University, 20 (2), p. 271-274 (2009)
(18) Kresse, G., Furthmuller, J.: Efficient Iterative Schemes for ab Initio Total-Energy Calculations Using a Plane-Wave Basis Set, Phys. Rev. B, 54, p. 11169-11186 (1996)
(19) Kresse, G., Joubert, D.: From Ultrasoft Pseudopotentials to the Projector Augmented-Wave Method, Phys. Rev. B, 59, p. 1758-1775 (1999)

Author


Terumi FURUTA


Mitsuya HOSOE


Izuru KANOYA


Hiroshi SAKAI

Analysis on Mechanism of Early Clogging in Suction Filter with Use of Ethanol Blended Fuel and Development of Long-life Filter

Shingo ARAI* Atsushi ITO* Tsubasa ISHII*
Hideaki ANDO* Keita KINOSHITA* Fujio UMEBAYASHI*

ABSTRACT

The authors have developed a long-life suction filter to cope with fuels containing ethanol. In the fuel system of small motorcycles, the suction filter protects parts such as the fuel pump, injector, pressure regulator, etc. from dusts in the fuel. It is known that in conventional suction filters, when compared with neat gasoline, the filter life is shorter by 50% if it is used with a fuel containing 25% ethanol. In addition to the study on the correlation between the ethanol concentration and the dust dispersion in the fuel, our study has clarified how the early clogging occurs, i.e., the dusts dispersed in the ethanol-containing fuel coagulate again when passing though the multi-layered suction filter, and trapped predominantly by the lower-most layer having the finest mesh-size. Considering that the cause of dust coagulation is the flow field that occurs in the filter layer, the coagulation acceleration layer that accelerates coagulation by creating flow fields, placed in the upper layer, has been added in the newly developed long life filter. The new filter permits trapping of dusts in the coarse upper layer of the multi-layered filter, preventing concentration of trapping in the fine, lower-most layer, thus doubling the filter life when compared to the conventional filter.

1. Introduction

Having the global environmental issues, soaring crude oil price, demands for freeing from petro-fuel dependence, etc. in the backgrounds, the sales of automotive fuel of ethanol blended gasoline are increasing worldwide in these days. It is highly likely that the areas where ethanol blended fuels are predominantly used will spread wider in the future. Under such circumstances, there has been such an issue that, in the fuel system of small motorcycles, the suction filter, which is located in the suction side of the fuel pump, becomes clogged in earlier stages when it is used with ethanol blended fuels. The clogging of suction filter may cause immediate effects on deteriorations of engine performances of the motorcycles. In view of that, short service cycle intervals are determined for the filter changes when ethanol blended fuels are used, and the periodical replacements are conducted at the service shops accordingly. However, from the customers' standpoint, in relation to the reduction of running cost, a long-life filter to cope with ethanol blended fuels has been called for.

We therefore analyzed how the early clogging of the filter occurred when the ethanol blended fuel was used, and targeted at the development of a long-life suction filter having a service life which was the same as or longer than the life of a conventional filter used with neat gasoline even when the ethanol blended fuel was used.

2. Overview of Fuel System in Small Motorcycles

Explained in this chapter is the fuel system of a small motorcycle. As Fig. 1 shows, a suction filter is incorporated in the fuel system in a small motorcycle to protect parts such as a fuel pump, an injector, a pressure regulator, etc. from damages caused by the dust contained in the fuel. Most of small motorcycles adopt the fuel system with only the suction side filter without the main filter, considering the benefits of cost reduction and small design, as shown in Fig. 2. However, as the system doesn't have the main filter, early clogging of the suction side filter becomes a concern.

With this type of system for small motorcycles, when the suction filter becomes clogged, the pressure loss between the filter and the fuel pump increases and may

* Motorcycle R&D Center

negatively affect the engine performances. Therefore, the suction filter should have the characteristics of trapping the large amount of dust yet not getting clogged in early stages. As Fig. 3 shows, the suction filter has the construction to trap dust particles of various sizes by each layer of laminated unwoven cloths having different mesh sizes. Note that the term "filter" used in this paper hereafter refers to the fuel suction filter having this multi-layered construction.

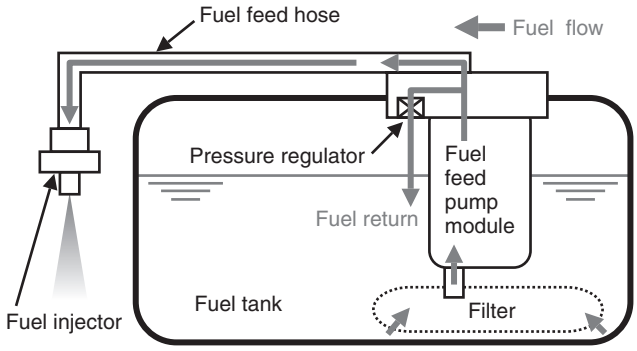


Fig. 1 Structure of fuel supply system on small motorcycles

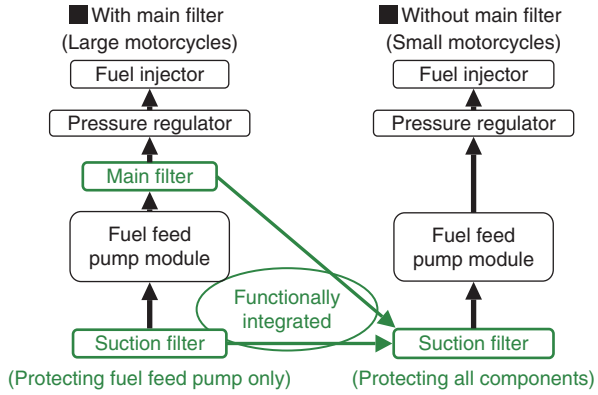


Fig. 2 Schematic diagram of fuel supply system for small motorcycles

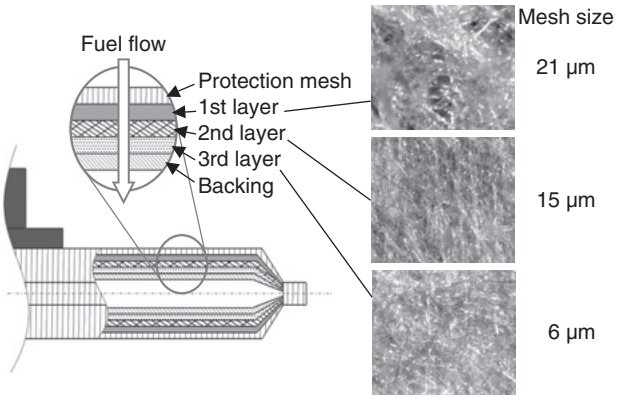


Fig. 3 Typical structure of multi-layered nonwoven fabric filter

3. Early Clogging of Suction Filter Caused by Ethanol Blended Fuel and Associated Issues

As Fig. 4 shows, it was confirmed that the filter, which was free of problem when used with gasoline, became clogged in shorter time when used with the gasoline containing 25% of ethanol (hereafter referred to as "E25"), and the filter replacement interval was halved. Figure 5 shows how the early clogged filter looks. It was revealed that dust was predominantly trapped in the finest (6 μm) layer of the unwoven cloths. With this result, we turned our attention to the differences in the degrees of the dust dispersion depending on the ethanol content. Figure 6 shows conditions of the dust when it is put in E25 and neat gasoline. As we can see from the figure, the dust in ethanol blended fuel is dispersed without forming lumps while the dust in neat gasoline settles in large-grain conditions.

Based on the facts described above, we assumed that early clogging would occur because of the concentration of trapped dust on a single layer of the fuel filter with its tendency to be dispersed in ethanol blended fuels. With this

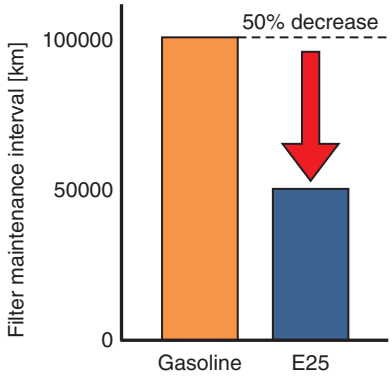


Fig. 4 Filter maintenance interval

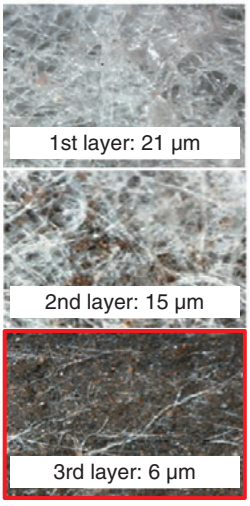


Fig. 5 States of filters in E25

assumption, we decided to put our research focus on the following three key points.

(1) To clarify the relationship between the ethanol concentration and the dust dispersion in the fuel
(2) To clarify the impacts of dust dispersion in the fuel to the clogging of a filter and its mechanism
(3) To develop a long-life fuel filter that can cope with ethanol blended fuels

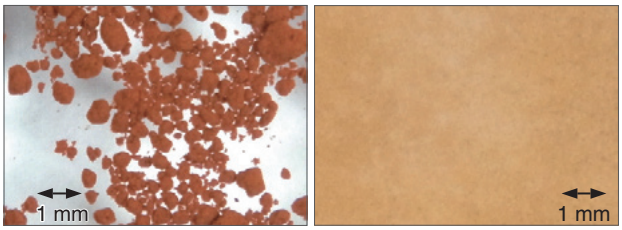


Fig. 6 Comparison of state of dispersion of dust particles in fuel

4. Clarify Relationship between Ethanol Concentration and Dust Dispersion in Fuel

To evaluate the states of dispersion and the coagulation of dust in the fuel for analyzing how they occur, it was necessary to quantify the conditions of dispersion and the status of coagulation. In this chapter, we introduce the physical nature of dust in the fuel, the dispersion assessment method, and how dust disperses.

4.1. Dusts in Fuel

Fuels for automotive applications contain a large amount of fine dust. 40000 to 300000 dust particles larger than 1 μm are contained in 1 ml while the amount varies from region to region. Figure 7 shows distribution of cumulative particle size (particle count basis, average of various countries). 99% of dust in fuel is smaller than 5 μm, which is smaller than the finest mesh size of the filter layer. The fine dust smaller than 10 μm is classified in the particle category referred to as "colloidal dispersion system," which is characterized by the property of being less affected by the gravity and/or the buoyancy in a liquid and staying in the liquid phase. In addition to that, 50% to 80% of the dust in fuel is composed of three compounds, i.e., SiO_2, Fe_2O_3, and Al_2O_3, which are the components of general soil and are blown up in the air by wind, etc., to creep into the fuel in the process of transportation or while filling the fuel.

4.2. Conditions of Dust Dispersed in Fuel

The conditions of dust dispersed in the fuel can be measured with the particle size analyzer utilizing laser diffraction scattering method. Figure 8 shows results of measurements conducted for each ethanol concentration with identical test powders of JIS Class 8 mixed in the fuels with the same concentration. The median diameter indicated in the result of measurements is the value that defines the condition of the dust dispersion, where the dust count based method was employed for the measurement. When the median diameter D50% is 0.6, it is defined that 50% of dust particles in the solution is of a diameter smaller than 0.6 μm. It can be remarked that the smaller the number, the more the dust is dispersed. It was understood from the results of measurements that the median diameter of dust became smaller as the ethanol concentration in the gasoline increased, and when ethanol was 100%, the median diameter was approximately 1/4 compared to neat gasoline. It was therefore understood that the dust in the fuel dispersed more along with an increase of ethanol content.

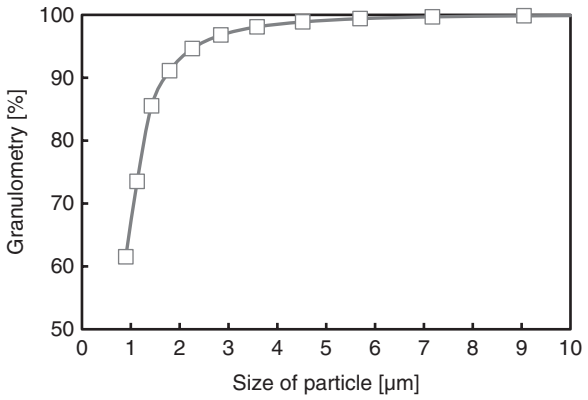


Fig. 7 Cumulative particle size distribution of average dust particles in fuel in major countries (Particle count basis)

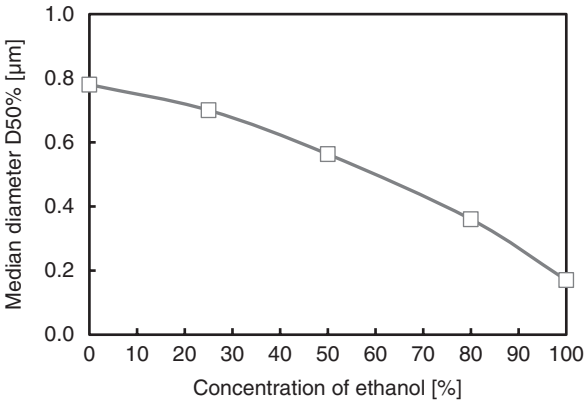


Fig. 8 Ethanol concentration in gasoline and median diameter of dust particles contained in fuel

5. Impacts of Dispersion of Dusts in Fuel on Clogging of Filter and How Clogging Occurs

To clarify the impacts of dust dispersion on the filter life by using actual motorcycle, it requires the corresponding

operational test of 100000 km. Therefore, it is practical to conduct unit test for evaluating the life of filter. Here, we introduce the filter life assessment method and the acquired results.

5.1. Introduction of Unit Test Device

Figure 9 shows overview of the filter life test device we used in the experiments. As shown, the suction filter was immersed in the test fuel, while the fuel pump was operated. And the dust of JIS Class 8 was put in as a test powder at a constant interval. As the dust clogged in the suction filter, the pressure difference between the filter and the fuel pump (filter pressure loss) increased. We assessed filter life from the amount of dust thrown into the fuel when the pressure loss exceeded 30 kPa. Hereafter the filter pressure loss is referred to as “pressure loss”.

5.2. Correlation between Filter Life and Ethanol Concentration

Figure 10 shows combined data of the filter life at each ethanol concentration measured by the test device shown in Fig. 9 and the results of median diameter D50% for different concentrations of ethanol. It was clarified that the more the dust in the fuel was dispersed, the shorter the filter life became.

Moreover, the suction filter, used in the unit test with E25 and clogged in early stage, was disassembled and the condition was checked to see captured dust in each layer. Through the tests, it was found that, as Fig. 11 shows, the dust was trapped predominantly in the finest 6 µm layer just like when the filter clogging occurred in the actual usage.

As mentioned in Chapter 5, more than 99% of dust was composed of particles smaller than 5 µm, which was smaller than the minimum mesh size of filter. We turned our eyes to why dust was predominantly trapped in the 6 µm mesh size layer, which should allow the dust particles to pass through, nevertheless.

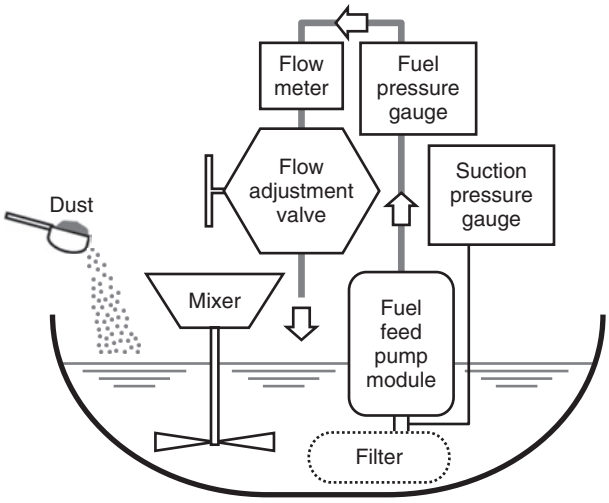


Fig. 9 Schematic view of filter test

In an attempt to clarify how the dust particles smaller than the filter mesh were trapped, we prepared the filter having only a single finest layer (6 µm) and the three-layered filter, which has the same specifications as mass production products, and conducted filter life tests using E25 fuel. Figure 12 shows the relationship between the amount of

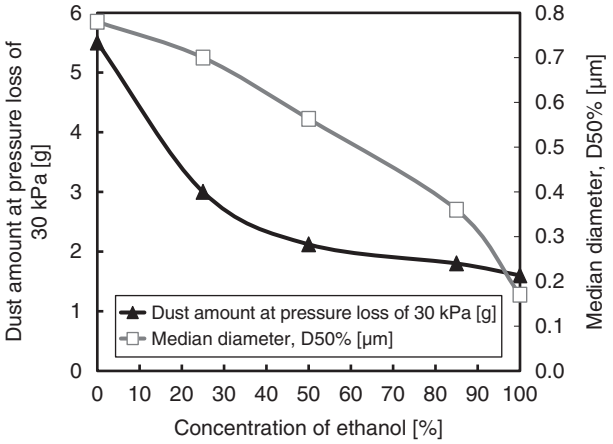


Fig. 10 Relationship between amount of dust particles and median diameter, D50%

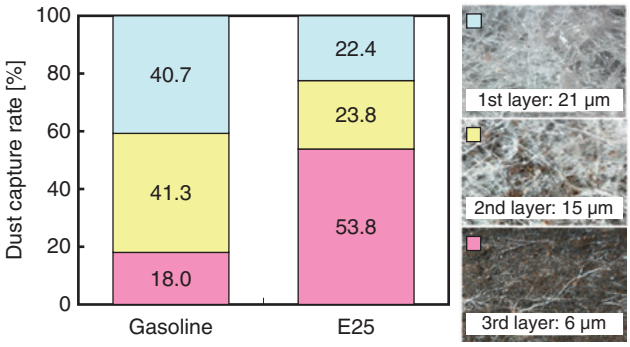


Fig. 11 Comparison of capture efficiency of filter in gasoline and E25

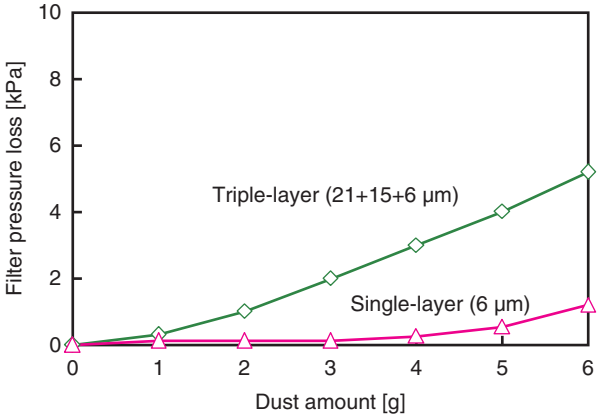


Fig. 12 Pressure loss for different filter structures

dust mixed into the fuel and the filter pressure loss for each type of filter. From the results, the filter life was shorter in the multi-layered filter than the single-layer filter. The pressure loss was increased by only approximately 1.0 kPa with the single-layer filter even after mixing 6 grams of dust. The reason was considered as the dust smaller than 5 μm, which was accounted for more than 90% of total dust in the fuel, passed through the filtering layer. Meanwhile, in the multi-layered construction, the dust that should have passed were trapped. We supposed some phenomenon occurred and the dust coagulated when passing through the filtering layers of the multi-layered construction and predominantly trapped in the lowermost finest layer. We therefore switched our attention onto the dynamics that work on the dust in the fuel, which is of colloidal dispersion.

5.3. Force That Affects Colloidal Particles in Liquid

In the colloidal chemistry, it is commonly known that the dispersion and the coagulation of colloidal particles are considered based on the balance between the repulsive force and the attractive force among the particles. The typical force that disperses colloidal particles is the repulsive force caused by electrostatic repulsive forces. Figure 13 shows the manner of repulsion of colloidal particles caused by the electrostatic repulsive force. Electrostatic repulsion forces are generated between colloidal particles which have the layer of the same polarity of ions formed by the pairs of opposite ions adhering on the surface of the colloidal particles.

On the other hand, regarding the force to coagulate colloids, the van der Waals force (or van der Waals interaction) works. Figure 14 shows the manner the coagulation of colloidal particles due to the van der Waals force. The van der Waals force works, just like when it works on atoms or other molecules, as an attractive force on the colloidal particles with the intensity inversely proportional to the sixth power of the distance between particles.

With expressing the electrostatic repulsive force (repelling force) as V_R, and the van der Waals force (attractive force) as V_A, here we call the combined force of these two forces as "total potential" (V_{total}). The dispersion and the coagulation of colloidal particles are determined by the total potential. That is what they call DLVO (Derjaguin-Landau-Verwey-Overveek) principle[1].

Figure 15 shows the relationship between the repulsive force, attractive force and V_{total} which are working on particles, in relation to the distance between particles. As the distance between particles shortens, the impacts of electrostatic repulsive force increase, causing the particles to repel each other. However, as the van der Waals force has such a nature that the force is inversely-proportional to the sixth power of the distance between particles, it is considered that when the particle-to-particle distance further shortens and becomes less than approximately 5 nm, the V_{total} turns to the side of attractive force[1]. Accordingly, in the situations in which collisions or contacts of particles occur, the distance between particles is shortened enough to make the V_{total} change to an attractive force, causing the particles to coagulate as a result[4].

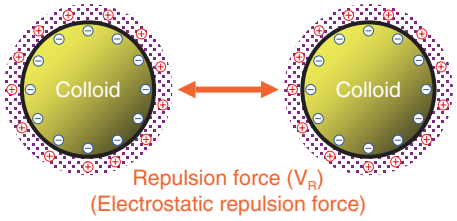


Fig. 13 Schematic representation of electrostatic repulsion force

5.4. Polarity of Solution and Dispersion and Coagulation of Colloidal Particles

The electrostatic repulsive force is significantly affected by the ion concentration in the solution. It is one of the known facts in the particle technology that the effect of ions on colloidal particles varies depending on the polarity of the solvent, because ions are situated in the status of being dissolved in water. The gasoline is a non-polar solvent

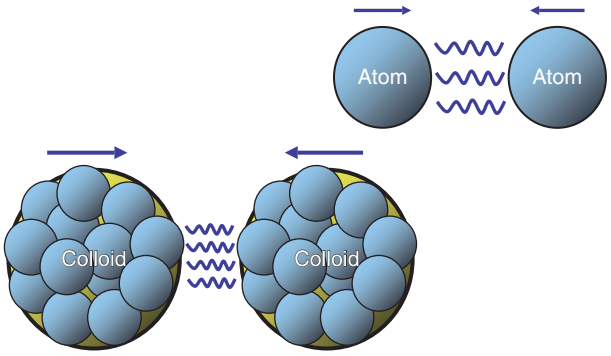


Fig. 14 Schematic representation of van der Waals force

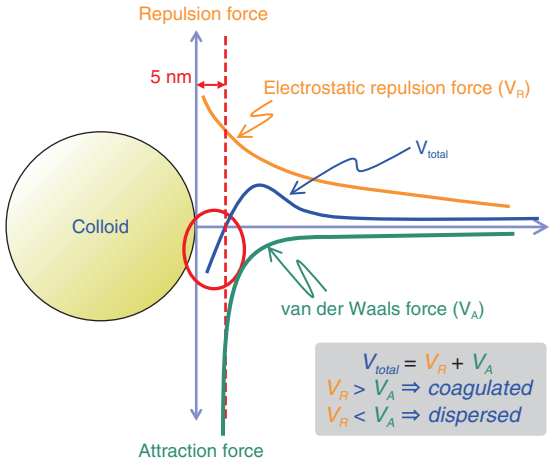


Fig. 15 Interactive action of repulsion and attraction forces and DLVO theory

and a hydrophobic solution having very low water content in the liquid. In the gasoline containing little water, only few ions adheres on the surfaces of colloidal particles as shown in Fig. 16[1]. Accordingly, the electrostatic repulsive force becomes weak, and the van der Waals force becomes predominant, allowing easy coagulation of colloidal particles.

On the other hand, it is known that ethanol is a solvent with polarity being able to be mixed with both water and gasoline, and ethanol molecules adhere on the surface of colloidal particles in radial direction pivoted by the hydrophilic groups which have absorbed molecules of water[2]. Figure 17 shows the manner of the said phenomenon. As the absorbing layer created by ethanol molecules becomes a cause of repelling force and blocks coagulation of colloidal particles with each other resulting in having the tendency of dispersion[2]. Consequently, as the ethanol concentration lowers, the influence of absorbing layer by the ethanol molecules adhered on the surface of colloids becomes weak, allowing easy coagulation of dust particles with each other.

5.5. How Clogging Occurs in Multi-layered Filter

According to the DLVO principle, it is necessary to reduce the distance between the particles to let the dispersed dust particles coagulate. To reduce the distance between dust particles in a liquid, a flow field, where a velocity gradient occurs in the flow speed, is necessary. The occurrence of a flow field can be seen in a simple flow structure such as in a cylinder. As the flow velocity in a cylinder differs on the cylinder wall and in the center, the flow field becomes uneven having a velocity gradient. Due to the close encounters of the dust particles with various velocities due to the flow field, a coagulating force works on the colloids in the liquid[4]. Figure 18 shows the manner the said phenomenon occurs. Similarly, the uneven flow field occurs everywhere in the filtering layer composed of unwoven cloth as Fig. 19 shows. Accordingly, it is presumed that the dust particles collide with each other repeatedly when passing through the filter fabric, causing progression of coagulation.

Figure 20 is an image picture of the manner the dust is trapped by the filter in the gasoline and in E25 fuel. In the gasoline, the dust in the fuel is under coagulated conditions to some extent, and is trapped even in the coarse upper layers. As the dust can be trapped gradationally by each layer depending on the dust size, the dust does not concentrate on a specific layer, allowing effective use of the multi-layered construction. Meanwhile in E25, the dust particles under the dispersed conditions travel in the filtering layers experiencing the congregation due to the flow fields inside of the filter when passing through the filter, and as a result, predominantly trapped by the finest layer in the lowermost layer. That's how the difference occurs in the filter lives between the situations in gasoline and in ethanol blended fuel.

From the findings above, the processes causing premature clogging when using ethanol blended fuel can be summarized into the following three factors.

(1) Dust is under dispersed conditions in the fuel.
(2) Dust coagulates when passing through the filter.
(3) Trapping concentrates in the lowermost fine layer.

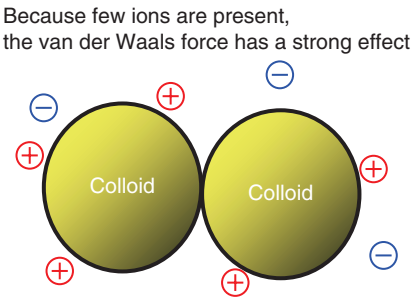


Fig. 16 Mechanism of coagulation in gasoline

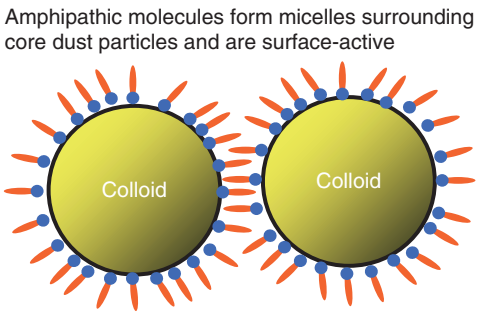


Fig. 17 Mechanism of dispersion in ethanol blended fuel

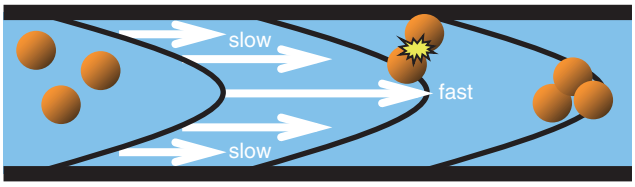


Fig. 18 Schematic representation of flow fields in cylinder

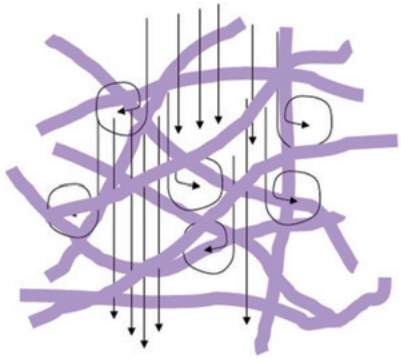


Fig. 19 Schematic representation of flow fields in suction filter

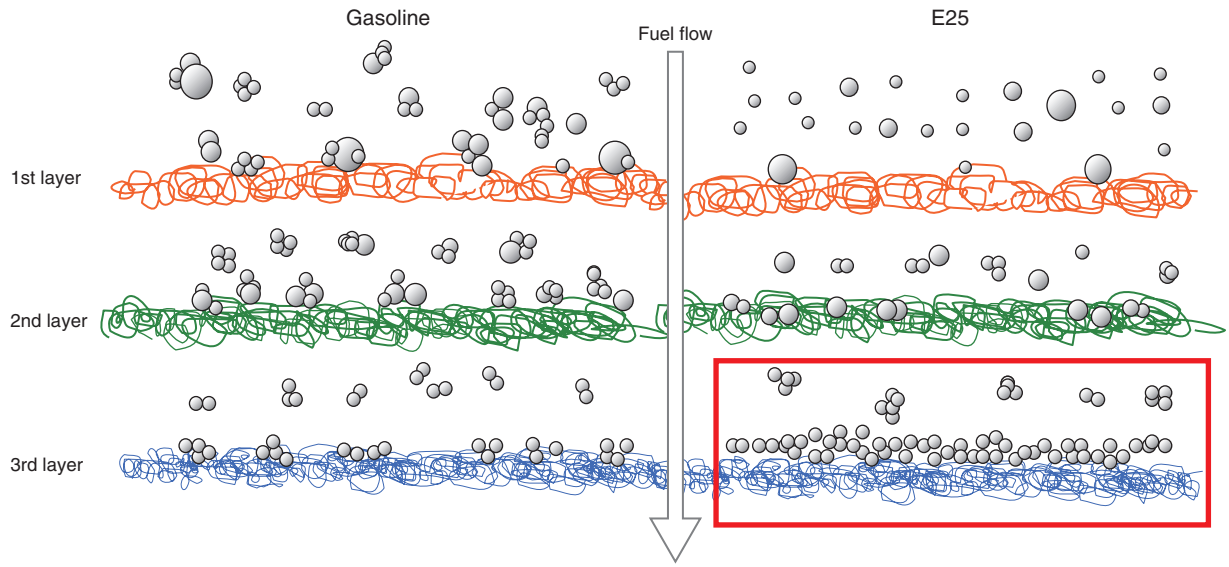


Fig. 20 Schematic representation of dust capture by the filter

6. Consideration of Long-life Filter That Copes with Ethanol Blended Fuel

6.1. Consideration of Coagulation Acceleration Layer

The cause of shorter filter life was the concentration of the dust in the finest filter layer at the lowermost position which hampered the effective use of filters in the upper layers. Keeping that in mind and to positively take advantage of the phenomenon that dust coagulate when passing through the filter, a spongy layer was added on the upper layer of filter. This layer was placed to accelerate the coagulation process to some extent before the dust reached the filtering layers. Figure 21 illustrates how it works. This layer was named as "coagulation acceleration layer". By adding the said layer it is aimed to extend its service life without making extensive modifications to the filter configuration currently existing.

6.2. Decision of Specs of Coagulation Acceleration Layer

The aim of coagulation acceleration layer was to create flow fields which make the dispersed dust particles collide with each other to have them coagulated. Accordingly, the coagulation acceleration layer itself is not aiming at trapping of the dust. Figure 22 is the schematic drawing of the coagulation acceleration layer. The holes in the acceleration layer create flow fields. The size of the holes affects the intensity of the flow fields, and the thickness of the coagulation acceleration layer influences the length of time the dust stays in the flow field.

In the attempt to select the specification that maximized the life extension effects, we considered two parameters, i.e., the thickness of the layer and the diameter of the holes. We assessed the coagulation effects from the standpoint of

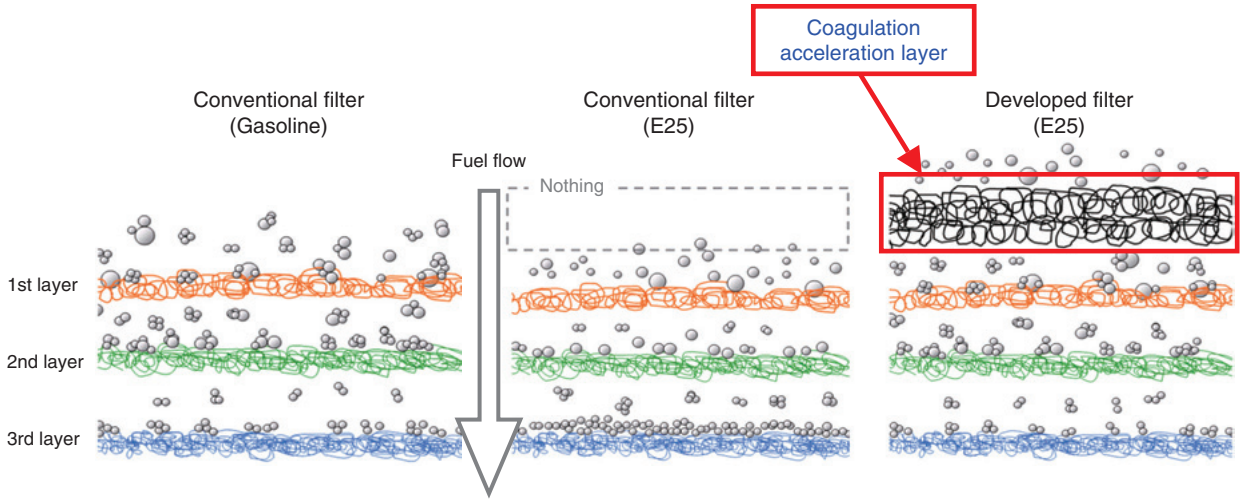
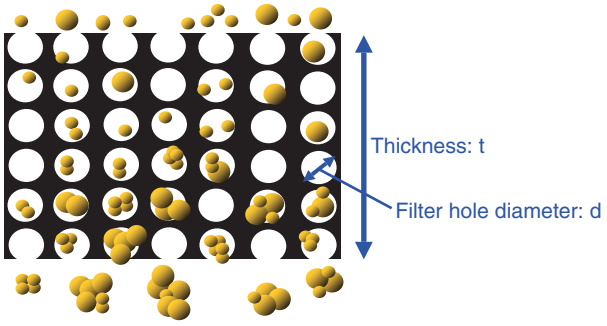


Fig. 21 Schematic representation of effect of coagulation acceleration layer

the average number of holes in the unwoven cloth through which the dust particles passed through for the entire thickness of the layer. Here, the thickness of accelerator layer divided by the average diameter of holes was defined as "mean hole number of dust passage."

Figure 23 shows the results of studies on the optimum design of coagulation acceleration construction using the index of the mean hole number of dust passage, as mentioned above. It was understood, from the relationship between the mean hole number of dust passage and the amount of the dust when the pressure loss reached to 30 kPa, that the effectiveness became the highest when the mean hole number got somewhere around 30.



Mean number of holes that a dust particle passes while it goes through the filter layer (coagulation acceleration layer) = t (Thickness) / d (Average filter hole diameter)

Fig. 22 Schematic representation of coagulation acceleration layer

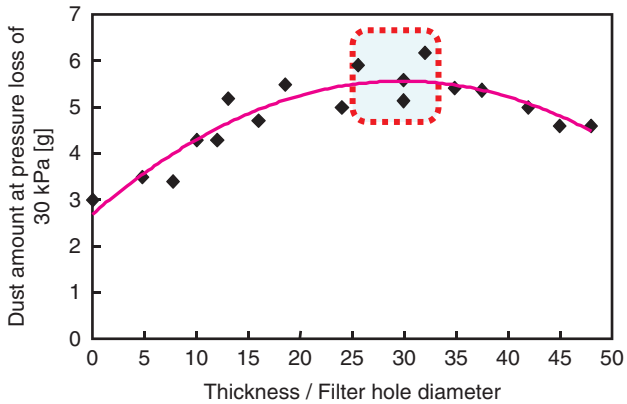


Fig. 23 Relationship between conditional parameters of coagulation acceleration layer and dust amount at predetermined pressure loss

7. Validation

Taking into consideration the test results shown in Fig. 23, we developed the new filter with the coagulation acceleration layer having mean hole number of 30 (Fig. 26), and compared the filter life with the conventional filter using E25 fuel. Fig. 24 shows the results of the validation tests. The new filter doubled the service life of a conventional filter without increasing the filters' surface area. Concerning the dust trapping composition of each filtering layer, the equivalent level of composition at each layer for dust trap, as with gasoline, was attained as shown in Fig. 25 without causing concentration in the lowermost layer.

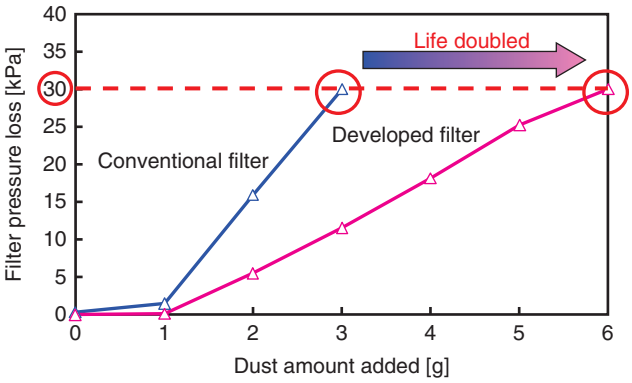


Fig. 24 Comparison of pressure loss between developed filter and conventional filter

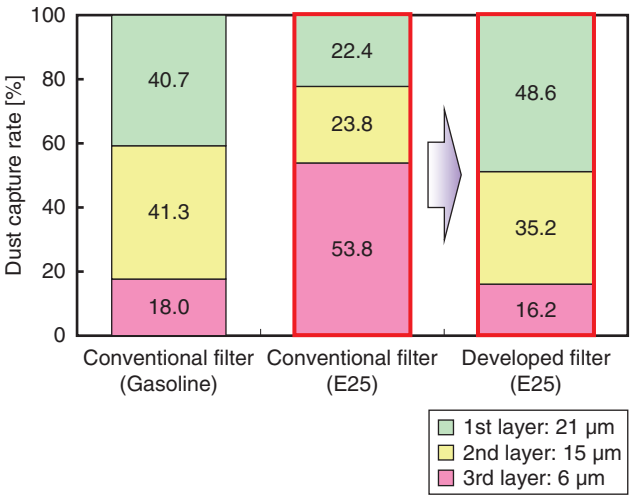


Fig. 25 Comparison of filter capture efficiency

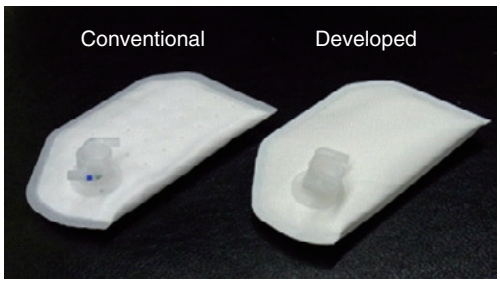


Fig. 26 External view of newly developed filter

8. Conclusion

We clarified the mechanism of how the early clogging of the filter with use of ethanol blended fuel occurs, and we developed the long-life suction filter that can cope with market demands on filter life where ethanol blended fuel was mainly used. The following process of early clogging was defined;

(1) In alcohol fuel, dust disperses, and coagulates when passing through the filter having a multi-layered construction.
(2) The coagulated dust is trapped predominantly by the fine bottom layer, reducing the service life of the filter.

We have developed the new filter with a coagulation acceleration layer added at the uppermost layer based on the findings mentioned above, thus doubling the service life while maintaining the same size of the filter.

Reference

(1) Naoyuki Ishida, Ko Higashitani, Yasuo Mori: "Publication of Society of Particle Technology of Japan: Dispersion of particles in liquid phase·coagulation and separation operations, Chapter 1" Nikkan Kogyo Shinbun p.10-43(2010)
(2) Shinto, H, M. Miyahara and K. Higashitani: "Interaction forces between colloidal particles in alcohol-water mixtures evaluated by simple model simulations", Langmuir, 16, 3361-3371 (2000)
(3) Higashitani, K. and Y. Matsuno: "Rapid Brownian coagulation of colloidal dispersions", J. Chem. Eng. Japan, Vol. 12, pp.460-465 (1979)
(4) Higashitani, K, S. Miyafusa, T. Matsuda, and Y. Matsuno: "Axial change of total particle concentration in Poiseuille flow", J. Colloid Interface Sci., Vol. 77, pp. 21-28 (1980)

■ Author ■


Shingo ARAI


Atsushi ITO


Tsubasa ISHII


Hideaki ANDO


Keita KINOSHITA


Fujio UMEBAYASHI

Development of Real-time Aerodynamic Design System

Takahiro FUKUSHIGE* Tokitomo ARIYOSHI* Yusuke UDA*
Yuki OKUMA* Tatsuya OKABE* Koichi YAMAMOTO**
Lars GRAENING*** Stefan MENZEL*** Markus OLHOFER***

ABSTRACT

A real-time aerodynamic design system has been developed. The new system makes possible real-time computation of the aerodynamic performance and shape sensitivity of passenger cars. The system is made up of technological elements including approximation modeling, categorizing, extraction of feature values, sensitivity analysis and automatic database update. It realizes real-time computation of aerodynamic performance through the combination of approximation modeling and categorizing technologies, computation of shape sensitivity by means of on-line sensitivity calculations, and continuous increase in accuracy by means of automatic learning.

Computational results for Computational Fluid Dynamics (CFD) and the real-time aerodynamic design system were compared in order to evaluate the performance of the system, verifying its effectiveness and ability to reduce computation time.

1. Introduction

The demand for enhanced automotive fuel efficiency has conspicuously increased the importance of reducing air resistance. Achieving a balance between aerodynamic performance and an attractive exterior form, a factor that has a considerable effect on commercial appeal, is therefore an issue.

Recently, wind tunnel experiments and CFD are used to evaluate aerodynamic performance. Wind tunnel experiments necessitate extensive investments of time and funds, for the construction of the facilities, the production of body models, and so on. By contrast with wind tunnel experiments, CFD does not require large-scale facilities. In addition, dramatic increases in computer speed have reduced computation time, bringing CFD to the stage of practical use as a design tool. Significant reductions in the person-hours spent on preparation for computation, realized through advancement of the algorithms for the generation of computational grids, has greatly increased expectations on CFD as a method of evaluation of aerodynamic performance in the initial stages of automotive body design. These initial stages of the body design process are characterized by a significant amount of change in the shape of the body and a large number of trials, and there is a strong need to reduce computation time. Because CFD linearizes and solves nonlinear conservation of mass, momentum and energy equations, the governing equations of fluid phenomena, using computational grids formed in space, an increase in the number of computational grids also increases computation time. At present, even when the latest parallel processors are employed, CFD computation of a grid resolution adequate for the reproduction of the aerodynamic performance of a vehicle body takes several hours. In addition, the results of CFD computations are physical quantities such as flow velocity and pressure, and the challenge represented by the process of deciding on guidelines for understanding the phenomena and modifying performance based on these results can be pointed to as an issue other than computation time presented by the method.

In an attempt to resolve these issues, a real-time aerodynamic design system has been developed with statistical approximation models based on machine learning (“approximation models” below) and online sensitivity analysis as the main element technologies. This paper will discuss the technologies making up the system and system performance, and will provide details of its usefulness together with relevant data.

* Fundamental Technology Research Center
** Automobile R&D Center
*** HONDA RESEARCH INSTITUTE EUROPE GMBH

2. System Composition

This chapter will discuss the technologies making up the real-time aerodynamic design system.

2.1. System Design

Figure 1 shows a conceptual diagram of the real-time aerodynamic design system. The green box at the left of the figure shows images of user screens, while on the right the figure shows the different computational sections of the system. As the green box on the left shows, the user inputs the shape of the body, and the system displays aerodynamic performance and shape sensitivity in real time. The computational sections of the system are shown on the right. As the figure indicates, computation is conducted in the following order:

(1) Shape feature values are extracted from the body shape;
(2) Appropriate categories for these shape feature values are selected from a database of previous computations; and
(3) Performance is computed using approximation models of the categories.

2.1.1. Creation of database of previous computations

To conduct computations using the real-time aerodynamic design system, it is necessary to create a database and generate approximation models in advance. This section will discuss the method of construction of the database of previous computations. Figure 2 shows an overview of the process of creation of the database of previous computations. To create the database, deformed shapes are first generated based on baseline vehicle shapes using free-form deformation (FFD)[1]. To help ensure that the deformed shapes are not biased in any specific direction, the FFD is controlled using Latin hypercube sampling (LHS)[2], a form of Design of Experiments (DOE). Aerodynamic performance values are calculated for the deformed shapes using CFD, and these are added to the database together with feature values. Following this, approximation models are generated using data in the database. This is the flow of procedures for the creation of the database of previous computations. The database is created automatically when the shape data is input.

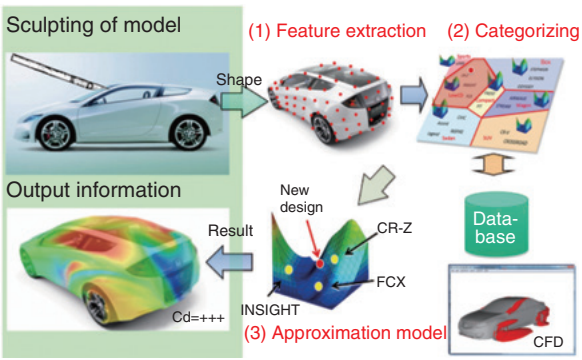


Fig. 1 Conceptual figure of real-time aerodynamic design system

2.1.2. Automatic accuracy increase function

If the difference between the body shape being designed and the data prepared in advance in the database is too great, it is possible that the generated approximation model may not provide sufficient predictive accuracy. When the real-time aerodynamic design system judges that predictive accuracy will be low, the processing discussed in Section 2.1.1 is conducted automatically, and data is added to the database. These automatic computations of additional data are implemented if the following conditions are satisfied:

(1) A new shape falls outside the design space in the database; and
(2) A new shape exists in a sparse area of the database.

The Euclidean distance from the center of the feature values in the database is used in the judgment of whether the body shape falls inside or outside the design space or whether it exists in a sparse or dense area.

2.1.3. GUI design

In order to increase user-friendliness, the real time aerodynamic design system has been designed as a plug-in for the Alias software manufactured by AutoDesk. Figure 3 shows a screenshot of the system. The system can be run by selecting it from the Alias tool bar and inputting vehicle specifications. The user is able to change body shapes and run computations while referring to the shape sensitivity

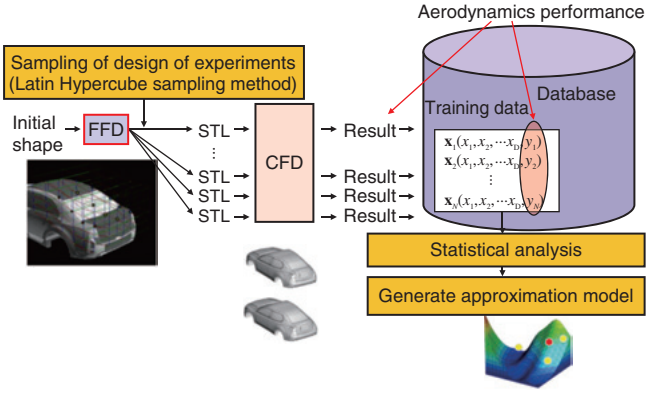


Fig. 2 Procedure of off-line learning for real-time aerodynamic design system

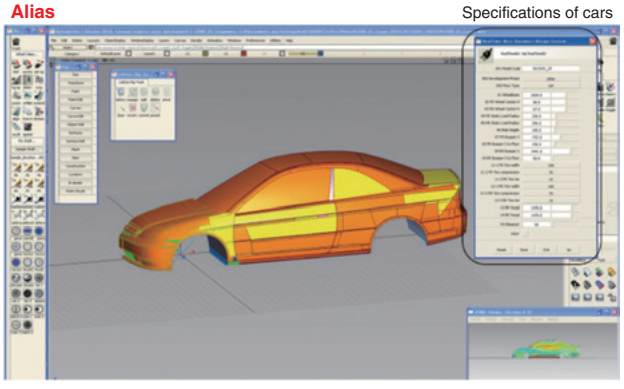


Fig. 3 GUI of real-time aerodynamic design system

screen until the desired aerodynamic performance values are obtained.

2.2. Data Management

The data accumulated in the real-time aerodynamic design system database is formulated by the process of generation of the database of previous computations, described in Section 2.1.1, and the process of automatic performance-boosting accuracy increase, described in Section 2.1.2. The open source data management software PostgreSQL is used for the management of this data. The real-time aerodynamic design system database is made up of polygon shape data, feature value data, and performance value data. A Database Management System (DBMS), which will be discussed from the next section onwards, was developed and put into operation to handle processing, including the interfaces used for writing to the database and other procedures. The use of the DBMS has helped to enable efficient data management and searching within the database. The DBMS is also able to respond to system elements including approximation models, categorizing, the automatic accuracy increase function, and sensitivity analyses.

2.2.1. Structure of Database

Like a standard database, the real-time aerodynamic design system database is not limited to aerodynamic performance values. Figure 4 shows the three-layered database structure. The system database is made up of design projects and design processes. Here, design projects play the role of grouping different design processes.

Design projects are generated based on the stage of the development process and the name of the model under development. Data including actual feature values and aerodynamic performance is stored in design processes together with the stage of development, the body data, and the user's user name. The various data stored in design processes are linked to body surface shape data defined by triangular unstructured grids.

2.2.2. Category management

The data in the database is classified into several categories based on similarity of shape. These categories are generated entirely automatically in order to increase the accuracy and reliability of the approximation models. The database is provided with hypothetical category boundaries for classification into categories.

Each time data is added, the category layers are reconstructed. Computation of the degree of displacement in design data and the learning of approximation models are conducted for each category. These processes are also rerun each time the category layers are reconstructed.

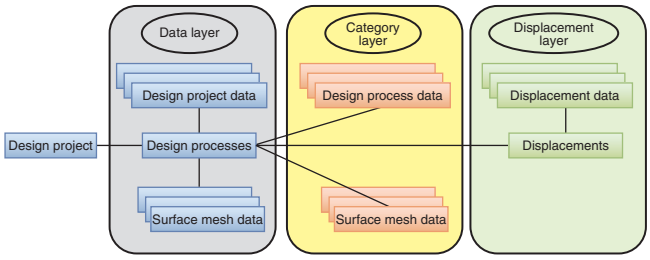


Fig. 4 Visualization of the three-layered database structure for managing design categories within the database

3. Approximation Models

The approximation models used in the real-time aerodynamic design system are functions that output aerodynamic performance with feature values extracted from body shapes as input values. Multiple parameters are incorporated in the approximation models. These values are estimated by machine learning using data in the database. The system uses Kriging[3), (4)] and variational Bayesian sparse regression (VBSR)[(5)] as approximation modeling methods. Overviews of these modeling methods and their characteristics are presented below.

3.1. Kriging

Because the Kriging method makes it possible to create high-accuracy approximation models, it is widely applied in engineering fields. Equation (1) shows the Kriging approximation equation.

$$\hat{y} = C_0 + \sum_{n=1}^{N} C_n f_n(\mathbf{x}_p) \,. \tag{1}$$

Here, $\hat{y}$ is the approximated performance value, $\mathbf{x}_p$ is the feature value for the prediction data, N is the number of sample points, and C_n and $f_n(\mathbf{x}_p)$ are an arbitrary coefficient and the radial basis function, respectively. Equation (1) shows that predictions via the Kriging method are the weighted sum of the radial basis functions (the second term on the right-hand side of the equation) added to bias C_0. Figure 5 shows a conceptual diagram of Kriging method prediction.

Equations (2) and (3) show the radial basis functions used in the Kriging method.

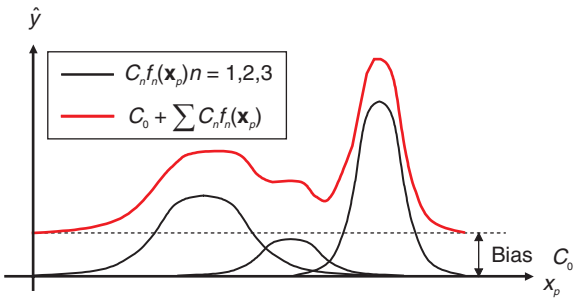


Fig. 5 Conceptual figure of Kriging

$$f_n = \mathbf{R}(\mathbf{x}_p, \mathbf{x}_m) , \tag{2}$$

$$\mathbf{R}(\mathbf{x}_i, \mathbf{x}_j) = \prod_{d=1}^{D} e^{-\theta^d \left| x_i^d - x_j^d \right|^{p^d}} . \tag{3}$$

Here, $\mathbf{x}_{tn}$ is the feature value for learned data, d is the feature value index, D is the number of feature values, and $\mathbf{R}(\mathbf{x},\mathbf{x})$ is the spatial correlation function (SCF). ρ and θ in $\mathbf{R}(\mathbf{x},\mathbf{x})$ are, respectively, parameters that decide the extension and smoothness of the radial basis function. Figure 6 shows changes in the radial basis function with changes in ρ and changes in θ. The left-hand graph shows that the higher the value of ρ, the more the radial basis function tends towards a smooth convex shape. The right-hand graph shows that the higher the value of θ, the narrower the range in which the effect of the corresponding learning points appears.

ρ and θ are unknown parameters for which only the number of feature values exists, and it is necessary to estimate them. The parameters are estimated based on maximum likelihood estimation (MLE). To help prevent convergence on a local solution, a global search using a genetic algorithm (GA) is first conducted, following which values are converged using hill-climbing, a local search method. The Kriging method has a greater number of parameters than other approximation modeling methods, and it offers a high degree of freedom in approximation functions. For this reason, it can be expected to construct high-accuracy models. However, the extended learning time necessary for the estimation of parameters represents an issue. Parameter estimation time is strongly dependent on the amount of learning data.

3.2. VBSR

VBSR is a method used in the discrimination of brain activity, and possesses the ability to automatically determine valid feature values for prediction during model learning. Because of this, it is also able to deal with the issue of an extremely large number of feature values (several thousand or more). Equation (4) is the approximation equation for VBSR.

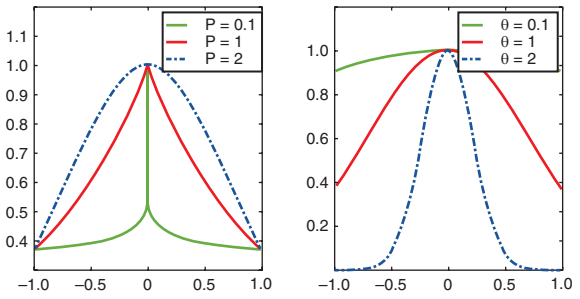


Fig. 6 Correlation of radial basis function with varying p (left), θ (right)

$$\hat{y} = \mu + \sigma y \sum_{i=1}^{D_{act}} w_i x_i . \tag{4}$$

Here, μ is the average value of learning data, σy is the standard deviation of learned data, i is valid feature values, D_{act} is the number of valid feature values, and w is the weighting of each feature value. Equation (4) shows that in VBSR, predictions are the sum of bias (μ; the first term on the right-hand side) and figures obtained using the linear weighted sum method. The approximation equation is a simple linear combination of feature values and weighting. Figure 7 shows a comparison of the Kriging and VBSR methods for a one-dimensional problem. As the graphs show, the Kriging method generates a curved line that passes through almost all of the learned data, while the VBSR method generates a straight line that maintains an undeviating distance from all of the learned data.

VBSR uses Bayesian estimation for parameter estimation. Like the maximum likelihood estimation that is used for parameter estimation in the Kriging method, Bayesian estimation is a statistical parameter estimation method, and because it treats parameters as probabilistic variables, it is able to respond to factors such as bias in the data. In addition, a major feature of Bayesian estimation is its ability to estimate parameters of parameters (hyper-parameters). Utilizing this feature of Bayesian estimation, the estimation of hyper-parameter $\boldsymbol{\alpha}$, which judges whether w is valid for prediction, in addition to parameter w, in the VBSR method has reduced the number of parameters involved in model learning. $\boldsymbol{\alpha}$ is known as an automatic relevance determination prior (ARD).

Model learning in VBSR avoids treating w and $\boldsymbol{\alpha}$ as unknown quantities simultaneously, using the variational Bayes method to alternately maximize the posteriori distribution of each, and continuing to update the values of the respective parameters until the values converge. When w is updated, if there is a value of w below the threshold value, it is excluded from model learning. This is a mechanism for reducing the number of feature values in VBSR. Learning time for the VBSR method is extremely short compared to the Kriging method. In addition, like the Kriging method, parameters are determined automatically, with no necessity for experience on the part of the user. Learning time in VBSR is strongly dependent on the number of feature values.

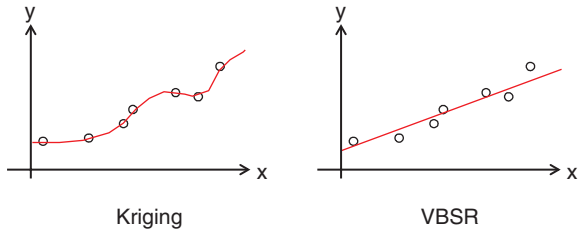


Fig. 7 Comparing phenomena of Kriging and VBSR

The real-time aerodynamic design system uses either the Kriging or the VBSR method depending on the prediction domain. In order to reduce learning time for the Kriging method, the system uses feature values reduced in number by the VBSR method for Kriging learning.

4. Categorizing

Figure 8 shows an overview of categorizing. Categorizing is broadly divided into Clustering, shown on the left, and Classifier, shown on the right. Clustering involves classification of data by the grouping of large amounts of data prepared in advance into groups of similar data called clusters. The prediction of categories for new data in relation to already classified data is called Classifier. Clustering methods include self-organizing map (SOM)[6] and K-means[7] and Classifier methods include neural network (NN)[8], sparse logistic regression (SLR)[5] and support vector machine (SVM)[9].

4.1. Categorizing in the System

In order to increase the accuracy of aerodynamic performance prediction by means of the use of approximation models, the real-time aerodynamic design system organizes shapes with a high degree of similarity into clusters, and generates approximation models for each cluster. Figure 9 shows images of the application of the categorizing technology in the system. The image on the left shows an example of the generation of an approximation model for all the data in the database. The image on the right shows an example of the generation of approximation models for each cluster following the organization of the data in the database into clusters based on shape.

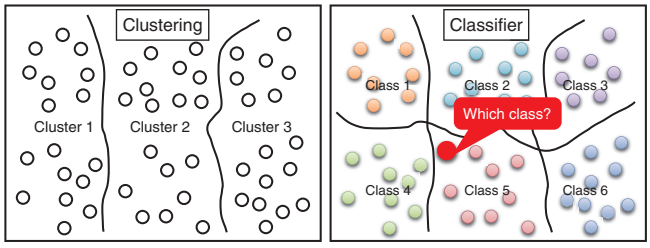


Fig. 8 Clustering and Classifier

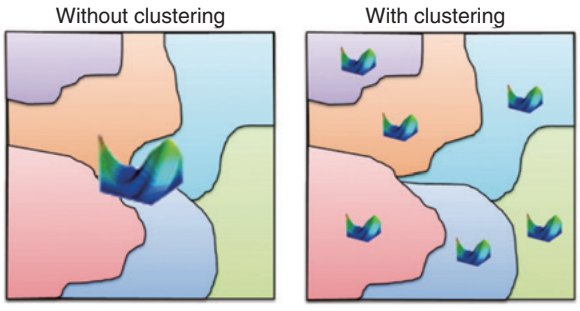


Fig. 9 Application of categorizing technique

Figure 10 shows an image of the data accumulated in the real-time aerodynamic design system database. In actual operation, classes are generated for each baseline body shape. The data in each class is generated from the baseline shape data via the method discussed in Section 2.1.1.

When new shape data is input, the appropriate class is determined by means of SLR. SLR is a method that expands logistic regression with Bayes estimation, and is applied as a method of assigning classes, with the weighted estimates for the discrimination of classes output by the method as probabilities of class membership.

4.2. Treatment of Category Boundaries

Figure 11 shows an image of class boundaries. When all data is classified into multiple classes, and predictions are made using the approximation models generated for each class, predictive accuracy at the class boundaries becomes an issue.

Figure 12 shows an image of the treatment of class boundaries in the real-time aerodynamic design system.

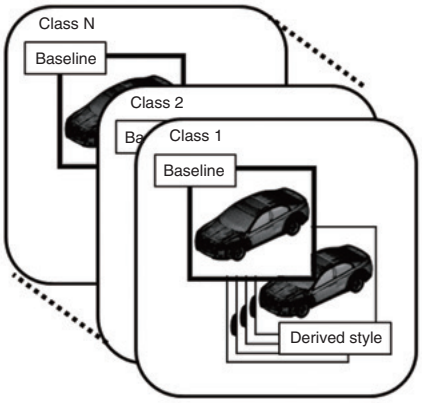


Fig. 10 Data structure image of DB

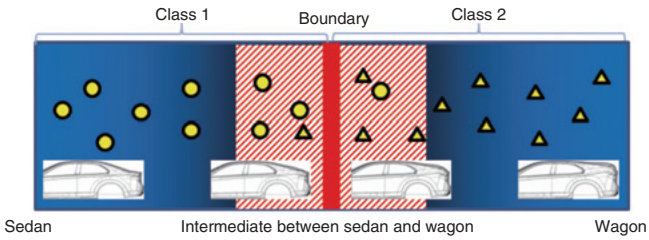


Fig. 11 Image of category boundary

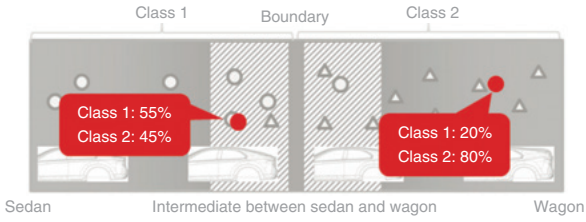


Fig. 12 Boundary treatment of real-time aerodynamic design system

In this system, in order to increase the accuracy of the approximation models, aerodynamic performance is predicted using a method (known as the probability method) in which the linear weighted sum of all the approximation models is determined using the probability of class membership output by SLR. Through the use of the probability of class membership, the probability method is able to linearly interpolate the boundary line domain in each class.

5. Extraction of Feature Values

The real-time aerodynamic design system uses feature values that represent body shapes as numerical parameters as input values for approximation modeling and categorizing. Position coordinates, surface angles, and curvature on the surface of the body are extracted as feature values. The extraction method is discussed in detail below.

5.1. Overview of Method

To make it possible for the real-time aerodynamic design system to treat any arbitrary body shape, it is necessary to be able to stably extract feature values at the desired position irrespective of body shape. A feature value extraction technology that is robust in relation to changes in body shape was developed by conducting system modifications with dynamic programming (DP) matching[(10)-(12)] as a base. DP matching is a method of matching the elements of two different time series patterns, and is widely employed, for example in voice recognition. Figure 13 shows an example of DP matching. The two-dimensional graph to the left of the figure is a reference pattern prepared in advance, and the two-dimensional graph at the bottom of the figure is a reference pattern for the subject of matching. The color contour map in the center of the figure shows absolute values for the difference in distance between the elements of the reference pattern and the subject of matching.

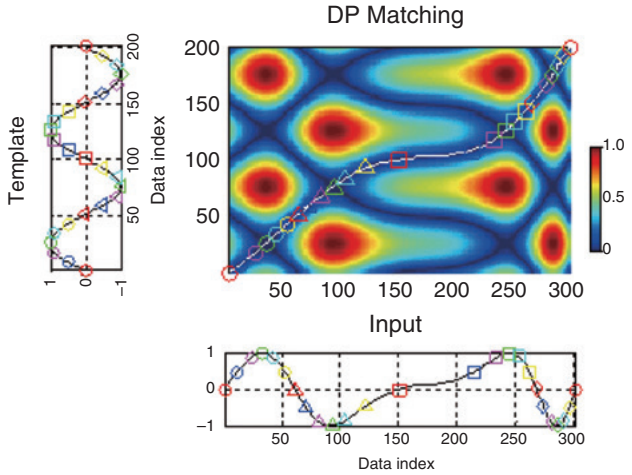


Fig. 13 DP matching method

In order to minimize the error between elements, DP matching determines the optimum path for matching while nonlinearly expanding and contracting the reference pattern. From multiple reference patterns, the pattern with the shortest cumulative distance for optimum paths is selected as the pattern most closely resembling the input pattern. Two major features can be indicated for DP matching: (1) It is able to absorb nonlinear shape changes in the input pattern even in the event that there are few reference patterns; and (2) It is able to automatically determine feature points even for unknown input patterns. With regard to computation time also, the use of DP matching makes it possible to break up optimization problems into partial problems for solution, meaning that computations can be conducted efficiently, with a reduced volume of operations.

To apply DP matching in the feature value extraction section of the real-time aerodynamic design system, two-dimensional cross-sections are extracted from three-dimensional shapes. In order to increase accuracy, one-dimensional complex feature vectors that consider the angle with a tangent to surface in addition to the distance from the center of gravity of the extracted cross-section lines are generated, and DP matching is applied.

5.2. Computation Procedures

Figure 14 shows the DP matching procedures. As the figure shows, feature values are extracted by means of the following four procedures:

(1) Two-dimensional cross-section lines for the body are extracted from three-dimensional shape data;

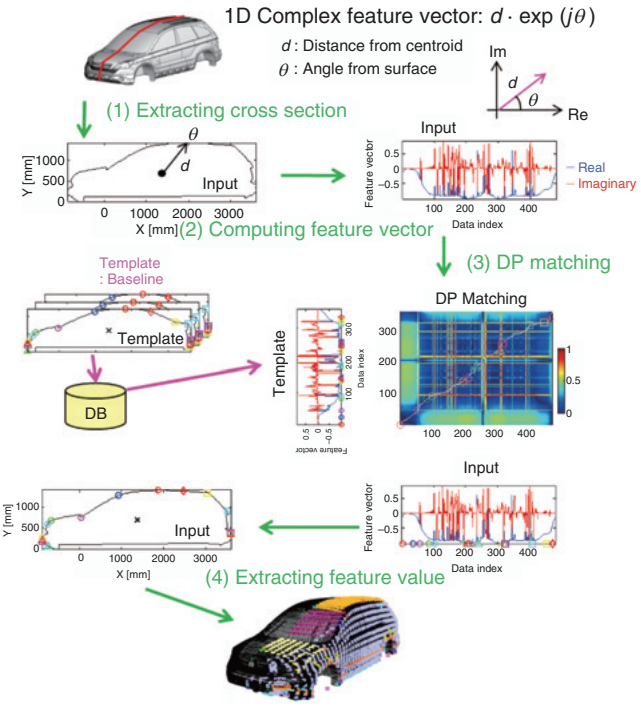


Fig. 14 Procedures of DP matching

(2) The two-dimensional cross-section lines are converted to one-dimensional complex feature vectors;
(3) Matching is conducted with the template in the database, and feature values are extracted; and
(4) With the feature points determined in (3) as a benchmark, feature values are extracted from the entire vehicle body in the form of a grid.

6. Sensitivity Analysis

The correlation between shape changes and aerodynamic performance is extremely important for the user. A variety of methods have been proposed for sensitivity analysis[13]. These methods can be broadly divided into two types: Global methods, which determine sensitivity from a range of data; and local methods, which calculate the gradient with the shape being focused on. While global methods are able to consider large deformations, local methods, as represented by adjoint[14], are only able to respond to small deformations.

In order to compute global sensitivity data at high speeds, the real-time aerodynamic design system uses an online sensitivity analysis system. This system has direct access to the data stored in the database from previous computations and automatic accuracy increase, and is thus able to realize high-speed computation. Spearman coefficients[15] are used as the coefficients of correlation.

6.1. Computation of Degree of Displacement

The degree of displacement is computed by calculating displacement for unstructured triangular data for two vehicle surfaces. The degree of displacement of each vertex is defined as

$$\delta_{i,j} = (v_j - v_i) \circ n_i \,. \tag{5}$$

Here, δ, v, and n are the displacement, apex, and normal vectors, respectively. The subscripts i and j are the shape at the beginning of displacement and the shape at the conclusion of displacement, respectively. The vertex of the shape at the conclusion of displacement is selected as the point of minimum distance from the apex of the shape at the beginning of displacement.

6.2. Online Sensitivity Analysis

Figure 15 shows the computation procedures involved in online sensitivity processing. The orange squares in the figures show processing, while the gray squares show results and data. As the figure shows, the aerodynamic performance values output from the feature values extracted from the body shape and the approximation models form the input for online sensitivity analysis. The details of each processing operation are presented below.

(1) Find best matching category

The category to which the body shape input by the user belongs is determined from feature values. For determination of the category, after the Euclidean distance is found from the category baseline data and the input body shape feature values, the data is assigned to the category in which the Euclidean distance is the lowest. The Euclidean distance is calculated using the following equation:

$$d(f^{new}, f^{base}) = \sqrt{\sum_n \left| f_i^{new} - f_i^{base} \right| \Big/ \left| f_i^{new} + f_i^{base} \right|} \,. \tag{6}$$

Here, f^{new} and f^{base} are the shape input by the user and the feature values of the baseline data in the category, respectively.

(2) Approximate displacements

Determination of the degree of displacement between the surface shapes in the design input by the user and the data classified in the same category is necessary for sensitivity analysis. Several thousand or more data exist in a single standard category, and an extremely long computation time is needed in order to determine all displacements. A method of significantly reducing computation time by rough estimation of the degree of displacement was therefore developed. First, the displacement of the data input by the user in relation to the baseline data in the category, $\delta^{n,b}$, is calculated. With $\delta^{n,b}$ as an offset value, the level of displacement against the remaining shapes in the category is estimated. The following equation is used for the calculation of the level of displacement of the shape data input by the user, n, and the data in the same category.

$$\tilde{\delta}^{n,m} = \delta^{n,b} + \delta^{b,m} + e^{n,m} \,. \tag{7}$$

Here, $\delta^{n,b}$ is the value calculated for the level of displacement against the baseline using Eq. (6), $\delta^{b,m}$ is the level of displacement extracted from the database, and $e^{n,m}$ is error.

Figure 16 shows the results of displacement calculations. The color contours on the left show displacement as calculated using Eq. (6), and those on the right show displacement as calculated using eq. (7). The error for displacement is 1.8%.

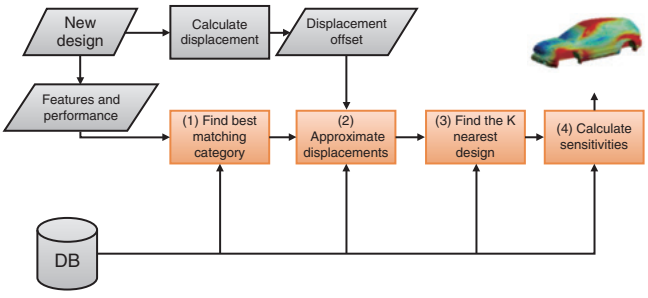


Fig. 15 Flow chart of the online sensitivity approximation

(3) Find the K-nearest designs

K-nearest neighbor (KNN) was introduced to the system in order to determine similar shapes to the shape input by the user. KNN searches for similar data from the level of displacement rather than searching for similar designs from the feature values of the body. The value of $\boldsymbol{K}$, which expresses the number of similar shapes, is determined empirically, and is set with consideration of the calculation time and the scope of the search.

(4) Sensitivity calculation

Spearman correlation coefficients are calculated based on the number of similar shapes, $\boldsymbol{K}$, the level of displacement of the respective shapes, $\tilde{\delta}^n$, and the aerodynamic performance values. The sensitivity, ρ_i^n, of the apex v_i of shape n input by the user is calculated based on linear approximation of the level of displacement and the displacement component of the aerodynamic performance values. Figure 17 shows the results of sensitivity analysis. The output results show the direction of increase or decrease in aerodynamic performance values. Positive values indicate an increase in aerodynamic performance values when the shape is deformed in the direction of the normal vectors of the body surface.

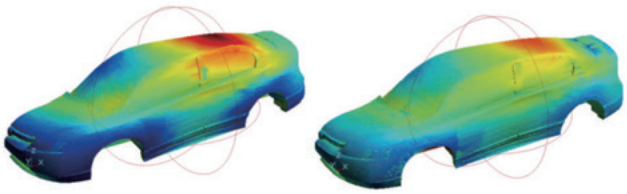


Fig. 16 Qualitative comparison between the calculated displacements on the left and the estimated displacements on the right. The displacement values are projected onto a color value between minimum (blue) and maximum (red) displacement value

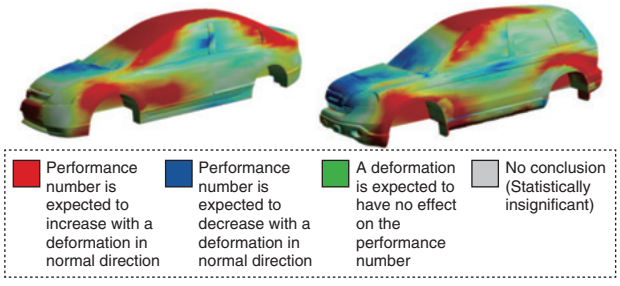


Fig. 17 Visualization of the sensitivity information, calculated concerning the Civic coupe model (left) and the CRV model (right)

7. System Performance

The performance of the real-time aerodynamic design system was evaluated. Figure 18 shows an outline of the evaluation method. First, data for the generation of approximation models and data for performance evaluation were generated using the procedure discussed in Section 2.1.1. Following this, performance values were predicted for the data for performance evaluation using the generated approximation models, and the performance of the approximation models was evaluated. 15942 cases of data for the generation of approximation models were generated from five baselines, and 1201 cases of test data for evaluation were generated from five baselines. The evaluation of the performance of the approximation models used the indexes discussed below.

(1) Correct rate, τ

The ratio of cases in which magnitude relationships for the performance of two randomly extracted designs is correctly judged was used for evaluation. In concrete terms, the number of successes and failures in predicting tendencies for all pairs that can be drawn from the data for performance evaluation was determined, and the cumulative ratio was used as the correct rate. This method of evaluation is generally known as the Kendall rank correlation coefficient. The correct rate, τ, is expressed in the following form:

$$\tau = N_{cp} \Big/ \frac{1}{2} n(n-1) \quad . \tag{8}$$

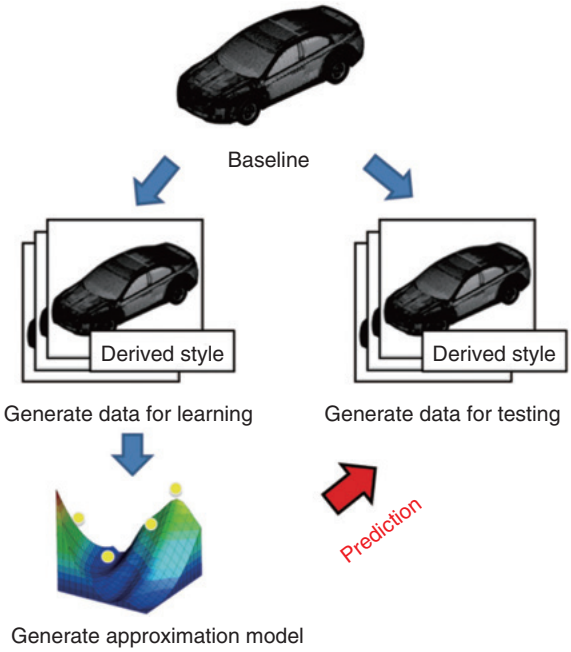


Fig. 18 Procedure of evaluation for real-time aerodynamic design system

Here, N_{cp} represents the number of pairs that successfully predicted tendency.

(2) Correlation coefficient, r_p

The correlation coefficient, r_p, is an index that expresses the correlation between two data sets (predicted values for data for evaluation and measured values), and is expressed as:

$$r_p = \frac{\sum_{n=1}^{N}(y_n - \overline{y})(\hat{y}_n - \overline{\hat{y}})}{\sqrt{\sum_{n=1}^{N}(y_n - \overline{y})^2}\sqrt{\sum_{n=1}^{N}(\hat{y}_n - \overline{\hat{y}})^2}} . \quad (9)$$

Here, y is the measured performance value (CFD calculation value) for the data for evaluation, made up of N data, and $\hat{y}$ is the predicted value. $\overline{y}$ is the average value of y, and $\overline{\hat{y}}$ is the average value of $\hat{y}$. The closer the correlation coefficient to 1, the stronger the correlation and the more accurate the reproduction by the model. The closer the correlation coefficient to 0, the weaker the correlation and the less accurate the reproduction by the model.

(3) Root mean square error (RMSE)

RMSE is calculated using Eq. (10). The higher the value, the greater the prediction error.

$$RMSE = \sqrt{\sum_{n=1}^{N}(y_n - \hat{y}_n)\Big/N} . \quad (10)$$

System performance was evaluated using the evaluation indexes discussed above. The approximation models achieved the following performance values:

- Correct rate: 91%
- Correlation coefficient: 0.95
- RMSE: 1.1%

In addition, excepting display time and certain other parameters, the system's time for prediction of aerodynamic performance was within several seconds.

These results indicate the effectiveness of the real-time aerodynamic design system from the perspectives of accuracy and computation time.

8. Conclusion

A real-time aerodynamic design system able to calculate aerodynamic performance and shape sensitivity in real time was developed. The developed system offers the following features:

- High-speed calculation through use of approximation models
- High-accuracy calculation of multiple approximation models by means of a categorizing technology
- Online calculation of sensitivity
- Automatic accuracy increase function

An evaluation of the system produced the following results:

- Correct rate: 91%
- Correlation coefficient: 0.95
- RMSE: 1.1%
- Calculation time (excepting display section and others): Within several seconds

References

(1) Sederberg, T.W., Parry, S.R.: Free-Form Deformation of Solid Geometric Models, Proceedings of ACM SIGGRAPH in Computers & Graphics, 20 (4), p. 151-160 (1986)

(2) Tang, B.: Orthogonal Array-Based Latin Hypercubes, Journal of the American Statistical Association, Vol. 88 (424), p. 1392-1397 (1993)

(3) Forrester, A., Keane A., Sobester, A.: Engineering Design via Surrogate Modelling: A Practical Guide, Wiley, 228p. (2008)

(4) Sasena, M.J.: Flexibility and Efficiency Enhancements for Constrained Global Design Optimization with Kriging Approximations, Doctoral paper of University of Michigan (2002)

(5) Yamashita, O., Sato, M., Yoshioka, T., Tong, F., Kamitani, Y.: Sparse estimation automatically selects voxels relevant for the decoding of fMRI activity patterns, Neuroimage, Vol. 42, Issue 4, p. 1414-1429 (2008)

(6) Kohonen, T.: Self-Organizing Maps, Springer, 501p. (2001)

(7) MacQueen, J. B.: Some Methods for Classification and Analysis of Multivariate Observations, Proceedings of Fifth Berkeley Symposium on Mathematical Statistics and Probability. University of California Press, MR0214227, p. 281–297 (1967)

(8) Hopfield, J. J.: Neural networks and physical systems with emergent collective computational abilities, Proc. Natl. Acad. Sci. USA, Vol. 79, p. 2554-2558 (1982)

(9) Cortes, C., Vapnik, V.: Support-Vector Networks, Machine Learning, Vol. 20, Issue 3, p. 273-297 (1995)

(10) Sakoe, H., Chiba, S.: Douteki keikaku hou wo riyoushita onsei no jikan seikika ni motozuku renzoku tango ninshiki, Nihon onkyo gakkaishi, Vol. 27, No. 9, p. 483-490 (1971)

(11) Sakoe, H., Chiba, S.: A Dynamic Programming Algorithm Optimization for Spoken Word Recognition, IEEE Trans. on Acoust. Speech and Signal Proc., Vol. 26, Issue 1, p. 43-49 (1978)

(12) Sakoe, H.: Two-level DP-matching- -A dynamic programming-based pattern matching algorithm for connected word recognition, IEEE Trans. on Acoust. Speech and Signal Proc., Vol. 27, No. 6, p. 588-595 (1979)

(13) Ascough II, J. C., Green, T. R., Ma, L., Ahjua, L. R.: Key criteria and selection of sensitivity analysis

methods applied to natural resource models, International Congress on Modeling and Simulation Proceedings (2005)
(14) Othmer, C.: CFD Topology and Shape Optimization with Adjoint Methods, VDI-Berichte, 1967, p. 61 (2006)
(15) Graening, L., Menzel, S., Hasenjaeger, M., Bihrer, T., Olhofer, M., Sendhoff, B.: Knowledge Extraction from Aerodynamic Design Data and its Application to 3D Turbine Blade Geometries, Journal of Mathematical Modelling and Algorithms, Vol. 7, Issue 4, p. 329-350 (2008)

■ Author ■


Takahiro FUKUSHIGE


Tokitomo ARIYOSHI


Yusuke UDA


Yuki OKUMA


Tatsuya OKABE


Koichi YAMAMOTO


Lars GRAENING


Stefan MENZEL


Markus OLHOFER

Development of High-strength and High-wear Resistance Nitrocarburizing Steel by Precipitation Strengthening of Mo-V Carbonitride

Hiroki MASUDA* Hideki MATSUDA* Ayumi YAMAZAKI**

ABSTRACT

The project discussed in this paper developed a nitrocarburizing steel that balances strength, wear resistance, and workability. The hardness of the steel is controlled as low as possible for machining after forging, and the heat applied in the nitrocarburizing process is then used to achieve high hardness in both the surface layer and the base material. As a result, the developed steel achieves at least 40% higher bending fatigue strength than a conventional nitrocarburized steel. The balance between high fatigue strength and workability in the developed steel is realized through the exploitation of Mo-V carbonitride precipitate strengthening. When the material is machined, the Mo and V are in a state of solid solution, but during the nitrocarburization process following machining, fine complex Mo and V carbonitrides are precipitated in lattices coherent with the base material, resulting in high hardness. The fact that the compound layer that formed during nitrocarburization was brittle and lacked ductility represented a disadvantage in terms of abrasive wear, and it was necessary to increase the toughness of the compound layer in order to increase wear resistance. The crystal grains in the compound layer were therefore refined by promoting the precipitation of Mo and V carbonitrides in the compound layer also, resulting in the realization of greater toughness and increased wear resistance.

1. Introduction

Today, against a background of increasingly stringent environmental regulations targeting factors such as CO_2 emissions, we are witnessing rising demands for the reduction of the environmental burden represented by automobiles, for example in the demand for increased automotive fuel efficiency in order to reduce CO_2 emissions. In the area of reciprocating engines, the realization of weight savings and increased compactness through reduction of size is demanded. In line with this, it is necessary to make engine parts more compact, which tends to increase the load on each part, necessitating the realization of high levels of strength and wear resistance. In the case of most engine, drivetrain and other powerplant parts, strength and wear resistance are increased by applying heat treatments such as carburizing, induction hardening or nitrocarburizing when the part has been machined following formation by means of forging or casting[(1), (2)]. Because machining processes cover a wide range of procedures involving lathe machining, drilling and grinding, good workability is essential, and the balancing of the achievement of high strength with workability is therefore strongly demanded[(3), (4)].

Given the fact that they impart minimal strain and tend not to result in dimensional change, nitrocarburizing treatments are applied to a variety of parts[(5), (6)]. However, because the realization of increased strength necessitates the use of high-hardness materials, a decline in workability is unavoidable, and limits therefore exist to potential strength increases[(7), (8)].

In addition, the compounds that form on the surface layer when ordinary carbon steels are nitrocarburized are brittle and display poor ductility[(9)], and this represents a disadvantage in wear environments in which abrasive wear is prominent.

The research discussed in this paper exploited the precipitation strengthening of molybdenum (Mo) and vanadium (V) during nitrocarburization in order to address the issues discussed above. The paper will analyze the mechanism of precipitation strengthening, and discuss the design of an optimal alloy composition and a microstructure that maximizes precipitation strengthening ability.

* Automobile R&D Center

** Daido Steel Co., Ltd.

2. Development Goals

The research discussed in this paper set out to develop a nitrocarburizing steel that would contribute to the realization of weight savings and increased compactness in engines and transmissions, would be suitable for use in sliding parts exposed to high-friction environments in diesel engines, and would display the following characteristics:

(1) High strength (40% or higher increase in bending fatigue against conventional nitrocarburizing steels); and
(2) High friction resistance.

3. Concept of Material Composition Design

Figure 1 shows the positions of the porous layer, compound layer, nitrided layer, and base material in a nitrocarburized steel. The porous layer is part of the compound layer, and is composed of the numerous pores that form on the outermost layer. The compound layer is a dense layer formed by the iron nitride compounds under the porous layer. The nitrided layer indicates the depth to which nitrogen diffused from directly below the compound layer during the nitrocarburizing process, and the base material indicates areas to which nitrogen did not diffuse.

3.1. Material Concept

Figure 2 shows hardness profiles for a conventional nitrocarburized steel (termed "conventional steel" below) after forging and after nitrocarburization. The increase in the hardness of the conventional steel after nitrocarburization (solid line) against its hardness after forging (broken line) results from the strengthening only of the nitrided layer due to the diffusion of nitrogen in the nitrocarburization process. However, when using the conventional method, because it is necessary to increase hardness following forging when seeking to increase the hardness profile in order to increase strength, a decline in workability is unavoidable. The present research therefore focused on precipitation strengthening using the heat from a nitrocarburizing treatment applied following machining. Figure 3 shows hardness profiles for the developed steel after forging and after nitrocarburization. In the developed steel, because the surface layer and the base material are both increased in hardness by the precipitation of carbonitrides in the nitrided layer of the surface layer and carbides in the base material during nitrocarburization (precipitation strengthening), the steel's hardness after forging (broken line) is lower than its hardness after nitrocarburization (solid line). The material therefore balances high strength with workability, realizing a high level of strength while sacrificing workability as little as possible. In addition, the compound layer that forms as the outermost layer during nitrocarburization is strengthened by precipitation strengthening at the same time.

3.2. Concept of Alloy Design for Precipitation Strengthening

Mo, V, Nb, and Ti are among the elements that display high precipitation strengthening ability[10]. Figure 4 shows precipitation strengthening ability when each of these elements is individually added to S20C carbon steel. The horizontal axis shows hardness prior to heat treatment at 600 °C for two hours, and the vertical axis shows hardness following heat treatment. The hardness differential, ΔHv, given by Equation (1) indicates precipitation strengthening ability.

$$\Delta Hv = (\text{Hardness after heat treatment}) - (\text{Hardness before heat treatment}) \quad (1)$$

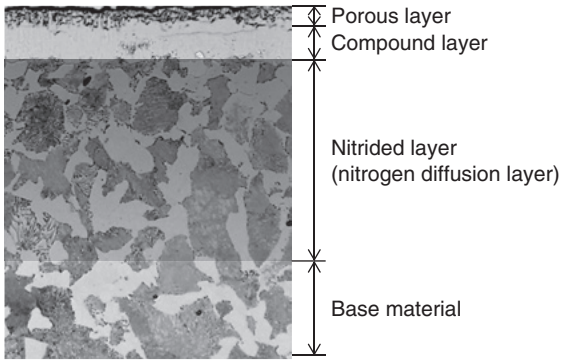


Fig. 1 Layers of nitrocarburizing steel

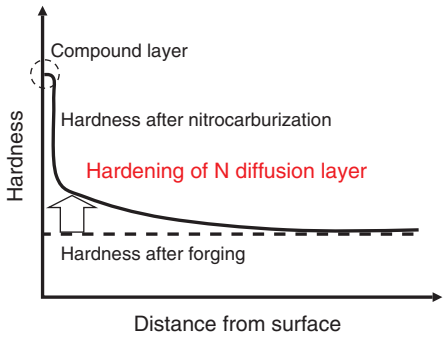


Fig. 2 Hardness distribution of conventional steel

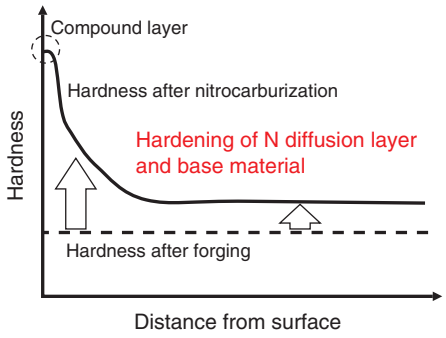


Fig. 3 Hardness distribution of developed steel

The results of this study showed that Mo and V displayed the greatest precipitation strengthening ability, and it was therefore decided to attempt to make effective use of these elements in the new material.

3.3. Mechanism of Precipitation Strengthening of Mo, V-added Steel (Nitrided Layer)

The precipitates in the nitrided layer following nitrocarburization at 600 °C for two hours were analyzed in conventional steel and in the Mo, V-added steel (termed Mo-V steel). Figure 5 shows the results of observation of the nitrided layer (the surface layer at a depth of 0.05 mm) of a conventional steel using transmission electron microscopy (TEM) and Fig. 6 shows the results of precipitate identification using energy-dispersive X-ray spectroscopy (EDS). Figure 7 shows an image of the lattice structure of the precipitates. As Fig. 5 shows, the precipitates in the conventional steel display an NaCl-type crystal structure. The crystal orientation in the plane of observation is the base material, Fe, and $[001]\alpha//[\bar{1}01]$ precipitates. That is, precipitation occurs in a Baker-Nutting orientation relationship. The results of analysis of the precipitates using EDS (Fig. 6) show high amounts of Mn and Cr, and they can be judged to be Mn-containing Cr nitrides. The results of the analysis shown in Fig. 5 indicate a precipitate distribution of 1.5×10^3 /μm^2 at an average precipitate size of 34.4 nm (Table 1). In addition, the image of the precipitate lattice (Fig. 7) indicates that the lattice of the Fe base material collapses at the boundary where the precipitates are macroaggregated; that is, the boundary has become incoherent.

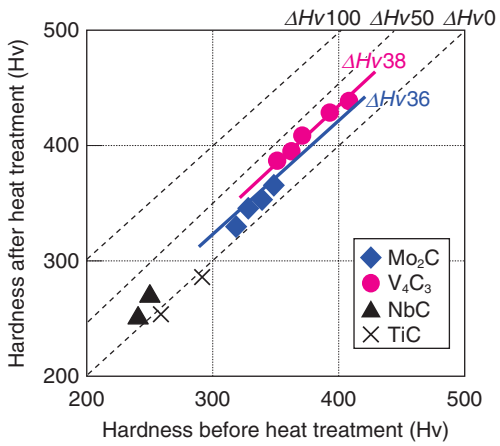


Fig. 4 Precipitate strengthening ability: ΔHv of alloy

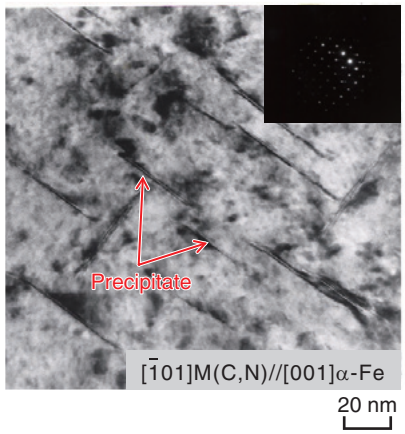


Fig. 5 Transmission electron micrograph taken from diffusion layer (0.05 mm depth) of conventional steel after nitrocarburization

Table 1 Precipitate length and number at 0.05 mm depth after nitrocarburization

	Precipitate length	Precipitate number (/μm^2)
Mo,V-added steel	8.2 nm	3.8×10^4
Conventional steel	34.4 nm	1.5×10^3

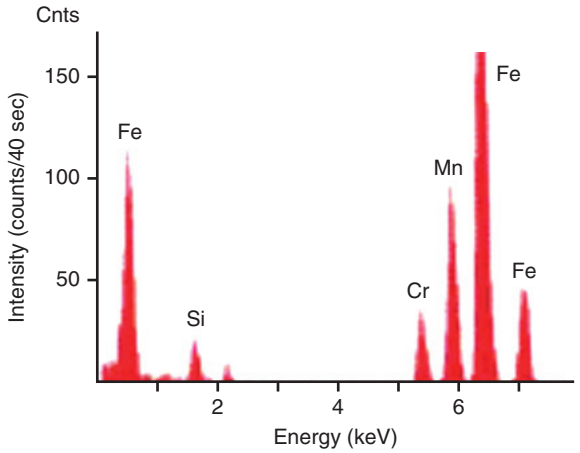


Fig. 6 Energy dispersive X-ray spectrometry analysis of conventional steel precipitate

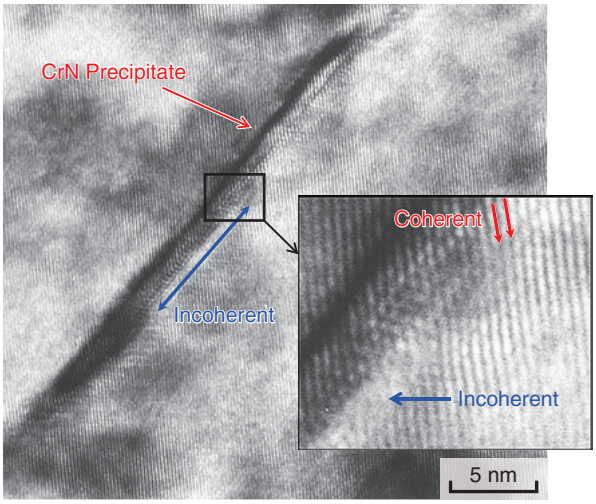


Fig. 7 Lattice image of CrN precipitate

Figure 8 shows the results of observation of the nitrided layer (the surface layer at a depth of 0.05 mm) of the Mo-V steel using TEM and Fig. 9 shows the results of precipitate identification using EDS. Figure 10 shows an image of the precipitate lattice structure. As Fig. 8 shows, the precipitates observed in the Mo-V steel also display an NaCl-type crystal structure. In addition, the crystal orientation in the plane of observation is the base material Fe and $[001]\alpha//[0\bar{1}1]$. The Mo-V steel therefore also resembles the conventional steel in the fact that precipitation occurs in a Baker-Nutting orientation relationship. The results of EDS analysis of the precipitates (Fig. 9) show them to contain large amounts of Mo and V, followed by Cr and Mn, and they can be judged to be Cr- and Mn-containing Mo-V carbonitrides. The results of the analysis shown in Fig. 8 indicate a precipitate distribution of 3.8×10^4 /μm^2 at an average precipitate size of 8.2 nm, with the precipitates both finer and existing in greater quantities than in the case of the conventional steel (Table 1). The image of the precipitate lattice (Fig. 10) shows that strain occurs in the lattice (termed "lattice strain") at the boundary between the Fe base material lattice and the Mo-V carbonitrides. No collapse in the Fe lattice is observed at the boundary, and the precipitate displays extremely good coherence with the Fe base material lattice. It can therefore be indicated that a high level of lattice strain occurs in the Mo-V steel.

Based on the results discussed above, it is considered that because the Mo-V steel, by contrast with the conventional steel, precipitates a large number of fine Mo-V carbonitrides in the nitride layer and the precipitate maintains good coherence with the lattice of the Fe base material, the steel possesses high precipitate strengthening ability.

3.4. Mechanism of Precipitate Strengthening of Mo-V Steel (Base Material)

Figure 11 shows the results of TEM observation of the base material of the Mo-V steel, where nitrogen does

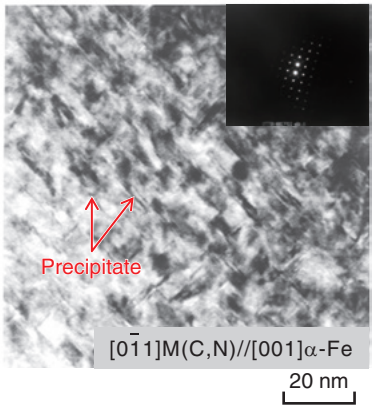


Fig. 8 Transmission electron micrograph taken from diffusion layer (0.05 mm depth) of Mo, V-added steel after nitrocarburization

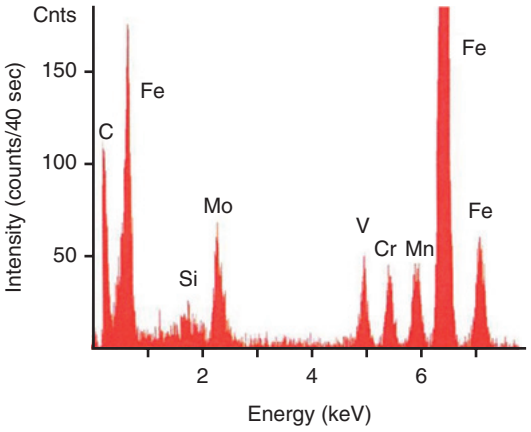


Fig. 9 Energy dispersive X-ray spectrometry analysis of Mo, V-added steel precipitate

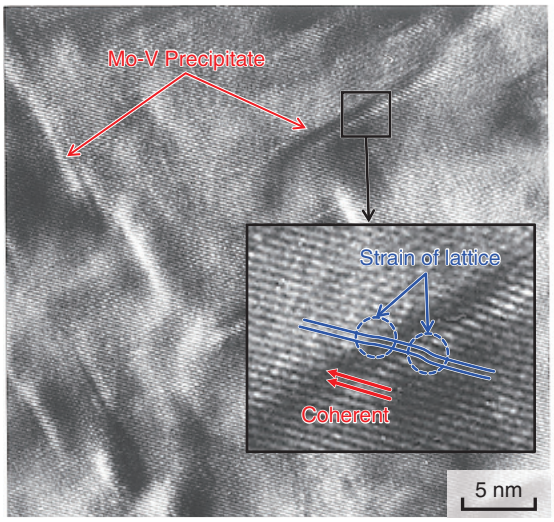


Fig. 10 Lattice image of Mo-V precipitate

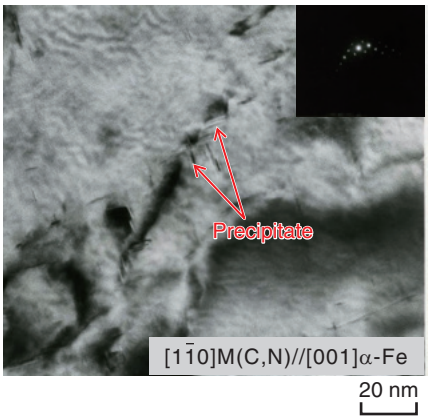


Fig. 11 Transmission electron micrograph taken from non-N diffusion layer of Mo, V-added steel after nitrocarburization

not diffuse, and Fig. 12 shows the results of identification of the precipitates in the base material using EDS. Figure 13 shows an image of the precipitate lattice. As Fig. 11 shows, as in the nitrided layer, the precipitates in the base material display an NaCl-type crystal structure, and the crystal orientation relationship is a Baker-Nutting relationship. Based on the results of the EDS precipitate analysis (Fig. 12), the precipitates contain Mo and V, and can be judged to be Cr, Mn-containing Mo-V carbides. It is believed that carbides are the main precipitate because no nitrogen diffusion occurs in the base material. The results of the analysis shown in Fig. 11 indicate a precipitate distribution of 5.1×10^3 /μm^2 at an average precipitate size of 6.8 nm, finer than the surface layer. The image of the precipitate lattice (Fig. 13) shows that strain occurs in the lattice (lattice strain) at the boundary between the Fe base material lattice and the Mo-V carbonitrides, as in the surface layer. No collapse in the Fe base material lattice was observed at the boundary, and the precipitate displays extremely good coherence with the Fe base material.

As this indicates, it is possible to precipitation-strengthen both the nitrided layer and the base material of the Mo-V steel by means of Mo-V carbonitrides (carbides). This high precipitation hardening ability is believed to increase yield strength, and to produce high fatigue strength.

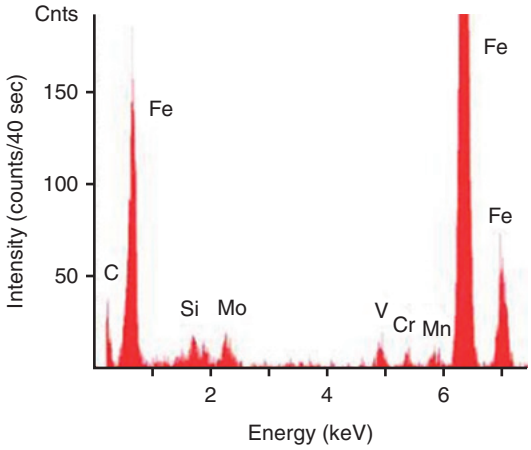


Fig. 12 Energy dispersive X-ray spectrometry analysis of inside precipitate in Mo, V-added steel

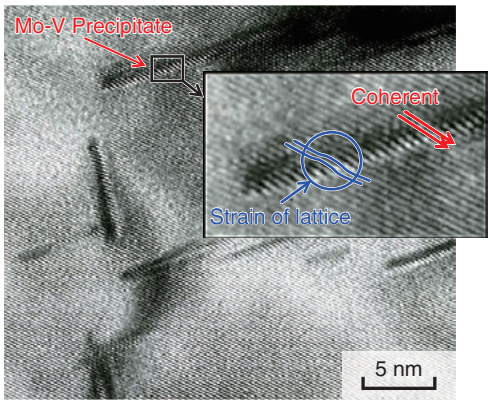


Fig. 13 Lattice image of Mo-V precipitate

3.5. Mechanism of Increase in Wear Resistance of Mo-V Steel Compound Layer

Figures 14 and 15 respectively show the results of TEM observation of cross-sections of the compound layers of conventional steel and the Mo-V steel. Figure 16 shows the results of EDS identification of the precipitates in the Mo-V steel. As Figs. 14 and 15 show, the Mo-V steel has finer crystal grains than the conventional steel. As Figs. 15 and 16 indicate, Mo-V carbonitrides of a grain size of around 10 nm are also precipitated in the compound layer of the Mo-V steel. These precipitates have a pinning effect, controlling grain growth and refining the compound layer. It is believed that this produces a high-toughness compound layer, resulting in a high level of wear resistance.

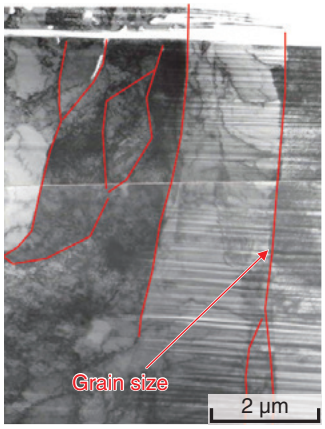


Fig. 14 Transmission electron micrograph taken from diffusion layer of conventional steel compound layer

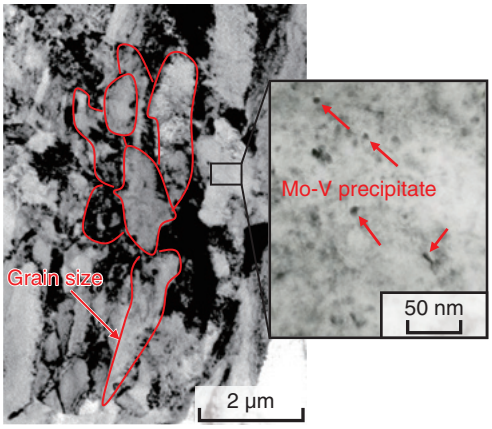


Fig. 15 Transmission electron micrograph taken from diffusion layer of developed steel compound layer

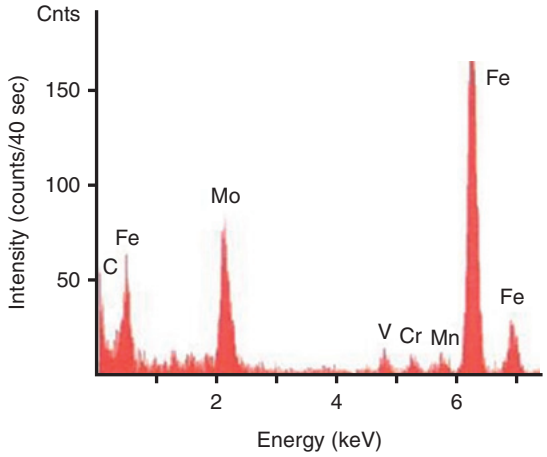


Fig. 16 Energy dispersive X-ray spectrometry analysis of precipitate in developed steel compound layer

4. Material Composition Design

4.1. Target Hardness and Microstructure

Prior to the design of the material composition, the target hardness profile following nitriding was set. Figure 17 shows the hardness profile (solid line) determined from the stress gradient necessary for the achievement of the target fatigue strength. It was necessary for the hardness profile of the developed material to exceed the hardness profile determined from the stress gradient[11), 12)]. For the developed material, the depth of nitrogen diffusion during nitrocarburization was set at 0.3 mm or more, and the hardness at a depth of 0.3 mm was set at 295 Hv or higher to help ensure that the fracture point would occur at a depth of 0.3 mm or more. The hardness at a depth of 0.05 mm in the surface layer was set at 450 Hv or higher.

With regard to the microstructure, in order to maximize the Mo-V precipitation strengthening ability necessary to help ensure fatigue strength and the wear resistance of the compound layer, it was necessary to maintain the Mo and V in a state of solid solution following forging and cooling. Ferrite forms in the steel during cooling following forging. Figure 18 shows a TEM image of the Mo-V carbides that form in the ferrite microstructure. When ferrite forms during cooling following forging, Mo and V do not maintain a state of solid solution, but rather, as Fig. 18 shows, Mo-V carbides are precipitated as large agglomerations. These Mo-V carbides precipitated in ferrite are more agglomerated and spherical than the Mo-V carbides precipitated in bainite shown in Figs. 11 and 13. This is identical to the state of precipitation of ferrite in general vanadium microalloyed steels. Because the precipitates became larger with the application of heat in the following nitrocarburization process, the expected precipitation strengthening ability could not be achieved. Figure 19 shows the results of a study of the precipitation strengthening ability of ferrite microstructures and bainite microstructures. The horizontal axis shows nitriding time, and the vertical axis shows hardness. The results indicate that the hardness differential before and after heat treatment, ΔHv, is lower for the ferrite microstructure than the bainite microstructure. A bainite microstructure was therefore selected for the material under development in order to boost the effectiveness of increasing strength with nitrocarburization.

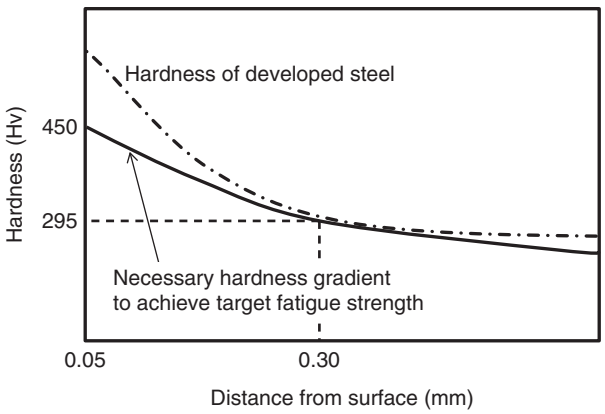


Fig. 17 Hardness transition curve design after nitrocarburization

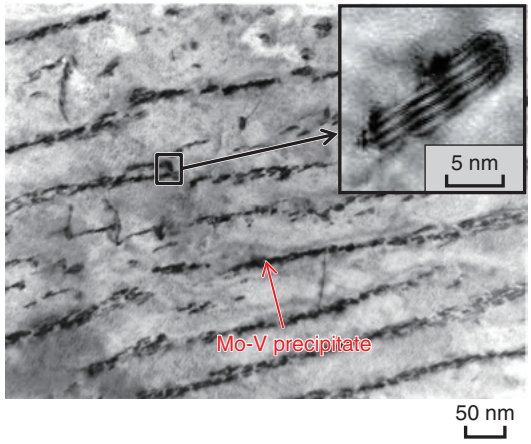


Fig. 18 Mo-V precipitate in ferrite after forging

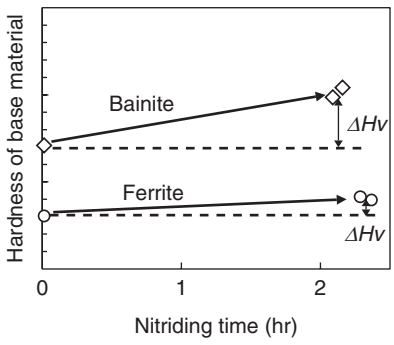


Fig. 19 Relationship between Mo-V precipitate strengthening ability and microstructure

4.2. Setting of Quantities of Mo and V for Addition

The amounts of Mo and V to be added were set on the basis of the amount of V, which displays a high level of precipitation strengthening ability. Figure 20 shows the relationship between the amount of V added and precipitation strengthening ability. At 0.25 mass% or more V, precipitation strengthening ability tends to become saturated, and in general the greater the quantity of V added, the higher the hardness of the base material after forging, resulting in a decline in workability. Given this, the upper limit for the amount of V to be added was set at 0.25 mass%.

Figure 21 shows the relationship between the amount of added Mo and V and hardness at a depth of 0.3 mm following nitrocarburization at 600 °C for two hours. Target values for the amount of added Mo and V to achieve a hardness of 295 Hv or higher were set at 0.20 mass% for Mo and 0.20 mass% for V.

The amounts of Mo and V to be added were set as described above with consideration of the realization of precipitation strengthening ability and the necessary level of hardness following nitrocarburization. In addition, the amounts of C, Si, Mn and Cr added were adjusted to produce the desired bainite microstructure.

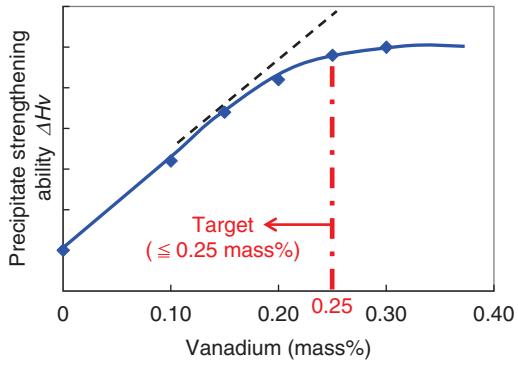


Fig. 20 Relationship between vanadium content and precipitate strengthening ability: ΔHv

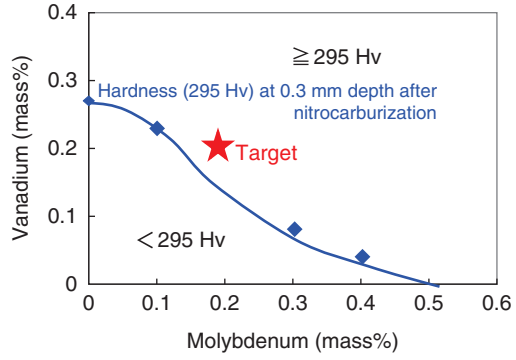


Fig. 21 Relationship between Molybdenum, Vanadium content and hardness at 0.3 mm depth after nitrocarburization

Table 2 Chemical composition of developed and conventional steel

(mass%)

	C	Si	Mn	Cr	Mo	V
Developed steel	0.20	0.50	1.85	0.20	0.20	0.20
Conventional steel	0.48	0.30	1.45	0.10	–	–

Table 2 shows the material composition set on the basis of the results discussed above. The table also shows the composition of conventional steel.

5. Material Characteristics

5.1. Fatigue Characteristic

Rotating-bending fatigue tests were conducted using the test specimen specifications shown in Fig. 22. Test specimens of 44 mm × 44 mm were produced by machining after microalloyed forging, following which they were subjected to nitrocarburizing treatment at 600 °C for two hours. Figure 23 shows hardness following forging (broken lines) and hardness profiles following nitrocarburization (solid lines). While the hardness of the developed material following forging is about 270 Hv (the blue broken line in the graph), following nitrocarburization the material's internal hardness increases by 30 Hv or more, reaching the target hardness (the black solid line in the graph), including in the nitrided layer. In addition, as Fig. 24 shows,

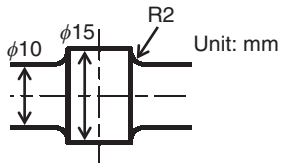


Fig. 22 Geometry of rotating-bending fatigue test specimen

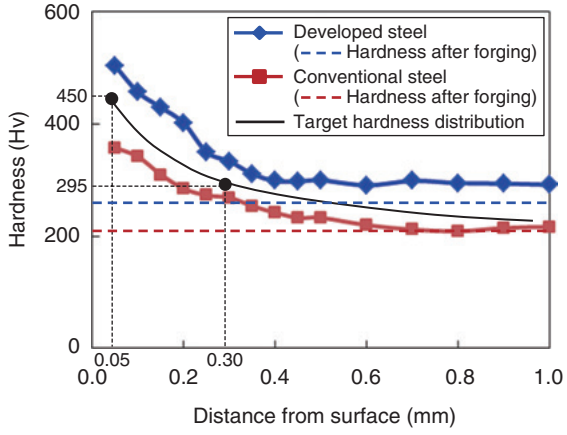


Fig. 23 Hardness distribution of test specimen after nitrocarburization

while the conventional steel displays a ferrite-pearlite microstructure, the developed steel realizes a monolayer bainite microstructure. The bending fatigue strength of the developed material is at least 40% higher than that of the conventional steel, as Fig. 25 shows.

5.2. Wear Resistance of Metal Sliding Shaft Parts

Toughness against abrasive wear due to hard particles such as carbon particles in deteriorated oil is demanded for engine parts. Using 20 × 20 × 10 mm (L × W × H) test specimens, scratch tests were therefore conducted on the conventional and the developed steel under a constant load of 80 N, and the characteristics of the compound layer formed on the outermost surface were evaluated. Scratch tests are suitable to evaluate the characteristics of compound layers in relation to abrasive wear due to hard particles.

The steels employed in the samples for the study of nitriding quality, as shown in Fig. 24, were used to produce the test specimens. The results of the tests indicated that the developed steel formed a compound layer approximately 80 Hv harder than the conventional steel. Figure 26 shows the results of an analysis of the crystal grains in cross-sections of the compound layers of the developed and conventional steels using electron backscattering patterns (EBSP). The results demonstrate that the developed steel forms a fine compound layer, with the crystal grain diameter of 1.04 μm around 1/3 of the figure for the conventional material of 3.12 μm. In order to verify the effect of this refinement of the crystal size in the compound layer on wear resistance, samples of the conventional and developed steels were produced in which the porous layer that forms on the outermost surface of the compound layer had been removed by abrasion prior to scratch tests. Following the scratch tests, the scratch marks were observed using an optical microscope in order to evaluate the detachment resistance of the compound layer (Fig. 27). The results show that while detachment occurred across the entire surface of the conventional steel, detachment did not occur in the developed steel. The results discussed above indicate that the developed steel forms a high-hardness and high-toughness compound layer.

Unit tests reproducing an actual engine environment were also conducted in order to evaluate wear resistance in an actual engine. Figure 28 shows a diagram of the test apparatus. This test uses oil with a high carbon content to reproduce deteriorated oil, and is suitable to quantitatively evaluate shaft wear in actual diesel engines, a severe abrasive wear environment, in a short period[13]. The results are shown in Fig. 29, with time on the horizontal axis and amount of wear on the vertical axis. As the figure shows, the amount of wear in the developed steel following 200 hours of testing was approximately 50% of that in the conventional steel, verifying that the developed steel forms a high-abrasion-resistance compound layer.

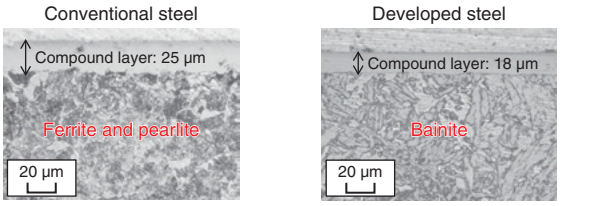


Fig. 24 Microstructure of test specimen after nitrocarburization

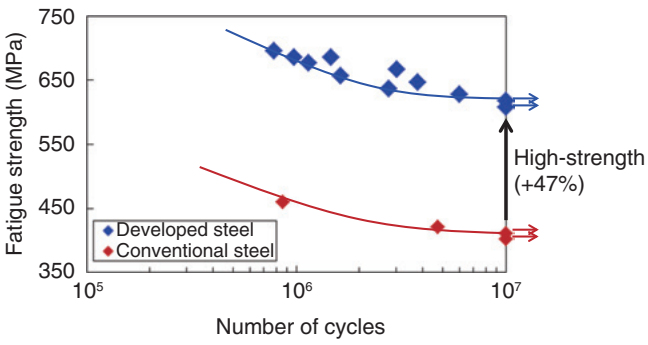


Fig. 25 Result of rotating-bending fatigue strength

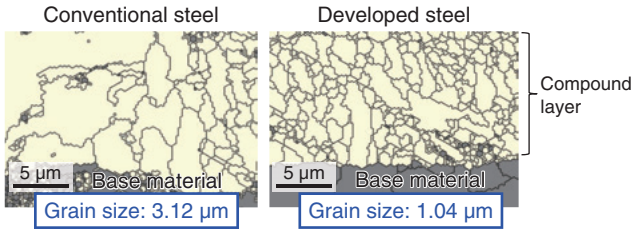


Fig. 26 EBSP analysis of compound layer

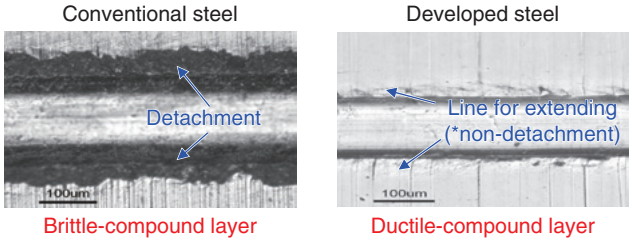


Fig. 27 Compound layer of developed steel and conventional steel after scratching test

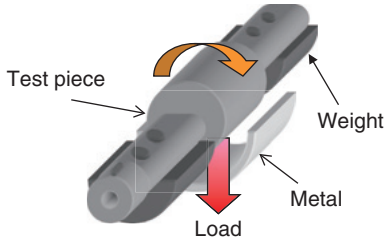


Fig. 28 Abrasion test of shaft

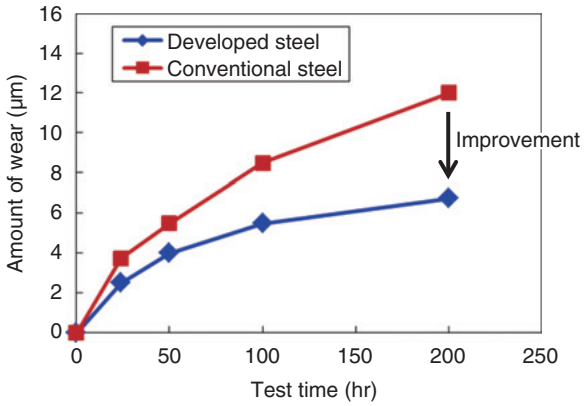


Fig. 29 Relation between test time and wear amount

6. Conclusion

A high-strength and high-wear-resistance nitrocarburizing steel has been developed using Mo-V carbonitride precipitation strengthening. The development produced the following findings:

(1) Using Mo-V carbonitride precipitation strengthening, it was possible to control the hardness of the base material to 270 Hv during machining and to achieve high hardness levels of 300 Hv or higher following nitriding, thus realizing high strength without sacrificing workability.

(2) The use of a bainite microstructure made it possible to maintain Mo and V in a state of solid solution following forging and cooling, helping to enable the realization of the maximum Mo and V age-hardening ability.

(3) The high strength achieved through the addition of Mo and V resulted from the high lattice strain produced by the precipitation of fine (about 8 nm) Mo-V precipitates coherent with the Fe lattice in the nitrided layer that forms during nitrocarburizing and the base material.

(4) The precipitation of Mo-V carbonitrides in the compound layer refined and increased the strength of the layer, helping to enable the realization of a compound layer displaying good wear resistance.

References

(1) Iwama, N.: Trend of Special Steel for Automotive Parts, JSAE, Vol. 55, No. 10, p. 64-68 (2001)

(2) Suzuki, N., Tani, K..: Recent Trend of Nitrided Products, Journal of the Japan Society for Heat Treatment, Vol. 32, No. 5, p. 262-266 (1992)

(3) Suwa, S., Kawaguchi, D., Murakami, A., Kimura, K., Tada, M.: Development of High-strength, Nitrocarburized Crankshaft with Control of Vanadium Carbonitride Precipitation by Normalization, Honda R&D Technical Review, Vol. 22, No. 1, p. 60-67

(4) Ogata, K.: Improvement of HCCI Combustion Stability by Detecting Rotational Fluctuation, JSAE, Vol. 66, No. 2, p. 15-20 (2012)

(5) Kurebayashi, Y.: Recent Trends of Surface Hardening Technology and High Strength Steel, Nishiyama Kinen Gijutsu Koza, The Iron and Steel Institute of Japan, p. 83-118 (2006) (in Japanese)

(6) Takitani, Y., Saito, I., Miyazaki, T., Kamiya, K.: Development of Nitrocarburized High-strength Crankshaft with No Rare Metals Added, Honda R&D Technical Review, Vol. 23, No. 2, p. 70-75

(7) Nomura, I.: Metallurgical Technology in Microalloyed Steels for Automotive Parts, Material Japan, Vol. 34, No. 6, p. 705-709 (1995)

(8) Hamazaki, A., Kobayashi, Y.: Current State of SMI's Die Forged Products for Automobiles, SUMITOMO METALS, Vol. 48, No. 4, p. 49-59 (1996)

(9) Kobayashi, M., Sakurada, T., Okabe, I.: Prediction Method of Fatigue Strength of GAS Soft-Nitrided and Ion Nitrided Steels, Transaction of the Japan Society of Mechanical Engineers, Series A, Vol. 62, No. 597, p. 1132-1139 (1996)

(10) Kimura, K., Takada, K., Hobo, M.: Effect of Alloying Element on Age-Hardening Characteristic of Mo-V added Low Carbon Steel, DENKI-SEIKO, Vol. 79, No. 1, p. 61-67 (2008)

(11) Nishizaka, T., Sato, Y.: A study on the Preventive Method of Fretting Corrosion Damage, Journal of Japanese Society of Tribologists, Vol. 40, No. 9, p. 768-775 (1995)

(12) Inoue, K., Matsumura, Y.: Influence of Alloying Elements on Hardness Distribution after Nitrocarburizing in Medium Carbon Steel, DENKI-SEIKO, Vol. 75, No. 1, p. 11-18 (2004)

(13) Onda, H., Asai, T., Fujiki, K., Kudo, H., Murofushi, K.: Development of High-strength Induction Hardened Crankshaft, Honda R&D Technical Review, Vol. 15, No. 2, p. 175-182

■ Author ■



Hiroki MASUDA



Hideki MATSUDA



Ayumi YAMAZAKI

Development of High-performance Engine Plant Model and Sequential System Identification Environment for Realization of Model-based Development

Shigeki FUJIMOTO* Yoshiyuki OHTAKA* Satoshi KODO*

ABSTRACT

Attempts to realize more efficient development by combining the V-model, a method used in software development, with model-based development (MBD) are proceeding among automotive manufacturers. The design and test processes for this combined development method are organized into corresponding levels, and different plant models are used for each level. Attempts to employ an MBD-V-model combination in engine development presented the issues of mismatches between models on the same level, and lack of consistency between models on different levels. A high-performance plant model able to be used in both design and test procedures on the same level was therefore developed, and an environment was created making it possible to use consistent plant models at all levels by means of sequential system identification of models for different levels. The functioning of models generated by this environment was studied in MILS and HILS environments, verifying the effectiveness of the developed environment.

1. Introduction

The V-model, which organizes the relationship of correspondence between design procedures and test procedures as a V shape, has been applied in standard software development[1] for some time.

In the V-model shown in Fig. 1,[2] processes are represented as an aligned diagram, with the design process in the left half of the diagram moving to the lower right, and the test process in the right half of the diagram moving to the upper right. In addition to expressing the software development process as a whole through the connection between processes, the diagram shows which aspect of the design process corresponds to which procedure of the test process via the relationship between left and right. Test procedures verify and validate the achievement of the demands set for the corresponding design procedure.

The vertical divisions of the left-right relationships of correspondence are termed levels. Goals and focal perspectives differ for each level, and design demands and test items therefore also differ.

Model-based development (MBD) has attracted attention as a means of helping to enable front-loading in order to increase the speed and quality of developments.[3] In MBD of standard control ECU, the controller and the functions of the plant that represent the object of control are modeled, and these models are employed in each procedure from the initial stage of development. Using these models, some of the verification procedures that had previously been conducted during the test process can be front-loaded in the design process, reducing the burden represented by extensive reworking such as modification of specifications, thus increasing the quality of the ECU and reducing development time.

Today, efforts to increase the efficiency of model use by combining V-model-based development and MBD and creating models for each level of the V-model are being advanced by automakers.[4]

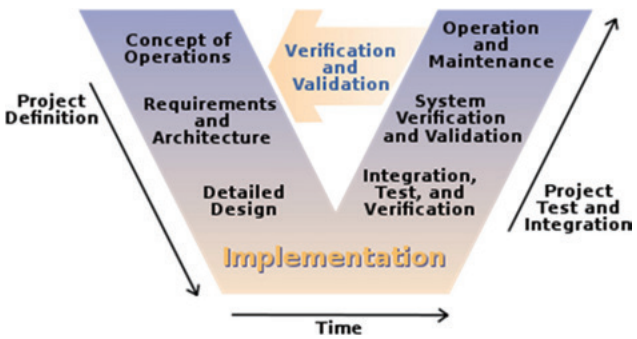


Fig. 1 Standard V-model

* Automobile R&D Center

Honda has also been working to push ahead with such an MBD-V-model fusion for some time. Figure 2 shows an overview of the combination of MBD and V-model-based development in an engine development process. The levels for the V-model are, from the top, vehicle, system, hardware and controller, and implementation. This development represented an attempt to realize a development process using models fitted to the goals of the procedures conducted at each of these levels.

However, in implementing this MBD-V-model combination, the plant models used to model the engine, the object of control, presented certain issues.

One of these was the fact that the plant models for the same level did not match. In order to front-load verification procedures in a development using an MBD-V-model combination, it is necessary to employ identical plant models for the same level. However, at the controller level, because there were severe restrictions on the speed of computation demanded from the plant model on the test process side due to use of a real-time simulator in the hardware-in-the-loop simulation (HILS), it was challenging to use the same plant model in the model-in-the-loop simulation (MILS) on the design process side.

The second problem was inconsistency between plant models for different levels. Conventionally, because goals and focal perspectives differ for each level, unique plant models have been formulated for each level and used in the development. Because of this, consistency has not been achieved between the behavior of plant models for different levels, and it has not been possible to directly reflect system conditions studied using plant models for the system level at the controller level. As a result, it has been challenging to front-load controller verification using MBD.

In order to resolve these two issues, a high-performance plant model able to be used for the controller level in both the design and test processes was first developed, following which an environment was created in which the behavior of different plant models could be harmonized between levels by employing this model in sequential system identification from the system level. This paper will discuss this development.

2. Development Goals

This section discusses the necessary conditions for the developed high-performance engine plant model (HPEM), provides an overview of the sequential system identification environment, and discusses the criteria established for judgment of the realization of goals.

2.1. Necessary Conditions for HPEM Development

For the development of a plant model able to be used in both HILS and MILS at the controller level, certain necessary conditions existed for model behavior and computation speed.

Necessary conditions for model behavior will be considered first. Due to increases in the number of actuators and sensors needing to be controlled and the need to respond to stringent laws and regulations, the complexity of control logic is increasing in today's engines. To take air-fuel ratio feedback control applied in order to respond to exhaust gas regulations as an example, control logics based on adaptive control theory using state estimators are being employed,[5] and in order to verify the functioning of these control logics, it is necessary for engine plant models to be able to reproduce dynamic behavior (dead time and lag elements) along with the course of time.

Necessary conditions for computation speed will now be considered. The purpose of HILS is to verify the functioning of ECUs. It operates in real time, using actual ECUs connected to a computer input with plant models.

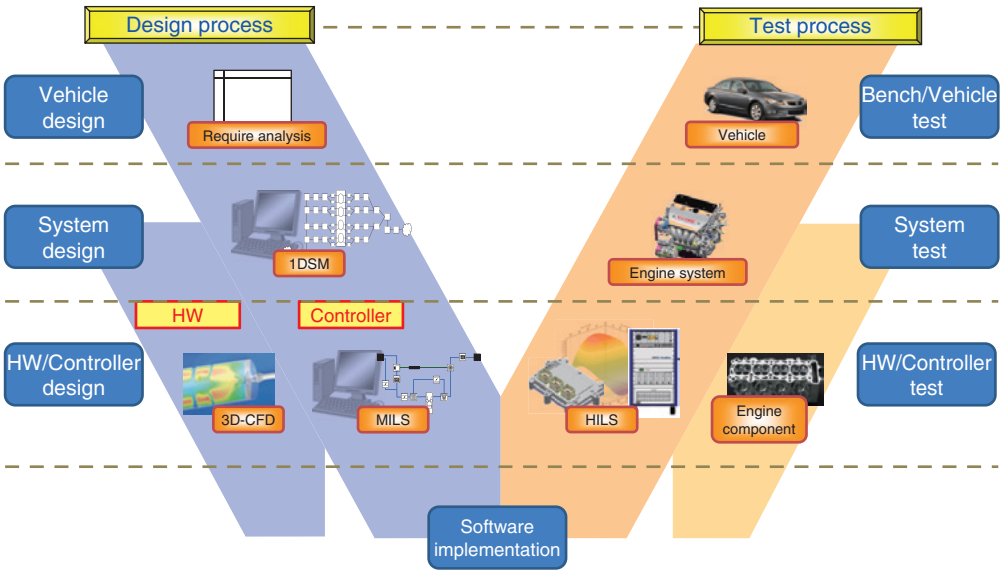


Fig. 2 Model-based development combined with V-model

Because of this, if the computation load for the plant models input to the computer is high, the engine state cannot be calculated in real time, and it is not possible to verify ECU performance. Whether calculations can be conducted in real time or not is dependent on the performance of the computer, but the processing power of real-time simulators available on the market at present is basically equivalent to that of standard PCs. It is necessary to formulate plant models that are able to conduct calculations in real time under these computation speed conditions.

Based on these necessary conditions for model behavior and computation speed, an HPEM was developed by customization of a standard mean value engine model (MVEM)[6] in response to engine specifications.

2.2. Overview of Sequential System Identification Environment

This section will discuss engine plant models and the purpose of their use.

2.2.1. 1D simulation model (1DSM)

The 1DSM is a model that performs computational fluid dynamics (CFD) analysis in the radial direction only. The model has a light computation load in comparison to 3D CFD, and is able to predict the performance of a system as a whole. Because of this, it is used in the system design process, chiefly for the consideration of intake and exhaust specifications, driving cycle of fuel efficiency calculations, and simple combustion evaluations.

2.2.2. Mean value engine model (MVEM)

This model averages and calculates the output of each combustion cycle on the time axis using a lumped parameter system that does not consider spatial extension. Because it does not perform CFD calculations, its computation load is even lighter than that of the 1DSM. However, the model cannot reproduce behavior for each crank angle, and therefore is not useful in hardware design. For this reason, it is used in MILS in the controller design process as a model for verification of control logic operation.

2.2.3. MAP engine model

A MAP engine model is a model that expresses the characteristics of each component of the engine as a simple map of input and output based on test results. These models are able to refer to values for the various engine states at high speeds, but to formulate the models it is necessary to perform measurements for all engine operating states or prepare calculation data in advance. These models are used in HILS for the verification of ECU performance in the controller test process, but today, when the number of actuators and sensors being employed is increasing, it is difficult to exhaustively input all engine states, and the models are therefore chiefly used in a limited range of applications, specifically debugging of control logic and verification of on-board diagnosis.

2.2.4. Flow of sequential system identification

The project discussed in this paper focused on the flow of controller development, and created an environment able to harmonize the behavior of different plant models between levels by using HPEM to perform the roles of MVEM and MAP engine models and sequentially identifying 1DSM and HPEM from an existing engine.

Figure 3 shows the flow of sequential system identification proposed in this project in order to harmonize plant models between levels. This figure shows the model

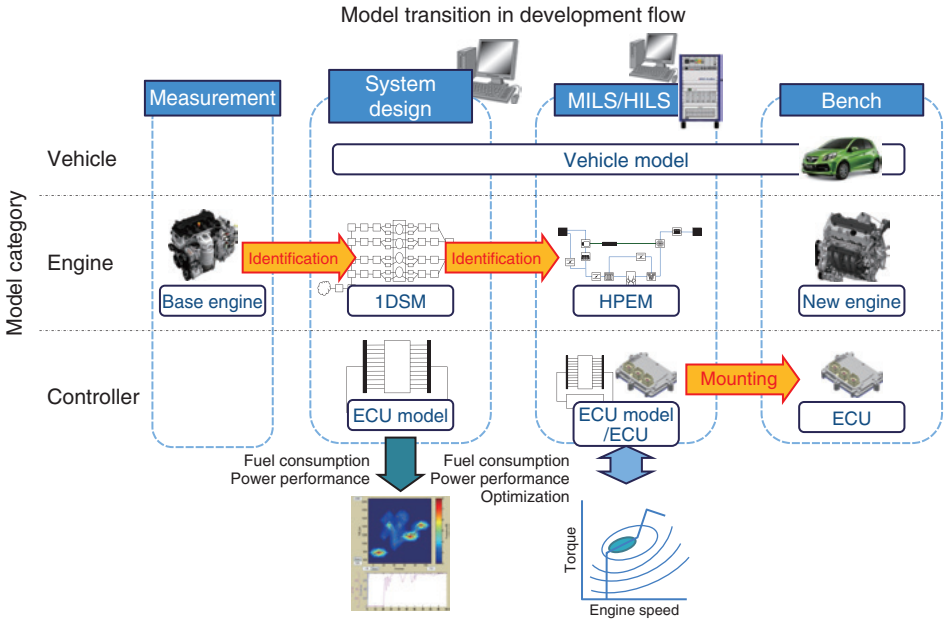


Fig. 3 Identification flow for engine plant model

categories and the transformation of the models in the development process. Considering the engine plant models that are the control objects, first a 1DSM is identified from bench measurement results for an existing engine. Next, the specifications of the 1DSM are changed to match the engine in development. Following this, the HPEM is identified from calculation results produced by the modified 1DSM. The use of the plant model obtained by means of this sequential identification in HILS and MILS makes it possible to directly reflect system conditions verified at the system level at the controller level, thus helping to enable front-loading of verification of ECU performance.

2.3. Criteria for Judgment of the Realization of Goals in Plant Models

The verification procedures and criteria for judgment of the realization of goals used to verify the validity of the sequential system identification environment and the HPEM discussed in Section 2.1 are discussed below.

2.3.1. Criteria for sequential system identification

In order to verify the functioning of the sequential system identification environment, first the results of identification of an existing engine and a 1DSM were compared in order to determine whether error fell within an acceptable range. The results of identification of 1DSM and an HPEM were then compared, and it was similarly determined that error was within an acceptable range. As criteria for judgment of the realization of goals, the range of error for the comparison of the existing engine and the 1DSM was set at an error of within 3% for the intake and exhaust system, and the range of error for the comparison of the 1DSM and the HPEM was set at an error of within 3% for BSFC.

The criterion for the comparison of the existing engine and the 1DSM was limited to the intake and exhaust systems because the combustion system of the 1DSM directly incorporated measurement results for the existing engine as empirical formulae, and therefore there was no need for a comparison of accuracy. The range of acceptable error was set at 3% in each case because the variation in measurements on an actual engine bench is around 3%, and if this figure were achieved, the plant model could be considered to have achieved sufficient accuracy as a control object.

2.3.2. Criteria for HPEM

In order to verify the performance of the HPEM, the plant model obtained through sequential system identification was first employed in MILS with a simple ECU simulation, and its operation was verified in each of the driving cycles used for calculation of fuel efficiency. Next, the same plant model was used in HILS, and its operation was again verified, this time connected to a real ECU. The criterion for judgment was the ability to conduct calculations in real time in the largest time steps for convergence of the calculations, using an HIL simulator available in the market. This was because the performance verification focused chiefly on the plant model's ability to function in actual use despite the fact that the time steps for convergence of calculations differ depending on the types of models and solvers employed in the computation.

3. Development of HPEM

3.1. Composition of HPEM

By contrast with the 1DSM used in the system design process, which successively calculates the intake and exhaust air and combustion state for each crank angle, a standard MVEM is an average value model that averages output for each combustion cycle on the time axis. Because MVEM do not conduct one-dimensional or three-dimensional CFD calculations, their computation load is low, and by contrast with MAP engine models, they are able to express dynamic behavior through the use of differential equations. For these reasons, they are employed as control object models during controller design.

In order to reduce the computation burden for the HILS, using an MVEM as a base, the HPEM empirical formulae and response surfaces created from formulae and measurement values widely known from standard textbooks and papers were sorted through based on considerations of calculation accuracy and computation load. With regard to the expression of characteristics by means of the formulae, the throttle valve, intake manifold, cylinder, exhaust manifold, turbine, compressor, intercooler, catalyzer and other parts were modeled individually in detail to make it possible to reflect the predicted values from the 1DSM (Fig. 4). Simplification of the large number of formulae employed for the individual components using formula processing software further reduced the computation load, and helped enable calculations to be performed in real time.

3.2. Overview of HPEM Calculations

The HPEM is composed of an intake and exhaust system model that calculates the flow of air and EGR gas and a combustion system model that performs calculations for combustion in the cylinders. Calculations are performed with the engine speed and ECU command values as the points of origin.

Air is taken into the cylinders by means of engine rotation, and this reduces intake manifold pressure. Indicated mean effective pressure (IMEP) is calculated from the volume of air taken into the cylinders and ECU command values fuel injection amount and ignition timing, and engine speed is calculated from this IMEP, pumping mean effective pressure (PMEP), friction mean effective pressure (FMEP), and load torque from the transmission and the engine's moment of inertia. In addition, turbine and compressor work is calculated from the exhaust gas from the cylinders and the degree of opening of the wastegate, an ECU command value, and the intake air is supercharged. The volume of air passing through the throttle is calculated from this supercharging before and after the throttle, the intake manifold pressure, and the opening of the throttle valve, an ECU command value.

3.2.1. Intake system model

The intake system model is a zero-dimension model using a lumped parameter system that does not consider spatial extension. Using equations of state for gases (PV = mRT), equations of continuity (conservation of mass), the relationship of quantity of heat, and orifice equations, this model is made up of receivers and orifices.

The throttle model formulae[6] are shown below for reference.

$$\dot{m} = C_d \cdot A(t) \cdot \frac{p_{in}(t)}{R \cdot \vartheta_{in}(t)} \cdot \Psi\left(\frac{p_{in}(t)}{p_{out}(t)}\right)$$

$$\Psi\left(\frac{p_{in}(t)}{p_{out}(t)}\right) = \begin{cases} \sqrt{\kappa\left[\frac{2}{\kappa+1}\right]^{\frac{\kappa+1}{\kappa-1}}} & \text{for } p_{out} < p_{cr} \\ \left(\frac{p_{out}}{p_{in}}\right)^{\frac{1}{\kappa}} \cdot \sqrt{\frac{2\kappa}{\kappa-1} \cdot \left[1-\left(\frac{p_{out}}{p_{in}}\right)^{\frac{\kappa-1}{\kappa}}\right]} & \text{for } p_{out} \geq p_{cr} \end{cases}$$

$$p_{cr} = \left(\frac{2}{\kappa+1}\right)^{\frac{\kappa+1}{\kappa-1}} \cdot p_{in}$$

t : Time
$\dot{m}(t)$: Mass flow through the valve
c_d : Discharge coefficient
$A(t)$: Open area of the valve
$p_{in}(t)$: Pressure upstream of the valve
$p_{out}(t)$: Pressure downstream of the valve
p_{cr} : Critical pressure where the flow reaches sonic conditions
R : Gas constant
$\vartheta_{in}(t)$: Air temperature
κ : Ratio of specific heats

3.2.2. Combustion system model

The combustion system model calculates in-cylinder pressure by substituting rate of heat generation and cylinder capacity defined by empirical formulae in the first law of thermodynamics, equations of state, and relationships of specific heat, and calculates IMEP by integrating this in-cylinder pressure based on changes in volume. This combustion model is also able to calculate changes in output due to ignition timing and combustion parameters such as location of 50% mass fraction burned and amount of heat generation.

4. Construction of Sequential System Identification Environment

Generally speaking, two methods of system identification are available depending on the object of the identification.

The first of these is gray box model identification. A gray box model is a model described by formulae based on the physical equations that govern the object of identification when the system structure is almost entirely clear. Parameters also exist for which the physical characteristics cannot be measured via this model, and system identification is conducted in order to estimate these parameters. This method is termed correlation.

The other method is black box model identification. A black box model is modeled based exclusively on numerical relationships in input and output without consideration of details of what is actually occurring in a system when the system structure is unclear or complex, making description difficult. For the identification of these models, approximation equations are formulated to match input and output using methods including the least squares method. This method is called response surface generation.

Depending on the characteristics of the individual

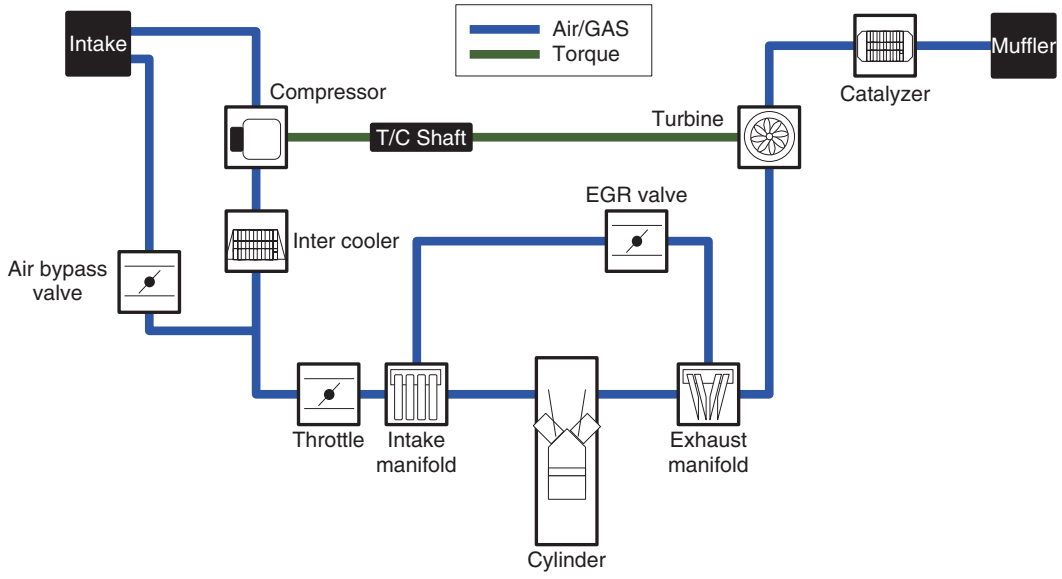


Fig. 4 High Performance Engine Plant Model (HPEM)

sections of the plant models, the correlation described above and the generation of response surfaces were employed in combination in the sequential identification of the 1DSM and HPEM from the existing engine.

Turning to actual identification procedures, first, the flow of identification of the engine intake and exhaust systems is shown in Fig. 5(a). Initially, correlation was performed with the cylinder wall temperature of the 1DSM as an identification parameter in order to match the volumetric efficiency of the 1DSM with the volumetric efficiency of the actual engine, set as an index value, within a specified range of error. The optimum value search method using a genetic algorithm (GA) was employed as the correlation algorithm. Next, response surfaces for the volumetric efficiency characteristic were generated from the 1DMS using Design of Experiments (DOE), with engine speed, target intake air pressure, ignition timing, VTC and other parameters as design variables. The formulae generated here were incorporated in the HPEM.

Figure 5(b) shows the flow of identification of the combustion system. Response surfaces for combustion center of gravity and combustion period are generated from the in-cylinder pressure waveform measured in the existing engine, with operation amounts that affect the combustion state as design variables. The equations for these response surfaces were incorporated in the Wiebe equations[7] in the 1DSM combustion model. The identification parameters were correlated using a GA to match the output of the HPEM combustion model with the output for combustion from the 1DSM, set as an index value, within a specified range of error.

Finally, parameters such as the detailed characteristics of each component and friction loss were determined by sequential system identification for the existing engine, 1DSM and HPEM, and engine plant models were produced in which output torque and BSFC matched within an acceptable range of error.

5. Operational Verification of Plant Model

Studies were conducted to verify the effectiveness of both the HPEM and the sequential system identification environment.

5.1. Verification of Effectiveness of Identification

In order to verify the effectiveness of the sequential system identification environment, the results of system identification for the intake and exhaust systems of a prototype engine and the 1DSM were first compared. Figure 6 shows a comparison of volumetric efficiency for the engine and the model.

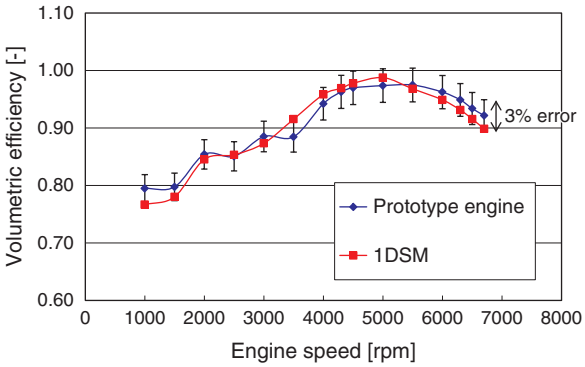


Fig. 6 Comparison between prototype engine and 1DSM

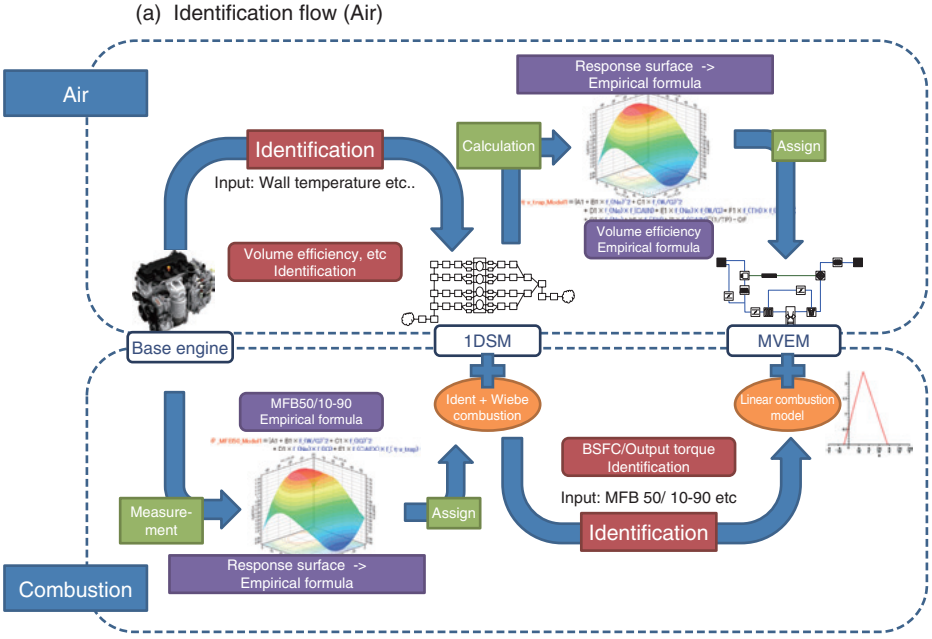


Fig. 5 Identification flow

The horizontal axis of the graph shows engine speed, and the vertical axis shows volumetric efficiency. These results indicate that error is within the acceptable range of up to 3%.

Next, the results of system identification for the 1DSM and the HPEM were compared. Figure 7 shows the results of a comparison of BSFC for both models. Results for BSFC are similarly within the acceptable range of error of up to 3% at all engine speeds.

In addition to this, input and output was studied for each component, and the behavior of the plant models was found to match within the acceptable range of error.

5.2. Verification of Effectiveness of Model

In order to verify the functioning of the HPEM, the plant model following sequential system identification was first employed in an MILS with a simple controller model, and its operation was verified in driving cycles employed for the calculation of fuel efficiency and acceleration performance. Next, the same plant model was employed in an HILS (the configuration will be discussed below), in which it was connected to an actual ECU, and put through the same operational verification.

Figure 8 shows the configuration of the HILS. The ECU and a real-time simulator were connected by means of a load rack. The load rack functioned to supplement signals that it was difficult to model in the simulator through actual devices, and contained elements including a linear solenoid, an injector, DBW, a heater resistance and a dummy load resistance.

Figure 9 shows results obtained by operating the prototype engine and the HILS plant model in two different fuel efficiency driving cycles, JC08 and NEDC. The volume of intake air for the engine bench and the HILS were compared for both operating driving cycles. The engine plant model displayed dynamic behavior close to that of the actual engine in both driving cycles, indicating that it possesses sufficient accuracy to be used in the verification of ECU performance without necessitating the employment of specific driving cycles.

Figure 10 shows the computation time for the HILS using the plant model. The graphs show how much actual computation time was necessary for each time step. The verification that produced these results used a sampling time of 200 μsec in order to converge the calculations. The computation time for the plant model for each sample in both driving cycles was less than 90 μsec, indicating the achievement of sufficient computation speed for real-time computation.

The results discussed above demonstrate that the developed HPEM realizes sufficient accuracy and computation speed for use in both the MILS and HILS employed in the controller level of the design and test processes.

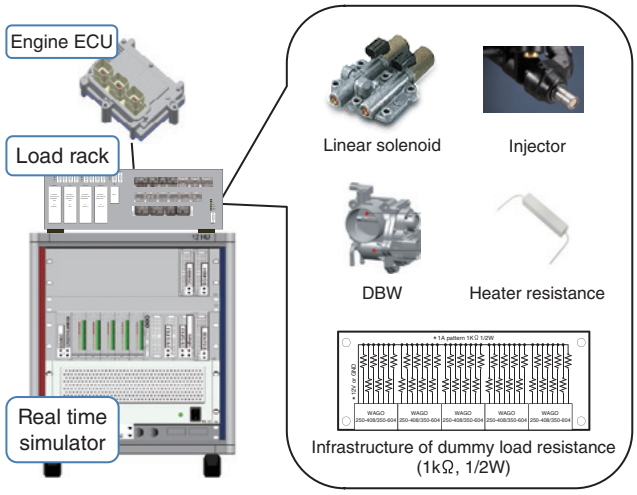


Fig. 8 Hardware-in-the-Loop Simulation (HILS)

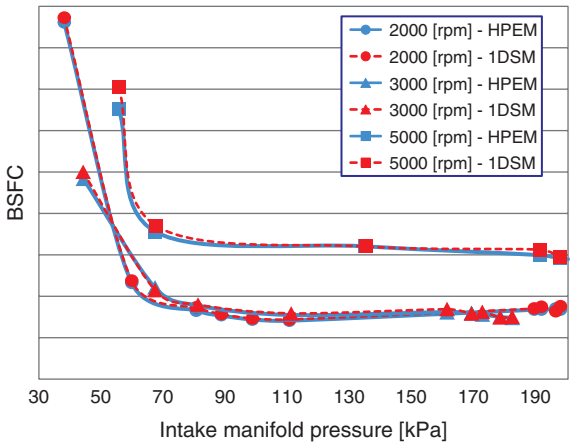


Fig. 7 Comparison of 1DSM and HPEM

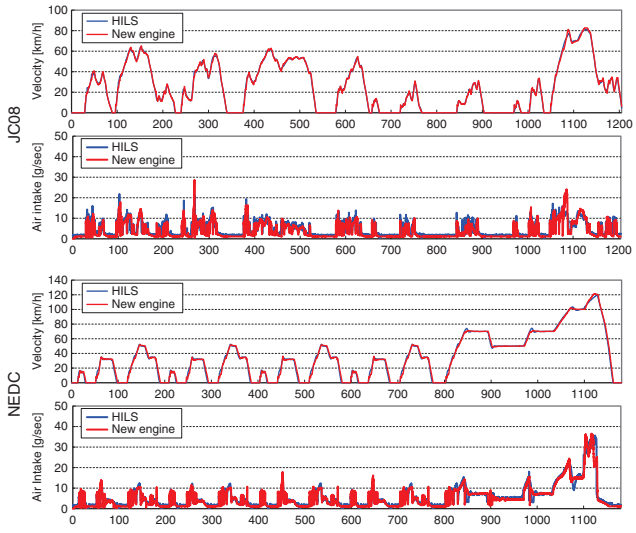


Fig. 9 HIL simulation result

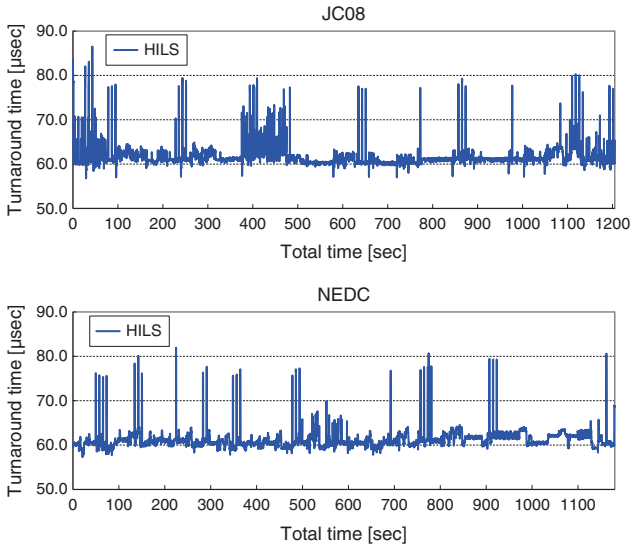


Fig. 10 Turnaround time of HIL simulation

6. Conclusion

In order to address the plant model-related issues of mismatches between models at the same level and inconsistency between models at different levels when realizing a combination of MBD and V-model-based development at Honda, the following technologies were developed and their effectiveness was verified.

(1) An HPEM able to be used in both the design and test processes at the controller level was developed, and its functioning was verified in MILS and HILS. This technology made it possible to realize a match between models at the same level.

(2) An environment making possible sequential system identification of 1DSM and HPEM from an existing engine was created, helping to enable the realization of consistency between models at different levels.

7. Afterword

The use of the developed HPEM and sequential system identification environment is expected to increase the efficiency of developments employing a combination of MBD and V-model-based development. In future the effectiveness of combined MBD and V-model-based development will be verified through the use of new control logics created using the new environment in developments.

The continued operation and management of these environments will be important in attempting to ensure that the combination of MBD and V-model-based development takes root. The education of engineers will also raise numerous issues, and the authors believe that it will be necessary for all development staff to share a vision of the future and strategically promote the new development method in order to address these issues.

References

(1) Forsberg, K., Mooz, H.: The Relationship of Systems Engineering to the Project Cycle, First Annual Symposium of the National Council on Systems Engineering (1991)

(2) Federal Highway Administration: Clarus Concept of Operations, FHWA-JPO-05-072, p. 20 (2005)

(3) Schatz, B., Pretschner, A., Huber, F., Philipps, J.: Model-based Development of Embedded Systems, Advances in Object-Oriented Information Systems, p. 331-336 (2002)

(4) Information-technology Promotion Agency, Japan: Kumikomi shisutemuno sentanteki moderubesu kaihatsu jittai chosa, Research report (2012) (in Japanese)

(5) Hasegawa, Y., Akazaki, S., Komoriya, I., Maki, H., Nishimura, Y., Hirota, T.: Individual Cylinder Air-Fuel Ratio Feedback Control Using an Observer, SAE Technical Paper 940376 (1994)

(6) Guzzella, L., Onder, C.: Introduction to Modeling and Control of Internal Combustion Engine Systems, Springer (2010)

(7) Wiebe, I. I.: The Combustion Speed in Internal Combustion Piston-Engines-fuel combustion rate equation combining an empirical and a theoretical approach, Collected works of piston engine research, Laboratory of Engines, Academy of Science (1956)

■ Author ■


Shigeki FUJIMOTO


Yoshiyuki OHTAKA


Satoshi KODO

Estimation of CO_2 Reduction Potential by Traffic-flow Smoothing and Eco-driving Promotion

Hidetoshi IMAIZUMI* Koji SENGOKU**

ABSTRACT

A case study was conducted by analyzing floating car data from throughout Japan to determine the CO_2 reduction potential due to traffic-flow smoothing and eco-driving promotion. The data used in this study is from hybrid cars equipped with Eco Assist, which has been reported in past studies to enhance fuel economy by approximately 10% as the number of driving times increases. First, multiple regression analysis was performed on the subject floating car data to obtain a polynomial with fuel economy as the explained variable and items related to traffic flow and eco-driving as the explanatory variables. The explanatory variables set the present distribution and the distribution under the assumed conditions of eco-driving promotion and smoothed traffic flow. These assumed conditions were applied to the polynomial to obtain the fuel economy frequency distributions for the present and assumed conditions, and the CO_2 reduction potential was calculated from the difference between the two. The assumed conditions were calculated to have a fuel economy enhancement potential of 18%, mainly due to traffic-flow smoothing. On the other hand, eco-driving was calculated to have fuel economy enhancement potential of 1% over and above the approximately 10% enhancement of Eco Assist. In addition, it was found that 2/3 of the CO_2 reduction potential was enhancement when driving at a travel speed of 30 km/h or less.

1. Introduction

In response to rising sentiment to reduce greenhouse gases and energy consumption, countries are strengthening fuel economy regulations in the passenger car sector. On the other hand, the importance of integrated approaches is being recognized in addition to enhancing the catalog fuel economy of individual cars. These approaches include diversification of fuels, promotion of efficient use such as eco-driving, traffic-flow smoothing, and other measures aimed at increasing fuel economy during actual driving.

The effects of lecture courses, virtual training systems, Eco Assist, aftermarket fuel economy meters, and other eco-driving aids have been individually evaluated, and fuel economy enhancement effects of 10% to 30% have been reported[1, 2]. In addition, various fuel economy enhancement effects have also been reported for individual traffic-flow-smoothing measures such as changes to signal control, road construction, Intelligent Transport Systems (ITS), and Traffic Demand Management (TDM)[3-5]. However, these effects depend largely on traffic conditions, and little data could be obtained correlating overall traffic flow and fuel economy for Japan. For this reason, no studies thus far have quantified the overall CO_2 reduction potential for Japan.

However, the authors analyzed driving data on public roads obtained from onboard GPS navigation systems that use wireless communication such as mobile phone lines, and calculated the CO_2 reduction potential under the assumed conditions of eco-driving promotion and smoothed traffic flow[6].

In addition to calculating the CO_2 reduction potential, this study also analyzed this potential to clarify how cars should be used to achieve greater fuel economy enhancement and CO_2 reduction effects.

2. Overview of Analysis Subject Data

2.1. Analysis Subject Cars

This study analyzed the floating car data of hybrid cars. Table 1 shows the specifications of the subject hybrid cars. These cars are equipped with the Ecological Drive Assist System (Eco Assist).

Eco Assist consists of an ECON mode function that performs control with priority on fuel economy simply by pressing an ECON switch such as shown in Fig. 1,

* Automobile R&D Center

** Honda Motor Co., Ltd.

Table 1 Specifications of hybrid cars

Type	1.3L i-VTEC+IMA
Number of engine cylinders and layout	Inline-4
Max. engine output	65 kW
Motor type	Synchronous motor
Max. motor output	10 kW
Transmission	CVT
Vehicle weight	1130 - 1150 kg

a coaching function that displays whether fuel-efficient driving is being performed in real time using a meter such as shown in Fig. 2, and a teaching function that scores the driver's eco-driving level and gives advice such as shown in Fig. 3 and Fig. 4.

It has been reported[1], through analysis of the fuel economy data from 5000 cars for the half-year immediately after new car delivery, that Eco Assist provides fuel economy enhancement effects of approximately 10% as shown in Fig. 5. This study calculated the additional CO_2 reduction potential due to eco-driving over and above this fuel economy enhancement of approximately 10% due to Eco Assist.

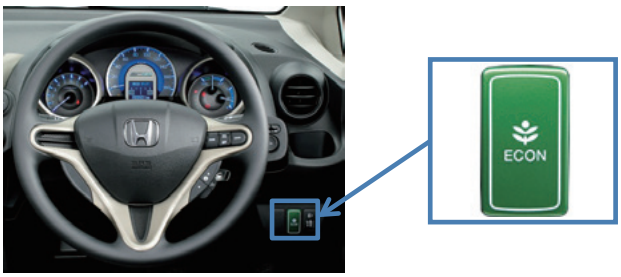


Fig. 1 ECON switch

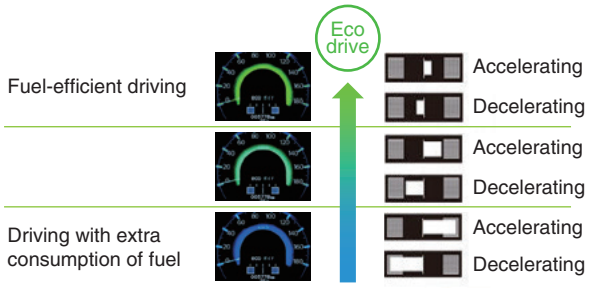


Fig. 2 Real-time fuel-efficient driving guidance at speedometer



Fig. 3 Display scores current driving performance

2.2. Floating Car Data

A traffic information system using floating car data (hereafter, "data") commenced service from 2003. This system collects and processes link travel times for roads driven by members at the Internavi Information Center, and distributes link travel times to the GPS navigation systems of each member as per request to complement the Vehicle Information and Communication System (VICS) data and recommend the ideal route (Fig. 6).

In addition, fuel consumption amounts and other data are also transmitted from some members' cars to the Center



Fig. 4 Advice for enhancing fuel economy at Internavi system display

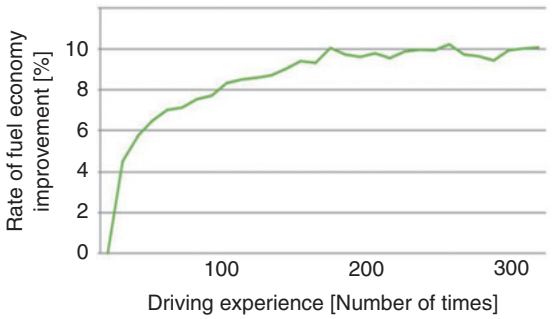


Fig. 5 Effect of fuel economy improvement due to the eco-assist system

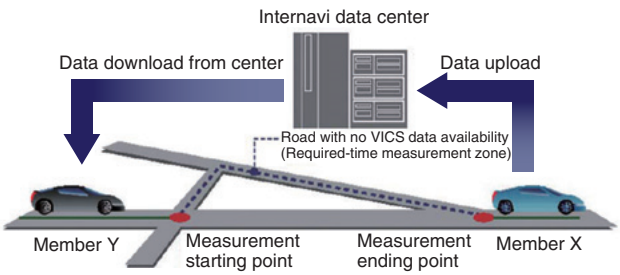


Fig. 6 Chart of floating car data traffic information system

where the data is analyzed to provide information such as fuel-saving routes to members.

The data uploaded from members comprised approximately 2 million km per day on weekdays and approximately 2.9 million km per day on weekends, and the cumulative distance exceeded approximately 1.8 billion km by the end of 2010. Figure 7 is a visualization of the data uploaded from members on August 15, 2009, and shows that data can be acquired from throughout Japan.

This study analyzed data comprising a total travel distance of 78.82 million km collected from hybrid cars throughout Japan from October 2010 to June 2011. The analyzed data consisted of various types of data acquired while driving, averaged in daily units such as the average fuel economy per day and average speed per day of each vehicle.

2.3. Relationship between Present Traffic Flow and Fuel Economy

Figure 8 shows the relationship between the average travel speed, fuel economy and driving amount obtained from the acquired data. Note that in this paper, fuel economy is expressed as a fuel economy index obtained by dividing each fuel economy value (L/km) by the overall average fuel economy γ (L/km).

The average travel speed in the data was 34.3 km/h, which is nearly the same as the average travel speed of 36.4 km/h during the 12-hour daytime period in the 2010 road traffic census, which is a survey conducted by the Ministry of Land, Infrastructure, Transport and Tourism every five years. However, the driving frequency was found to peak between 20 to 30 km/h instead of near the average travel speed.

In addition, the fuel economy index was also widely distributed, and exhibited higher values over a wider distribution as the travel speed decreased.

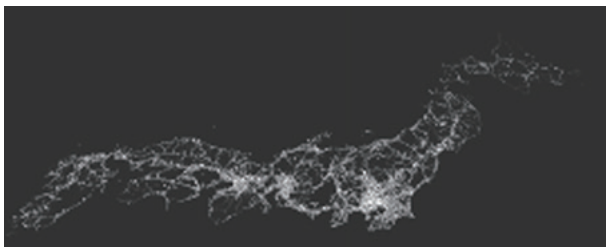


Fig. 7 Visualization of floating car data

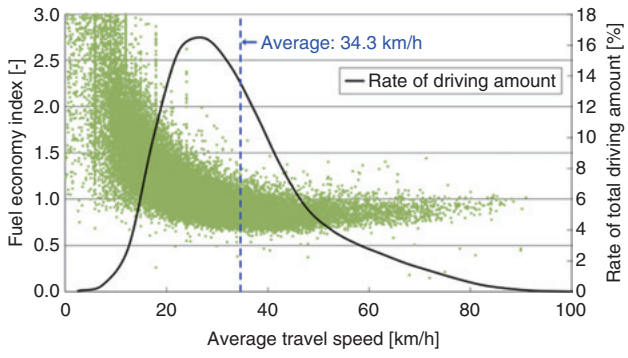


Fig. 8 Average travel speed and fuel economy index

3. Method for Calculating CO_2 Reduction Potential

3.1. Overview of Calculation Method

The method of calculating the CO_2 reduction potential due to eco-driving promotion and traffic-flow smoothing, and the method for clarifying how cars should be used to achieve greater fuel economy enhancement and CO_2 reduction effects are described below.

3.1.1. Calculation of CO_2 reduction potential

This study calculated the potential for enhancing the average fuel economy, that is to say the CO_2 reduction potential, from the difference between the fuel economy distributions under the present and assumed conditions as shown in Fig. 9.

The fuel economy distributions under the present and assumed conditions were created by the following method (Fig. 10).

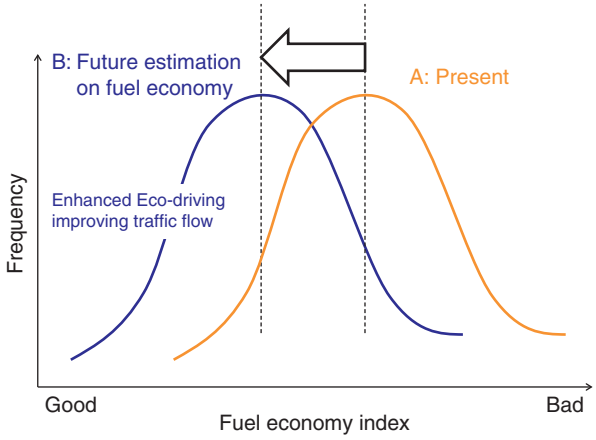


Fig. 9 How to estimate CO_2 reduction potential

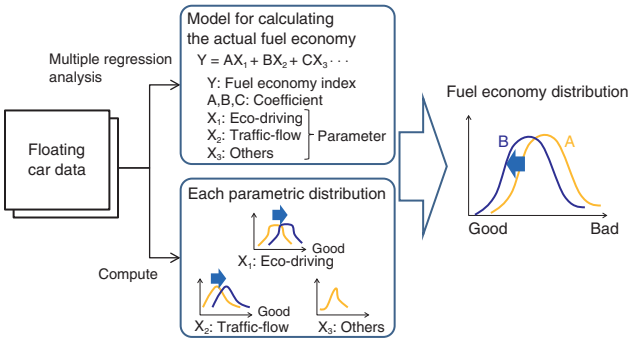


Fig. 10 How to estimate fuel economy distribution

Table 2 In-use fuel economy factors

Factors	Explanatory variable
Efficiency of engine and transmission	Average travel speed
Wasted heat from braking	Acceleration energy equivalent
Driver behavior	Eco-driving rating result
Warm up	Distance Outdoor temperature
Air conditioner	Outdoor temperature
Electricity load	Not adopted
Air pressure in a tire	Not adopted
Road surface, grade	Not adopted
Maintenance defects	Not adopted

(1) Create an actual fuel economy calculation model that includes explanatory variables related to eco-driving and traffic flow by performing multiple regression analysis on the data.
(2) Obtain the distributions of the explanatory variables related to eco-driving and traffic flow from the data.
(3) Apply the distribution of each explanatory variable to the model, and calculate the present fuel economy distribution.
(4) Set the distribution of each explanatory variable under the assumed conditions of eco-driving promotion and traffic-flow smoothing.
(5) Apply the distribution of each explanatory variable to the model, and calculate the fuel economy distribution under the assumed conditions.

3.1.2. Method for calculating fuel economy enhancement and CO_2 reduction distributions

How cars should be used to achieve greater fuel economy enhancement and CO_2 reduction effects was clarified by graphing and analyzing the relationship between each explanatory variable related to eco-driving and traffic flow and the fuel economy enhancement rate and CO_2 reduction amount.

3.2. Creation of Actual Fuel Economy Calculation Model

Data extracted randomly from among the acquired data was analyzed and a multiple regression model that describes the fuel economy index Y was created.

The explanatory variables used were based on factors that may cause fuel economy to drop other than the test mode such as shown in Table 2. These explanatory variables were the reciprocal of the average travel speed τ [s/m], acceleration energy equivalent per unit length A [m/s^2], eco-driving rating results P [pt: points], the reciprocal of the travel distance d [1/m], and the average daily temperature at the starting point T [C°]. Here, the acceleration energy equivalent is the sum total of subtracting the square of the initial speed when accelerating from the square of the arrival speed when accelerating, as described in the study by Oguchi et al.[7] The eco-driving rating results are the driver evaluation results according to the eco-driving index, as calculated by the Eco Assist mounted in the subject hybrid cars (Fig. 11). Note that in addition to the explanatory variables used, there are also other factors that may cause the actual fuel economy to drop, such as electrical load and tire air pressure, but these were not used for reasons of data acquisition.

3.3. Actual Fuel Economy Model

Equation (1) gives the model obtained by multiple regression analysis (multiple correlation coefficient $R = 0.88$, number of data $n = 914$).

$$Y = 0.62 + 10.3\tau + 0.97A - 1.6 \times 10^{-3}P - 7.6 \times 10^{-3}T + 212d \quad (1)$$

Some explanatory variables were not used for reasons of data acquisition, but an extremely high correlation coefficient could be obtained.

Figures 12 to 14 show the relationship between each explanatory variable related to traffic flow and eco-driving and the fuel economy index within the obtained model. Note that in these graphs, the average values are substituted for all other explanatory variables.

This shows that the fuel economy index decreases as the average travel speed increases (Fig. 12).

In addition, the fuel economy index also decreases as the acceleration energy equivalent per unit length decreases



Fig. 11 Vehicle onboard display for eco-driving rating results

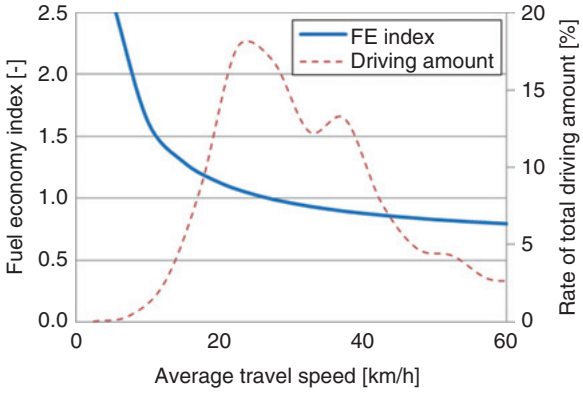


Fig. 12 Relation between average travel speed and fuel economy index for model

(Fig. 13). Furthermore, fuel economy is widely distributed relative to both the average travel speed and the acceleration energy equivalent per unit length, indicating that fuel economy may be increased by enhancing these factors.

On the other hand, the eco-driving rating results distribution is concentrated around a high score (Fig. 14). This is thought to be because the subject hybrid cars are equipped with Eco Assist, and the drivers providing the data have acquired high eco-driving skills.

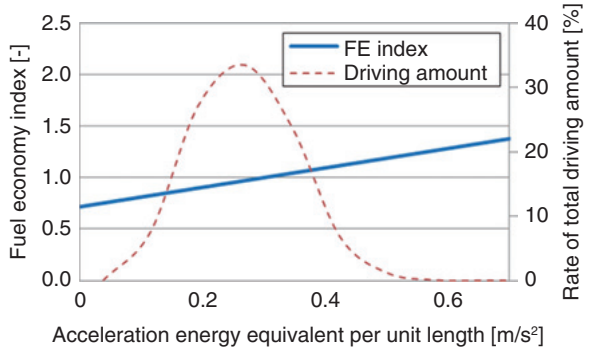


Fig. 13 Relation between acceleration energy equivalent per unit length and fuel economy index for model

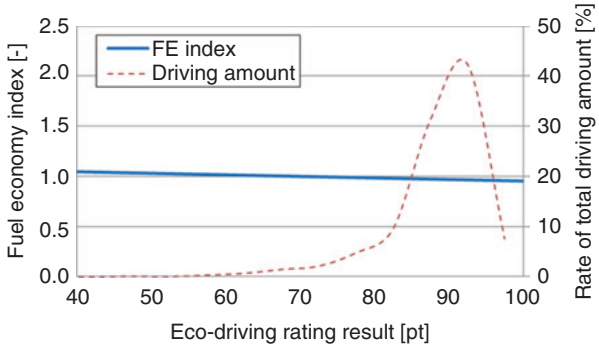


Fig. 14 Relation between eco-driving rating result and fuel economy index for model

4. Estimation of CO_2 Reduction Potential

A case study was performed to determine the potential for reducing CO_2 under conditions assuming traffic-flow smoothing and eco-driving promotion.

4.1. Assumed Conditions

The explanatory variables related to traffic flow and eco-driving used to change the distributions when performing the calculations were the reciprocal of the average travel speed τ, the acceleration energy equivalent per unit length A, and the eco-driving rating results P.

Note that the frequencies of the acceleration energy equivalent per unit length and the eco-driving rating results are biased according to the travel speed range (Fig. 15, Fig. 16), so the frequency was changed for each travel speed range.

This study assumed that the frequency of the acceleration energy equivalent per unit length changes so that the current maximum value is the center value, and the frequency of the eco-driving rating results changes so that the minimum value is the center value, in each travel speed range (Fig. 17).

It is expected that these changes can be realized by measures such as the Green Wave Running Assistance System that enables drivers to reduce unnecessary

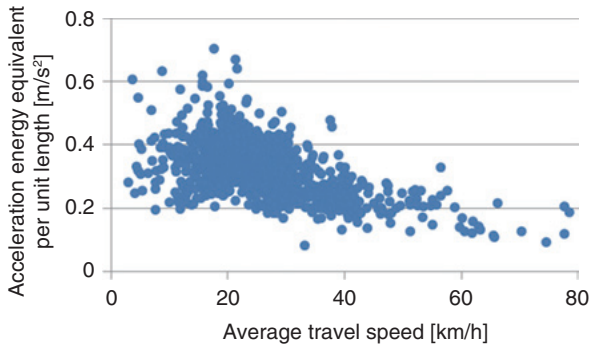


Fig. 15 Relation between average travel speed and acceleration energy equivalent

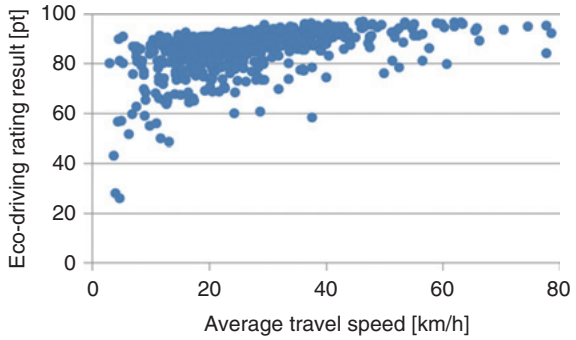


Fig. 16 Relation between average travel speed and eco-driving rating result

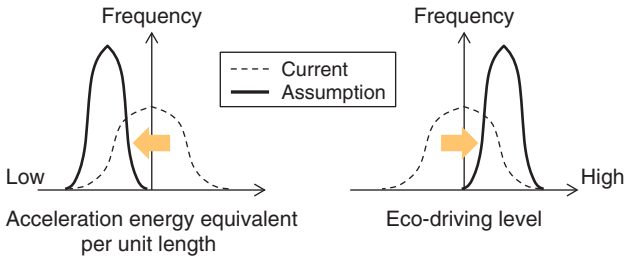


Fig. 17 Assumption for fuel economy improvement

Table 3 Travel-speed smoothing

Type	Effect
Profile signal control	10 km/h
Bypass road construction	6 km/h

acceleration and braking in accordance with signal information.

On the other hand, the references for the average travel speed were past cases of advanced signal control[3] and road construction such as bypass road construction[4] as shown in Table 3. The synergistic effects of the respective measures can also be estimated, but this study set a uniform increase of 10 km/h with an upper limit of 60 km/h.

4.2. Fuel Economy Estimation Results and CO_2 Reduction Potential

4.2.1. Traffic-flow smoothing

Figure 18 shows the change in the fuel economy distribution due to enhancing the acceleration energy equivalent per unit length and the travel speed, as calculated by the method described in section 3.1.1. The calculations showed that average fuel economy enhancement effects and CO_2 reduction potential of 8% could be realized by enhancing the acceleration energy equivalent per unit length, and 18% by also enhancing the travel speed.

4.2.2. Eco-driving

Likewise, the change in fuel economy due to enhancement of eco-driving rating results was also calculated by the method described in section 3.1.1. The subject hybrid cars are equipped with Eco Assist, and the results showed that additional fuel economy enhancement effects of 1% could be realized over and above the approximately 10% increase reported by Imai et al.[1]

4.3. Fuel Economy Enhancement and CO_2 Reduction Distributions

The fuel economy enhancement and CO_2 reduction potential distributions under the assumed conditions were analyzed. The potential calculation results in section 4.2.2 indicate that eco-driving has a small effect, so the distribution was analyzed for traffic-flow smoothing, that is to say enhancement of acceleration energy equivalent per unit length and travel speed.

Figure 19 shows the distribution of fuel economy enhancement due to enhancement of acceleration energy equivalent per unit length and travel speed. Here, the data with a low average travel speed and high acceleration energy equivalent per unit length exhibits a large fuel economy enhancement width. In particular, effects equal to or greater than the average fuel economy enhancement rate of 18% calculated in section 4.2.1 can be confirmed from the data for 30 km/h or less.

On the other hand, Fig. 20 shows the breakdown by travel speed of the CO_2 reduction potential of 18% due to traffic-flow smoothing that takes into account the driving amount. This shows that the travel speed range of 30 km/h or less not only has a large fuel economy enhancement width, but also accounts for most of the driving distance (Fig. 8). As a result, this speed range accounts for 2/3 of the CO_2 reduction potential.

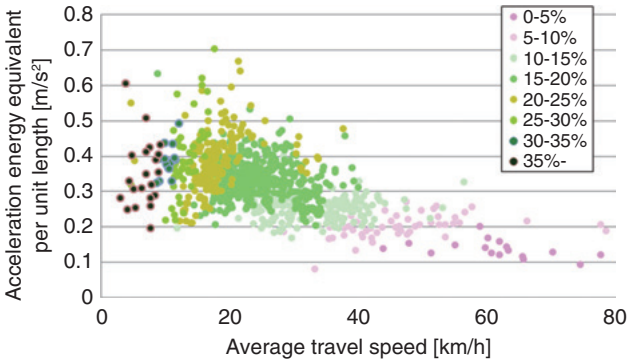


Fig. 19 Distribution of fuel economy improvement

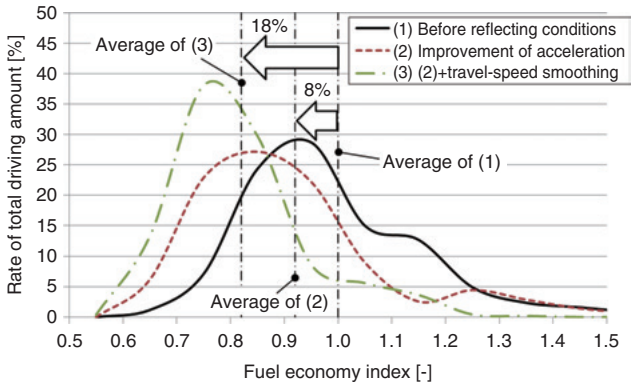


Fig. 18 Potential for fuel economy improvement

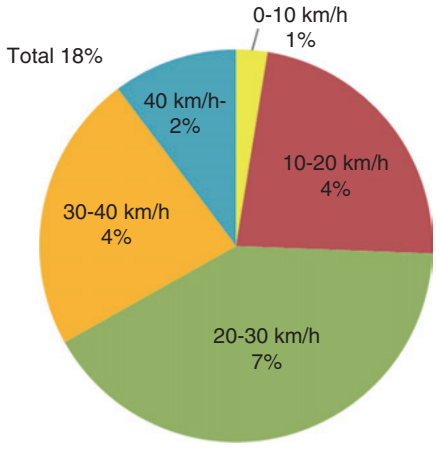


Fig. 20 Distribution of CO_2 reduction potential

5. Conclusion

This study obtained a polynomial that expresses a fuel economy index from floating car data, and attempted to calculate the CO_2 emissions reduction potential due to traffic-flow smoothing and eco-driving promotion under assumed conditions.

The results estimated a CO_2 reduction potential of 18% mainly due to traffic-flow smoothing. Past studies have reported Eco Assist effects of 10%, and eco-driving was calculated to have an additional CO_2 reduction potential of 1%.

In addition, the fuel economy enhancement rate and CO_2 reduction potential were found to be high at a travel speed of 30 km/h or less.

As shown above, the CO_2 reduction potential due to traffic-flow smoothing and eco-driving promotion under the assumed conditions was estimated and confirmed to have large expected effects. This indicates the importance of integrated approaches in addition to individual car measures, and also the importance of measures for areas with low travel speeds such as urban centers.

In addition to CO_2 reduction, traffic-flow smoothing and eco-driving promotion are also effective for shortening travel times and reducing fuel consumption. Therefore, it is hoped that methods for realizing the assumed conditions in this study will be investigated, and society-wide efforts made.

References

(1) Imai, T., Masuda, T., Ishido, Y., Sengoku, K. Teitansoshakai jitsugennimukete, telematics ga dekirukoto -senshinno telematics service niyoru kankyouheno torikumi, JSAE Convention Proceedings, No. 48-10, p. 11-14 (2009) (in Japanese)
(2) Foundation for Promoting Personal Mobility and Ecological Transportation: Eco-drive no fukyuhokokusho, p. 46 (2007) (in Japanese)
(3) Miyagi, H.: The Experiment on Intelligent Signal Control by Profile Signal Control, ITS World Congress (2009)
(4) Road Bureau, Ministry of Land, Infrastructure and Transport: Chikyuondankaboshinotameno doroseisakukaigi: Chikyuondankaboshinotameno doroseisakukaigihokoku, p. 22 (2005) (in Japanese)
(5) Energy ITS kenkyukai, Energy ITS no fukyunimukete, p. 24 (2008) (in Japanese)
(6) Imaizumi, H., Sengoku, K.: Floating car data no kaisekiniyoru kotsuryukaizen oyobi eco-drive deno CO_2 sakugen potential no kento, Conference on Energy, Economy, and Environment, (2012) (in Japanese)
(7) Oguchi, T., Katakura, M., Taniguchi, M.: Carbondioxide Emission Model in Actual Urban Road Vehicular Traffic Conditions, Proceedings of JSCE, No. 695/IV-54, p. 125-136 (2002)

■ Author ■



Hidetoshi IMAIZUMI



Koji SENGOKU

Honda R&D Co., Ltd.
Honda R&D Technical Paper Committee

Motorcycle R&D Center
Automobile R&D Center
Power Products R&D Center
Aircraft Engine R&D Center
Fundamental Technology Research Center
Honda R&D Americas

Editorial Afterword

Where does the motivation for engineers in a corporation to write a paper come from, I wonder?

Their time is taken up every day with product development, research projects, and other work of that kind. I think it requires strong motivation for people who are so busy and have such limited time to complete an article.

A paper is a logical embodiment of the belief that one's own research is valid and has novelty with respect to past research. The reasons for writing a paper could include, for example, to publish one's own research results and so contribute to society, to make one's own results publicly known, to protect intellectual property rights in one's results, and to prevent one's research results from becoming scattered and lost.

The psychologist Abraham Maslow classified the basic needs of human beings in a hierarchy of five stages that goes from (1) physiological needs at the bottom up to (2) the need for safety, (3) the need for love and belonging, (4) the need for esteem and recognition, and (5) the need for self-actualization. In light of Maslow's ideas, the need to publish a paper probably comes under the need for recognition or the need for self-actualization, which places it as a high-level need at the fourth or fifth level.

The kinds of incentives that could raise the motivation for writing a paper might include financial compensation and reflection in one's work performance evaluation, but these are things that would satisfy the lowest level, that of physiological need. They are far different from the fourth- and fifth-level needs. Moreover, the lower-level needs have to be satisfied before a need at the next level up will be stimulated. This means that it is necessary to satisfy the first-to-third-level needs. There is a question, however, as to whether those first-to-third-level needs are fulfilled in the workplace environment found in corporations today.

What this means is that inspiring the motivation to write a paper that is felt by engineers in corporations will first of all require having the environment in place and in order. Then it will be necessary to take measures of some kind, in addition to that, to enable paper writers to satisfy their need for recognition and their need for self-actualization.

Akira Suto

©2012 Honda Motor Co., Ltd. (All rights reserved)

ISSN 1881-6223

Published by:
Honda Motor Co., Ltd.
2-1-1, Minami-Aoyama, Minato-ku,
Tokyo 107-8556, Japan

Edited by:
Honda R&D Co., Ltd.
Honda R&D Technical Paper Committee

Printed:
Sep. 1, 2012

